Mathematical Modeling of Blood-Gas Kinetics for the Volatile Organic Compounds Isoprene and Acetone

DISSERTATION

by

Julian King

submitted to the Faculty of Mathematics, Computer
Science and Physics of the University of Innsbruck

in partial fulfillment
of the requirements for the degree of
doctor of science

supervised by
Prof.(FH) DI Dr. Univ.-Doz. Karl Unterkofler

Breath Research Unit

ÖAW
Austrian Academy
of Sciences

Innsbruck, November 2010

Acknowledgements

I am very grateful to my supervisors **Karl Unterkofler**, **Anton Amann**, and **Gerald Teschl** for their mentoring over the last three years, for the constructive criticism and the constant support of my work.

Thanks are also due to all other people working at the Breath Research Institute of the Austrian Academy of Sciences, particularly to **Helin Koç**, **Paweł Mochalski**, and **Alexander Kupferthaler** for the many fruitful discussions and the close collaboration within a theoretical and experimental framework.

I wish to express my deep thanks to my family, especially to my grandparents **Eva** and **Walter**, to **Angela**, and to **Isabel** and her family, for all the support, the patience, the understanding, and the love I have received ever since I can remember.

Last but not least, I greatly appreciate the financial support by the Austrian Academy of Sciences through a DOC-fellowship at the Breath Research Institute.

Abstract

Mathematics Subject Classification 92C45 · 92C35 · 93C10 · 93B07
PACS 87.80.-y · 82.80.Ms · 47.63.mh · 47.63.Ec · 87.19.U

Breath gas analysis is based on the compelling concept that the exhaled breath levels of endogenously produced volatile organic compounds (VOCs) can provide a direct, non-invasive window to the blood and hence, by inference, to the body. In this sense, breath VOCs are regarded as a comprehensive repository of valuable physiological and clinical information, that might be exploited in such diverse areas as diagnostics, therapeutic monitoring or general dynamic assessments of metabolic function, pharmacodynamics (e.g., in drug testing) and environmental exposure (e.g., in occupational health).

Despite this enormous potential, the lack of standardized breath sampling regimes as well as the poor mechanistic understanding of VOC exhalation kinetics could cast a cloud over the widespread use of breath gas analysis in the biomedical sciences. In this context, a primary goal of the present thesis is to provide a better quantitative insight into the breath behavior of two prototypic VOCs, isoprene and acetone. A compartmental modeling framework is developed and validated by virtue of real-time breath measurements of these trace gases during distinct physiological states. In particular, the influence of various hemodynamic and ventilatory parameters on VOC concentrations in exhaled breath is investigated. This approach also complements previous steady state investigations in toxicology.

From a phenomenological point of view, both acetone and isoprene concentrations in end-tidal breath are demonstrated to exhibit a reproducible non-steady state behavior during moderate workload challenges on a stationary bicycle. However, these dynamics depart drastically from what is expected on the basis of classical pulmonary inert gas elimination theory. More specifically, the start of exercise is accompanied by an abrupt increase in breath isoprene levels, usually by a factor of 3 to 4 compared with the steady state value during rest. This phase is followed by a gradual decline and the development of a new steady state after about 15 min of pedaling. Acetone concentrations closely resemble the profile of alveolar ventilation, resulting in slightly increased, roughly stable levels during the individual workload segments.

While for acetone the above-mentioned discrepancy can be explained by reference to gas exchange mechanisms in the conductive airways, a major part of breath isoprene variability during exercise conditions can be attributed to an increased fractional perfusion of potential storage and production sites, leading to higher levels of mixed venous blood concentrations at the onset of physical activity. In this context, various lines of supportive evidence for an extrahepatic tissue source of isoprene are presented.

The results discussed within the framework of this thesis are a first step towards new guidelines for the breath gas analysis of isoprene as well as acetone and are expected to have general relevance for quantitatively examining the exhalation, storage, transport, and biotransformation processes associated with volatile organic compounds in vivo.

Keywords: breath gas analysis, volatile organic compounds, acetone, isoprene, modeling, proton transfer reaction mass spectrometry, gas chromatography mass spectrometry

To Isabel and my parents

Contents

1 Introduction **3**
1.1 Medical background and perspectives . . . 3
1.2 Measurement principles . . . 6
1.3 Quantitative modeling in breath gas analysis . . . 7
1.4 Outline and contributions . . . 9

I Mathematical tools for VOC modeling **11**

2 Modeling principles for VOC kinetics **13**
2.1 The ideal gas law . . . 13
2.2 Diffusion and Henry's law . . . 14
2.3 Compartmental mass transport . . . 15

3 Off-line identification **21**
3.1 A priori identifiability . . . 21
3.2 Nonlinear least squares methodology . . . 26
3.3 Multiple shooting . . . 27
3.3.1 Numerical setup . . . 27
3.3.2 Optimality conditions and convergence . . . 32
3.3.3 Globalization of convergence . . . 35
3.4 Confidence intervals . . . 36
3.4.1 Direct methods . . . 36
3.4.2 Bootstrap confidence intervals . . . 38

4 On-line identification **43**
4.1 Stochastic difference equations . . . 43
4.1.1 Discretization . . . 43
4.1.2 Stochastic framework . . . 44
4.2 Nonlinear filtering . . . 46
4.2.1 Sequential Bayes filter . . . 47
4.2.2 Kalman filtering . . . 48
4.2.3 Particle filtering . . . 51
4.2.4 Dual estimation . . . 55
4.3 Anesthetic monitoring . . . 59
4.3.1 Problem statement . . . 59
4.3.2 Sevoflurane monitoring . . . 61
4.A Stochastic simulation . . . 66
4.A.1 Pseudo-Randomness . . . 67
4.A.2 General simulation principles . . . 67

Bibliography **71**

II Experimental results **77**

5 Paper A **79**

6 Paper B **97**

III Modeling results **115**

7 Paper C **117**

8 Paper D **131**

9 Paper E **165**

Curriculum Vitae **185**

Chapter 1

Introduction

1.1 Medical background and perspectives

"Physicians have diagnosed what is ailing the patient from the breath since the days of Hippocrates. The modern era of breath testing commenced in 1971, when Nobel Prize winner Linus Pauling demonstrated that human breath is a complex gas, containing well over 200 different volatile organic compounds in picomolar concentrations." [114]

The identification of physiological status and disease based on the composition of human breath has a long tradition in medical practice. It dates back to the fundamental observation that certain pathogenic processes give rise to a characteristic smell of the patient and its exhalate. Even though the nature of the underlying disease was not always understood, such aromas allowed for the distinction between numerous "evil humors", that have nowadays been linked to specified physiological or metabolic abnormalities. Prominent examples include the well-known *fetor hepaticus* (the smell of musty fish due to sulfur compounds) associated with liver failure or the odor of decaying apples accompanying severe diabetes (which has later been attributed to the excessive amounts of acetone emitted in the breath and from the skin of such patients).

Odor	Disease
Sweet, fruity (decomposing apples)	Ketoacidosis (e.g., diabetes)
Fishy	Uremia
Musty (raw liver)	Hepatic failure
Feculent, foul	Intestinal obstruction
Urine-like (ammoniacal)	Uremia
Foul, putrid	Lung abscess, empyema, intranasal foreign body
Sweaty feet, cheesy	Isovaleric academia

Table 1.1: Summary of typical breath aromas that have been related to specific disorders [108].

While characteristic breath odors had served as diagnostic parameters since antiquity, further exploitation of their full potential was naturally limited by the sensitivity of the human olfactory system[1]. However, interest into this kind of patient assessment was soon renewed with the emergence of powerful novel analytical techniques during the 1950s, most notably gas chromatography combined with mass spectrometric detection (GC–MS). These methodologies for the first time enabled the extraction of detailed information on the chemical composition of breath, thus going beyond the main respiratory gases nitrogen (N_2), oxygen (O_2), and carbon dioxide (CO_2). In 1971, Nobel laureate Linus Pauling and co-workers demonstrated that human breath is a complex gas mixture, containing well over 200 different volatile organic compounds (VOCs[2]) in picomolar concentrations [123, 165]. Even though Pauling could not identify these trace gases at the time, his findings marked the beginning of a new era of breath testing. In particular, it was recognized that volatile compounds in breath might carry valuable clinical information on the status of an individual that is complementary to the insight gained from standard diagnostic routines (e.g., serum or urine probes, which predominantly center on the analysis of large molecular weight, non-volatile indicators such as ions or proteins).

---

[1] Note, however, that several studies have investigated the extraordinary scenting ability of other mammals in this context, e.g., dogs sniffing out lung and breast cancer in its early stages of development [110].

With the advent of high-sensitivity analysis methods, detection and quantification procedures of VOCs in human exhaled breath were continuously improved. This also motivated increased experimental efforts aiming at the identification of potential breath biomarkers[3]. The first substantial review of the field of breath gas analysis was published by Manolis [108]. A few years later, Preti suggested that exhaled breath analysis could be used for the detection of lung cancer [130]. Ground-breaking work on nitric oxide NO (produced in the lungs and the sinuses and considered to be reflective of airway inflammation) was initiated by Gustafsson, Lundberg and Weitzberg [67, 106, 4, 107] and by Kharitonov and Barnes [87, 86] in the 1990s. During the same time, Phillips published a series of papers on exhaled breath analysis of lung cancer patients and patients suffering from mamma carcinoma [126, 127]. Pioneering results on the production of acetaldehyde by cancer cell cultures were described by Smith and Španěl [152]. Moreover, several groups proposed nominal levels for a series of VOCs in normal healthy populations [143, 91, 169, 168, 170].

In recent years, several hundreds of specific compounds have been established as regular constituents of normal human breath. Some major examples together with their tentative physiological sources are listed in Table 1.2. Breath concentrations of these VOCs typically range from ppb (parts per billion, i.e., one molecule in 10^9 particles of air) to ppm (parts per million, i.e., one molecule in 10^6 particles of air).

Compound	Concentration	Physiological / pathological source
Acetone	ppm	Decarboxylation of acetoacetate, diabetes
Ammonia	ppm	Protein metabolism, liver and renal disease
Carbon dioxide	%	Product of respiration, Helicobacter pylori
Carbon disulfide	ppb	Gut bacteria, schizophrenia
Carbon monoxide	ppm	Production catalyzed by heme oxygenase
Carbonyl sulphide	ppb	Gut bacteria, liver disease
Ethane	ppb	Lipid peroxidation and oxidative stress
Ethanol	ppb	Gut bacteria
Ethylene	ppb	Lipid peroxidation, oxidative stress, cancer
Hydrocarbons	ppb	Lipid peroxidation/metabolism
Hydrogen	ppm	Gut bacteria
Isoprene	ppb	Cholesterol biosynthesis
Methane	ppm	Gut bacteria
Methanethiol	ppb	Methionine metabolism
Methanol	ppb	Metabolism of fruit
Nitric oxide	ppb/ppm	Production catalyzed by nitric oxide synthase
Pentane	ppb	Lipid peroxidation, oxidative stress
Water	%	Product of respiration

Table 1.2: Summary of major constituents of exhaled breath together with their tentative synthetic pathways [111].

VOCs appearing in exhaled breath may roughly be classified into two major groups, depending on whether their origin is primarily exogenous or endogenous. Exogenous volatile compounds penetrate the human body mainly by ingestion, inhalation or dermal routes and thus reflect environmental exposure. Contrarily, endogenous volatile compounds are released within the human organism (e.g., as a result of normal metabolic activity or due to pathological disorders), may enter the blood stream and are eventually excreted via exhalation, skin emission, urine, etc. (see also Fig. 2.1). While the discrimination between these two groups is critical for breath gas analysis (in the sense that only endogenous compounds can potentially qualify as biomarkers) it is not as trivial as it may seem at first glance[4]. Moreover, even for VOCs that are widely regarded as endogenous, the precise sources or biochemical pathways responsible for their formation often remain obscure. Further in vitro investigations of volatiles released from bacteria and cell cultures will be required to bridge this gap.

---

[2] The definition of a VOC has not been standardized. However, a common characteristic of all such molecules is their significant vapor pressure, thus leading to a high evaporation rate even at relatively low (e.g., ambient) temperature ranges.

[3] referring to compounds that might be used for detecting disease according to their (increased/decreased) appearance or lack in breath as compared to a healthy state.

The fact should be stressed that while the search for disease-specific biomarkers can be seen as the driving force for the development of breath gas analysis as an independent area of research, breath gas analytical investigations appear to have a much broader scope than previously envisaged. Indeed, the detection and quantification of these trace gases seems to fulfill all the demands and desires for non-invasive investigations and has been put forward as a versatile tool for general biomonitoring applications. These include therapy control as well as dynamic assessments of normal physiological function (e.g., in an intra-operative setting, see also Section 4.3), pharmacodynamics (drug testing) or body burden in response to environmental exposure (e.g., in occupational health) [6, 7, 5, 29, 134, 113, 128, 8]. Exhaled breath can nowadays be measured on a breath-by-breath resolution, therefore rendering breath gas analysis as an optimal choice for gaining *continuous* information on the metabolic and physiological state of an individual. Furthermore, as has been impressively demonstrated in the Nobel prize-winning work by Furchgott, Ignarro and Murad on the small inorganic molecule nitric oxide, trace gases can themselves actively participate in the regulation of physiological events [82, 19]. This renders VOCs as a promising tool for examining more fundamental endogenous processes.

Summarizing, breath gas analysis holds great promise for the biomedical sciences. In particular, it enjoys several advantages over traditional experimental and diagnostic procedures based, e.g., on blood or urine samples or biopsies. Apart from its non-invasive nature and the obvious improvement in patient compliance/tolerability, major hallmarks of breath testing comprise unlimited sample extraction as well as rapid on-the-spot evaluation or even *real-time* analysis, cf. Section 1.2. Despite this terrific potential, only a few breath tests have already been introduced into clinical routine, see Table 1.3.

Breath VOC	Area of application
Ethanol	Law enforcement
Hydrogen	Carbohydrate malabsorption
Nitric oxide	Asthma
Carbon monoxide	Neonate jaundice
$^{13}CO_2$	Helicobacter pylori infection
Branched hydrocarbons	Heart transplant rejection

Table 1.3: Summary of clinically employed breath tests as approved by the United States Federal Drug Administration FDA [7].

This can mainly be traced back to the fact that multiple confounding factors may affect breath gas analysis results, including contamination from ambient air, interference from other molecules, the subject's cardiopulmonary status, pre-measurement exposure, tobacco use, etc. [138]. Consequently, further methodological efforts are needed before breath analysis can become the “new blood test” . Particularly, drawing reproducible breath samples remains an intricate task that has not been fully standardized yet. Moreover, inherent error sources introduced by the complex mechanisms driving pulmonary gas exchange have not been investigated in sufficient depth, cf. Section 1.3.

---

[4] Consider methanol for instance, which is a byproduct of fruit fermentation in the stomach but can also be considered as a common constituent of laboratory air due to its widespread use as a solvent.

1.2 Measurement principles

The renewed interest in breath analysis is also a reflection of the remarkable advances in analytical chemistry instrumentation. These developments have led to a continuous lowering of detection limits and have gone hand in hand with the construction of more compact and even hand-held monitoring devices suitable for *point-of-care* examinations.

From an analytical viewpoint, human breath is an extraordinarily complex matrix to measure. Quantitative assessments are primarily complicated by the consistency of the breath sample itself (e.g., due to interferences with the high amount of moisture and carbon dioxide), but also by fact that the involved VOCs cover an extremely wide spectrum of distinct physico-chemical properties (ranging, e.g., from the diatomic, inorganic and low-soluble molecule nitric oxide to polyatomic, highly soluble structures such as alcohols and ketones). Consequently, the range of measurement techniques employed for breath gas analytical investigations is extremely diverse and each method comes with its specific strengths and weaknesses. Key technologies in this context include gas chromatography with mass spectrometric detection (GC–MS), proton transfer reaction mass spectrometry (PTR–MS), selected ion flow tube mass spectrometry (SIFT–MS), ion mobility spectrometry, ion mobility reaction mass spectrometry, laser absorption spectrometry and photoacoustic spectrometry. Additionally, several electrochemical, optical or semiconductor sensors may be used. Recent overviews of the available methods can be found in [31, 7]. In this thesis, focus will be given to GC–MS and PTR–MS.

Traditionally, breath gas analysis has its roots in GC–MS measurements. Extensive background material on this technique is provided in [63, 66]. Briefly, the decisive feature of GC–MS is that the individual components of a complex gas mixture are pre-separated by means of a chromatographic column. The interior of the latter is coated with active material (the so-called *stationary phase*, usually consisting of a microscopic layer of polymers such as polydimethylsiloxane), designed to interact with the sample such that different components elute from the column at different times. For fixed analysis conditions this retention time is a compound-specific parameter that can be used for substance identification. Subsequently, the eluted VOCs undergo ionization and the resulting cracking patterns are determined by virtue of conventional mass spectrometry. These mass spectra can then be compared to spectral libraries of known compounds, hence providing further means for confirming the previous identification step. Quantification of identified trace gases may be achieved by comparison with measurements of *standard samples*, involving known concentrations of pure compounds. GC–MS is widely regarded as *gold standard* for breath gas analysis. However, a major drawback is that time-intensive preconcentration steps are mandatory with this technique (due to the typically small total amounts of VOCs present in the sample), thus precluding its use in real-time evaluations of VOC behavior in exhaled breath. Moreover, GC–MS measurements are usually carried out by collecting and storing the breath sample in some container (e.g., *Tedlar* bags) prior to analysis. This intermediate step is a rather error-prone task, especially with respect to potential losses or contaminations.

Contrarily, during the last 15 years fascinating mass spectrometric techniques have been developed that permit the measurement of exhaled breath with breath-by-breath resolution, i.e., on a time-scale of less than 0.5 s [5]:

- proton transfer reaction mass spectrometry (PTR–MS) by Werner Lindinger, Tilmann Märk, and Armin Hansel at the Institute of Ion Physics in Innsbruck [97, 98],
- selected ion flow tube mass spectrometry (SIFT–MS) by David Smith and Patrik Španěl at Keele University and the Heyrovsky Institute of Physical Chemistry in Prague [151, 150], and
- Xenon/Krypton charge transfer mass spectrometry (marketed under the name *Airsense*) by Johannes Villinger in the company V&F (Absam near Innsbruck) [75].

In particular, these techniques avoid the above-mentioned issues by "directly breathing into the analytical device". A typical picture of this situation is shown in Chapter 8, Fig. 2. The fact is stressed that these devices generally act like a specific sensor for a selected ensemble of previously identified substances. In other words, the above mass spectrometers are primarily intended for monitoring applications rather than identification purposes[5]. On the other hand, their real-time capability can be viewed as an essential requirement for relating changes in breath VOC concentrations to quick variations in hemodynamic or respiratory flow, cf. Section 1.3.

For an extensive overview of PTR–MS methodology the interested reader is referred to [97, 98, 24]. In brief, this analytical technique has proven to be a sensitive method for the quantification of volatile molecular species M on the basis of “soft” chemical ionization within a drift chamber[6]. More specifically, it takes advantage of the proton transfer

$$\mathrm{H_3O^+ + M \rightarrow MH^+ + H_2O}$$

from primary hydronium precursor (reagent) ions originating in an adjoint hollow cathode. Specifically, this reaction scheme is selective to VOCs with proton affinities higher than water (166.5 kcal/mol), thereby avoiding the ionization of the bulk composition exhaled air, N_2, O_2 and CO_2. Count rates of the resulting product ions $\mathrm{MH^+}$ or fragments thereof appearing at specified mass-to-charge ratios m/z can subsequently be converted into absolute concentrations of the protonated compounds. Further details on quantification can be found in [142] .

Even though sufficiently accurate and fast instrumental techniques are vital for exhaled breath analysis, further methodological issues have to be addressed. Specifically, the breath sampling step itself has emerged as a crucial factor for reliable breath analysis. In fact, different breathing patterns or collection regimes can make a dramatic difference to the measured VOC concentrations of interest, thus promoting the establishment of unified sampling guidelines [35, 6]. A prototypic example is the implementation of standardized procedures for determining exhaled lower respiratory nitric oxide and nasal nitric oxide [1].

While similar guidelines for the sampling of other trace gases would be desirable, in everyday measurement practice breath is simply collected in an *end-tidal* manner. This means that the first part of the exhalation – corresponding to the gas volume filling the anatomical dead space and hence not participating in gas exchange according to classical pulmonary inert gas elimination theory – is discarded and only the last exhalation segment (reflecting “alveolar air”) is kept for analysis. In more sophisticated sampling systems, end-tidal extraction is triggered by virtue of simultaneously measured CO_2- and/or flow-data [72, 23], see also Chapter 5. While such setups are an important contribution to current standardization efforts in breath sampling, they are far from being perfect. Specifically, these sampling systems can not account for the variability of breath VOC concentrations stemming from varying physiological conditions.

1.3 Quantitative modeling in breath gas analysis

As has already been indicated in the previous section, a fundamental yet underestimated aspect of breath gas analysis concerns the blood-gas kinetics of the VOCs under scrutiny. With active research predominantly focusing on the explorative search for potential biomarkers, it is sometimes argued that *“... from the perspective of point-of-care clinical practice, empirical methods for pattern recognition are sufficient to make a valid diagnosis and ... knowledge of the specific biochemical pathways may not be necessary*[7]*.”* This appears to be an acceptable standpoint if future breath tests can eventually be reduced to binary outcomes, in the sense that the detection/rejection of a disease can be based solely on the appearance or complete lack of specific substances in breath. However, the applicability of such a yes-no scheme is highly unlikely and recent results indicate that the discrimination between diseased and healthy states will mainly hinge on concentration differences. In such cases, a thorough physiological understanding of the underlying blood-gas kinetics becomes imperative.

To illustrate this point, consider the population study result in Fig. 1.1 (cf. [15]), which may suggest the detection of lung cancer patients on the basis of decreased isoprene levels in end-tidal breath.

---

[5] Note, however, that high-end PTR–MS devices based on time-of-flight mass spectrometry enable the separation of isobaric molecules, thus providing a mass resolution that might be sufficient for compound identification [32].

[6] Here, “soft” refers to the fact that no pronounced fragmentation of the nascent product ions occurs.

[7] M. Phillips, PittCon 2010, cf. [129]

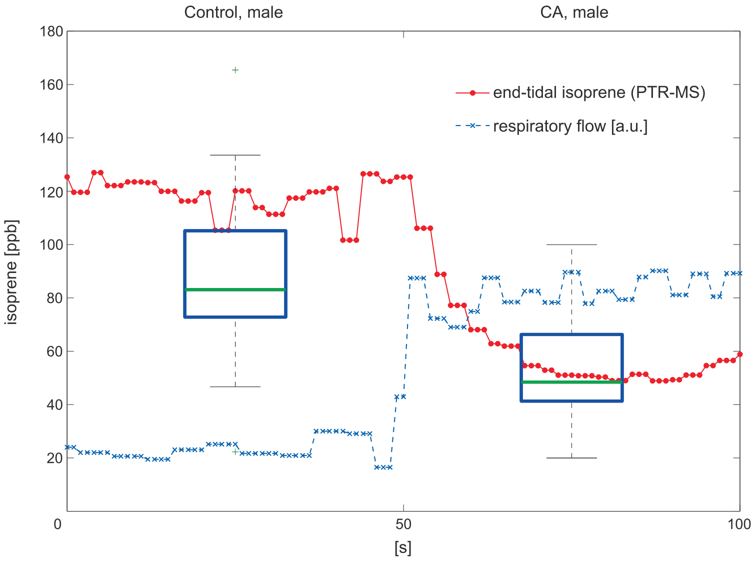

Figure 1.1: Overlay depicting the variability of end-tidal isoprene concentrations during hyperventilation of one single volunteer as compared to the population boxplots associated with healthy test subjects and lung cancer patients.

Effectively, from the respective boxplots a tentative discriminatory value of about 70 ppb might be established. Note, however, that from a procedural point of view this observation will be of limited use, since any further attempt to classify a specific individual will strongly depend on the hemodynamic and respiratory status of the test subject investigated. Correspondingly, by measuring end-tidal isoprene levels with breath-by-breath resolution (e.g., using PTR–MS), it can be demonstrated that a normal healthy male volunteer at rest might easily switch between the two groups above merely by changing his breathing pattern (for example by breathing faster or with an increased tidal volume). Doing so leads to an instantaneous drop of breath isoprene levels and might thus provoke a misclassification of this volunteer. Consequently, any screening study results like the one above must be complemented by information on their variability with changes of ventilation or blood flow.

The above line of argumentation nicely demonstrates some of the pitfalls that can be encountered when overlooking the impact of physiological parameters on the interpretation of breath gas analysis results. It also emphasizes the fact that the knowledge of a potential biomarker VOC is simply not enough: in order to make breath tests operational, a detailed insight into the diverse physiological factors affecting the breath levels of such compounds will be required [138]. Much can be learnt in this context from the cumbersome development of the nitric oxide breath test, which nowadays ranges among the most widely reported exploitations of breath gas analysis within a clinical setting [6]. This paradigmatic example shows that good quantitative assessment of the underlying exhalation kinetics is mandatory when aiming at the successful introduction of a clinically applicable breath test.

The general assumption is that VOCs present in end-tidal air evolve from the blood and that their concentrations in the exhalate (gaseous phase) are representative of the respective blood concentrations. In classical pulmonary inert gas elimination theory this relationship is captured by the so-called Farhi equation [50] (see also Chapter 5 for a derivation), predicting a direct proportionality between the alveolar concentration C_{A} of a VOC (presumed to be accessible from end-tidal exhalation segments as described before) and its concentration $C_{\bar{\mathrm{v}}}$ in mixed venous blood. Here, the associated proportionality factor depends on the substance-specific blood:gas partition coefficient $\lambda_{\mathrm{b:air}}$ (describing the diffusion equilibrium in the respiratory microvasculature, cf. Section 2.3), alveolar ventilation $\dot{V}_{\mathrm{A}}$ (governing the transport of the compound through the respiratory tree), and cardiac output $\dot{Q}_{\mathrm{c}}$ (controlling the rate at which the VOC is delivered to the lungs), viz.,

$$C_{\mathrm{measured}} = C_{\mathrm{A}} = \frac{C_{\bar{\mathrm{v}}}}{\lambda_{\mathrm{b:air}} + \frac{\dot{V}_{\mathrm{A}}}{\dot{Q}_{\mathrm{c}}}}. \tag{1.1}$$

The Farhi equation offers a first simplified description of mass balance principles in the lungs and can be seen as a starting point for the present thesis. More specifically, a natural question to ask is whether the previous relationship can be expected to have general relevance for a reasonably wide range of volatile compounds as well as experimental scenarios. In this context, the fact is stressed that the Farhi equation is essentially a steady state concept that might not be suited for explaining non-steady state behavior, e.g., in response to relatively quick physiological changes (for instance during exercise). Correspondingly, a major objective of this work will be to critically review and possibly extend classical pulmonary inert gas elimination theory by examining the exhalation dynamics of two highly abundant, endogenous trace gases found in human breath:

- isoprene, which is low-soluble in blood (as reflected by a small blood:gas partition coefficient $\lambda_{\mathrm{b:air}} \approx 0.75$), lipophilic and presumed to be correlated with cholesterol synthesis [159] and
- acetone, which has a high affinity for blood ($\lambda_{\mathrm{b:air}} \approx 340$), has been linked to fat catabolism and might serve as biomarker for diabetic disorders [83].

From the above, both isoprene and acetone can be viewed as prototypic examples for the analysis of two major classes of VOCs, even though they cannot cover the whole spectrum of different physico-chemical properties. Furthermore, these two compounds rank among the most notable VOCs studied in the context of breath gas analysis and thus represent paradigmatic choices for a more detailed assessment of observable trace gas behavior in exhaled breath.

In summary, while breath gas analysis would greatly profit from a more causal understanding of VOC kinetics in response to distinct physiological states, the development of quantitative formulations relating breath concentrations to the underlying systemic levels clearly lags behind the enormous analytical progress in the field. This situation calls for the establishment of a proper modeling framework, striving for validated mechanistic descriptions of VOC dynamics in different parts of the organism. As an outlook, from an operational point of view such modeling studies can

1. help to identify potential confounding factors affecting the interpretation of breath test results and propose corrective measures.
2. guide the ongoing standardization of sampling procedures and provide formal means for evaluating the information content of newly proposed experimental settings.
3. enhance the fundamental understanding of the physiological role of VOCs, e.g., by relating phenomenological features of observable breath concentration profiles to specific distribution, transport, biotransformation and excretion processes of these substances.
4. stimulate biochemical investigations exploring the endogenous (e.g., cellular) sources of VOCs

The last two points are directed towards further consolidating the potential role of breath gas analysis in biomonitoring applications and can be seen as a chief motivation for this thesis.

1.4 Outline of the thesis and overview of the contributions

The present dissertation is arranged in three parts. While the last two parts contain articles published in scientific journals, the first one is introductory.

Part I is intended to familiarize the reader with some basic physical and mathematical tools that have proven useful for quantitative descriptions of VOC kinetics. The *direct problem* of physiological model building will be discussed and several powerful concepts from *inverse problem* methodology will be reviewed in a roughly self-contained manner. The latter primarily comprise methods for parameter estimation in dynamic systems (both on an off-line and on-line basis) and will be employed in Part III for extracting unknown model quantities from measured breath data. Furthermore, in order to demonstrate the viability of these approaches at hand of a real-world application, a novel monitoring scheme for the volatile anesthetic sevoflurane during general inhalation anesthesia will be developed.

Part II is devoted to experimental techniques for acquiring VOC concentration profiles and comprises the two manuscripts *"Isoprene and acetone concentration profiles during exercise on an ergometer"* (Paper A), and *"Dynamic profiles of volatile organic compounds in exhaled breath as determined by a coupled PTR-MS/GC-MS study"* (Paper B), published in the *Journal of Breath Research* and *Physiological Measurement*, respectively. In the first article an experimental setup efficiently combining real-time PTR–MS trace gas measurements with data streams reflecting hemodynamic and respiratory parameters is developed. This setup then serves to illuminate the evolution of breath isoprene and acetone (and other VOCs) in conjunction with decisive physiological factors during rest and ergometer challenges. Such synchronized profiles represent a indispensable phenomenological basis pertinent to the present modeling approach. As a key feature, the aforementioned instrumentation introduces an innovative algorithm for automatic, selective breath-by-breath sampling of arbitrary exhalation segments based on volumetric flow data. In the second paper, a methodology for complementing PTR–MS measurements with independent GC–MS analyses is discussed. Such a simultaneous sample acquisition allows for a rigorous cross-validation of the experimental findings reported in Paper A. Moreover, it also aims at placing isoprene and acetone measurements in a broader context by comparing their non-steady state behavior with the profiles of VOCs expected to show similar exhalation kinetics.

These experimental efforts culminate in Part III, which is dedicated to novel quantitative descriptions of the physiological flow of isoprene and acetone in the human body. It contains the two articles *"Physiological modeling of isoprene dynamics in exhaled breath"* (Paper C), and *"A mathematical model for breath gas analysis of volatile organic compounds with special emphasis on acetone"* (Paper D), which have been published in the *Journal of Theoretical Biology* and the *Journal of Mathematical Biology*, respectively. Additionally, in the preprint *"A modeling based evaluation of isothermal rebreathing for breath gas analysis of highly soluble volatile organic compounds"* (Paper E), isothermal rebreathing will be investigated as an interesting experimental framework for corroborating the physical appropriateness and assessing the predictive power of the proposed acetone description. The presented models are derived in direct agreement with the respective breath behavior during distinct experimental scenarios (mainly exercise), thus demonstrating that dynamic patterns of breath VOCs reflect fundamental physiological changes that can potentially be used for exploring the fate of volatile molecular species in the human body. This rationale also opens up a new framework for non-invasively estimating substance-specific parameters from observable breath data, including quantities that would otherwise be difficult to access such as endogenous production/metabolization rates or kinetic rate constants for the exchange between air, blood, and different tissue compartments of the body. In this sense, the above contributions complement previous steady-state investigations in toxicology and are a first step towards new guidelines for reliable breath gas analyses of isoprene and acetone.

The fact is stressed that both the experimental and the modeling part are treated with equal attention. This allows for a continuous re-evaluation of the proposed models by means of suitably designed and newly adapted experimental regimes and may be considered as a particular achievement of the present work.

As first author of all articles compiled in this thesis I took a leading role in all stages of the publishing process, while greatly benefiting from the specific expertise of my co-authors. In particular, my contributions to Part II comprise the design and realization of the experimental setup, data gathering, formulation of the phenomenological results and the preparation of the manuscripts. The GC–MS measurements were carried out by P. Mochalski. In Part III, I was responsible for the development of the mathematical models, their numerical implementation as well as their experimental validation. Moreover, I drafted the corresponding manuscripts.

Part I

Mathematical tools for VOC modeling

Chapter 2

Modeling principles for VOC kinetics

Contents

2.1 **The ideal gas law** 13

2.2 **Diffusion and Henry's law** 14

2.3 **Compartmental mass transport** 15

The following sections briefly summarize the fundamental physical and methodological principles underlying the derivation of physiologically based models capturing the distribution of molecular trace gases (which will henceforth be denoted by M) within the human body. General discussion largely follows standard expositions on thermodynamics and biological mass transport, see [2, 167] for instance. Specific interpretations with respect to respiratory physiology are indicated where appropriate.

Remark 1. While a good grasp of elementary respiratory and cardiovascular physiology is essential for reading the papers in Part II and Part III, a detailed treatment of these topics would be beyond the scope of the present thesis. For a compact overview of some fundamental concepts the interested reader is referred to the excellent textbooks by West [179] as well as Mohrman and Heller [115]. A comprehensive modeling approach to cardiopulmonary physiology can be found in [166].

2.1 The ideal gas law

A gas consists of free molecules in a state of random motion. These molecules fill any container in which they are enclosed. By colliding with one another and with the walls of the container a pressure is exerted. This situation is captured by the *ideal gas law*,

$$PV = nRT, \tag{2.1}$$

where P denotes pressure, V is the volume occupied, n is the amount of gas in moles, and T is the absolute temperature[1]. In respiratory physiology, P is often measured in kilopascals (kPa) (or mmHg), V in liters (l), and T in Kelvin (K). The constant $R = 8.314\ \mathrm{l} \cdot \mathrm{kPa} \cdot \mathrm{mol}^{-1} \cdot \mathrm{K}^{-1}$ is called the universal gas constant.

The ideal gas law can be seen as a combination of three empirical gas laws. Firstly, it states that if temperature is kept constant, increasing/decreasing the pressure of the gas will decrease/increase the volume occupied (Boyle-Mariotte law). Also, at a constant volume, the pressure exerted by a gas is proportional to the absolute temperature (Gay-Lussac's law). Finally, under constant external conditions with regard to pressure and temperature, equal volumina of different ideal gases contain the same number of molecules

---

[1] Alternatively one may write $PV = NkT$, where N is the number of particles and k is Boltzmann's constant.

(Avogadro's law). In particular, under ambient conditions ($P = 101$ kPa and $T = 298$ K) one mole of an ideal gas occupies a volume of approximately 24.5 l.

Gases obeying the ideal gas law are referred to as *ideal gases*. Note, however, that the concept of an ideal gas is merely an idealized model, valid only within certain pressure and temperature ranges depending on the specific gas under scrutiny. Loosely spoken, it applies whenever the gas molecules can be considered as isolated points in space, having negligible volumes and exerting no intermolecular forces other than those resulting from perfectly elastic collisions between the molecules. As these conditions are usually fulfilled at the low pressures encountered in respiratory physiology, virtually all volatile compounds M considered in the present framework can be regarded as ideal gases[2].

Equation (2.1) holds true for mixtures of ideal gases as well. Specifically, for an ensemble of m gas species we may write

$$PV = (n_1 + ... + n_m)RT, \tag{2.2}$$

where P is the total pressure exerted by the gas mixture. Motivated by the previous relation, we may define the partial pressure P_i of the ith gas as

$$P_i = \frac{n_i RT}{V}. \tag{2.3}$$

It is the pressure that would be exerted by the gas species i alone, that is, if all other gas components were removed and if it occupied the entire volume of the container by itself. Relations (2.2) and (2.3) imply that the total pressure P of a gas mixture is equal to the sum of the partial pressures of its components, viz.,

$$P = P_1 + P_2 + ... + P_m. \tag{2.4}$$

This relation is called *Dalton's law*, stating that each gas exerts a pressure that is independent of the pressures of the other gases in the mixture. We may hence treat each component individually.

2.2 Diffusion and Henry's law

Fick's first law of diffusion states that the net flux J quantifying diffusional transport of a gas species M between two spatially homogeneous control volumes A and A' is proportional to the associated difference in partial pressure, i.e.,

$$J = k_{\text{diff}}(P_{M,A} - P_{M,A'}), \tag{2.5}$$

where the non-negative diffusion constant k_{diff} has dimensions of amount (in mol) divided by pressure and time. If the gas under scrutiny is in dissolved state rather than in gas phase, P_M is referred to as gas tension, defined as the partial pressure that would be exerted by the gas above the liquid if both were in equilibrium (e.g., oxygen tension in blood). In the following we will omit the subscript M. Equation (2.5) can also be expressed via a difference in concentrations. We will distinguish the following three cases:

(i). Firstly, if A as well as A' represent a gaseous medium and M can be treated as an ideal gas then – by the ideal gas law – its partial pressure P_A may be written as

$$P_A = C_A RT, \tag{2.6}$$

and analogously for $P_{A'}$. Here, $C_A := n_A/V_A$ is defined as the molecular concentration of M. Hence,

$$J = k_{\text{diff}}(C_A RT - C_{A'} RT) = \tilde{k}_{\text{diff}}(C_A - C_{A'}), \tag{2.7}$$

where $\tilde{k}_{\text{diff}}$ is defined by the above equation.

---

[2] For perspective, according to the van der Waals equations of state the true molar volume of acetone at the above-mentioned ambient conditions is about 23.98 l (cf. [96]), suggesting that the derivation from the "ideal" mole volume is negligible.

(ii). Similarly, if both A and A' are liquids, we can make use of Henry's law stating that the amount of a gas M that can dissolve in a liquid under equilibrium conditions [3] is directly proportional to the respective tension, viz.,

$$C = HP. \tag{2.8}$$

Here the solute- and solvent-specific Henry constant $H = H(T)$ is inversely related to temperature. Substituting the last expression into Equation (2.5) yields

$$J = k_{\text{diff}} \left(\frac{C_A}{H_A} - \frac{C_{A'}}{H_{A'}} \right). \tag{2.9}$$

(iii). Finally, let us assume that A' represents a liquid, while A is a gas volume. The prototypic example for this situation in the present context is the blood-gas interface, separating the respiratory microvasculature from the alveoli. In this case, by combining (2.6) and (2.8) we arrive at

$$J = k_{\text{diff}} RT \left(C_A - \frac{C_{A'}}{H_{A'}RT} \right) = \tilde{k}_{\text{diff}} \left(C_A - \frac{C_{A'}}{H_{A'}RT} \right). \tag{2.10}$$

In case of a diffusion equilibrium, i.e., if $J = 0$, we deduce from Equation (2.9) that

$$\frac{C_{A'}}{C_A} = \frac{H_{A'}}{H_A} =: \lambda_{A':A}, \tag{2.11}$$

where the positive dimensionless quantity $\lambda_{A':A}$ is the so-called partition coefficient between A' and A (e.g., $\lambda_{\text{blood:fat}}$). Analogously, its reciprocal value is denoted by $\lambda_{A:A'}$.

Similarly, from (2.10) the ratio between the liquid phase concentration and gas phase concentration of M in equilibrium is given by

$$\frac{C_{A'}}{C_A} = H_{A'}RT. \tag{2.12}$$

The expression $H_{A'}RT$ again represents a partition coefficient denoted by $\lambda_{A':A}$ (e.g., $\lambda_{\text{blood:air}}$) and is a measure of the solubility of the gas M in the solvent A'. Hence, $\lambda_{A':A}$ allows to classify M as low or highly soluble with respect to A'. In respiratory physiology $H_{A'}RT$ is also termed the *Ostwald solubility coefficient*.

Remark 2. Henry's law (2.8) exclusively refers to the physically dissolved gas molecules, i.e., it is only valid for gases that do not form chemical combinations with some component of the solvent (e.g., blood). Such gases are called *inert gases*. While in the context of VOC modeling most volatile compounds M will fall into this category, some important exceptions in the field of respiratory physiology include oxygen (O_2), carbon dioxide (CO_2) and carbon monoxide (CO). When carried in blood, due to a number of reactions (primarily with hemoglobin and water) the physically dissolved fraction of these gases is small compared to the chemically bound amount. Accordingly, the relation (2.8) must be replaced by more complicated *dissociation functions*.

2.3 A primer on compartmental mass transport

The development of mechanistic descriptions for biological and physiological processes is complex for several reasons [132]. Firstly, unlike in other fields such as physics and engineering, quantitative relationships between biological and physiological variables are often formulated on an empirical or heuristic basis rather than being derived from first principles. Moreover, in the former domains the system components are usually known a priori (consider the ensemble of electrical elements comprising an electronic circuit for instance) and one might hence predict all the important features of the system as a whole. On the contrary, when it comes to modeling *in vivo* phenomena associated with, e.g., human physiology and biochemistry, a delicate preliminary task consists in *identifying* the basic mechanisms affecting an experimentally observed behavior.

---

[3] When a gas and a liquid are at an (dynamic) equilibrium, the number of molecules escaping the liquid statistically equals the number of molecules dissolving in it.

The issues raised above are inherent to quantitative assessments of VOC dynamics in the human body. Nevertheless, like any physical system, these dynamics have to respect a set of fundamental laws that can be employed for guiding the modeling process. An elementary but particularly useful tool in this context is the concept of *mass balance*, coupled with a *compartmental* model design. A quite general formal definition of a compartment has been given in [18] as follows: if a substance M is present in a system in several distinguishable forms or locations and if M passes from one form or location to another form or location at a measurable rate, then each form or location constitutes a separate compartment for M. Similarly, a compartment might be seen as any discrete, functional unit of the investigated system in which M can reasonably be postulated to behave uniformly. We shall refer to a compartment model as a set of compartments interacting by exchanging material. In graphical representations, the compartments are usually depicted as boxes, while an exchange mechanism between two compartments is indicated by a directed arrow.

Within a physiological framework, the compartmental approach to mass transfer traditionally consists in dividing the body into an ensemble of roughly homogeneous anatomic structures or tissue control volumes that are interconnected via the arterial and venous network [131, 94, 9, 62, 54]. This yields a simplified representation of the human organism, reflecting known or hypothesized physiology and biochemistry. A typical example is shown in Fig. 2.1.

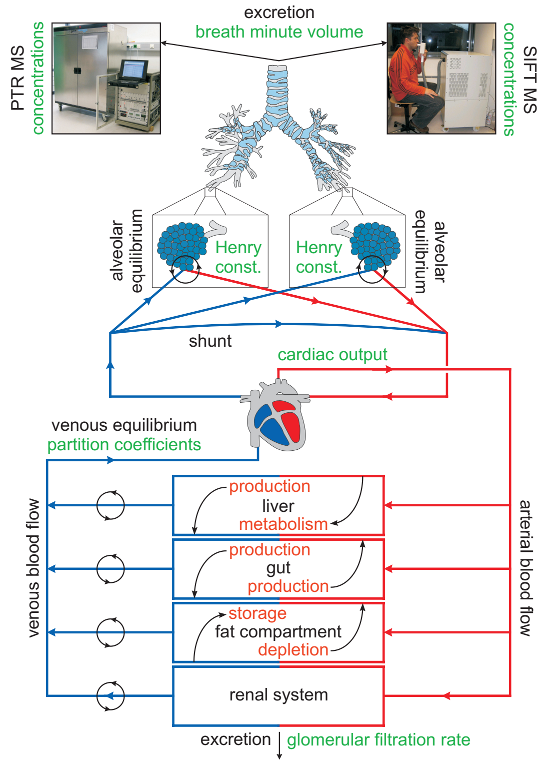
excretion
breath minute volume
PTR MS
concentrations
SIFT MS
concentrations
alveolar equilibrium
Henry const.
Henry const.
alveolar equilibrium
shunt
cardiac output
venous equilibrium
partition coefficients
production
liver
metabolism
production
gut
production
storage
fat compartment
depletion
renal system
excretion
glomerular filtration rate
venous blood flow
arterial blood flow

Figure 2.1: Physiologically based compartment model for the distribution of an endogenous volatile organic compound M within the human body. Green items indicate known or measured variables according to the experimental setup, while production, metabolism, storage, and depletion rates represent (unknown) quantities that are expected to affect the tissue distribution of M.

As has been indicated above, the number and configuration of the compartments defining such a physiological model is seldom fixed a priori. In fact, the level of detail included will primarily be determined by the physico-chemical characteristics of M, the (qualitative) features of experimental evidence as well as the anticipated use of the model. Consequently, a compromise must be achieved between a model structure that is sufficiently accurate and yet simple enough to allow for a tractable and physiologically plausible parameterization. In this sense, the goal is to maintain a compartmentalization as parsimonious as possible. Typical reasons for including a specific organ or tissue group A individually rather than incorporating it into a lumped compartment might comprise [131]:

1. Biotransformation or uptake/clearance processes are expected to occur within A.
2. A is an integral part of the experimental question/setup or is affected by the experimental regime.
3. Measurements capturing the behavior of M in A are available.

Since their introduction by Teorell in the 1930s [163, 164], compartment models have received widespread attention in the biomedical sciences. The reason for this popularity is that the model structures bear a direct correspondence with the underlying physiology, thereby maintaining a clear-cut interpretation of the involved parameters. Moreover, once a specific compartmentalization has been selected, one can straightforwardly arrive at a set of model equations by writing down the associated mass balance relations.

For the sake of illustration, consider two homogeneous compartments A and A' with volumes V_A and $V_{A'}$, respectively. Both compartments interact by diffusion and are affected by additional input rates $\dot{I}$ and effluent output rates $\dot{O}$, cf. Fig. 2.2. Here, the terms $\dot{I}$ and $\dot{O}$ typically represent possible sources (e.g., production and uptake) or sinks (metabolism and clearance/excretion), respectively.

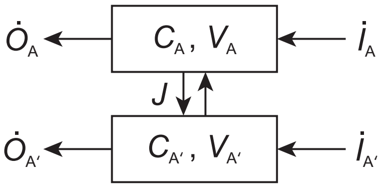

Figure 2.2: A simple two-compartment model. Both compartments A and A' interact by diffusion and are affected by additional input rates $\dot{I}$ and effluent output rates $\dot{O}$.

Progression of matter in A and A' is governed by conservation of mass, stating that the rate at which the compartmental amount (viz., $V_A C_A$) of M changes per time unit equals the rate of mass transfer into the compartment less the rate of removal from the compartment. Accordingly, assuming that the corresponding compartment volumes remain constant over time, the mass balances for the above system read

$$\frac{\mathrm{d}(V_A C_A)}{\mathrm{d}t} = V_A \frac{\mathrm{d}C_A}{\mathrm{d}t} = -J + \dot{I}_A - \dot{O}_A \tag{2.13}$$

and

$$\frac{\mathrm{d}(V_{A'} C_{A'})}{\mathrm{d}t} = V_{A'} \frac{\mathrm{d}C_{A'}}{\mathrm{d}t} = J + \dot{I}_{A'} - \dot{O}_{A'}, \tag{2.14}$$

respectively. Hence, the convenience of compartmental modeling stems from the fact that the underlying model structure can directly be expressed as a set of ordinary differential equations (ODEs). In particular, the resulting ODE systems share a wide range of interesting properties with respect to their qualitative behavior, see [80, 11].

Note that the assumption of well-mixing is central to compartmentalization and can often only be justified heuristically, either by examining factors that contribute to rapid distribution (e.g., convection) or by considering small volumes. If heterogeneity within a compartment is expected to be substantial or the main focus is on the spatial distribution of M (e.g., for predicting the concentration of a volatile drug M at specific locations within a target site), general mass transport equations leading to PDEs have to be employed [167].

A crucial aspect of diffusional mass transfer of volatile organic compounds M within various body tissues is the distinction between diffusion-limited and perfusion-limited gas exchange [147]. In order to clarify these notions consider Equations (2.13) and (2.14) again. Perfusion limitation essentially characterizes the situation in which diffusion is “fast” compared to the other dynamics influencing the system. Consequently, C_A as well as $C_{A'}$ will instantaneously approach their steady state values and a permanent diffusion equilibrium can be assumed to hold between A and A'. In this case we may replace $C_{A'}$ in (2.14) with $C_A\lambda_{A':A}$ (cf. Equation (2.11)) and deduce that the ODE system above simplifies to the one-dimensional differential equation

$$\big(V_{A'}\lambda_{A':A} + V_A\big)\frac{\mathrm{d}C_A}{\mathrm{d}t} = \dot{I}_{A'} - \dot{O}_{A'} + \dot{I}_A - \dot{O}_A. \tag{2.15}$$

The factor $\tilde{V}_A := (V_{A'}\lambda_{A':A} + V_A)$ can be seen as *effective* volume of the combined compartment. It is important to note that according to Equation (2.15) the amount of gas transferred from A to A' and vice versa solely depends on the amount presented via the respective inflows.

Example 1. There is strong evidence that in normal healthy persons the alveolar exchange of inert gases is a perfusion-limited process. The branching capillary network of the respiratory microvasculature will generally promote a fast equilibration between end-capillary blood A' and the free gas phase A. This is likely to hold true also under moderate, sub-anaerobic exercise conditions [173]. From a modeling perspective, a commonly encountered error in this context is to neglect the contribution of $V_{A'}\lambda_{A':A}$ to the effective alveolar volume, as the end-capillary blood volume $V_{A'} \approx 0.15$ l is argued to be much smaller than the normal lung volume $V_A \approx 3$ l. Note, however, that this is only acceptable for low soluble inert gases with blood:air partition coefficient close to 1.

Contrarily, if the diffusional flux is small, i.e., if J regulates the amount of gas exchanged between A and A', mass transfer is said to be diffusion-limited. Typical factors contributing to the development of a diffusion limitation include the separation of both regions by some physical barrier (hindering the passage of M from A to A' and vice versa) as well as insufficient residence times within the respective compartments (e.g., due to a high convective flow).

Example 2. A paradigmatic example for an effective diffusion limitation is the brain-blood barrier, where the tight junctions of the capillary endothelium restrict the diffusional mass transfer between the vascular space and the cerebral interstitium. As far as pulmonary gas exchange is concerned, oxygen uptake is usually perfusion-limited under normal conditions. However, a diffusion limitation can commonly be observed during heavy exercise [174] (due to reduced pulmonary capillary red cell transit times) or pulmonary fibrosis [3] (due to a thickening of the blood-gas barrier).

From (2.15) and Example 1 it should be evident that a particular convenience of postulating perfusion-limited gas exchange stems from the possibility of lumping together various physical sub-compartments into one single functional entity (e.g., end-capillary blood and the alveolar gas space are combined to form the lung compartment). This can drastically reduce the number of parameters required for setting up the model equations. However, it generally is the modeler's responsibility to decide whether a diffusion- or perfusion-limitation is a more appropriate description of the underlying physiological situation.

Example 3. As a general guidance, for tissue groups exerting a high degree of vascularization the intracellular space A can be assumed to rapidly equilibrate with the extracellular space A' (including the vascular blood and the interstitial space). In other words, gas exchange from the vascular blood to the cellular space will be perfusion-limited rather than diffusion-limited (see, however, Example 2 for an important exception). In this case, a venous equilibrium is said to hold, i.e., the concentration $C_{A'}$ of M in blood leaving the tissue group is related to the actual tissue concentration C_A via Equation (2.11).

While physiological realism represents a particular strength of the compartmental modeling approach, it also is one of its most severe drawbacks. The reason for this is that the developed models necessarily require extensive physiological, physico-chemical and biochemical information, which has to be obtained via calculated values from the literature or by direct experimentation. Depending on the specific experimental question and/or setup under scrutiny, the spectrum of model parameters can roughly be divided into fixed, measured and unknown quantities (see also Fig. 2.1). In the present context, the first class typically comprises quantities that have been determined a priori and are assumed to remain constant during the course of experimentation, such as approximate tissue volumes or partition coefficients. Information of this type has been compiled by several investigators, see, e.g., [131] and references therein. Measured parameters include quantities that are accessible by virtue of the given experimental setup, while unknown parameters will have to be extracted by fitting the model to available experimental data.

Summarizing, we may conclude that the canonical structure for *deterministic* models representing an ensemble of mass balance kinetics are ODE systems of the form

$$\dot{\mathbf{x}}(t) = \mathbf{g}(\mathbf{x}(t), \mathbf{u}(t), \boldsymbol{\vartheta}), \quad \mathbf{x}(t_0) = \mathbf{x}_0. \tag{2.16}$$

These equations describe the evolution of a *state* variable $\mathbf{x}(t)$, belonging to an open set $X \subseteq \mathbb{R}^n$, within an observation interval $[t_0, t_{\max}]$. The right-hand side $\mathbf{g}$ depends on a set of measured, time-varying variables $\mathbf{u} \in U \subseteq \mathbb{R}^q$ that are postulated to be uniformly bounded over $[t_0, t_{\max}]$ as well as on a vector $\boldsymbol{\vartheta} \in \Theta \subseteq \mathbb{R}^p$ lumping together a set of *constant*, unknown model parameters. The latter will have to be estimated from available process data (possibly together with some components the initial conditions $\mathbf{x}_0$). In the present context of VOC modeling, $\mathbf{x}$ typically reflects molecular concentrations of the trace gas M within the tissue compartments introduced; $\mathbf{u}$ stands for external inputs (flows, temperature, etc.) that can be modified by experimentation; $\boldsymbol{\vartheta}$ includes kinetic constants such as endogenous production or metabolization rates. Furthermore, information on the model dynamics can be collected via the scalar *measurement equation*

$$y(t) = h(\mathbf{x}(t), \boldsymbol{\vartheta}), \tag{2.17}$$

reflecting the underlying experimental setup. Specific examples for the framework introduced above can be found in Part III.

In the following we assume that $\mathbf{g}$ and h are continuously differentiable with respect to $\boldsymbol{\vartheta}$ and $\mathbf{x}$. Moreover, it will be a general premise underpinning further discussion that the *direct modeling problem* is well-posed, i.e., that the system formed by (2.16) and (2.17) gives rise to unique solutions that depend continuously on $\mathbf{x}_0$ and $\boldsymbol{\vartheta}$. By virtue of the Theorem of Picard-Lindelöf (see [14] for instance), such a property can be confirmed by checking that $\mathbf{g}$ is uniformly Lipschitz with respect to $\mathbf{x} \in X$ (e.g., by proving uniform boundedness of the Jacobian $\mathrm{d}\mathbf{g}/\mathrm{d}\mathbf{x}$).

Chapter 3

Off-line identification

Contents

3.1 A priori identifiability **21**
3.2 Nonlinear least squares methodology **26**
3.3 Multiple shooting **27**
  3.3.1 Numerical setup 27
  3.3.2 Optimality conditions and convergence 32
  3.3.3 Globalization of convergence 35
3.4 Confidence intervals **36**
  3.4.1 Direct methods 36
  3.4.2 Bootstrap confidence intervals 38

Once a presumed model structure has been selected, we will strive to achieve (quantitative) congruency of the model behavior with the observable features of the experimental system. This is typically accomplished by trying to identify and estimate a series of relevant parameter values affecting the model output. From a slightly different perspective, as modeling attempts are often aimed at inferring process characteristics from measured data, the determination of these unknown parameters may become a major investigative goal by itself. In the following chapters several methodological aspects regarding parameter estimation in physiological models will be reviewed. In particular, these techniques underpin the model fitting procedures indicated in Part III. For extensive methodological overviews of this vast field of research the interested reader is referred to [176, 21].

3.1 A priori identifiability

Often over-looked, assessing the a priori (or structural) identifiability/observability of a given model is a necessary step that should precede any numerical approach to parameter estimation. The objective is to clarify whether in the ideal context of an error-free (i.e., "correct") model and noise-free measurements there exist functions $\mathbf{u}$ (or, in other words, conductible experiments) such that the associated output y (the observable data) carries enough information to allow for an unambiguous determination of all unknown states and parameters. Particularly, this avoids an inherent over-parameterization of the model.

As the time evolution of the system (2.16) for a given $\mathbf{u}$ is fixed once the initial conditions $\mathbf{x}_0$ at the start of the experiment are known, the analysis of a priori identifiability/observability hence amounts to studying (local) injectivity of y with respect to $\mathbf{x}_0$ and $\boldsymbol{\vartheta}$. Evidently, if such a property does not hold then any attempt to reliably estimate these quantities is doomed to failure from the start, as several different parameter combinations might yield exactly the same data.

Remark 3. Since the unknown parameters $\boldsymbol{\vartheta}$ can be interpreted as additional states with time derivative zero, it will be sufficient to confirm the injectivity of y with respect to a (possibly augmented) vector of initial conditions $\mathbf{x}_0$.

Several concepts for tackling the structural identifiability/observability problem as introduced above have been developed in the literature. Most of these have their roots in nonlinear control theory and hinge on widely distinct methodological backgrounds including differential algebra [103, 109], similarity transformations [171] and field extensions [145, 41]. A good account of various earlier techniques can be found in [175]. Here, will adopt a differential-geometric approach [73] which – despite its simplicity and local nature – proves to be a flexible tool for capturing the essence of a priori observability for most nonlinear models considered within the present framework.

In the following, we focus on the case where the inputs $\mathbf{u}$ are constant and hence can be interpreted as additional parameters of the system

$$\begin{aligned} \dot{\mathbf{x}} &= \mathbf{g}(\mathbf{x}), \quad \mathbf{x}(t_0) = \mathbf{x}_0, \\ y &= h(\mathbf{x}). \end{aligned} \tag{Σ}$$

Here, it is assumed that $\mathbf{g} : X \to \mathbb{R}^n$ as well as $h : X \to \mathbb{R}$ are real analytic functions. The output $y = y(t, \mathbf{x}_0)$ is viewed as a function of the initial condition $\mathbf{x}_0$. Systems of the form (Σ) are a valid description for many biological processes under constant measurement conditions and represent a sufficient framework for the type of models and experiments considered in this thesis. Results in the sequel are mainly collected from [73, 120, 154] and [13]. These references also provide extensive details with respect to questions of a priori observability in a more general setting than the one above.

Intuitively, as has been indicated before, local observability reflects the fact that $\mathbf{x}_0$ can be instantaneously distinguished from any of its neighbors by using the system response. This is made explicit in the following definition.

Definition 1. Let $U \subseteq X$. Two initial conditions $\mathbf{x}_0, \tilde{\mathbf{x}}_0 \in U$ are U-indistinguishable ($\mathbf{x}_0 \sim_U \tilde{\mathbf{x}}_0$) if for every $T > 0$ such that the corresponding trajectories remain in U it holds that

$$y(t, \mathbf{x}_0) = y(t, \tilde{\mathbf{x}}_0)$$

for all $t \in [0, T]$. A system (Σ) is called locally observable at $\mathbf{x}_0 \in X$, if there exists a neighborhood $U \subseteq X$ of $\mathbf{x}_0$ such that for all points $\tilde{\mathbf{x}}_0$ in U the relation $\mathbf{x}_0 \sim_U \tilde{\mathbf{x}}_0$ implies that $\mathbf{x}_0 = \tilde{\mathbf{x}}_0$.

In other words, local observability characterizes the fact that $\mathbf{x}_0 \mapsto y(., \mathbf{x}_0)$ is injective for arbitrarily small T.

For the sake of illustration, consider the system

$$\begin{pmatrix} \dot{x}_1 \\ \dot{x}_2 \\ \dot{x}_3 \end{pmatrix} = \begin{pmatrix} -(x_2 + x_3)x_1 \\ 0 \\ 0 \end{pmatrix}, \quad y = x_1, \tag{3.1}$$

then

$$y = x_{1,0} \exp(-(x_{2,0} + x_{3,0})t).$$

Evidently, this toy model is not locally observable as the slightly perturbed initial conditions $\tilde{x}_{2,0} := x_{2,0} + \varepsilon$ and $\tilde{x}_{3,0} := x_{3,0} - \varepsilon$ result in exactly the same response y for any $\varepsilon > 0$. If we interpret x_1 and x_2 as constant parameters, the above situation corresponds to a typical case of over-parameterization, i.e., adding x_3 does not provide a more detailed description of the observable output. On the other hand, from the reversed viewpoint of estimation, this means that we will never be able to simultaneously estimate both $x_{2,0}$ and $x_{3,0}$ from the available process data but can only assess their sum. An equivalent characterization of this fact can be given in the context of sensitivities, i.e., by considering the partial derivatives of the output with respect to the parameters. Indeed, we immediately see that

$$\frac{\partial y}{\partial x_{2,0}} = \frac{\partial y}{\partial x_{3,0}},$$

i.e., the sensitivities are linearly dependent, which is well-known to preclude a joint estimation of both parameters, see [34, 79]. Intuitively, the reason for this is that from the the Taylor expansion of first order

$$y(\tilde{x}_{2,0}, \tilde{x}_{3,0}) \approx y(x_{2,0}, x_{3,0}) + \frac{\partial y}{\partial x_{2,0}}\varepsilon - \frac{\partial y}{\partial x_{3,0}}\varepsilon = y(x_{2,0}, x_{3,0}),$$

which again confirms that any small change in $x_{2,0}$ can be compensated for by an appropriate change in $x_{3,0}$ to yield almost the same output. A rigorous statement of this fact in the general unconstrained case is given in [21]. In contrast, as will be illustrated henceforth, local observability guarantees linear independence of the derivatives of y with respect to $\mathbf{x}_0$. This also is a necessary requirement for the broad class of numerical parameter estimation schemes based on the minimization of a given cost functional using first-order information, cf. Section 3.2.

In more complex models, where an analytical expression for y can usually not be derived, we have to resort to differential-geometric methods for investigating local observability. These tools will only be developed to the extent necessary for stating the final observability criterion, but are usually defined in a much more general framework than the one presented here.
For this purpose, first note that using the chain rule, the time derivative of the output equals the Lie derivative $L_{\mathbf{g}}h$ of the output function h with respect to the vector field $\mathbf{g}$, i.e.,

$$\dot{y} = (\nabla h) \cdot \mathbf{g} =: L_{\mathbf{g}}h$$

which again is analytic. Here, $\nabla = (\frac{\partial}{\partial x_1}, \ldots, \frac{\partial}{\partial x_n})$ denotes the gradient and $\cdot$ denotes the scalar product in $\mathbb{R}^n$. Similarly, by iteratively defining

$$L_{\mathbf{g}}^{(k)}h = L_{\mathbf{g}}L_{\mathbf{g}}^{(k-1)}h, \quad L_{\mathbf{g}}^{(0)}h := h,$$

we immediately see that

$$y^{(k)}(\mathbf{x}_0) := \frac{\partial^k}{\partial t^k} y(t, \mathbf{x}_0)\Big|_{t=0} = L_{\mathbf{g}}^{(k)}h(\mathbf{x}_0).$$

By our analyticity assumption on the system (Σ), the system response y is analytic with respect to both t and $\mathbf{x}_0$ and can hence be represented by a convergent power (Lie) series around $t = 0$:

$$y(t, \mathbf{x}_0) = \sum_{k=0}^{\infty} \frac{t^k}{k!} y^{(k)}(\mathbf{x}_0) = \sum_{k=0}^{\infty} \frac{t^k}{k!} L_{\mathbf{g}}^{(k)}h(\mathbf{x}_0). \tag{3.2}$$

As a result, the relation $\mathbf{x}_0 \sim_U \tilde{\mathbf{x}}_0$ is characterized by the fact that for all $k \geq 0$ it holds that

$$L_{\mathbf{g}}^{(k)}h(\mathbf{x}_0) = L_{\mathbf{g}}^{(k)}h(\tilde{\mathbf{x}}_0).$$

This motivates the following definition

Definition 2. The linear space over $\mathbb{R}$ of all iterated Lie derivatives

$$\mathcal{O}(\mathbf{x}_0) := \operatorname{span}_{\mathbb{R}}\{L_{\mathbf{g}}^{(k)}h(\mathbf{x}_0),\ k \geq 0\},$$

is called the observation space of the model. Moreover, $\nabla\mathcal{O} := \{\nabla H,\ H \in \mathcal{O}\}$ denotes the associated observability co-distribution.

The following criterion [73] now yields a sufficient condition for local observability.

Theorem 3.1. *The model* (Σ) *is locally observable at* $\mathbf{x}_0$ *if*

$$\dim \nabla\mathcal{O}(\mathbf{x}_0) = n. \tag{3.3}$$

Proof. The proof is merely an application of the Inverse Function Theorem. Accordingly, if the above condition holds, then we can choose n functions $H_k \in \mathcal{O}$ such that the map $\boldsymbol{H} := (H_1, \ldots, H_n)^T$ has a non-singular Jacobian at $\mathbf{x}_0$. Hence, there exists a neighborhood W of $\mathbf{x}_0$ such that $\boldsymbol{H} : W \to \boldsymbol{H}(W)$ is a diffeomorphism. Now, choose an open subset $U \subseteq W$ with $\mathbf{x}_0, \tilde{\mathbf{x}}_0 \in U$ and $y(t, \mathbf{x}_0) = y(t, \tilde{\mathbf{x}}_0)$ in U. From the series expansion (3.2) we thus deduce that

$$L_{\mathbf{g}}^{(k)} h(\mathbf{x}_0) = L_{\mathbf{g}}^{(k)} h(\tilde{\mathbf{x}}_0)$$

for all $k \geq 0$. This shows that $\boldsymbol{H}(\mathbf{x}_0) = \boldsymbol{H}(\tilde{\mathbf{x}}_0)$ and by injectivity of $\boldsymbol{H}$ we hence find that $\mathbf{x}_0 = \tilde{\mathbf{x}}_0$, thereby concluding the proof. □

Conversely, the following result can be derived [120, p. 97].

Corollary 1. *Assume that the system* (Σ) *is locally observable. Then* $\dim \nabla\mathcal{O}(\mathbf{x}) = n$ *for* $\mathbf{x}$ *in an open and dense subset of* X.

Hence, if (Σ) is locally observable, the criterion in Theorem 3.1 will be fulfilled generically. This is further discussed below.

Note that condition (3.3) is equivalent to finding n indices k_j such that the gradients $\nabla L_{\mathbf{g}}^{(k_j)} h(\mathbf{x}_0)$ are linearly independent. In fact, it turns out that only the first n iterated Lie derivatives have to be computed in order to decide if such indices exist [13].

Lemma 1. *(*Rank criterion for local observability*) Condition* (3.3) *is equivalent to the algebraic rank criterion*

$$\operatorname{rank} J(\mathbf{x}) := \operatorname{rank}\left(\nabla L_{\mathbf{g}}^{(0)} h(\mathbf{x}_0)^T, \ldots, \nabla L_{\mathbf{g}}^{(n-1)} h(\mathbf{x}_0)^T\right) = n. \tag{3.4}$$

Proof. To show this we have to introduce the Lie derivative of a row vector of analytic functions $\mathbf{f} = (f_1(\mathbf{x}), \ldots, f_n(\mathbf{x}))$ (a co-vector field), which is again a co-vector field defined by

$$L_{\mathbf{g}}\mathbf{f} := \mathbf{g}^T J_{\mathbf{f}}^T + \mathbf{f} J_{\mathbf{g}},$$

where J is the Jacobian. Note that $L_{\mathbf{g}}$ is linear with respect to $\mathbf{f}$. Furthermore, for the special case $\mathbf{f} = \nabla h$, from the component-wise argument

$$(\nabla L_{\mathbf{g}} h)_j = \sum_{l=1}^{n} g_l \frac{\partial h}{\partial x_l \partial x_j} + \sum_{l=1}^{n} (\nabla h)_l \frac{\partial g_l}{\partial x_j} = (L_{\mathbf{g}} \nabla h)_j,$$

we deduce that ∇ and $L_{\mathbf{g}}$ commute. Now, assume that for $\alpha_j \in \mathbb{R}$

$$\nabla L_{\mathbf{g}}^{(k)} h(\mathbf{x}_0) = \sum_{j=0}^{k-1} \alpha_j \nabla L_{\mathbf{g}}^{(j)} h(\mathbf{x}_0),$$

i.e., $\nabla L_{\mathbf{g}}^{(k)} h(\mathbf{x}_0)$ is linearly dependent on the $(k-1)$ previously calculated gradients. Then,

$$\nabla L_{\mathbf{g}}^{(k+1)} h(\mathbf{x}_0) = \nabla(L_{\mathbf{g}} L_{\mathbf{g}}^{(k)} h) = L_{\mathbf{g}}(\nabla L_{\mathbf{g}}^{(k)} h) = \sum_{j=0}^{k-1} \alpha_j \nabla L_{\mathbf{g}}^{(j+1)} h(\mathbf{x}_0) =$$

$$\sum_{j=0}^{k-1} (\alpha_{k-1}\alpha_j + \alpha_{j-1}) \nabla L_{\mathbf{g}}^{(j)} h(\mathbf{x}_0),$$

(we set $\alpha_{-1} := 0$ for notational simplicity) which again is a linear combination of the first $(k-1)$ gradients.

Hence, either $\nabla L_{\mathbf{g}}^{(k)} h(\mathbf{x}_0),\ k = 0, \ldots, n-1$, are linearly independent and the model is locally observable at $\mathbf{x}_0$ or $\dim \nabla\mathcal{O}(\mathbf{x}_0) < n$. □

Remark 4. Note that for a linear system

$$\dot{\mathbf{x}} = A\mathbf{x},$$
$$y = C\mathbf{x}$$

the above condition simplifies to

$$\operatorname{rank}\left(C^T, A^T C^T, \dots, A^{(n-1)\,T} C^T\right) = n,$$

which is the well-known criterion introduced by Kalman (see, e.g., [154]). Obviously, if the linear model is locally observable at one particular initial condition, local observability holds for every other initial condition as well.

To conclude this section some words are in order regarding the practical implementation of Lemma 1. For this purpose, let us assume for the moment that $\mathbf{g}$ and h belong to the field of rational functions in $\mathbf{x} = (x_1, \dots, x_n)$ and $\mathbf{u} = (u_1, \dots, u_q)$ over $\mathbb{R}$, i.e., $\mathbf{g}, h \in \mathbb{R}(\mathbf{x}, \mathbf{u})$ with no real poles in X. Consequently, the entries of the matrix $J(\mathbf{x}, \mathbf{u})$ defined in (3.4) belong to $\mathbb{R}(\mathbf{x}, \mathbf{u})$ and hence its rank can be defined as the maximum size of a submatrix whose determinant is a non-zero rational function. This so-called generic rank can easily be determined by symbolic calculation software. Hence, if the generic rank of J is n, the rank of $J(\mathbf{x}, \mathbf{u})$ evaluated at one specific point $(\mathbf{x}, \mathbf{u}) \in \mathbb{R}^{n+q}$ will also be n except for certain singular choices that are algebraically dependent over $\mathbb{R}$. As these special points constitute a set of measure zero, we may thus claim that if the generic rank of $J(\mathbf{x}, \mathbf{u})$ equals n, almost every experiment corresponding to a choice of constant input variables $\mathbf{u}$ will suffice to immediately distinguish a particular unknown initial condition $\mathbf{x}_0$ from its neighbors by giving rise to a distinct system output y. Conversely, if the generic rank of $J(\mathbf{x}, \mathbf{u})$ is smaller than n, from Corollary 1 it may be concluded that the system (Σ) is not locally observable in the sense of Definition 1. This indicates a potential over-parameterization of the model.

The above results are strengthened further by applying the Universal Input Theorem for analytic systems due to Sussmann [161], ensuring that if a pair of unknown initial conditions can be distinguished by some (e.g., constant) input, it can also be distinguished by almost every input belonging to $\mathcal{C}^\infty([0,T]),\ T > 0$ (see also [178] for a rigorous statement as well as a self-contained proof). Note, that in the context of physiological models this is the appropriate class of functions for capturing a wide range of applicable physiological conditions. The following *Mathematica* code summarizes the findings of the last paragraph and can be used for checking the a priori identifiability of a given rational model (Σ) in practical situations.

Algorithm 1 (*Rank criterion for local observability*)

Consider the model (Σ) with $\mathbf{g}$ and h ($\neq$ const.) rational and analytic on the state space $X \subseteq \mathbb{R}^n$. Then condition (3.4) can be verified as follows.

```
J = {D[h, {{x1,...,xn}}]}; r = 1;
While[r < n,
 newRow = D[J[[r]].g, {{x1,...,xn}}];
 (* iterated Lie derivatives *)
 J = Append[J, newRow];
 If[MatrixRank[J] == r,
  Print[Rank criterion not fulfilled.]; Break[];,
  r = r + 1];
];
```

Remark 5. Note that the above line of argumentation remains valid also for general analytic functions $\mathbf{g}$ and h. However, the generic rank in this case usually has to be estimated, e.g., by computing the rank of J evaluated at some randomly assigned points $(\mathbf{x}, \mathbf{u}) \in \mathbb{R}^{n+q}$.

While from the above an affirmative outcome of the rank test guarantees that every initial condition within a neighborhood of the “true” value $\mathbf{x}_0$ will yield a distinct output y when conducting a generic experiment with smooth inputs, the effective reconstruction of $\mathbf{x}_0$ from partially observed and error-corrupted data remains a challenging problem. For instance, despite a positive result of the rank criterion, nothing can be said about the degree of linear independence between the derivatives of the output with respect to the initial conditions. In fact, the associated sensitivity matrix can still be rank-deficient in a numerical sense, indicating a high correlation among some of the components to be recovered (cf. Remark 17). This is the context of practical identifiability or estimability by means of numerical estimation schemes, which will be discussed in the next sections.

3.2 Nonlinear least squares methodology

So far, we have focused exclusively on parameter identifiability in the ideal context of continuous and exact measurements. In practical applications, however, process information might only be available at $N+1$ discrete time instants $t_0 < t_1 < \cdots < t_N = t_{\max}$ and will often be corrupted by measurement noise. We hence have access to longitudinal output data $y_i := h(\mathbf{x}(t_i), \boldsymbol{\vartheta}) + v_i$, which are realizations corresponding to the additive *statistical model* (cf. Equation (2.17))

$$Y_i := h(\mathbf{x}(t_i), \boldsymbol{\vartheta}) + V_i,\ i = 0, \ldots, N. \tag{3.5}$$

Here, the noise terms V_i are assumed to be independent and identically distributed (*iid*) random variables having zero mean and constant variance, i.e., for the random vector $\mathbf{V} := (V_0, \ldots, V_N)^T$ it holds that $E\{\mathbf{V}\} = \mathbf{0}$ and $\operatorname{cov}\{\mathbf{V}\} = \beta^2 I$. The common factor β may generally be unknown. The above requirements are usually assessed by virtue of an a posteriori analysis of the *residuals* v_i, cf. Remark 20.

Following common practice, we postulate the existence of “true” values $(\underline{\boldsymbol{\vartheta}}, \underline{\mathbf{x}}_0)$ generating the observations Y_i according to Equation (3.5). These values are assumed to be (at least locally) unique within an admissible set $\Omega \subseteq \Theta \times X$. Both assumptions partially ensure the well-posedness of the *inverse problem* of recovering $\underline{\boldsymbol{\vartheta}}$ and $\underline{\mathbf{x}}_0$ from available data. Existence is usually justified heuristically by reference to model validation (i.e., the flexibility of the model to effectively capture the process dynamics for the experimental framework under scrutiny), while testing (local) uniqueness leads to the notion of a priori or structural identifiability/observability discussed in the previous section.

A standard framework for estimating $\underline{\boldsymbol{\vartheta}}$ and $\underline{\mathbf{x}}_0$ is to employ ordinary least squares (OLS) methodology [144, 18], which aims at minimizing the mean squared distance between the model predictions and the observed data by solving the *constrained* optimization problem

$$\underset{(\boldsymbol{\vartheta}, \mathbf{x}_0) \in \Omega}{\arg\min} \sum_{i=0}^{N} \big(Y_i - h(\mathbf{x}(t_i), \boldsymbol{\vartheta})\big)^2. \tag{3.6}$$

Although several alternative loss functions might be considered here, the popularity of OLS stems from the fact that under the assumptions of the previous paragraph and if the noise terms $\mathbf{V} \sim \mathcal{N}(\mathbf{0}, \beta^2 I)$ are normally distributed, the expression (3.6) represents a *Maximum Likelihood Estimate* [144], which by definition maximizes the probability of the given data with respect to the parameters. It is important to note that the solution of the above optimization problem is a random variable itself and therefore has to be complemented with an estimate of its accuracy, see Section 3.4. As usual, a *point* OLS estimate can be derived by replacing the random variables in the above expression with their associated realizations, i.e.,

$$\big(\widehat{\boldsymbol{\vartheta}}, \widehat{\mathbf{x}}_0\big) = \underset{(\boldsymbol{\vartheta}, \mathbf{x}_0) \in \Omega}{\arg\min} \sum_{i=0}^{N} \big(y_i - h(\mathbf{x}(t_i), \boldsymbol{\vartheta})\big)^2 =: \underset{(\boldsymbol{\vartheta}, \mathbf{x}_0) \in \Omega}{\arg\min} \|\mathbf{f}_1(\boldsymbol{\vartheta}, \mathbf{x}_0)\|_2^2. \tag{3.7}$$

For the ease of further illustration we will assume that the admissible region Ω (comprising possible constraints among the parameters and initial conditions) can be represented by a set of nonlinear equations

$$\Omega = \{\boldsymbol{\omega} \mathrel{\hat{=}} (\boldsymbol{\vartheta}^T, \mathbf{x}_0^T)^T \in \mathbb{R}^{p+n};\ \mathbf{f}_2(\boldsymbol{\omega}) = \mathbf{0}\} \tag{3.8}$$

with $\mathbf{f}_2 : \Omega \to \mathbb{R}^{n_2}$ sufficiently smooth and $n_2 < p+n$. For perspective, in the framework of concentration dynamics, the function $\mathbf{f}_2$ might typically include initial steady state relations. The treatment of possible *inequality* constraints among the components of $\boldsymbol{\omega}$ will be limited to simple cases which can be relaxed to the unconstrained case by suitable monotonous transformations, such as positivity or boundedness of individual components ω_i within a real-valued interval $[a, b] \subset \mathbb{R}$. For perspective, positivity for ω_i can easily be guaranteed by setting $\omega_i = \exp(\nu_i)$ and optimizing with respect to the unconstrained variable $\nu_i \in \mathbb{R}$. This also results in an automatic scaling of the ν_i. Similarly, the ansatz $\omega_i = a + 0.5(b-a)(1+\tanh(\nu_i))$ ensures that $\omega_i \in [a, b]$ for all $\nu_i \in \mathbb{R}$. More general inequality constraints can be treated within the framework to be presented below by considering active set strategies as described, e.g., in [26, 57]. Since these topics do not constitute a central part of this work, they will not be elaborated further here.

As inverse parameter estimation problems of the type (3.7) can seldom be solved analytically, several *iterative* approaches have been proposed. Global minimization techniques, including stochastic optimization and evolutionary algorithms, generally suffer from high computational cost as they rely on an extensive number of function evaluations, see, e.g., the review of Banga et al. [16]. This drawback certainly limits their usability in time-intensive models. In contrast, traditional minimization routines (e.g., steepest descent, Gauss-Newton, and augmented Lagrangian methods [57, 58]) are based on the successive refinement of an initial guess for the OLS estimate introduced above. The idea is to repeatedly solve the associated initial value problem (IVP) over the *entire* observation interval $[t_0, t_{\max}]$ and correct the current guess according to a *local* descent direction, which is chosen in order to decrease the objective function in (3.7). Potential obstacles encountered when using these techniques mainly stem from the following issues:

1. For poor choices of the initial guess the trajectory can become unstable and might diverge before the final integration point $t_{\max}$ is reached.
2. The algorithm gets stuck in a local minimum with the associated trajectory being far off the measured data points.

Both problems can partially be traced back to the very inefficient way in which the classical IVP approach makes use of available information. Indeed, the set of data points y_i offers a comparatively huge body of prior knowledge with respect the solution y that is almost completely neglected. This observation provides the heuristic motivation for a more sophisticated solution routine which we shall discuss in the following section.

3.3 Multiple shooting

This section serves to introduce multiple shooting as a powerful numerical technique for iteratively solving ordinary least squares problems, circumventing the above-mentioned problems. The intention is to give a self-contained overview including the major details relevant for a successful re-implementation of the method, together with an outline of the theoretical background scattered in the literature.

The main idea underlying the multiple shooting approach is treat (3.7) in the framework of multipoint boundary value problems, which have originally been investigated by Stoer and Bulirsch [158]. These numerical schemes were subsequently refined and mathematically analyzed by Bock [26], who also recognized their widespread applicability in more general classes of parameter identification problems, including, e.g., differential algebraic equations (DAEs). For further details regarding the general scope of multiple shooting as well as its superior stability compared with classical solution schemes we refer to [25, 124, 172]. For a variety of applications and modifications proposed for covering PDEs and delay differential equations see [118, 74]. The illustration in the sequel closely follows the original work by Bock [26].

3.3.1 Numerical setup

We begin by choosing intermediate multiple shooting nodes $t_0 = \tau_0 < \cdots < \tau_M = t_{\max}$, partitioning the observation interval into M subintervals. On each of these subintervals Equation (2.16) will be solved using auxiliary initial values $\mathbf{x}(\tau_j) = \mathbf{s}_j \in \mathbb{R}^n$ (i.e., $\mathbf{s}_0 = \mathbf{x}_0$). Thus, a *discontinuous* trajectory is generated, with its piecewise representation being denoted by $\mathbf{x}(t; \mathbf{s}_j, \boldsymbol{\vartheta})$ for $t \in [\tau_j, \tau_{j+1}]$. The vectors $\mathbf{s}_j$ constitute additional degrees of freedom in the optimization procedure, which, however, enter the problem in the highly constrained format of M *matching conditions*

$$\mathbf{z}_j(\mathbf{s}_j, \mathbf{s}_{j+1}, \boldsymbol{\vartheta}) := \mathbf{x}(\tau_{j+1}; \mathbf{s}_j, \boldsymbol{\vartheta}) - \mathbf{s}_{j+1} = \mathbf{0},\ j = 0, \ldots, M-1. \tag{3.9}$$

These matching conditions are introduced in order to enforce the continuity of the final trajectory.

By substituting the sub-trajectories $\mathbf{x}(t_i; \mathbf{s}_j, \boldsymbol{\vartheta})$ into (3.7) for $t_i \in [\tau_j, \tau_{j+1})$, one defines an *augmented* nonlinear optimization problem

$$\min_{\boldsymbol{\omega} \in \Omega} \|\mathbf{f}_1(\boldsymbol{\omega})\|_2^2, \tag{3.10}$$

in the unknown vector $\boldsymbol{\omega} = (\boldsymbol{\vartheta}^T, \mathbf{s}_0^T, \ldots, \mathbf{s}_M^T)^T$, where the admissible set Ω (cf. (3.8)) is now given by

$$\Omega := \{\boldsymbol{\omega} \in \mathbb{R}^{p+(M+1)n};\ \mathbf{f}_2(\boldsymbol{\omega}) = \mathbf{0} \text{ and } \mathbf{z}(\boldsymbol{\omega}) := (\mathbf{z}_0(\boldsymbol{\omega})^T, \ldots, \mathbf{z}_{M-1}(\boldsymbol{\omega})^T)^T = \mathbf{0}\}. \tag{3.11}$$

Remark 6. It should be noted that further constraints with respect to the auxiliary variables $\mathbf{s}_j$ can straightforwardly be incorporated into the function $\mathbf{f}_2$. This is especially beneficial in the treatment of DAEs, where additional algebraic relations among the trajectories need to be taken into account.

Several solvers can be employed to tackle the equality constrained problem (3.10). However, in order to fully exploit the special structure introduced via the continuity constraints in Equation (3.9), Bock [26] proposes a *generalized Gauss-Newton method*, which iteratively refines an initial guess $\boldsymbol{\omega}^0$ according to

$$\boldsymbol{\omega}^{k+1} = \boldsymbol{\omega}^k + \Delta\boldsymbol{\omega}^k. \tag{3.12}$$

The increment $\Delta\boldsymbol{\omega}^k$ is obtained by solving the *linearized* subproblem

$$\min_{\Delta\boldsymbol{\omega}^k} \|\mathbf{f}_1(\boldsymbol{\omega}^k) + F_1(\boldsymbol{\omega}^k)\Delta\boldsymbol{\omega}^k\|_2^2 \tag{3.13}$$

subject to the linearized constraints

$$\begin{cases} \mathbf{f}_2(\boldsymbol{\omega}^k) + F_2(\boldsymbol{\omega}^k)\Delta\boldsymbol{\omega}^k & = \mathbf{0} \\ \mathbf{z}(\boldsymbol{\omega}^k) + Z(\boldsymbol{\omega}^k)\Delta\boldsymbol{\omega}^k & = \mathbf{0}. \end{cases} \tag{3.14}$$

Here, capital letters denote the respective Jacobians.

Remark 7. For notational convenience, the explicit dependence of the above expressions on the current estimate $\boldsymbol{\omega}^k$ as well as the iteration index itself will be omitted in the following.

Remark 8. (*Integration and derivative generation*) A commonly encountered characteristic of systems describing mass balance or chemical reaction kinetics is that they incorporate dynamics proceeding with widely differing time scales. Loosely spoken, such systems are being referred to as *stiff* and require special attention with respect to their numerical solution, see, e.g., [69]. In our *Matlab* implementation of the multiple shooting method, the routine `ode15s` is used for this purpose. In addition to the system trajectories, under the previous assumptions on the function $\mathbf{g}$ the necessary sensitivities $\partial\mathbf{x}(t; \mathbf{s}_j, \boldsymbol{\vartheta})/\partial\boldsymbol{\vartheta}$ and $\partial\mathbf{x}(t; \mathbf{s}_j, \boldsymbol{\vartheta})/\partial\mathbf{s}_j$ for setting up the above Jacobians can be computed by simultaneously integrating the matrix *variational equations* (cf. [68])

$$\frac{\mathrm{d}}{\mathrm{d}t}\left(\frac{\partial\mathbf{x}(t; \mathbf{s}_j, \boldsymbol{\vartheta})}{\partial\boldsymbol{\vartheta}}\right) = \frac{\partial\mathbf{g}}{\partial\mathbf{x}}\frac{\partial\mathbf{x}(t; \mathbf{s}_j, \boldsymbol{\vartheta})}{\partial\boldsymbol{\vartheta}} + \frac{\partial\mathbf{g}}{\partial\boldsymbol{\vartheta}}, \quad \frac{\partial\mathbf{x}(\tau_j; \mathbf{s}_j, \boldsymbol{\vartheta})}{\partial\boldsymbol{\vartheta}} = \mathrm{O} \tag{3.15}$$

and

$$\frac{\mathrm{d}}{\mathrm{d}t}\left(\frac{\partial\mathbf{x}(t; \mathbf{s}_j, \boldsymbol{\vartheta})}{\partial\mathbf{s}_j}\right) = \frac{\partial\mathbf{g}}{\partial\mathbf{x}}\frac{\partial\mathbf{x}(t; \mathbf{s}_j, \boldsymbol{\vartheta})}{\partial\mathbf{s}_j}, \quad \frac{\partial\mathbf{x}(\tau_j; \mathbf{s}_j, \boldsymbol{\vartheta})}{\partial\mathbf{s}_j} = I. \tag{3.16}$$

Here, O and I denote the zero and identity matrices of appropriate dimensions, respectively. Equations (3.15) and (3.16) are obtained by formal derivation of the original ODE system with respect to $\boldsymbol{\vartheta}$ and $\mathbf{s}_j$, respectively. Note that calculating the Jacobians $\partial\mathbf{g}/\partial\boldsymbol{\vartheta}$ and $\partial\mathbf{g}/\partial\mathbf{x}$ by hand can be a time intensive and error-prone task. It is therefore recommended to use symbolic computation software or automatic differentiation packages (see [53] for instance) in this context. The results can subsequently be confirmed by standard finite differencing schemes.

Note that the above Jacobians are large, but sparse and highly structured. More specifically, F_1 is a $(N+1) \times (p+(M+1)n)$ matrix given by

$$F_1 = \begin{pmatrix} F_{1,\boldsymbol{\vartheta}} & F_{1,\mathbf{s}_0} & \cdots & F_{1,\mathbf{s}_M} \end{pmatrix} := \begin{pmatrix} H_0^{\boldsymbol{\vartheta}} & H_0^{\mathbf{s}} & & \\ \vdots & & \ddots & \\ H_M^{\boldsymbol{\vartheta}} & & & H_M^{\mathbf{s}} \end{pmatrix}, \tag{3.17}$$

where the rows of $H_j^{\boldsymbol{\vartheta}}$ and $H_j^{\mathbf{s}}$ are given by the derivatives $\partial h(\mathbf{x}(t;\mathbf{s}_j,\boldsymbol{\vartheta}),\boldsymbol{\vartheta})/\partial\boldsymbol{\vartheta}$ and $\partial h(\mathbf{x}(t;\mathbf{s}_j,\boldsymbol{\vartheta}),\boldsymbol{\vartheta})/\partial\mathbf{s}_j$ evaluated at $t_i \in [\tau_j, \tau_{j+1})$, respectively. The matrix F_2 reads

$$F_2 = \begin{pmatrix} \frac{\partial\mathbf{f}_2}{\partial\boldsymbol{\vartheta}} & \frac{\partial\mathbf{f}_2}{\partial\mathbf{s}_0} & \cdots & \frac{\partial\mathbf{f}_2}{\partial\mathbf{s}_M} \end{pmatrix} \in \mathbb{R}^{n_2 \times (p+(M+1)n)}. \tag{3.18}$$

Analogously, for the Jacobian Z associated with the matching conditions (3.9) we recognize the cyclic block structure

$$Z = \begin{pmatrix} G_0^{\boldsymbol{\vartheta}} & G_0^{\mathbf{s}} & & -I & \\ \vdots & & \ddots & & \ddots \\ G_{M-1}^{\boldsymbol{\vartheta}} & & & G_{M-1}^{\mathbf{s}} & -I \end{pmatrix} \in \mathbb{R}^{Mn \times (p+(M+1)n)}, \tag{3.19}$$

where the matrices

$$G_j^{\boldsymbol{\vartheta}} := \frac{\partial\mathbf{x}(\tau_{j+1};\mathbf{s}_j,\boldsymbol{\vartheta})}{\partial\boldsymbol{\vartheta}} \quad \text{and} \quad G_j^{\mathbf{s}} := \frac{\partial\mathbf{x}(\tau_{j+1};\mathbf{s}_j,\boldsymbol{\vartheta})}{\partial\mathbf{s}_j} \tag{3.20}$$

are the propagation matrices of the variational equations (3.15) and (3.16) on the subinterval $[\tau_j, \tau_{j+1}]$, respectively.

By taking advantage of the specific structure of the matrix Z, the linearized problem (3.13) can efficiently be reduced to a lower dimensional problem of the original size $p+n$ by Gaussian block elimination. For this purpose, we first note that due to (3.14) the increments $\Delta\mathbf{s}_j$ can be determined from $\Delta\mathbf{s}_0$ by

$$\Delta\mathbf{s}_{j+1} = G_j^{\boldsymbol{\vartheta}}\Delta\boldsymbol{\vartheta} + G_j^{\mathbf{s}}\Delta\mathbf{s}_j + \mathbf{z}_j. \tag{3.21}$$

By recursively substituting these expressions into (3.13) and (3.14) for $j = (M-1), \ldots, 0$, one arrives at a *condensed* problem

$$\begin{aligned} \min_{\Delta\mathbf{s}_0,\Delta\boldsymbol{\vartheta}} & \|d_1^0 + P_1^0\Delta\boldsymbol{\vartheta} + S_1^0\Delta\mathbf{s}_0\|_2^2, \\ & d_2^0 + P_2^0\Delta\boldsymbol{\vartheta} + S_2^0\Delta\mathbf{s}_0 = \mathbf{0}, \end{aligned} \tag{3.22}$$

where the respective matrices are defined for $j = M, \ldots, 1$ by the backward recursions

$$\begin{aligned} d_l^{j-1} &= d_l^j + S_l^j\mathbf{z}_{j-1}, \quad l = 1,2, \\ P_l^{j-1} &= P_l^j + S_l^j G_{j-1}^{\boldsymbol{\vartheta}}, \quad l = 1,2, \\ S_1^{j-1} &= F_{1,\mathbf{s}_{j-1}} + S_1^j G_{j-1}^{\mathbf{s}}, \\ S_2^{j-1} &= \frac{\partial\mathbf{f}_2}{\partial\mathbf{s}_{j-1}} + S_2^j G_{j-1}^{\mathbf{s}} \end{aligned} \tag{3.23}$$

with $d_1^M := \mathbf{f}_1$, $d_2^M := \mathbf{f}_2$, $P_1^M := F_{1,\boldsymbol{\vartheta}}$, $P_2^M := \partial\mathbf{f}_2/\partial\boldsymbol{\vartheta}$, $S_1^M := F_{1,\mathbf{s}_M}$ and $S_2^M := \partial\mathbf{f}_2/\partial\mathbf{s}_M$.

Remark 9. The above-mentioned backward recursions can be seen as a block decomposition of the matrix $F := \begin{pmatrix} F_1^T & F_2^T & Z^T \end{pmatrix}^T$. In particular, with the abbreviation

$$C_j^k := \begin{cases} G_{k-1}^{\mathbf{s}} \cdots G_j^{\mathbf{s}} & k > j \\ I & k \le j \end{cases} \tag{3.24}$$

it holds that

$$S_1^j = \sum_{k=j}^{M} F_{1,\mathbf{s}_k} C_j^k, \quad S_2^j = \sum_{k=j}^{M} \frac{\partial \mathbf{f}_2}{\partial \mathbf{s}_k} C_j^k, \tag{3.25}$$

and consequently

$$P_1^j = F_{1,\boldsymbol{\vartheta}} + \sum_{k=j}^{M-1} S_1^{k+1} G_k^{\boldsymbol{\vartheta}}, \quad P_2^j = \frac{\partial \mathbf{f}_2}{\partial \boldsymbol{\vartheta}} + \sum_{k=j}^{M-1} S_2^{k+1} G_k^{\boldsymbol{\vartheta}}. \tag{3.26}$$

From (3.26) we find the decomposition

$$F := \begin{pmatrix} F_1^T & F_2^T & Z^T \end{pmatrix}^T =$$

$$\begin{pmatrix} I & -\begin{pmatrix} S_1^1 \\ S_2^1 \end{pmatrix} & \cdots & -\begin{pmatrix} S_1^M \\ S_2^M \end{pmatrix} \\ & I & & \\ & & \ddots & \\ & & & I \end{pmatrix} \begin{pmatrix} \begin{pmatrix} P_1^0 & S_1^0 \\ P_2^0 & S_2^0 \end{pmatrix} & & & \\ & I & & \\ & & \ddots & \\ & & & I \end{pmatrix} \begin{pmatrix} I_{(p+n)} & \mathrm{O}_{(p+n)\times Mn} \\ & Z \end{pmatrix},$$

which, by the Frobenius rank inequality, allows us to deduce that

$$\operatorname{rank} F = \operatorname{rank} \begin{pmatrix} P_1^0 & S_1^0 \\ P_2^0 & S_2^0 \end{pmatrix} + \operatorname{rank} Z = \operatorname{rank} \begin{pmatrix} P_1^0 & S_1^0 \\ P_2^0 & S_2^0 \end{pmatrix} + Mn. \tag{3.27}$$

As the above decomposition holds true as well for arbitrary submatrices that are derived by deleting rows from $\begin{pmatrix} F_1^T & F_2^T \end{pmatrix}^T$, it follows that

$$\operatorname{rank} \begin{pmatrix} F_1 \\ F_2 \end{pmatrix} = \operatorname{rank} \begin{pmatrix} P_1^0 & S_1^0 \\ P_2^0 & S_2^0 \end{pmatrix}. \tag{3.28}$$

Similarly, by applying the above decomposition to $\begin{pmatrix} F_2^T & Z^T \end{pmatrix}^T$ rather than F we find that $\operatorname{rank} F_2 = \operatorname{rank} \begin{pmatrix} P_2^0 & S_2^0 \end{pmatrix}$.

Under the general regularity condition that F_2 has full rank, the extraction of $\Delta\boldsymbol{\vartheta}$ and $\Delta\mathbf{s}_0$ from the condensed formulation (3.22) can be achieved by standard routines for solving linear least squares problems with linear constraints [157, 93]. According to the previous remark, if F_2 is full-ranked, the same holds true for the matrix $\begin{pmatrix} P_2^0 & S_2^0 \end{pmatrix} \in \mathbb{R}^{n_2 \times (p+n)}$. Using QR-decomposition, we can thus find an orthogonal matrix Q and an $n_2 \times n_2$ upper triangular matrix R with non-zero diagonal elements such that

$$\begin{pmatrix} P_2^{0^T} \\ S_2^{0^T} \end{pmatrix} = Q \begin{pmatrix} R \\ \mathrm{O} \end{pmatrix} \Rightarrow \begin{pmatrix} P_2^0 & S_2^0 \end{pmatrix} Q = \begin{pmatrix} R^T & \mathrm{O} \end{pmatrix}. \tag{3.29}$$

Hence, by defining

$$\begin{pmatrix} \Delta\boldsymbol{\vartheta} \\ \Delta\mathbf{s}_0 \end{pmatrix} =: Q \begin{pmatrix} \mathbf{a}_1 \\ \mathbf{a}_2 \end{pmatrix}, \quad \mathbf{a}_1 \in \mathbb{R}^{n_2 \times 1} \tag{3.30}$$

the condensed problem (3.22) can be solved by determining $\mathbf{a}_1$ according to the transformed constraints $d_2^0 + R^T \mathbf{a}_1 = \mathbf{0}$ and computing $\mathbf{a}_2$ from the *unconstrained* least squares problem

$$\min_{\mathbf{a}_2} \| d_1^0 + \begin{pmatrix} P_1^0 & S_1^0 \end{pmatrix} Q \begin{pmatrix} \mathbf{a}_1 \\ \mathbf{a}_2 \end{pmatrix} \|_2^2 =: \min_{\mathbf{a}_2} \| \mathbf{b}_2 + A_2 \mathbf{a}_2 \|_2^2. \tag{3.31}$$

Note that (3.31) can again be solved by QR- or singular value decomposition. Effectively, in the latter case we calculate two orthogonal matrices U_1 and U_2 such that

$$A_2 = U_1 \begin{pmatrix} \sigma_1 & & \\ & \ddots & \\ & & \sigma_m \\ & \mathrm{O} & \end{pmatrix} U_2^T, \quad (m = p + n - n_2) \tag{3.32}$$

where $\sigma_1 \geq \cdots \geq \sigma_m \geq 0$ are the singular values of A_2 [64]. As multiplication of $\mathbf{b}_2 + A_2\mathbf{a}_2$ with U_1^T does not change the norm in (3.31), with $\underline{\mathbf{b}}_2 := U_1^T\mathbf{b}_2$ we find that

$$\mathbf{a}_2 = U_2(\underline{b}_{2,1}/\sigma_1, \ldots, \underline{b}_{2,m}/\sigma_m)^T. \tag{3.33}$$

A direct solution of the normal equations associated with (3.31) should generally be avoided due to potential numerical instabilities, see [93, Ch. 19] for instance.

A typical picture displaying the performance of the iteration scheme in (3.12) is presented in Fig. 3.1.

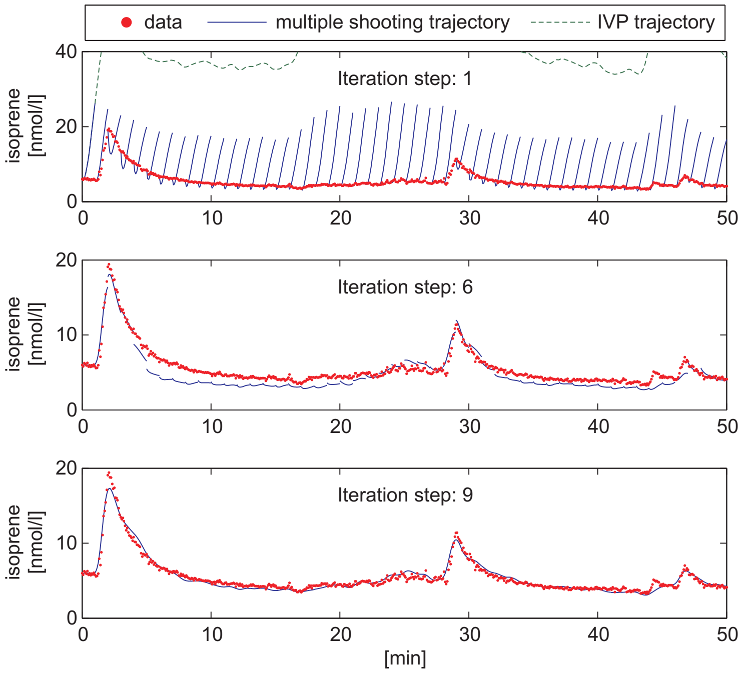

Figure 3.1: Schematic illustration of the multiple shooting approach, applied to the identification of the isoprene model in Chapter 7 with the multiple shooting approach. A length of 1 min is imposed for each multiple shooting interval. The states $\mathbf{x}$ and a set of unknown parameters $\boldsymbol{\vartheta}$ are estimated by observing noisy data from the first component $\mathbf{x}_1$ of the state vector (corresponding to the isoprene concentration in exhaled breath). Convergence is achieved after 9 iterations.

In this example, the multiple shooting method is employed for calibrating a model describing isoprene kinetics in the human body by virtue of measured breath concentration profiles during exercise. Further details can be found in Chapter 7. Starting from an initial guess for the set of unknown model parameters, note that while the first trial trajectory integrated over the entire interval $[t_0, t_{\max}]$ might soon loose contact with the observed data, the discontinuous multiple shooting trajectory can be forced to stay close to the measurements by assigning adequate a priori guesses to the initial conditions $\mathbf{s}_j$ at the multiple shooting nodes τ_j. Such a priori guesses are usually available from physical considerations or from the given data points (for instance if $y = x_m$ for some component of the state vector, as in the example above). This allows the user to directly bring in accessible information about the process dynamics and will prevent the piecewise solution from departing too drastically from the measurements. Furthermore, by an appropriate choice of the grid points τ_j, it can be ensured that every local sub-trajectory $\mathbf{x}(t; \mathbf{s}_j, \boldsymbol{\vartheta})$ can be continued to the next node, i.e., divergence is largely avoided. In particular, this dampens the impact of poor estimates for the model parameters $\boldsymbol{\vartheta}$ on the solution process.

While the greater flexibility of multiple shooting at first glance seems to come at the price of a drastically increased computational cost due to a higher dimensional formulation, in Equation (3.22) we have shown that the special structure of the matching conditions can be exploited to reduce the number of optimization variables in each iteration step to the original problem size $p + n$. An implementation should take advantage of this fact. Furthermore, it is emphasized that the integration of the local IVPs on each sub-interval (representing the most time intensive step in the numerical setup) can easily be parallelized.

3.3.2 Optimality conditions and convergence

In the following we will briefly review the criteria for the solvability of constrained optimization problems of the form (3.10). For notational convenience $\mathbf{f}_2$ and $\mathbf{z}$ are lumped together into one single constraint function $\mathbf{f}_c := (\mathbf{f}_2^T, \mathbf{z}^T)^T : D \subseteq \mathbb{R}^{n_v} \to \mathbb{R}^{n_c}$, with D open and convex. Accordingly, the nonlinear problem (3.10) together with the constraints in (3.11) can be written as

$$\min_{\boldsymbol{\omega}} \|\mathbf{f}_1(\boldsymbol{\omega})\|_2^2 \quad \text{subject to} \quad \mathbf{f}_c(\boldsymbol{\omega}) = \mathbf{0}, \tag{3.34}$$

while its linearized version according to (3.13) reads

$$\min_{\Delta\boldsymbol{\omega}} \|\mathbf{f}_1(\boldsymbol{\omega}) + F_1(\boldsymbol{\omega})\Delta\boldsymbol{\omega}\|_2^2 \quad \text{subject to} \quad \mathbf{f}_c(\boldsymbol{\omega}) + F_c(\boldsymbol{\omega})\Delta\boldsymbol{\omega} = \mathbf{0}. \tag{3.35}$$

Here $F_c := \begin{pmatrix} F_2^T & Z^T \end{pmatrix}^T$ denotes the Jacobian associated with $\mathbf{f}_c$.

Two general requirements will have to be fulfilled in the following.

Hypothesis 1. (*Constraint qualification* [CQ]) For all $\boldsymbol{\omega} \in D$ it holds that $\boldsymbol{\omega}$ is regular, i.e.,

$$\operatorname{rank} F_c(\boldsymbol{\omega}) = n_c. \tag{3.36}$$

Hypothesis 2. (*Positive definiteness* [PD]) For all $\boldsymbol{\omega} \in D$ it holds that

$$\operatorname{rank} F(\boldsymbol{\omega}) := \operatorname{rank} \begin{pmatrix} F_1(\boldsymbol{\omega}) \\ F_c(\boldsymbol{\omega}) \end{pmatrix} = n_v. \tag{3.37}$$

Remark 10. We emphasize the fact that [PD] is closely related to the concept of local identifiability as introduced in the previous chapter. In particular, this condition will be satisfied if the sensitivities of the model output with respect to the unknown initial conditions and model parameters are linearly independent.

The last condition can easily be shown to be equivalent to

$$\Delta\boldsymbol{\omega}^T F_1^T F_1 \Delta\boldsymbol{\omega} > 0 \text{ for all } \Delta\boldsymbol{\omega} \neq \mathbf{0} \text{ with } F_c \Delta\boldsymbol{\omega} = \mathbf{0}, \tag{3.38}$$

which will yield sufficient conditions for a Kuhn-Tucker point of (3.35) to be a strict minimizer. To illustrate this point, we need to recall the following fundamental result.

Theorem 3.2. *(*Necessary and sufficient conditions for optimality*) Let $\boldsymbol{\omega}^* \in D$ be regular and a minimizer of* (3.34). *Then $\boldsymbol{\omega}^*$ is feasible, i.e.*

$$\mathbf{f}_c(\boldsymbol{\omega}^*) = \mathbf{0}, \tag{3.39}$$

and there exist Lagrange multipliers $\boldsymbol{\lambda}^*$ such that for the gradient of the Lagrange function

$$\mathcal{L}(\boldsymbol{\omega}, \boldsymbol{\lambda}) := \frac{1}{2}\|\mathbf{f}_1(\boldsymbol{\omega})\|_2^2 - \boldsymbol{\lambda}^T \mathbf{f}_c(\boldsymbol{\omega}) \tag{3.40}$$

it holds that

$$\frac{\partial}{\partial \boldsymbol{\omega}} \mathcal{L}(\boldsymbol{\omega}^*, \boldsymbol{\lambda}^*) = \mathbf{f}_1(\boldsymbol{\omega}^*)^T F_1(\boldsymbol{\omega}^*) - \left(\boldsymbol{\lambda}^*\right)^T F_c(\boldsymbol{\omega}^*) = \mathbf{0}. \tag{3.41}$$

Conversely, let $\boldsymbol{\omega}^*$ be a Kuhn-Tucker (KT) point of (3.34)*, i.e., there exist multipliers $\boldsymbol{\lambda}^*$ such that* (3.39) *and* (3.41) *are satisfied. If, additionally, the Hessian of $\mathcal{L}$ satisfies*

$$\boldsymbol{\omega}^T \frac{\partial^2}{\partial \boldsymbol{\omega}^2} \mathcal{L}(\boldsymbol{\omega}^*, \boldsymbol{\lambda}^*) \boldsymbol{\omega} > 0 \textit{ for all } \boldsymbol{\omega} \neq \mathbf{0} \textit{ with } F_c \boldsymbol{\omega} = \mathbf{0}, \tag{3.42}$$

then $\boldsymbol{\omega}^*$ is a strict solution of (3.34) *in D.*

For a proof we refer to standard textbooks on optimization theory, e.g., [57].

Applying the previous theorem to the linearized problem (3.35) shows that under the assumptions [CQ] and [PD] there exists a unique minimizer $\Delta\boldsymbol{\omega}^*$ for every $(\mathbf{f}_1^T(\boldsymbol{\omega}), \mathbf{f}_c^T(\boldsymbol{\omega}))^T$, i.e., the increment in each iteration step associated with (3.12) is well-defined. Indeed, the stationarity and feasibility conditions (3.41) and (3.39) in this case read

$$\begin{pmatrix} F_1^T \mathbf{f}_1 \\ \mathbf{f}_c \end{pmatrix} + \begin{pmatrix} F_1^T F_1 & F_c^T \\ F_c & \mathrm{O} \end{pmatrix} \begin{pmatrix} \Delta\boldsymbol{\omega} \\ -\boldsymbol{\lambda} \end{pmatrix} = \mathbf{0}, \tag{3.43}$$

respectively. Subsequently, from (3.38) and by the argument

$$\begin{pmatrix} F_1^T F_1 & F_c^T \\ F_c & \mathrm{O} \end{pmatrix} \begin{pmatrix} \mathbf{a}_1 \\ \mathbf{a}_2 \end{pmatrix} = \mathbf{0} \Rightarrow \mathbf{a}_1^T F_1^T F_1 \mathbf{a}_1 + \mathbf{a}_1^T F_c^T \mathbf{a}_2 = \mathbf{a}_1^T F_1^T F_1 \mathbf{a}_1 = 0 \overset{[\mathrm{PD}]}{\Rightarrow}$$

$$\mathbf{a}_1 = \mathbf{0} \overset{[\mathrm{CQ}]}{\Rightarrow} \mathbf{a}_2 = \mathbf{0} \tag{3.44}$$

the above system matrix is non-singular and hence there exists a *unique* Kuhn-Tucker point

$$\Delta\boldsymbol{\omega}^* = -\begin{pmatrix} I & \mathrm{O} \end{pmatrix} \begin{pmatrix} F_1^T F_1 & F_c^T \\ F_c & \mathrm{O} \end{pmatrix}^{-1} \begin{pmatrix} F_1^T & \mathrm{O} \\ \mathrm{O} & I \end{pmatrix} \begin{pmatrix} \mathbf{f}_1 \\ \mathbf{f}_c \end{pmatrix} =: -F^+ \begin{pmatrix} \mathbf{f}_1 \\ \mathbf{f}_c \end{pmatrix}, \tag{3.45}$$

which additionally satisfies the sufficient condition (3.42) for minimality due to [PD] (note that the Hessian of the Lagrange function in the linearized case is $F_1^T F_1$).

The increment $\Delta\boldsymbol{\omega}$ can hence formally be obtained in every iteration step by multiplying the vector combining the residuals $\mathbf{f}_1$ and the constraints $\mathbf{f}_c$ with a *generalized inverse* F^+ satisfying the fundamental relationship

$$F^+ F = F^+ \begin{pmatrix} F_1 \\ F_c \end{pmatrix} = \begin{pmatrix} I & \mathrm{O} \end{pmatrix} \begin{pmatrix} F_1^T F_1 & F_c^T \\ F_c & \mathrm{O} \end{pmatrix}^{-1} \begin{pmatrix} F_1^T F_1 & F_c^T \\ F_c & \mathrm{O} \end{pmatrix} \begin{pmatrix} I \\ \mathrm{O} \end{pmatrix} = I. \tag{3.46}$$

In the unconstrained case $\mathbf{f}_c = \mathbf{0}$, as can easily be seen from (3.43), the generalized inverse $F^+ = (F_1^T F_1)^{-1} F_1^T$ reduces to the Moore-Penrose pseudoinverse and the iterations (3.12) correspond to the usual Gauss-Newton method.

Remark 11. Due to potential numerical instabilities, $\Delta\boldsymbol{\omega}$ should never be calculated on the basis of the explicit formula (3.45) but via the condensed problem (3.22) and the recursions (3.21).

Adopting the notation from above, the following convergence theorem can be proven.

Theorem 3.3. *(*Local contraction of the generalized Gauss-Newton iteration*)*
Let $\mathbf{f} := (\mathbf{f}_1^T, \mathbf{f}_c^T)^T$ *be a continuously differentiable mapping defined on an open and convex subset* $D \subseteq \mathbb{R}^{n_v}$ *and let* F^+ *denote the generalized inverse defined in* (3.45)*. Moreover, let there be constants* $\kappa < 1$ *and* $\nu < \infty$ *such that the following two Lipschitz conditions are fulfilled for some norm* $\|\cdot\|$*:*

(a) For all $s \in [0,1]$ *and* $\boldsymbol{\omega}_2 = \boldsymbol{\omega}_1 - F^+(\boldsymbol{\omega}_1)\mathbf{f}(\boldsymbol{\omega}_1)$ *in* D *it holds that*

$$\|F^+(\boldsymbol{\omega}_2)(F(\boldsymbol{\omega}_1 + s(\boldsymbol{\omega}_2 - \boldsymbol{\omega}_1)) - F(\boldsymbol{\omega}_1))(\boldsymbol{\omega}_2 - \boldsymbol{\omega}_1)\| \le \nu s \|\boldsymbol{\omega}_2 - \boldsymbol{\omega}_1\|^2. \tag{3.47}$$

(b) If $R := \mathbf{f} - F(F^+\mathbf{f})$ *denotes the residual of the linear problem* (3.35) *then for all* $\boldsymbol{\omega}_1, \boldsymbol{\omega}_3 \in D$ *it holds that*

$$\|F^+(\boldsymbol{\omega}_3)R(\boldsymbol{\omega}_1)\| \le \kappa \|\boldsymbol{\omega}_3 - \boldsymbol{\omega}_1\|. \tag{3.48}$$

Consequently, if an initial guess $\boldsymbol{\omega}^0$ *can be found such that*

$$\delta^0 := \frac{\nu}{2}\|\Delta\boldsymbol{\omega}^0\| + \kappa < 1 \quad \left(\delta^k := \frac{\nu}{2}\|\Delta\boldsymbol{\omega}^k\| + \kappa\right) \tag{3.49}$$

and the ball $\mathcal{B} := \{\boldsymbol{\omega};\ \|\boldsymbol{\omega} - \boldsymbol{\omega}^0\| \le \|\Delta\boldsymbol{\omega}^0\|/(1 - \delta^0)\}$ *is in* D*, then*

1. *The iteration* $\boldsymbol{\omega}^{k+1} = \boldsymbol{\omega}^k + \Delta\boldsymbol{\omega}^k$ *is well-defined and* $\boldsymbol{\omega}^k \in \mathcal{B}$ *for* $k \geq 1$.
2. *The refinements* $\boldsymbol{\omega}^k$ *converge to a fixed point* $\boldsymbol{\omega}^* \in \mathcal{B}$ *with*

$$-\Delta\boldsymbol{\omega}^* = F^+(\boldsymbol{\omega}^*)\mathbf{f}(\boldsymbol{\omega}^*) = \mathbf{0}. \tag{3.50}$$

3. *The convergence is linear with* $\|\Delta\boldsymbol{\omega}^{k+1}\| \leq \delta^k \|\Delta\boldsymbol{\omega}^k\| < \|\Delta\boldsymbol{\omega}^k\|$. *In particular, the final rate of convergence is* $\kappa(\boldsymbol{\omega}^*)$.

Proof. Here we only give a sketch of the proof which follows the line of argumentation for similar convergence results, see [39, 38]. Further details are elaborated in [26, Th. 3.1.44]. The central point is the third assertion, which can be seen to hold due to the fact that

$$\begin{aligned} \|\Delta\boldsymbol{\omega}^{k+1}\| &= \|F^+(\boldsymbol{\omega}^{k+1})\big(\mathbf{f}(\boldsymbol{\omega}^{k+1}) - R(\boldsymbol{\omega}^k) + R(\boldsymbol{\omega}^k)\big)\| \\ &= \|F^+(\boldsymbol{\omega}^{k+1})(\mathbf{f}(\boldsymbol{\omega}^{k+1}) - \mathbf{f}(\boldsymbol{\omega}^k) - F(\boldsymbol{\omega}^k)\Delta\boldsymbol{\omega}^k) + F^+(\boldsymbol{\omega}^{k+1})R(\boldsymbol{\omega}^k)\| \\ &= \|F^+(\boldsymbol{\omega}^{k+1})\{\int_0^1 F(\boldsymbol{\omega}^k + s\Delta\boldsymbol{\omega}^k)\Delta\boldsymbol{\omega}^k \mathrm{d}s - F(\boldsymbol{\omega}^k)\Delta\boldsymbol{\omega}^k\} + F^+(\boldsymbol{\omega}^{k+1})R(\boldsymbol{\omega}^k)\| \\ &\leq \|\int_0^1 F^+(\boldsymbol{\omega}^{k+1})\big(F(\boldsymbol{\omega}^k + s\Delta\boldsymbol{\omega}^k) - F(\boldsymbol{\omega}^k)\big)\Delta\boldsymbol{\omega}^k \mathrm{d}s\| + \|F^+(\boldsymbol{\omega}^{k+1})R(\boldsymbol{\omega}^k)\| \\ &\leq \frac{\nu}{2}\|\Delta\boldsymbol{\omega}^k\|^2 + \kappa\|\Delta\boldsymbol{\omega}^k\| = \delta^k\|\Delta\boldsymbol{\omega}^k\|. \end{aligned} \tag{3.51}$$

With the above assumptions this shows that δ^k as well as $\|\Delta\boldsymbol{\omega}^k\|$ is strictly monotonically decreasing and that $\boldsymbol{\omega}^k \in \mathcal{B}$. In particular, the iterates $\boldsymbol{\omega}^k$ form a Cauchy sequence and hence $\boldsymbol{\omega}^k \to \boldsymbol{\omega}^* \in \mathcal{B}$. Equation (3.50) now follows from $\Delta\boldsymbol{\omega}^k = -F^+(\boldsymbol{\omega}^k)\mathbf{f}(\boldsymbol{\omega}^k) \to \mathbf{0}$ and the continuity of $F^+\mathbf{f}$. □

Substituting $\Delta\boldsymbol{\omega}^* = \mathbf{0}$ into (3.43) according to Equation (3.50) shows that the final iterate $\boldsymbol{\omega}^*$ will be a KT point of (3.34), i.e., it satisfies the necessary conditions for optimality associated with the original nonlinear problem.

Remark 12. Note that the essential condition (3.48) – by taking into account (3.50) – can be reformulated in the solution point $\boldsymbol{\omega}^*$ as

$$\sup_{\boldsymbol{\omega} \in D} \frac{\|F^+(\boldsymbol{\omega})\mathbf{f}(\boldsymbol{\omega}^*)\|}{\|\boldsymbol{\omega} - \boldsymbol{\omega}^*\|} < 1. \tag{3.52}$$

In particular, this excludes convergence for problems with "too large" final residuals $\mathbf{f}(\boldsymbol{\omega}^*)$. Such a situation can be interpreted as an inherent incompatibility of the model with the data. In other words, if [CQ] and [PD] can be assumed to hold, divergence of the iteration scheme (3.12) suggests that the model might not be adequate for capturing the observed data. Insufficiencies of this type can only be resolved by a modification of the model structure. Contrarily, in the compatible case $\mathbf{f}(\boldsymbol{\omega}^*) = \mathbf{0}$, i.e., for problems with vanishing residuals, we find that κ can be set to zero in the final iterations and from the last line of (3.51) it can hence be deduced that the method will converge quadratically. In [26, Th. 3.1.64] it is further demonstrated that the condition $\kappa < 1$ indeed ensures the strict minimality of $\boldsymbol{\omega}^*$ according to the sufficient conditions (3.42).

Remark 13. (*Ill-conditioning*) If the system matrix in (3.43) becomes rank deficient (or nearly so), the solution to the linear subproblem, i.e., the resulting increment $\Delta\boldsymbol{\omega}$ is not unique (or badly determined). A typical case where this is likely to happen is when F_1 is ill-conditioned near the solution point (e.g., if the associated sensitivities of the model output are almost linearly dependent) and if $\mathbf{f}_2 = \mathbf{0}$, i.e., there is no further information on $\boldsymbol{\vartheta}$ and the $\mathbf{s}_j$ in the form of additional equality constraints.

Considering the situation in (3.31), ill-conditioning is reflected by singular values of A_2 that are close to zero. Such cases can be handled by employing a pseudo-inversion method for the solution of (3.31), which typically is based on a numerical rank decision. For this purpose, we may set individual singular values σ_i

to zero if they are below a certain threshold value, e.g., if $\sigma_i \leq \varepsilon \|A_2\|_\infty$, where ε is the relative accuracy of the entries of A_2 [64]. Substitution of $a_{2,i} = 0$ for the corresponding components yields a minimum norm solution for $\mathbf{a}_2$ and ensures that all components of $\boldsymbol{\omega}$ contributing to the ill-conditioned directions are frozen at their current value. While convergence in the rank-deficient case can still be guaranteed under conditions similar to those stated in Theorem 3.3, it should be noted that the extracted fixed point $\boldsymbol{\omega}^*$ then is a KT point of a modified problem rather than the original one given in (3.34) (see [26, Th. 4.3.38] for further details). In this sense, pseudo-inversion should only be seen as a convenient way of increasing algorithmic stability in cases where rank-deficiency occurs during *isolated* iterations, rather than as a general remedy for ill-conditioned problems.

Remark 14. (*Termination criterion*) According to the previous theorem, we can deduce that

$$\begin{aligned} \|\boldsymbol{\omega}^{k+1} - \boldsymbol{\omega}^*\| = \|\boldsymbol{\omega}^{k+1} - \boldsymbol{\omega}^{k+2} + \boldsymbol{\omega}^{k+2} - \cdots\| &\leq \|\Delta\boldsymbol{\omega}^{k+1}\| + \|\Delta\boldsymbol{\omega}^{k+2}\| + \cdots \\ &\leq \sum_{j=1}^{\infty} (\delta^k)^j \|\Delta\boldsymbol{\omega}^k\| = \frac{\delta^k}{1-\delta^k} \|\Delta\boldsymbol{\omega}^k\|. \end{aligned} \quad (3.53)$$

Furthermore, from (3.51) δ^k might be estimated as $\hat{\delta}^k := \|\Delta\boldsymbol{\omega}^{k+1}\| / \|\Delta\boldsymbol{\omega}^k\|$. Hence, a prototypical stopping criterion can be derived by applying relative scaling to the individual components $\Delta\omega_i^k$ and requiring that

$$\frac{\hat{\delta}^k}{1-\hat{\delta}^k} \|(\Delta\omega_1^k/\mathrm{sc}_1, \ldots, \Delta\omega_{n_v}^k/\mathrm{sc}_{n_v})\| \leq \mathrm{TOL}. \quad (3.54)$$

Here, TOL is a prescribed error tolerance and the scaling variables are defined by $\mathrm{sc}_i = \max(\mathrm{sc}_{\min}, |\omega_i^k|)$, where $\mathrm{sc}_{\min} > 0$ is introduced to maintain the relative error concept for cases in which ω_i^k is close to zero.

3.3.3 Globalization of convergence

With the notation of Theorem 3.3, a problem often encountered in practice is that the initial guess $\boldsymbol{\omega}^0$ is situated too far from the fixed point $\boldsymbol{\omega}^*$ to satisfy the conditions for local convergence, in the sense that (3.49) is violated. In such cases, the initial increment $\Delta\boldsymbol{\omega}^0$ might actually point away from $\boldsymbol{\omega}^*$, see Fig. 3.2.

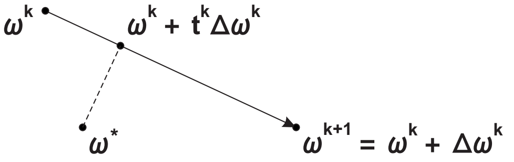
ω^k
$\omega^k + t^k\Delta\omega^k$
ω^*
$\omega^{k+1} = \omega^k + \Delta\omega^k$

Figure 3.2: Full step versus relaxed update scheme.

In order to circumvent this problem, a common approach for enlarging the convergence domain is to replace the basic iteration (3.12) with a damped or *relaxed* version

$$\boldsymbol{\omega}^{k+1} = \boldsymbol{\omega}^k + t^k \Delta\boldsymbol{\omega}^k, \quad (3.55)$$

where the steplength $t^k \in (0, 1]$ is chosen such that the distance between $\boldsymbol{\omega}^{k+1}$ and $\boldsymbol{\omega}^*$ decreases. For this purpose, the level function

$$T(\boldsymbol{\omega}) := \|F^+(\boldsymbol{\omega}^*)\mathbf{f}(\boldsymbol{\omega})\|_2^2 \quad (3.56)$$

is introduced. Linearization around $\boldsymbol{\omega}^*$ yields

$$T(\boldsymbol{\omega}) = \|F^+(\boldsymbol{\omega}^*)(\mathbf{f}(\boldsymbol{\omega}^*) + F(\boldsymbol{\omega}^*)(\boldsymbol{\omega} - \boldsymbol{\omega}^*) + \mathcal{O}(\|\boldsymbol{\omega} - \boldsymbol{\omega}^*\|_2^2)\|_2^2 \quad (3.57)$$

and hence by (3.50) and (3.46)

$$T(\boldsymbol{\omega}) = \|\boldsymbol{\omega} - \boldsymbol{\omega}^*\|_2^2 + \mathcal{O}(\|\boldsymbol{\omega} - \boldsymbol{\omega}^*\|_2^3). \quad (3.58)$$

Thus, T measures the distance between $\boldsymbol{\omega}$ and $\boldsymbol{\omega}^*$ up to third order in the vicinity of the solution and ideally adapts to the local geometry of the admissible region. As $\boldsymbol{\omega}^*$ is a priori unknown, by using the heuristic $F^+(\boldsymbol{\omega}^*) \approx F^+(\boldsymbol{\omega}^k)$, the iteratively weighted *natural level function* [38] can be defined as

$$T^k(\boldsymbol{\omega}) := \|F^+(\boldsymbol{\omega}^k)\mathbf{f}(\boldsymbol{\omega})\|_2^2. \tag{3.59}$$

Since for the gradient of T^k it holds that

$$-\nabla T^k(\boldsymbol{\omega}^k) = -2(\mathbf{f}(\boldsymbol{\omega}^k)^T F^+(\boldsymbol{\omega}^k)^T F^+(\boldsymbol{\omega}^k) F(\boldsymbol{\omega}^k))^T \overset{(3.46)}{=} -2F^+(\boldsymbol{\omega}^k)\mathbf{f}(\boldsymbol{\omega}^k) = 2\Delta\boldsymbol{\omega}^k, \tag{3.60}$$

the increment $\Delta\boldsymbol{\omega}^k$ is just the steepest descent direction of T^k. On the basis of this observation the optimal relaxation coefficient t^k can then be determined by solving the one-dimensional line search problem

$$t^k = \underset{t\in(0,1]}{\arg\min}\, T^k(\boldsymbol{\omega}^k + t\Delta\boldsymbol{\omega}^k) =: \underset{t\in(0,1]}{\arg\min}\, \tilde{T}^k(t), \tag{3.61}$$

which can be treated by standard techniques [57]. For instance, a simple ad hoc algorithm for an approximate minimization would be

1. Find an estimate $\hat{t}^k$ of t^k, e.g., $\hat{t}^k = t^{k-1}$.
2. If $\tilde{T}^k(\hat{t}^k) \geq \tilde{T}(0)$ find the smallest $l \geq 1$ such that $\tilde{T}^k(\hat{t}^k 2^{-l}) < \tilde{T}(0)$ and set $t_k := \hat{t}^k 2^{-l}$.
3. If $\tilde{T}^k(\hat{t}^k) < \tilde{T}(0)$ find the smallest $l \geq 0$ such that $\tilde{T}^k(\hat{t}^k 2^{l+1}) > \tilde{T}^k(\hat{t}^k 2^l)$ and set $t_k := \min\{1, \hat{t}^k 2^l\}$.

For more sophisticated procedures based on a similar predictor-corrector strategy as above we refer to [26, 124]. The fact is stressed that for each evaluation of $\tilde{T}^k(t)$ the values $\mathbf{f}(\boldsymbol{\omega}^k + t\Delta\boldsymbol{\omega}^k)$ have to be obtained, which implies a complete solution of the underlying ODE system and might therefore be a time-intensive task. However, the increased computational cost of a damping procedure is offset in many cases by a dramatically accelerated convergence of the overall iteration.

3.4 Confidence intervals

As has been indicated in Section 3.2, the OLS minimization procedure only leads to a *point estimate* $\boldsymbol{\omega}^*$ of the underlying "true" value $\underline{\boldsymbol{\omega}}$, which necessarily needs to be complemented with some measure of its reliability (usually taking the form of confidence intervals). In other words, we must quantify the extent to which $\boldsymbol{\omega}^*(\mathbf{V})$ varies with the random error terms $\mathbf{V}$, cf. Equation (3.6). This statistical analysis is of paramount importance for examining the quality of the computed estimates and assists in deciding whether these estimates are satisfactory or whether additional experiments should be conducted in order to improve their accuracy. Two different approaches will be discussed in this context, whereby a clear focus on the multiple shooting technique discussed in the previous section will be maintained.

Remark 15. An interesting aspect related to uncertainty assessments for the fitted variables in the specific case of multiple shooting is that confidence intervals might also be constructed for the auxiliary variable $\mathbf{s}_j$, thus providing a discrete measure of accuracy for the entire solution trajectory. This is particularly useful in applications where certain state components x_i cannot be accessed by direct measurements.

3.4.1 Direct methods

Direct methods for constructing confidence intervals in nonlinear regression problems are mainly based on linear perturbation analysis. For this purpose, for fixed $\mathbf{V}$ we first interpret the residual vector $\mathbf{f}_1(\boldsymbol{\omega}, \mathbf{V})$ as a function of $\boldsymbol{\omega}$ and $\mathbf{V}$ satisfying

$$\mathbf{f}_1(\underline{\boldsymbol{\omega}}, \mathbf{0}) = \mathbf{0}. \tag{3.62}$$

Furthermore we define the auxiliary function

$$\mathcal{G}(\boldsymbol{\omega}, \boldsymbol{\lambda}, \mathbf{V}) := \begin{pmatrix} F_1(\boldsymbol{\omega})^T \mathbf{f}_1(\boldsymbol{\omega}, \mathbf{V}) + F_c(\boldsymbol{\omega})^T \boldsymbol{\lambda} \\ \mathbf{f}_c(\boldsymbol{\omega}) \end{pmatrix}, \tag{3.63}$$

incorporating the stationarity and feasibility conditions (3.41) and (3.39), respectively. As $\underline{\boldsymbol{\omega}}$ fulfills the necessary conditions for optimality in the noise-free case $\mathbf{V} = \mathbf{0}$ we conclude that there exist Lagrange multipliers $\underline{\boldsymbol{\lambda}}$ such that

$$\mathcal{G}(\underline{\boldsymbol{\omega}}, \underline{\boldsymbol{\lambda}}, \mathbf{0}) = \mathbf{0}. \tag{3.64}$$

In particular, due to the regularity condition [CQ] it must then hold that $\underline{\boldsymbol{\lambda}} = \mathbf{0}$. By applying the Implicit Function Theorem to (3.64), it can now be shown that the KT point $\boldsymbol{\omega}^* = \boldsymbol{\omega}^*(\mathbf{V})$ and $\boldsymbol{\lambda}^* = \boldsymbol{\lambda}^*(\mathbf{V})$ vary smoothly with $\mathbf{V}$, which is a fundamental prerequisite for the well-posedness of the inverse parameter estimation problem. In fact, the Jacobian of $\mathcal{G}$ at $(\underline{\boldsymbol{\omega}}, \mathbf{0}, \mathbf{0})$ is given by

$$\frac{\partial \mathcal{G}}{\partial(\boldsymbol{\omega}, \boldsymbol{\lambda})}\Big|_{(\underline{\boldsymbol{\omega}},\mathbf{0},\mathbf{0})} = \begin{pmatrix} F_1^T F_1 + \sum\limits_{i=0}^{N} H_{f_{1,i}} f_{1,i} & F_c^T \\ F_c & \mathrm{O} \end{pmatrix}\Big|_{(\underline{\boldsymbol{\omega}},\mathbf{0},\mathbf{0})} \overset{(3.62)}{=} \begin{pmatrix} F_1^T(\underline{\boldsymbol{\omega}}) F_1(\underline{\boldsymbol{\omega}}) & F_c^T(\underline{\boldsymbol{\omega}}) \\ F_c(\underline{\boldsymbol{\omega}}) & \mathrm{O} \end{pmatrix}$$

Here, H denotes the Hessian. In analogy to (3.44), the last matrix is non-singular due to [PD] and [CQ]. As a result,

$$\begin{pmatrix} \frac{\partial \boldsymbol{\omega}^*}{\partial \mathbf{V}} \\ \frac{\partial \boldsymbol{\lambda}^*}{\partial \mathbf{V}} \end{pmatrix}(\mathbf{0}) = -\left(\frac{\partial \mathcal{G}}{\partial(\boldsymbol{\omega}, \boldsymbol{\lambda})}^{-1} \frac{\partial \mathcal{G}}{\partial \mathbf{V}}\right)\Big|_{(\underline{\boldsymbol{\omega}},\mathbf{0},\mathbf{0})} = -\begin{pmatrix} F_1^T(\underline{\boldsymbol{\omega}}) F_1(\underline{\boldsymbol{\omega}}) & F_c^T(\underline{\boldsymbol{\omega}}) \\ F_c(\underline{\boldsymbol{\omega}}) & \mathrm{O} \end{pmatrix}^{-1} \begin{pmatrix} F_1^T(\underline{\boldsymbol{\omega}}) \\ \mathrm{O} \end{pmatrix}$$

and thus the first-order approximation

$$\begin{aligned} \boldsymbol{\omega}^*(\mathbf{V}) \approx \boldsymbol{\omega}^*(\mathbf{0}) + \frac{\partial \boldsymbol{\omega}^*}{\partial \mathbf{V}}(\mathbf{0})\mathbf{V} = \underline{\boldsymbol{\omega}} - \begin{pmatrix} I & \mathrm{O} \end{pmatrix} \begin{pmatrix} F_1^T(\underline{\boldsymbol{\omega}}) F_1(\underline{\boldsymbol{\omega}}) & F_c^T(\underline{\boldsymbol{\omega}}) \\ F_c(\underline{\boldsymbol{\omega}}) & \mathrm{O} \end{pmatrix}^{-1} \times \\ \begin{pmatrix} F_1^T(\underline{\boldsymbol{\omega}}) & \mathrm{O} \\ \mathrm{O} & I \end{pmatrix} \begin{pmatrix} \mathbf{V} \\ \mathbf{0} \end{pmatrix} = \underline{\boldsymbol{\omega}} - F^+(\underline{\boldsymbol{\omega}}) \begin{pmatrix} \mathbf{V} \\ \mathbf{0} \end{pmatrix}. \end{aligned} \tag{3.65}$$

can be established. From the assumptions on $\mathbf{V}$ in Section 3.2 we conclude that $E\{\boldsymbol{\omega}^*\} \approx \underline{\boldsymbol{\omega}}$ and

$$\mathrm{cov}\{\boldsymbol{\omega}^*\} \approx E\{F^+(\underline{\boldsymbol{\omega}}) \begin{pmatrix} \mathbf{V} \\ \mathbf{0} \end{pmatrix} \begin{pmatrix} \mathbf{V}^T & \mathbf{0} \end{pmatrix} F^+(\underline{\boldsymbol{\omega}})^T\} = F^+(\underline{\boldsymbol{\omega}}) \begin{pmatrix} \beta^2 I & \mathrm{O} \\ \mathrm{O} & \mathrm{O} \end{pmatrix} F^+(\underline{\boldsymbol{\omega}})^T. \tag{3.66}$$

Remark 16. As $\underline{\boldsymbol{\omega}}$ is unknown, the estimator covariance matrix $\mathrm{cov}\{\boldsymbol{\omega}^*\}$ is usually approximated in the last iteration step by

$$\mathrm{cov}\{\boldsymbol{\omega}^*\} \approx F^+(\boldsymbol{\omega}^*) \begin{pmatrix} \beta^2 I & \mathrm{O} \\ \mathrm{O} & \mathrm{O} \end{pmatrix} F^+(\boldsymbol{\omega}^*)^T = C(\boldsymbol{\omega}^*). \tag{3.67}$$

Hence, $\mathrm{cov}\{\boldsymbol{\omega}^*\}$ can be computed via the generalized inverse without further computational effort, thus allowing for a very convenient a posteriori analysis of the extracted estimates. Following the previous line of argumentation, in the unconstrained case $\mathbf{f}_c = \mathbf{0}$ we recover the familiar covariance estimate

$$\mathrm{cov}\{\boldsymbol{\omega}^*\} \approx \beta^2 (F_1^T F_1)^{-1}, \tag{3.68}$$

which in the case of Gaussian error terms is just the inverse of the Fisher information matrix. If the common factor β^2 of the measurement variance is unknown, it can be estimated from the final residuals by

$$\hat{\beta}^2 = \frac{\|\mathbf{f}_1(\boldsymbol{\omega}^*)\|_2^2}{l_2}, \tag{3.69}$$

where $l_2 := N + 1 - l_1$ and $l_1 := n_v - n_c$ is the number of fitted parameters [26].

From (3.67), approximate standard errors $\sigma\{\omega_i^*\}$ are given by

$$\hat{\sigma}\{\omega_i^*\} = \sqrt{C(\boldsymbol{\omega}^*)_{i,i}}. \tag{3.70}$$

On the basis of these results, *non-parametric* confidence intervals for each component ω_i^* might be constructed by considering Tchebycheff's inequality, asserting that

$$\Pr\big(|\omega_i^* - E\{\omega_i^*\}| > d_\alpha\big) < \alpha \tag{3.71}$$

for $d_\alpha = \sigma\{\omega_i^*\}/\alpha$. A corresponding $100(1-\alpha)\%$ confidence interval for ω_i^* can hence be computed by

$$\mathrm{CI}_\alpha(\omega_i^*) \approx [\omega_i^* - \hat{\sigma}\{\omega_i^*\}/\alpha,\ \omega_i^* + \hat{\sigma}\{\omega_i^*\}/\alpha]. \tag{3.72}$$

Additionally, from (3.65) the estimate $\boldsymbol{\omega}^*$ is a weighted average of *iid* random variables and hence an appropriate version of the Central Limit Theorem yields that, asymptotically,

$$\boldsymbol{\omega}^* \sim \mathcal{N}(\underline{\boldsymbol{\omega}}, C(\underline{\boldsymbol{\omega}})). \tag{3.73}$$

From this, parametric confidence intervals can be computed by replacing $C(\underline{\boldsymbol{\omega}})$ with the obvious estimate. A rigorous proof of the above result is elaborated in [144]. Less conservative direct assessments usually require further assumptions on the error distribution, e.g., $\mathbf{V} \sim \mathcal{N}(\mathbf{0}, \beta^2 I)$, see [144, 26]. The latter premise can be investigated by means of standard graphical and formal methods from residual analysis (e.g., quantile-quantile plots or Kolmogorov-Smirnov tests).

Note that the quality of the standard errors and confidence intervals introduced above strongly depends on the extent to which the linearization (3.65) is valid. Thus, if the intrinsic curvature of the objective function $\|\mathbf{f}_1\|_2^2$ at $\underline{\boldsymbol{\omega}}$ is high, the coverage probability of the confidence intervals based on linear perturbation analysis can differ drastically from its nominal level.
In order to surmount these obstacles, alternative confidence intervals can be constructed on the basis of bootstrapping, which we shall briefly illustrate in the next subsection.

Remark 17. (*Information content of the covariance matrix*) Some key measures related to practical estimability can be distilled from the *correlation matrix* R defined by

$$R_{i,j} := \frac{C(\boldsymbol{\omega}^*)_{i,j}}{\sqrt{C(\boldsymbol{\omega}^*)_{i,i} C(\boldsymbol{\omega}^*)_{j,j}}} \in [-1, 1], \tag{3.74}$$

containing the approximate correlation coefficients quantifying the degree of interplay between the ith and jth parameter under scrutiny [46, 144, 79, 139]. A value of $R_{i,j}$ near $+1$ or -1 provides strong indications for a lack of identifiability when both parameters are estimated simultaneously, as a change in the model output caused by a perturbation of the component ω_i can nearly compensated by an appropriate change in ω_j. The prototypical situation in which such obstacles arise is if the experimental scenario only provides data that are insufficiently rich in information for jointly determining both parameters (despite the fact that the individual sensitivity of the model output with respect to each of these parameters is reasonably large). An equivalent viewpoint is that the model structure is over-parameterized in the present experimental context, as a modified description with one of the two parameters being replaced by an adequately scaled version of the second one will do almost as well in explaining the observed data.

Remark 18. (*Optimal experiments*) As a second practical remark, it should be noted the explicit formula (3.67) for $C = C(\boldsymbol{\omega}^*, \mathbf{u})$ can be exploited for designing *optimal experiments*. Loosely spoken, this amounts to finding feasible input functions $\mathbf{u}$ for which some measure of the "size" of C (determining the length of confidence intervals or the volume of confidence regions for $\boldsymbol{\omega}^*$) is minimized. A typical criterion for instance is to find a minimum of

$$\Phi(C) = \frac{1}{n_v} \operatorname{trace} C, \tag{3.75}$$

representing the average variance of the fitted parameters. For further details we refer to [20, 51]. Evidently, optimal experimental design for maximizing the statistical reliability of the estimates is particularly appealing in cases where the conductible measurements are costly in some sense (which in a physiological setting usually means invasive and/or time-intensive).

3.4.2 Bootstrap confidence intervals

Suppose that we were able to repeat the experiment leading to the observed data $y_i := h(\mathbf{x}(t_i, \underline{\boldsymbol{\omega}}), \underline{\boldsymbol{\omega}}) + v_i$ under exactly the same conditions. This would yield a second data set $\{y_i^b;\ i = 0, \dots, N\}$ and would subsequently permit the calculation of an additional OLS point estimate $\boldsymbol{\omega}^{*,b}$. By iterating this procedure

B times we would finally arrive a set of values $\{\boldsymbol{\omega}^{*,b};\ b = 0,\ldots,B\}$, approximating the distribution of $\boldsymbol{\omega}^*$ as a function of the measurement error $\mathbf{V}$.

Bootstrapping [47, 48, 146, 77, 42, 17] essentially mimics this idea and *artificially* creates new data points y_i^b by means of extensive resampling from the extracted residuals. The popularity of this approach mainly stems from the fact that it is completely automatic and can be applied irrespective of model complexity and the actual error distribution, as long as it can be ensured that the individual error terms V_i are independent and identically distributed (*iid*). The necessity of this requirement will become evident from the discussion below.

As a second advantage, bootstrapping does not rely on linearization, rendering it as a robust tool if the nonlinearity of the least squares functional at the solution point is anticipated to be substantial. This flexibility, however, comes at the price of high computational burden, which can rapidly become prohibitive in cases where the underlying optimization process is very time-intensive.

From the perturbation argument in Section 3.4.1, the OLS estimation procedure in Section 3.2 can be reformulated as a transformation of random variables

$$\omega_i^* = \mathcal{R}(\mathbf{V}), \tag{3.76}$$

i.e., the distribution of the component ω_i^* depends on the the joint distribution function $P_{\mathbf{V}}$ of the error terms. Here, $\mathcal{R}$ can be considered as an appropriate smooth functional reflecting the estimation algorithm. In order to quantify the accuracy of the components of $\boldsymbol{\omega}^*$ we are thus primarily interested in the distribution function $P_{\mathcal{R}}$ of $\mathcal{R}$. Under the assumption of *iid* error terms V_i with common distribution function P_V, the latter can formally be written as

$$P_{\mathcal{R}}(r) \overset{\text{iid}}{=} \int \chi_{(-\infty,r]}\left(\mathcal{R}(\mathbf{V})\right) \prod_{i=0}^{N} \mathrm{d}P_V, \tag{3.77}$$

where χ denotes the characteristic function and the integration is over $\operatorname{supp}\{V\}^{N+1}$. Since P_V is a priori unknown, it has to be approximated in some way. One fruitful approach to do this is by employing what Efron [48] calls the *plug-in principle*. One merely replaces P_V in (3.77) by its empirical distribution function

$$\widehat{P}_V(v) = \frac{1}{N+1}\sum_{i=0}^{N} \chi_{(-\infty,v]}(v_i), \tag{3.78}$$

thus yielding the so-called theoretical bootstrap estimator

$$P_{\mathcal{R}}^{\text{boot}}(r) = \int \chi_{(-\infty,r]}\left(\mathcal{R}(V_0,\ldots,V_N)\right) \prod_{i=0}^{N} \mathrm{d}\widehat{P}_V(V_i). \tag{3.79}$$

This plug-in principle is intuitively reasonable, since the discrete distribution function $\widehat{P}_V$ will approach its continuous counterpart P_V for large data length $N+1$ (pointwise, this is just a consequence the Strong Law of Large Numbers).

In a next step, $P_{\mathcal{R}}^{\text{boot}}$ is approximated by Monte Carlo integration, which allows for the calculation of high-dimensional integrals by interpreting them as expectations of certain random variables. For this purpose, first note that (3.79) can be reformulated as

$$P_{\mathcal{R}}^{\text{boot}}(r) = E_{\prod_{i=0}^{N}\mathrm{d}\widehat{P}_V}\{\chi_{(-\infty,r]}(\mathcal{R}(V_0,\ldots,V_N))\} \tag{3.80}$$

Hence, by the Strong Law of Large Numbers we can easily deduce the approximation

$$P_{\mathcal{R}}^{\text{boot}} \approx P_{\mathcal{R}}^{\text{boot},B}(r) = \frac{1}{B}\sum_{b=1}^{B} \chi_{(-\infty,r]}(\mathcal{R}(\mathbf{v}^b)), \tag{3.81}$$

where $\mathbf{v}^b$ is an independent random sample generated according to the probability measure

$$\mathbf{v}^b \sim \prod_{i=0}^{N} \mathrm{d}\widehat{P}_V \tag{3.82}$$

and B is the number of bootstrap simulations. Note that $\widehat{P}_V$, unlike P_V, is a known distribution, namely the one putting mass $(N+1)^{-1}$ on each residual v_i, i.e.,

$$\widehat{P}_V \sim \mathcal{U}(\{v_0, \ldots, v_N\}). \tag{3.83}$$

Thus, realizing a sample $\mathbf{v}^b$ as above amounts to simulating $N+1$ independent realizations following a uniform distribution over the set $\{v_0, \ldots, v_N\}$, which can easily be implemented by means of standard random variate generators, cf. Remark 30.

Remark 19. As the aforementioned mechanism actually is equivalent to taking $N+1$ *resamples with replacement* from the set $\{v_0, \ldots, v_N\}$, bootstrapping is often classified as data resampling technique. Note, however, that resampling merely represents a convenient way for evaluating the integral in (3.79) rather than a necessary step. Moreover, if a specific distribution $\tilde{P}_V$ can be identified that fits the extracted residuals, the error terms might be resampled using that distribution rather than $\widehat{P}_V$ (cf. (3.78)). This variant is called *parametric* bootstrapping.

The above discussion paves the way for a sampling-based approximation of the distribution function $P_{\mathcal{R}}$, from which any desired statistical measure on ω_i^* can be derived. In particular, the following algorithm summarizes the necessary steps for the construction of approximate standard errors $\hat{\sigma}\{\omega_i^*\}$. This variant is referred to in the literature as *bootstrapping residuals* (see, e.g., [77]). An application of the scheme below can be found in Chapter 7, where bootstrap standard errors are calculated for the model parameters extracted from the fitting procedure presented in Fig. 3.1.

Algorithm 2 (*Bootstrapping residuals*)

Let $\boldsymbol{\omega}^{*,0} := \boldsymbol{\omega}^*$ denote the minimizer from the original OLS estimation procedure.

1. For b from 1 to B do
    - → Create $N+1$ samples $v_i^b \sim \mathcal{U}(\{v_0, \ldots, v_N\})$ as well as *synthetic* data points $y_i^b = h(\mathbf{x}(t_i, \underline{\boldsymbol{\omega}}), \underline{\boldsymbol{\omega}}) + v_i^b \approx h\big(\mathbf{x}(t_i, \boldsymbol{\omega}^{*,0}), \boldsymbol{\omega}^{*,0}\big) + v_i^b$.
    - → Obtain $\boldsymbol{\omega}^{*,b} = \mathcal{R}(\mathbf{v}^b)$, i.e., solve the OLS problem with underlying data y_i^b. Here, the original OLS estimate $\boldsymbol{\omega}^{*,0}$ can serve as an appropriate initial guess.
2. Calculate $\hat{\sigma}\{\omega_i^*\}$ as the empirical standard deviation of the population $\{\omega_i^{*,b};\ b = 0, \ldots, B\}$.

Analogously, an approximate confidence interval $\mathrm{CI}_\alpha(\omega_i^*)$ for ω_i^* might be constructed from the $\alpha/2$- and $(1-\alpha/2)$-percentiles associated with $\{\omega_i^{*,b};\ b = 0, \ldots, B\}$. Apart from this so-called bootstrap percentile interval, several other variants exist [48, 146].

It is clear that due to the use of an approximation for P_V as well as due to the Monte Carlo procedure (3.81), the coverage probability of such confidence intervals will generally differ from the desired nominal level $(1-\alpha)$. Proofs of consistency, i.e.,

$$\Pr\left(\omega_i^* \in \mathrm{CI}_\alpha(\omega_i^*)\right) \to 1 - \alpha \tag{3.84}$$

as N and B tend to infinity can be found in [48, 146] and references therein and will not further be elaborated here. Ultimately the convergence above relies on the extent to which the empirical distribution function $\widehat{P}_V$ is able to mimic the decisive characteristics of P_V for fixed N. In particular, if N is small it should be recognized that bootstrap confidence intervals can only provide a "quick" check of the robustness of the calculated estimates. Moreover, the potential improvement of coverage performance by increasing B is limited – in practice, a moderate value of $B \approx 200$ usually suffices [77].

Remark 20. (*Residual analysis and practical remarks*) The central requirements of independent and identically distributed error terms (stemming from (3.77)) can be verified a posteriori by various standard techniques from residual analysis. Simple visual tests that often prove sufficient for picking up violations of aforementioned assumptions include plots of the residuals vs. time, i.e., plots of the points (t_i, v_i), as well as of the residuals vs. the model predictions $h(\mathbf{x}(t_i, \boldsymbol{\omega}^*), \boldsymbol{\omega}^*)$. A random pattern in the first suggests that the assumption of independence is reasonable, while a random, non-increasing pattern in the second provides a strong indication for homoscedasticity [18]. Formal statistical assessments can be achieved by testing for the significance of serial correlations among the residuals, e.g., using a Ljung-Box portmanteau test or a runs test [100, 27]. Some strategies for handling cases in which the *iid* assumption above is violated are indicated in [42] (see also Chapter 7).

Chapter 4

On-line identification

Contents

4.1 Stochastic difference equations 43
  4.1.1 Discretization 43
  4.1.2 Stochastic framework 44
4.2 Nonlinear filtering 46
  4.2.1 Sequential Bayes filter 47
  4.2.2 Kalman filtering 48
  4.2.3 Particle filtering 51
  4.2.4 Dual estimation 55
4.3 Anesthetic monitoring 59
  4.3.1 Problem statement 59
  4.3.2 Sevoflurane monitoring 61
4.A Stochastic simulation 66
  4.A.1 Pseudo-Randomness 67
  4.A.2 General simulation principles 67

This chapter is devoted to *on-line* methods for approaching the system identification problem introduced in Chapter 3. The aim will be to develop algorithmic schemes that allow for a *sequential* estimation of the states and parameters governing the behavior of physiological models as described in Section 2.3. Such on-line procedures are usually summarized under the term *filtering* and play a prominent role in various fields of engineering and science. We emphasize that from a methodological viewpoint these procedures are rather different from the off-line techniques discussed in Chapter 3. While the latter are based on batch processing and hence require the entire experiment to be completed and all output data being collected beforehand, we would now like to improve our knowledge about the underlying system while data acquisition is still running. This is of utmost importance in applications where actions or decisions need to be taken in the course of ongoing measurement, see also Section 4.3. Much of the background material on filtering covered here is taken from standard textbooks such as [81, 60, 10]. References regarding more advanced concepts will be given where appropriate.

4.1 Stochastic difference equations

4.1.1 Discretization

So far we have exclusively focused on continuous-time ODE models of the type (2.16). While such models offer a natural description of many real world phenomena, triggered measurements as well as numerical treatment invariably require model formulations in discrete time. In the sequel we will hence mainly deal with parameterized *difference equations* of the form

$$\begin{aligned} \mathbf{x}_k &= \mathbf{g}_{k-1}(\mathbf{x}_{k-1}, \boldsymbol{\vartheta}), \quad k \geq 1 \\ y_k &= h_k(\mathbf{x}_k, \boldsymbol{\vartheta}). \end{aligned} \tag{4.1}$$

The first expression is generally referred to as evolution equation, capturing the dynamics of the state $\mathbf{x} \in \mathbb{R}^n$ on a discrete time horizon $t_k = k\Delta t$. Here, $\Delta t > 0$ denotes a (constant) discretization step size or sampling interval. The second relationship is called the measurement equation and yields an observable model output. The assumption of y_k being scalar has merely been made for the ease of notation. Most of the facts to be presented generalize to the multiple output case in a straightforward manner. Equation (4.1) constitutes a *state space representation* of the model. Again, the vector $\boldsymbol{\vartheta} \in \mathbb{R}^p$ lumps together a set of *constant* model parameters that may be partially unknown. As in the previous chapter, the functions $\mathbf{g}_k$ and h_k are assumed to be continuously differentiable with respect to both arguments at all time instants considered.

Remark 21. The time-dependence of $\mathbf{g}$ and h implicitly covers possible influences of time-varying input functions on the discrete system (4.1).

Several approaches have been proposed for transforming continuous-time models into their discrete-time counterparts, see, e.g., [71]. Most of these mappings take the form of explicit integration schemes familiar from numerical analysis, such as truncated Taylor series approximations or Runge-Kutta methods. For instance, a simple Euler discretization yields

$$\dot{\mathbf{x}} = \mathbf{g}(t, \mathbf{x}, \boldsymbol{\vartheta}) \;\rightsquigarrow\; \mathbf{x}_k = \mathbf{x}_{k-1} + \mathbf{g}(t_{k-1}, \mathbf{x}_{k-1}, \boldsymbol{\vartheta})\Delta t =: \mathbf{g}_{k-1}(\mathbf{x}_{k-1}, \boldsymbol{\vartheta}). \tag{4.2}$$

The final discretization technique generally has to be selected according to the specific problem at hand, taking into account computational burden as well as stability. In the special case of linear ODE systems,

$$\dot{\mathbf{x}} = A(t, \boldsymbol{\vartheta})\mathbf{x} + B(t, \boldsymbol{\vartheta}) \tag{4.3}$$

a particularly convenient choice is zero-order hold sampling [148]. By assuming that the matrices $A \equiv A_{k-1}$ as well as $B \equiv B_{k-1}$ are constant on the interval $[t_{k-1}, t_k]$ we can derive the exact relationship

$$\mathbf{x}_k = G_{k-1}(\boldsymbol{\vartheta})\mathbf{x}_{k-1} + \mathbf{f}_{k-1}(\boldsymbol{\vartheta}), \tag{4.4}$$

where

$$G_{k-1} := \exp\left(A_{k-1}\Delta t\right) \tag{4.5}$$

and

$$\begin{aligned} \mathbf{f}_{k-1} := \big(\exp\left(A_{k-1}\Delta t\right) \int_0^{\Delta t} \exp\left(-A_{k-1}\tau\right)\mathrm{d}\tau\big) B_{k-1} = \\ \exp\left(A_{k-1}\Delta t\right)\big(I - \exp\left(-A_{k-1}\Delta t\right)\big) A_{k-1}^{-1} B_{k-1}. \end{aligned} \tag{4.6}$$

The last equality holds if A_{k-1} is invertible.

4.1.2 Stochastic framework

Equation (4.1) provides a description of the process dynamics in the ideal context of an error-free model structure as well as perfect measurements. In a more realistic setting, however, both the state and the measurement equation are known only approximately. Uncertainties can result, for instance, from noisy input and output measurement, modeling errors or external disturbances acting on the system. It is hence necessary to complement the aforementioned deterministic model with a *probabilistic* model reflecting the aforementioned imperfections. For this purpose we introduce the (possibly nonlinear) stochastic difference equation

$$\begin{aligned} \mathbf{x}_k &= \mathbf{g}_{k-1}(\mathbf{x}_{k-1}, \boldsymbol{\vartheta}, \mathbf{w}_{k-1}), \quad k \geq 1 \\ y_k &= h_k(\mathbf{x}_k, \boldsymbol{\vartheta}, v_k), \end{aligned} \tag{4.7}$$

where $\mathbf{w}_k$ and v_k are mutually independent random variables with zero mean, usually referred to as process (or plant) noise and measurement noise, respectively [153].

Remark 22. We stress the fact that several alternative frameworks have been put forward for capturing uncertainty in this context, particularly imprecise probabilities and interval-valued noise descriptions. For more details see, e.g., [88, 30].

The structure (4.7) motivates the following basic definition.

Definition 3. A discrete-time stochastic process is a family of random variables $\{\mathbf{x}_k\}$ defined on a common probability space, where the time k belongs to a discrete index set I (mostly, $I = \mathbb{N}$ or $I = \mathbb{Z}$). A realization of $\{\mathbf{x}_k\}$ is referred to as sample path or time series.

For the sake of simplicity, no explicit distinction is made between the generating random processes $\{\mathbf{x}_k\}$ (or $\{y_k\}$) induced by (4.7) and their realizations. The meaning will be clear from the given context.

Generally, we will postulate the existence of appropriate continuous probability density functions (pdfs) p, describing the probability law of the random vectors $\mathbf{x}_k$ and y_k with respect to the standard Lebesgue measure. At a specified time index k this reads, for instance,

$$\mathbf{x}_k \sim p_{\boldsymbol{\vartheta}}(\mathbf{x}_k). \tag{4.8}$$

For the sake of notational simplicity, we will omit the dependence of p on $\boldsymbol{\vartheta}$ for the moment. Under suitable regularity conditions the *conditional* density of $\mathbf{x}_k$ given y_k can be defined as

$$p(\mathbf{x}_k|y_k) := \frac{p(\mathbf{x}_k, y_k)}{p(y_k)} = \frac{p(y_k|\mathbf{x}_k)p(\mathbf{x}_k)}{\int p(y_k|\mathbf{x}_k)p(\mathbf{x}_k)\mathrm{d}\mathbf{x}_k}. \tag{4.9}$$

Here, the second equality sign denotes the well-known *Bayes' theorem.* In the present context $p(\mathbf{x}_k|y_k)$ is usually referred to as posterior density, while $p(y_k|\mathbf{x}_k)$ and $p(\mathbf{x}_k)$ are the likelihood and the prior, respectively. Note that it will be a tacit assumption in the sequel to always integrate over the entire domain of respective random variable.

Using the above notation, the independence assumption on $\mathbf{w}_k$ and v_k translates to

$$p(\mathbf{w}_k|\mathbf{w}_l) = p(\mathbf{w}_k), \quad k > l \tag{4.10}$$

and similarly for v_k. In light of the previous requirement it is customary to call $\{\mathbf{w}_k\}$ a *white* random sequence. Returning to (4.7) one can immediately see that given $\mathbf{x}_{k-1}$, $\mathbf{x}_k$ depends only on $\mathbf{w}_k$, which is independent of the previous states. Hence, Equation (4.10) ensures that the stochastic process $\{\mathbf{x}_k\}$ becomes a Markov process, characterized by the following defining property.

Definition 4. A discrete-time stochastic process $\{\mathbf{x}_k\}$ is called a Markov process if the conditional pdf satisfies

$$p(\mathbf{x}_k|\mathbf{x}_{k-1}, \ldots, \mathbf{x}_0) = p(\mathbf{x}_k|\mathbf{x}_{k-1}), \quad k \geq 1. \tag{4.11}$$

Similarly, given $\mathbf{x}_k$ the random variable y_k defined via (4.7) will be conditionally independent of the past states, hence

$$p(y_k|\mathbf{x}_k, \ldots, \mathbf{x}_0) = p(y_k|\mathbf{x}_k). \tag{4.12}$$

Equation (4.11) has also been termed the general causality principle: the present state $\mathbf{x}_k$ contains all past information that has any impact on the future behavior of the process. Moreover, it states that Markov processes propagate uncertainty by means of the so-called *transition densities* $p(\mathbf{x}_k|\mathbf{x}_{k-1})$. In particular, the marginal pdf of $\mathbf{x}_k$ can be determined by virtue of the Chapman-Kolmogorov equation

$$p(\mathbf{x}_k) = \int p(\mathbf{x}_k|\mathbf{x}_{k-1})p(\mathbf{x}_{k-1})\mathrm{d}\mathbf{x}_{k-1}, \tag{4.13}$$

which is a reformulation of the law of total probability. It is precisely this last expression that is decisive for inferring the statistical behavior of $\mathbf{x}_k$ (and later also of $\boldsymbol{\vartheta}$), as it opens up a possibility for extracting potentially informative indices such as $E\{\mathbf{x}_k\}$, $\mathrm{var}\{\mathbf{x}_k\}$ or associated confidence intervals.

A further generalization of the situation above emerges from the concept of a priori information, which is introduced by additionally assigning a probability law to the initial state $\mathbf{x}_0$:

$$\mathbf{x}_0 \sim p(\mathbf{x}_0) \tag{4.14}$$

This pdf is called an *initial prior* and lumps together all probabilistic knowledge about the state of the system before any observation has been made.

In summary, (4.7) turns out to be a special case of of the following general stochastic system.

Definition 5. A hidden (unobserved) Markov model is represented by the stochastic dynamics

$$\begin{aligned} &\mathbf{x}_0 \sim p(\mathbf{x}_0) \\ &\mathbf{x}_k \sim p(\mathbf{x}_k|\mathbf{x}_{k-1}), \quad k \geq 1 \\ &y_k \sim p(y_k|\mathbf{x}_k). \end{aligned} \tag{4.15}$$

Hidden Markov models have received widespread attention in the literature due to their adequate description of a broad spectrum of practically interesting stochastic processes. The general formulation (4.15) will be instrumental for the treatment of the nonlinear filtering problem outlined in the next section.

4.2 Nonlinear filtering

This section provides an overview of nonlinear filtering theory for hidden Markov models as defined above. It can by no means offer a complete exposition of all branches in this active area of system engineering research, but rather serves as a survey on several existing techniques that appear useful in the given context of physiological modeling and estimation. In this regard, we will adopt a practitioner's viewpoint and develop the underlying theory only to the extent relevant for this thesis.

Loosely spoken, the filtering problem amounts to computing a state estimate $\hat{\mathbf{x}}_k$ of the stochastic system (4.7) from the collection of available output values $Y_k := (y_k, \ldots, y_1)$ up to time k. The presentation here will adopt a Bayesian perspective, which offers a unifying approach to nonlinear state estimation and underpins the logic of various apparently distinct algorithms developed for this purpose. The central object of interest within this framework is the conditional (*posterior*) probability distribution $p(\mathbf{x}_k|Y_k)$ which according to the Bayesian paradigm can be seen as the complete solution of the nonlinear filtering problem just introduced. This is due to the fact that $p(\mathbf{x}_k|Y_k)$ by definition embodies all accessible information on $\mathbf{x}_k$ up to time k.

Given $p(\mathbf{x}_k|Y_k)$, an obvious estimate for the state variable $\mathbf{x}_k$ is the conditional mean

$$\hat{\mathbf{x}}_k := E\{\mathbf{x}_k|Y_k\} = \int \mathbf{x}_k p(\mathbf{x}_k|Y_k)\mathrm{d}\mathbf{x}_k, \tag{4.16}$$

which can be shown to have minimal variance, see Lemma 2. In other words, $\hat{\mathbf{x}}_k$ is optimal in a minimum mean squared error (MMSE) sense.

Lemma 2.

$$\arg\min_{\mathbf{x}} E\{\|\mathbf{x}_k - \mathbf{x}\|_2^2 | Y_k\} = E\{\mathbf{x}_k | Y_k\}. \tag{4.17}$$

Proof. The assertion is proven using the fact that

$$\begin{aligned} E\{\|\mathbf{x}_k - \mathbf{x}\|_2^2 | Y_k\} &= E\{(\mathbf{x}_k - \mathbf{x})^T(\mathbf{x}_k - \mathbf{x}) | Y_k\} \\ &= E\{\|\mathbf{x}_k\|_2^2 | Y_k\} - 2\mathbf{x}^T E\{\mathbf{x}_k | Y_k\} + E\{\|\mathbf{x}\|_2^2 | Y_k\} \\ &= E\{\|\mathbf{x} - E\{\mathbf{x}_k|Y_k\}\|_2^2 | Y_k\} - \|E\{\mathbf{x}_k|Y_k\}\|_2^2 + E\{\|\mathbf{x}_k\|_2^2 | Y_k\}. \end{aligned} \tag{4.18}$$

As the last two terms are independent of $\mathbf{x}$ the claim follows. □

Moreover, $\hat{\mathbf{x}}_k$ is unbiased due to

$$E\{\mathbf{x}_k - \hat{\mathbf{x}}_k\} = E\{\mathbf{x}_k\} - E\{E\{\mathbf{x}_k|Y_k\}\} = \mathbf{0}, \tag{4.19}$$

using the law of iterated expectations.

Remark 23. Other point estimates $\hat{\mathbf{x}}_k$ of $\mathbf{x}_k$ are conceivable, such as for instance the maximum a posteriori (MAP) estimate maximizing the value of $p(\mathbf{x}_k|Y_k)$. In the Gaussian case, both MMSE and MAP estimates coincide.

4.2.1 Sequential Bayes filter

The main intention of this section is to deduce a recursion formula allowing for the sequential computation of the desired posterior density $p(\mathbf{x}_k|Y_k)$. One of the primary motivations for devising such an iterative update scheme is its natural real-time setting. Information can be processed on-line, i.e., as soon as a new measurement y_k becomes available. This feature clearly distinguishes nonlinear filtering from the off-line estimation techniques discussed in Chapter 3 and renders it as a valuable tool for monitoring and tracking problems, requiring an estimate of the state while the process is still running. We give the following fundamental result [155].

Theorem 4.1. *(*Sequential Bayes filter*) Consider a hidden Markov model* (4.15). *The conditional density* $p(\mathbf{x}_k|Y_k)$ *of* $\mathbf{x}_k$ *given the stacked observations* $Y_k = (y_k, \dots, y_1)$ *obeys the recursion*

$$p(\mathbf{x}_k|Y_k) = \frac{p(y_k|\mathbf{x}_k)}{p(y_k|Y_{k-1})} \int p(\mathbf{x}_k|\mathbf{x}_{k-1}) p(\mathbf{x}_{k-1}|Y_{k-1}) \mathrm{d}\mathbf{x}_{k-1}. \tag{4.20}$$

Proof. Using Bayes' rule (4.9) we find that

$$\begin{aligned} p(\mathbf{x}_k|Y_k)p(y_k|Y_{k-1}) &= p(\mathbf{x}_k|y_k, Y_{k-1})p(y_k|Y_{k-1}) \\ &= \frac{p(y_k|\mathbf{x}_k, Y_{k-1})p(\mathbf{x}_k, Y_{k-1})}{p(y_k, Y_{k-1})} \frac{p(y_k, Y_{k-1})}{p(Y_{k-1})} \\ &= p(y_k|\mathbf{x}_k, Y_{k-1})p(\mathbf{x}_k|Y_{k-1}) = p(y_k|\mathbf{x}_k)p(\mathbf{x}_k|Y_{k-1}). \end{aligned} \tag{4.21}$$

Here, the last equality is justified by the form of the measurement equation in (4.15). Thus,

$$p(\mathbf{x}_k|Y_k) = \frac{p(y_k|\mathbf{x}_k)}{p(y_k|Y_{k-1})} p(\mathbf{x}_k|Y_{k-1}). \tag{4.22}$$

The denominator might be written as

$$p(y_k|Y_{k-1}) = \int p(y_k|\mathbf{x}_k)p(\mathbf{x}_k|Y_{k-1}) \mathrm{d}\mathbf{x}_k, \tag{4.23}$$

and can be seen as a normalization constant, ensuring that $p(\mathbf{x}_k|Y_k)$ integrates to unity. Moreover, from Equation (4.13) and due to the fact that, given $\mathbf{x}_{k-1}$, the random variable $\mathbf{x}_k$ does not depend on Y_{k-1}, the second factor in (4.22) can be expressed as

$$p(\mathbf{x}_k|Y_{k-1}) = \int p(\mathbf{x}_k|\mathbf{x}_{k-1}) p(\mathbf{x}_{k-1}|Y_{k-1}) \mathrm{d}\mathbf{x}_{k-1}. \tag{4.24}$$

Combining (4.22) and (4.24) hence yields the assertion. □

The importance of Theorem 4.1 stems from the fact that it establishes a sequential update mechanism for the conditional density $p(\mathbf{x}_k|Y_k)$ as time proceeds from $(k-1)$ to k. Note that (4.20) resembles an inherent predictor-corrector structure: $p(\mathbf{x}_k|Y_{k-1})$ as in Equation (4.24) predicts the posterior density on the basis of the last estimate $p(\mathbf{x}_{k-1}|Y_{k-1})$ and the process equation reflected by the transition density $p(\mathbf{x}_k|\mathbf{x}_{k-1})$. This is often called the *time update*. In a second step, the prediction is refined by means of additional information provided by the measurement equation, which enters via $p(y_k|\mathbf{x}_k)$ (this is termed the *measurement update*).

While the preceding theorem already encapsulates the conceptual solution of the filtering problem, from a practical point of view Equation (4.20) is of limited use. The involved densities rarely admit a closed analytical form and one therefore has to resort to approximations or special cases. In the following subsections we will review some of the major findings in this context. The presentation is no doubt incomplete, as the aim can merely be to give a brief, however roughly self-contained overview of various relevant results scattered in the literature.

4.2.2 Kalman filtering

The most important case of a stochastic dynamical system which lends itself to a tractable solution of the filtering problem as given in Equation (4.20) are linear, Gaussian structures of the type

$$\begin{aligned} \mathbf{x}_k &= G_{k-1}\mathbf{x}_{k-1} + \mathbf{f}_{k-1} + \mathbf{w}_{k-1} \\ y_k &= H_k\mathbf{x}_k + d_k + v_k. \end{aligned} \tag{4.25}$$

It will be a general premise in this subsection to require that the state transition matrix G_k is nonsingular for all k and that $\{\mathbf{w}_k\}$ and $\{v_k\}$ are Gaussian, white, zero-mean and have known symmetric positive definite covariance matrices $Q_k > 0$ and $R_k > 0$, respectively:

$$\begin{aligned} \mathbf{w}_k &\sim \mathcal{N}(\mathbf{0}, Q_k) \\ v_k &\sim \mathcal{N}(\mathbf{0}, R_k) \\ E\{\mathbf{w}_k\mathbf{w}_l^T\} &= Q_k\delta_{kl} \\ E\{v_k v_l^T\} &= R_k\delta_{kl} \\ E\{v_k\mathbf{w}_l^T\} &= \mathbf{0}. \end{aligned} \tag{4.26}$$

Here, δ denotes the Kronecker delta function. Furthermore, we assume that the initial state $\mathbf{x}_0$ is independent of both $\{\mathbf{w}_k\}$ as well as $\{v_k\}$ and that its initial prior is given by a Gaussian distribution $\mathbf{x}_0 \sim \mathcal{N}(\hat{\mathbf{x}}_0^+, P_0^+)$, where (we set $Y_0 := \emptyset$)

$$\begin{aligned} \hat{\mathbf{x}}_0^+ &:= E\{\mathbf{x}_0|Y_0\} = E\{\mathbf{x}_0\} \\ P_0^+ &:= \operatorname{cov}\{\mathbf{x}_0|Y_0\} = \operatorname{cov}\{\mathbf{x}_0\} = E\{(\mathbf{x}_0 - \hat{\mathbf{x}}_0^+)(\mathbf{x}_0 - \hat{\mathbf{x}}_0^+)^T\}. \end{aligned} \tag{4.27}$$

In the following, the superscript "+" will stand for an a posteriori (or corrected) estimate. The matrix P_0^+ is a part of the problem statement and quantifies the uncertainty regarding the initial state of the system before filtering starts. If the latter is perfectly known, then P_0^+ is a zero matrix, i.e., $P_0^+ = \mathrm{O}$. Contrarily, if we are completely ignorant regarding $\mathbf{x}_0$ we may set $P_0^+ = \kappa I$, with $\kappa \gg 1$.

As will be illustrated below, the special status held by systems of the form (4.25) stems from the fact that the conditional densities indicated in (4.20) remain Gaussian in every iteration. Consequently, it is sufficient to propagate the respective conditional mean vectors and covariance matrices in every time step. In this special situation the sequential Bayes filter state will be finite, whereas in the general case it is infinite. The solution scheme developed in Theorem 4.1 then reduces to the celebrated Kalman filter recursions [84].

Corollary 2. (Kalman filter) *Consider the linear, Gaussian system* (4.25) *and an initial prior* $p(\mathbf{x}_0) \sim \mathcal{N}(\hat{\mathbf{x}}_0^+, P_0^+)$. *Under the assumptions stated above, the sequential Bayes filter* (4.20) *reads*

$$\text{time update} \quad \begin{cases} p(\mathbf{x}_k|Y_{k-1}) \sim \mathcal{N}(\hat{\mathbf{x}}_k^-, P_k^-) \\ \hat{\mathbf{x}}_k^- = G_{k-1}\hat{\mathbf{x}}_{k-1}^+ + \mathbf{f}_{k-1} \\ P_k^- = G_{k-1}^T P_{k-1}^+ G_{k-1} + Q_{k-1} \end{cases}$$

$$\text{measurement update} \quad \begin{cases} p(\mathbf{x}_k|Y_k) \sim \mathcal{N}(\hat{\mathbf{x}}_k^+, P_k^+) \\ \hat{\mathbf{x}}_k^+ = \hat{\mathbf{x}}_k^- + K_k(y_k - H_k\hat{\mathbf{x}}_k^- - d_k) \\ P_k^+ = (I - K_kH_k)P_k^-(I - K_kH_k)^T + K_kR_kK_k^T, \end{cases}$$

where

$$K_k := P_k^- H_k^T (H_k P_k^- H_k^T + R_k)^{-1} \tag{4.28}$$

denotes the Kalman gain.

Proof. We start by computing the time update. Assume by induction that $p(\mathbf{x}_{k-1}|Y_{k-1}) \sim \mathcal{N}(\hat{\mathbf{x}}_{k-1}^+, P_{k-1}^+)$. Since the measurement equation is linear and $\mathbf{w}_{k-1}$ is Gaussian it holds that

$$p(\mathbf{x}_k|\mathbf{x}_{k-1}) \sim \mathcal{N}(G_{k-1}\mathbf{x}_{k-1} + \mathbf{f}_{k-1}, Q_{k-1}). \tag{4.29}$$

Then, from (4.24) we have that

$$p(\mathbf{x}_k|Y_{k-1}) = \\ \frac{1}{K_1}\int \exp\left(-\frac{1}{2}\|\mathbf{x}_k - G_{k-1}\mathbf{x}_{k-1} - \mathbf{f}_{k-1}\|^2_{Q_{k-1}^{-1}}\right)\exp\left(-\frac{1}{2}\|\mathbf{x}_{k-1} - \hat{\mathbf{x}}_{k-1}^+\|^2_{(P_{k-1}^+)^{-1}}\right)\mathrm{d}\mathbf{x}_{k-1}, \tag{4.30}$$

where the indicated norm is defined as $\|\mathbf{x}\|_A^2 := \mathbf{x}^T A\mathbf{x}$ for some symmetric positive definite matrix A and

$$K_1 := (2\pi)^n\big(\det Q_{k-1}\det P_{k-1}^+\big)^{\frac{1}{2}}. \tag{4.31}$$

By applying the transformation $G_{k-1}\mathbf{x}_{k-1} + \mathbf{f}_{k-1} =: \mathbf{z}$ in the above integration we find that

$$p(\mathbf{x}_k|Y_{k-1}) = \\ \frac{1}{K_2}\int \exp\left(-\frac{1}{2}\|\mathbf{x}_k - \mathbf{z}\|^2_{Q_{k-1}^{-1}}\right)\exp\left(-\frac{1}{2}\|\mathbf{z} - G_{k-1}\hat{\mathbf{x}}_{k-1}^+ - \mathbf{f}_{k-1}\|^2_{(G_{k-1}^T P_{k-1}^+ G_{k-1})^{-1}}\right)\mathrm{d}\mathbf{z}, \tag{4.32}$$

where the normalization constant now is given by

$$K_2 := (2\pi)^n\big(\det Q_{k-1}\det(G_{k-1}^T P_{k-1}^+ G_{k-1})\big)^{\frac{1}{2}}. \tag{4.33}$$

The fact is stressed that $p(\mathbf{x}_k|Y_{k-1})$ as given (4.32) can be interpreted as the convolution

$$(p_1 * p_2)(\mathbf{x}_k) = \int p_1(\mathbf{x}_k - \mathbf{z})p_2(\mathbf{z})\mathrm{d}\mathbf{z} \tag{4.34}$$

of the densities $p_1 \sim \mathcal{N}(\mathbf{0}, Q_{k-1})$ and $p_2 \sim \mathcal{N}(G_{k-1}\hat{\mathbf{x}}_{k-1}^+ + \mathbf{f}_{k-1}, G_{k-1}^T P_{k-1}^+ G_{k-1})$, representing two independent, n-dimensional Gaussian random variables. Since this convolution is well known to yield the pdf of the sum of the corresponding random variables (see, e.g., [81, Example 2.15]), by taking into account the addition theorem for Gaussian distributions we can thus conclude that

$$p(\mathbf{x}_k|Y_{k-1}) \sim \mathcal{N}(G_{k-1}\hat{\mathbf{x}}_{k-1}^+ + \mathbf{f}_{k-1}, G_{k-1}^T P_{k-1}^+ G_{k-1} + Q_{k-1}) =: \mathcal{N}(\hat{\mathbf{x}}_k^-, P_k^-). \tag{4.35}$$

The conditional mean $\hat{\mathbf{x}}_k^- = E\{\mathbf{x}_k|Y_{k-1}\}$ and covariance matrix $P_k^- = \mathrm{cov}\{\mathbf{x}_k|Y_{k-1}\}$ represent the so-called a priori (or predicted) estimates. Note that P_k^- will again be symmetric positive definite.

We now turn to the measurement update. Firstly, from the linearity of the measurement function we have that $p(y_k|\mathbf{x}_k) \sim \mathcal{N}(H_k\mathbf{x}_k + d_k, R_k)$. As a result, from (4.22) and (4.35)

$$p(\mathbf{x}_k|Y_k) \propto \exp\left(-\frac{1}{2}\|y_k - H_k\mathbf{x}_k - d_k\|^2_{R_k^{-1}} - \frac{1}{2}\|\mathbf{x}_k - \hat{\mathbf{x}}_k^-\|^2_{(P_k^-)^{-1}}\right). \tag{4.36}$$

It can be shown that $p(\mathbf{x}_k|Y_k) \sim \mathcal{N}(\hat{\mathbf{x}}_k^+, P_k^+)$ is indeed Gaussian again. The proof of this assertion is implicitly covered by the proof of Lemma 4 and will hence be omitted here. The interested reader is referred to Remark 29. Assuming Gaussianity to hold, we can continue by exploiting the fact that

$$\hat{\mathbf{x}}_k^+ = E\{\mathbf{x}_k|Y_k\} = \arg\max_{\mathbf{x}_k} p(\mathbf{x}_k|Y_k) = \arg\min_{\mathbf{x}_k} \Big(\|y_k - H_k\mathbf{x}_k - d_k\|^2_{R_k^{-1}} + \|\mathbf{x}_k - \hat{\mathbf{x}}_k^-\|^2_{(P_k^-)^{-1}}\Big).$$

By differentiation with respect to $\mathbf{x}_k$ the a posteriori estimate $\hat{\mathbf{x}}_k^+$ hence must fulfill

$$-H_k^T R_k^{-1}(y_k - H_k\hat{\mathbf{x}}_k^+ - d_k) + (P_k^-)^{-1}(\hat{\mathbf{x}}_k^+ - \hat{\mathbf{x}}_k^-) \overset{!}{=} \mathbf{0}, \tag{4.37}$$

which is equivalent to

$$\hat{\mathbf{x}}_k^+ = \big(H_k^T R_k^{-1} H_k + (P_k^-)^{-1}\big)^{-1}\big(H_k^T R_k^{-1}(y_k - d_k) + (P_k^-)^{-1}\hat{\mathbf{x}}_k^-\big). \tag{4.38}$$

Using general matrix identities (see, for instance, [81, Appendix 7.B]) the last expression can finally be simplified to

$$\hat{\mathbf{x}}_k^+ = \hat{\mathbf{x}}_k^- + K_k(y_k - H_k\hat{\mathbf{x}}_k^- - d_k), \tag{4.39}$$

where

$$K_k := P_k^- H_k^T (H_k P_k^- H_k^T + R_k)^{-1}. \tag{4.40}$$

For the purpose of deducing an update formula for the conditional covariance matrix we note that

$$\begin{aligned} \mathbf{x}_k - \hat{\mathbf{x}}_k^+ &= \mathbf{x}_k - \hat{\mathbf{x}}_k^- - K_k(y_k - H_k\hat{\mathbf{x}}_k^- - d_k) \\ &= \mathbf{x}_k - K_k H_k \mathbf{x}_k - (I - K_k H_k)\hat{\mathbf{x}}_k^- - K_k v_k \\ &= (I - K_k H_k)(\mathbf{x}_k - \hat{\mathbf{x}}_k^-) - K_k v_k \end{aligned} \tag{4.41}$$

and thus

$$P_k^+ = \operatorname{cov}\{\mathbf{x}_k|Y_k\} = E\{(\mathbf{x}_k - \hat{\mathbf{x}}_k^+)(\mathbf{x}_k - \hat{\mathbf{x}}_k^+)^T\} = (I - K_k H_k)P_k^-(I - K_k H_k)^T + K_k R_k K_k^T, \tag{4.42}$$

where the fact has been used that v_k is independent of $\mathbf{x}_k$. □

Remark 24. It should be emphasized that several equivalent expressions exist for the posterior covariance matrix $P_k^+ = \operatorname{cov}\{\mathbf{x}_k|Y_k\}$. However, the presented form is preferable from a numerical point of view as it guarantees that P_k^+ will remain symmetric positive definite if the same property holds true for P_0^+.

The previous theorem provides explicit recursions for an iterative update of the conditional mean $\hat{\mathbf{x}}_k^+ = E\{\mathbf{x}_k|Y_k\}$ and the conditional covariance matrix $P_k^+ = \operatorname{cov}\{\mathbf{x}_k|Y_k\}$ by efficiently combining noisy observations with predictions from the known dynamic model. In particular, $\hat{\mathbf{x}}_k^+$ is optimal in both the MMSE and MAP sense.

The key essence of the previous theorem is that it re-derives the Kalman filter as a special case of the recursive Bayes filter as introduced in Theorem 4.1. In fact, there is an abundance of several alternative concepts which can be employed in order to obtain these recursions, including, e.g., orthogonal projections or recursive least squares. The interested reader may consult [81, Ch. 7.3] for further details. In particular, the derivation above fails to reveal another interesting property of the Kalman filter: if the requirement of Gaussianity in the characterization of the noise sequences $\{\mathbf{w}_k\}$ and $\{v_k\}$ is dropped, the Kalman filter can still be shown to be optimal among all *linear* filters (i.e., filter structures using only linear combinations of states and observations). A good review of Kalman filtering and its wide range of applications is given in [148].

Remark 25. (Extended Kalman filter) Being confronted with a nonlinear system of the form

$$\begin{aligned} \mathbf{x}_k &= \mathbf{g}_{k-1}(\mathbf{x}_{k-1}) + \mathbf{w}_{k-1} \\ y_k &= h_k(\mathbf{x}_k) + v_k \end{aligned} \tag{4.43}$$

the ideas of Kalman filtering can still be applied by linearization around the current estimate. More specifically, if we define

$$G_{k-1} := \frac{\partial \mathbf{g}_{k-1}(\mathbf{x})}{\partial \mathbf{x}}|_{\mathbf{x}=\hat{\mathbf{x}}_{k-1}^{+}}, \quad \mathbf{f}_{k-1} := \mathbf{g}_{k-1}(\hat{\mathbf{x}}_{k-1}^{+}) - G_{k-1}\hat{\mathbf{x}}_{k-1}^{+}, \tag{4.44}$$

as well as

$$H_k := \frac{\partial h_k(\mathbf{x})}{\partial \mathbf{x}}|_{\mathbf{x}=\hat{\mathbf{x}}_k^{-}}, \quad d_k := h_k(\hat{\mathbf{x}}_k^{-}) - H_k\hat{\mathbf{x}}_k^{-}, \tag{4.45}$$

then Equation (4.25) constitutes a first order approximation of (4.43). Applying Corollary 2 to this new system yields the so-called extended Kalman filter (EKF). While having received widespread attention in the literature due to its simplicity and straightforward applicability to a vast number of practically interesting filtering tasks, the EKF often suffers from serious convergence problems. For more details on this issue as well as a fruitful modification we refer to [133, 102, 101].

4.2.3 Particle filtering

We now return to the nonlinear stochastic system (4.7), driven by possibly non-Gaussian, white noise sequences $\{\mathbf{w}_k\}$ and $\{v_k\}$. In this case, the conditional densities of the Bayes filter (4.20) are generally not tractable in an analytical way and some alternative strategy has to be employed in order to implement the associated recursions. With the advent of considerable computing power, particle filters (also referred to as sequential Monte Carlo methods) have emerged as a flexible tool within this framework, capable of handling any type of functional non-linearity in the state transition or measurement model. Moreover, they can be applied to any specific distribution of process or measurement noise.

The intuitive logic underpinning particle filtering is to shift the focus in the sequential Bayes filter from densities to samples. Note that these are essentially dual representations of the underlying probability law. In particular, given the latter, we might re-create the former by a variety of approximation schemes, ranging from histograms to kernel density estimates. This observation motivates the use of Monte Carlo sampling methods for deriving the required prior and posterior densities in (4.20). As will be elaborated below, particle filters aim at simulating a large number of possible state trajectories, propagating the desired posterior density $p(\mathbf{x}_k|Y_k)$ in accordance with the incoming observations. Our account is primarily based on [65, 89, 44]. An interesting coverage of recent theoretical and practical advances in the field of particle filtering is given in [43].

Remark 26. As the aforementioned methods heavily rely on the assumption that the user is able to generate random variates from quite general probability distributions, a review of the most prominent methods stochastic simulation is given in Appendix 4.A.

A major ingredient in the theory of particle filtering is Monte Carlo integration, which aims at approximating high-dimensional integrals by re-interpreting them as expectations of certain random variables. For the sake of illustration, let $\mathbf{x}$ denote a continuous random vector in $\mathbb{R}^n$ that admits a probability density function p. Moreover, let $\{\mathbf{x}_j\}$ be a sequence of independent samples identically distributed according to p. Then, by the strong law of large numbers, for an arbitrary measurable function ϕ it holds that as $m \to \infty$,

$$\frac{1}{m}\sum_{j=1}^{m} \phi(\mathbf{x}_j) \to E\{\phi(\mathbf{x})\} = \int \phi(\mathbf{x})p(\mathbf{x})\mathrm{d}\mathbf{x} \tag{4.46}$$

almost surely, provided that the above expectation exists. For fixed m, the arithmetic mean on the left-hand side of (4.46) hence can be seen as a finite sample approximation of $E\{\phi(\mathbf{x})\}$. Equivalently,

$$p(\mathbf{x}) \cong \frac{1}{m}\sum_{j=1}^{m} \delta_{\mathbf{x}_j}(\mathbf{x}) \tag{4.47}$$

produces an empirical estimate of the respective pdf. Here, δ denotes the Dirac delta point measure.

In the same spirit, particle filters attempt to approximate the complete posterior characterizing the Bayes filter (4.20) at time k by a cloud of $m \gg 1$ points (or particles) $\{\mathbf{x}^+_{k,1}, \ldots, \mathbf{x}^+_{k,m}\}$, viz.

$$p(\mathbf{x}_k | Y_k) \cong \frac{1}{m} \sum_{j=1}^{m} \delta_{\mathbf{x}^+_{k,j}}(\mathbf{x}_k). \tag{4.48}$$

Ideally, these points represent independent and identically distributed draws from $p(\mathbf{x}_k|Y_k)$. The representation in (4.48) might subsequently be used for assessing any statistical property of $\mathbf{x}_k$ given the available evidence Y_k. For instance, the approximate posterior probability of $\mathbf{x}_k$ falling in some region of the state space is simply given by the relative frequency of particles within that region.

A convenient way to generate a collection of particles as sketched above is the classical sampling importance resampling (SIR) or Bayesian bootstrap algorithm developed by Gordon et al. [65]. In the sequel, we shall briefly discuss the decisive steps underlying this method. In general, the SIR filter inherits the predictor-corrector structure of the sequential Bayes filter and can therefore again be split into a time update (corresponding to a sampling stage) and measurement update (corresponding to a resampling stage). As before, the superscripts "$-$" and "$+$" will refer to the associated prior and posterior densities, respectively.

Starting with the time update, assume that at time $(k-1)$ we have at hand an ensemble of particles $\{\mathbf{x}^+_{k-1,1}, \ldots, \mathbf{x}^+_{k-1,m}\}$ yielding, via (4.48), an empirical estimate of $p(\mathbf{x}_{k-1}|Y_{k-1})$. In view of (4.24), the prior $p(\mathbf{x}_k|Y_{k-1})$ then is given by

$$\begin{aligned} p(\mathbf{x}_k|Y_{k-1}) = \int p(\mathbf{x}_k|\mathbf{x}_{k-1}) p(\mathbf{x}_{k-1}|Y_{k-1}) \mathrm{d}\mathbf{x}_{k-1} \cong \\ \frac{1}{m} \sum_{j=1}^{m} \int p(\mathbf{x}_k|\mathbf{x}_{k-1}) \delta_{\mathbf{x}^+_{k-1,j}}(\mathbf{x}_{k-1}) \mathrm{d}\mathbf{x}_{k-1} = \frac{1}{m} \sum_{j=1}^{m} p(\mathbf{x}_k|\mathbf{x}^+_{k-1,j}), \end{aligned} \tag{4.49}$$

which is a composition of the transition densities governing the state evolution in (4.15). Consequently, a set of samples $\{\mathbf{x}^-_{k,1}, \ldots, \mathbf{x}^-_{k,m}\}$ from the the prior density $p(\mathbf{x}_k|Y_{k-1})$ can be generated by drawing its members according to

$$\mathbf{x}^-_{k,j} \sim p(\mathbf{x}_k|\mathbf{x}^+_{k-1,j}). \tag{4.50}$$

This completes the sampling stage. Subsequently, a swarm of posterior particles $\{\mathbf{x}^+_{k,1}, \ldots, \mathbf{x}^+_{k,m}\}$ following

$$p(\mathbf{x}_k|Y_k) = \frac{p(y_k|\mathbf{x}_k)}{p(y_k|Y_{k-1})} p(\mathbf{x}_k|Y_{k-1}). \tag{4.51}$$

can be simulated based on the asymptotic result given in the next lemma [149].

Lemma 3. *Let $\{\mathbf{x}_1, \ldots, \mathbf{x}_m\}$ denote a set of independent samples, identically distributed according to a pdf s. Furthermore, let a second pdf π be given by*

$$\pi(\mathbf{x}) := \frac{r(\mathbf{x})}{\int r(\mathbf{x}) \mathrm{d}\mathbf{x}}, \tag{4.52}$$

where r is an appropriately defined known function such that $r(\mathbf{x}) > 0$ implies $s(\mathbf{x}) > 0$. Then the multinomial density $\mathcal{M}\{(\mathbf{x}_j, q_j),\ j = 1, \ldots, m\}$ placing mass

$$q_j := \frac{r(\mathbf{x}_j)/s(\mathbf{x}_j)}{\sum_{l=1}^{m} r(\mathbf{x}_l)/s(\mathbf{x}_l)} \geq 0 \tag{4.53}$$

on $\mathbf{x}_j$ will tend to π in distribution as $m \to \infty$.

Proof. Let $\mathbf{x} \sim \mathcal{M}\{(\mathbf{x}_j, q_j),\ j = 1, \ldots, m\}$ be a sample of the discrete distribution introduced above. Furthermore, let $\mathcal{A}$ belong to the underlying σ-algebra and let $\chi_{\mathcal{A}}$ denote the usual indicator function. Then, using the strong law of large numbers,

$$\begin{aligned}
\Pr(\mathbf{x} \in \mathcal{A}) &= \sum_{j=1}^{m} q_j \chi_{\mathcal{A}}(\mathbf{x}_j) \\
&= \frac{\frac{1}{m}\sum_{j=1}^{m} r(\mathbf{x}_j)/s(\mathbf{x}_j)\chi_{\mathcal{A}}(\mathbf{x}_j)}{\frac{1}{m}\sum_{l=1}^{m} r(\mathbf{x}_l)/s(\mathbf{x}_l)} \xrightarrow{m\to\infty} \frac{E_s\{\frac{r(\mathbf{x})}{s(\mathbf{x})}\chi_{\mathcal{A}}(\mathbf{x})\}}{E_s\{\frac{r(\mathbf{x})}{s(\mathbf{x})}\}} \\
&= \frac{\int_{\mathcal{A}} r(\mathbf{x})\mathrm{d}\mathbf{x}}{\int r(\mathbf{x})\mathrm{d}\mathbf{x}} = \int_{\mathcal{A}} \pi(\mathbf{x})\mathrm{d}\mathbf{x}.
\end{aligned} \tag{4.54}$$

□

Remark 27. It is instructive to note that Lemma 3 exploits the general principle of importance sampling [22]. Instead of generating realizations from a complicated (simulation-wise) density π as above, a point mass approximation of the latter can also be produced by drawing samples $\mathbf{x}_j \sim s(\mathbf{x})$ following a simpler *importance (or proposal) density* s and assigning an individual *importance weight* $q_j \geq 0$ to each of these samples. Thus,

$$\pi(\mathbf{x}) \cong \sum_{j=1}^{m} q_j \delta_{\mathbf{x}_j}(\mathbf{x}), \quad \sum_{j=1}^{m} q_j = 1. \tag{4.55}$$

Evidently, the quality of this approximation heavily relies on the effective sample size, i.e., the number of samples that have a significant weight associated with them. Particularly, if the high probability regions of π and s are widely disjoint, only a few weights will be different from zero and thus the number of samples substantially contributing to the above approximation is greatly reduced. In practice, the goal hence must be to select s in order to resemble the target density π as closely as possible. Specifically, the "perfect" choice $s = \pi$ would yield a uniform weight distribution $q_j = m^{-1}$.

Returning to the situation after the time update (4.50), we might now straightforwardly apply the preceding lemma with the a priori particles $\{\mathbf{x}_{k,1}^-, \ldots, \mathbf{x}_{k,m}^-\}$, $p(\mathbf{x}_k|Y_{k-1})$, and $p(y_k|\mathbf{x}_k)p(\mathbf{x}_k|Y_{k-1})$ taking the roles of $\{\mathbf{x}_1, \ldots, \mathbf{x}_m\}$, s, and r, respectively. Doing so shows that a set of posterior particles $\{\mathbf{x}_{k,1}^+, \ldots, \mathbf{x}_{k,m}^+\}$ approximately following $p(\mathbf{x}_k|Y_k)$ can be simulated by drawing m independent samples from the multinomial distribution

$$\mathbf{x}_{k,j}^+ \sim \mathcal{M}\{(\mathbf{x}_{k,j}^-, q_j),\ j = 1, \ldots, m\}, \quad q_j := \frac{p(y_k|\mathbf{x}_{k,j}^-)}{\sum_{l=1}^{m} p(y_k|\mathbf{x}_{k,l}^-)}, \tag{4.56}$$

which can easily be realized by exploiting Remark 30. This resampling step completes the measurement update of the SIR filter.

The above selection stage is a major algorithmic ingredient, as it effectively avoids some degeneracy problems associated with earlier particle filters. In order to help intuition, note that the weights q_j represent the normalized likelihoods of the observed y_k given $\mathbf{x}_{k,j}^-$ and might hence be interpreted as acceptance probabilities for the a priori particles. Effectively, q_j quantifies the extent to which the jth a priori particle is compatible with the observed data. Consequently, (4.56) ensures that a priori particles with high probability of producing y_k will be cloned, whereas particles that are unlikely to yield y_k are discarded. The previous mechanism hence adaptively concentrates particles in regions of high posterior probability according to the incoming data.

Recapitulating, the considerations outlined above lead to the following generic version of the particle filter. From the viewpoint of an efficient implementation it should be noted that both stages of the algorithm can easily be parallelized.

Corollary 3. (SIR filter) *Consider the general hidden Markov model* (4.15) *and a swarm of* m *prior particles* $\{\mathbf{x}_{0,1}^+, \ldots, \mathbf{x}_{0,m}^+\}$ *distributed according to* $p(\mathbf{x}_0)$. *Then, an approximate set of* m *posterior particles distributed according to* $p(\mathbf{x}_k|Y_k)$ *can be obtained by recursively repeating the following two steps.*

$$\text{time update} \quad \left\{ \begin{array}{l} \text{For } j = 1, \ldots, m \\ \quad \text{Simulate } \mathbf{x}_{k,j}^- \sim p(\mathbf{x}_k | \mathbf{x}_{k-1,j}^+) \end{array} \right. .$$

$$\text{measurement update} \quad \left\{ \begin{array}{l} \text{For } j = 1, \ldots, m \\ \quad \text{Resample } \mathbf{x}_{k,j}^+ \text{ according to Equation (4.56)} \end{array} \right. .$$

Here, m is chosen as a trade-off between computational feasibility and estimation accuracy.

□

After resampling, for any measurable function ϕ we might directly infer $E\{\phi(\mathbf{x}_k)|Y_k\}$ as well as $\operatorname{cov}\{\phi(\mathbf{x}_k)|Y_k\}$ by forming the arithmetic mean and empirical covariance matrix of the samples $\phi(\mathbf{x}_{k,j}^+)$, respectively. Equivalently, with (4.55) in mind an alternative choice is to use the non-uniformly weighted estimator

$$T_k^\phi := \sum_{j=1}^m q_j \phi(\mathbf{x}_{k,j}^-). \tag{4.57}$$

It can be shown that the (asymptotic) variance of T_k^ϕ is smaller than the variance of the standard estimate based on the resampled particles. This is intuitively reasonable, as the resampling procedure will always degrade the diversity among the particles.

While Corollary 3 is the core of particle filtering, it is worth noting that several slightly different implementations of this simple scheme have been proposed. For instance, taking into account Remark 27, instead of executing a resampling step it is also possible to use properly weighted representations of the form (4.55) for approximating $p(\mathbf{x}_k|Y_k)$. The weights q_j are then carried forward in time by an separate update scheme. This early variant has become known as the sequential importance sampling (SIS) method [99].

Another idea is to use acceptance-rejection sampling for propagating prior to posterior particles. This approach essentially replaces the measurement update mechanism implied by Lemma 3 by Lemma 6 in Appendix 4.A and accepts a prior particle $\mathbf{x}_{k,j}^-$ as a posterior particle $\mathbf{x}_{k,j}^+$ with acceptance probability

$$a(\mathbf{x}_{k,j}^-) := \frac{p(y_k|\mathbf{x}_{k,j}^-)}{\sup\limits_{\mathbf{x}} p(y_k|\mathbf{x})}, \tag{4.58}$$

cf. Remark 33. Here, $p(\mathbf{x}_k|Y_k)$ and $p(\mathbf{x}_k|Y_{k-1})$ take the roles of $p_{\mathbf{X}}$ and $p_{\mathbf{Z}}$ in Lemma 6, respectively[1]. In contrast to resampling, this technique provides exact rather than approximate samples of the posterior distribution. A major drawback, however, is that the posterior sample size will generally be random and decreasing. In fact, it can readily be verified using Remark 34 that given a prior sample of size m the expected posterior sample size is $m\kappa^{-1} \leq m$. One possible modification to get rid of this defect is to generate new a priori particles from a continuous approximation of the discrete prior pdf. This is also referred to as the regularized particle filter. Further details on the acceptance-rejection approach can be found in [117].

Remark 28. The validity of Corollary 3 is essentially justified by virtue of asymptotical results based on the strong law of large numbers. While this ensures the consistency of estimators of the form (4.57), it gives little insight into their rate of convergence. Moreover, no assertions have been made regarding the precision of the derived estimates for a finite number of particles. An excellent compendium of recent thoughts in this context is [36], which also discusses almost sure convergence of the empirical posterior distribution functions to the true ones.

Despite being the most general method available for nonlinear filtering, a major obstacle hindering the usability of the particle filter is its computational burden. Sampling from high-dimensional spaces as orchestrated in the time update above can be fairly inefficient and in order to arrive at a faithful point mass approximation of $p(\mathbf{x}_k|Y_{k-1})$ the number of particles will rise rapidly with the dimension of the state space. As will be elaborated in the next section, efficient particle filters aim at alleviating this problem by exploiting certain sub-structures in the respective process and measurement models.

---

[1] In particular, if the indicated supremum exists the required constant κ is given by $\kappa = p(y_k|Y_{k-1})^{-1} \sup_{\mathbf{x}} p(y_k|\mathbf{x})$.

4.2.4 Dual estimation: marginalized particle filtering

So far, in our study of stochastic dynamical systems of the form (4.7) we have limited ourselves to pure state filtering, assuming the parameter vector $\boldsymbol{\vartheta}$ to be known. Contrarily, the overall goal now will be to devise schemes that permit to estimate $\mathbf{x}_k$ and $\boldsymbol{\vartheta}$ simultaneously. This is often termed the *dual estimation problem*, see also [177]. Following common practice we shall adopt a rather pragmatic approach here: instead of viewing $\boldsymbol{\vartheta}$ as a static parameter vector, we impose artificial dynamics on the latter, modeling its variation by a random walk

$$\boldsymbol{\vartheta}_k = \boldsymbol{\vartheta}_{k-1} + \mathbf{e}_{k-1}. \tag{4.59}$$

As above, the noise sequence $\{\mathbf{e}_k\}$ is required to be zero-mean, white with positive definite covariance matrices $E_k \geq 0$ and independent of the system and measurement noise as well as of the initial condition $\mathbf{x}_0 \sim p(\mathbf{x}_0)$. As in (4.14), all available prior information on $\boldsymbol{\vartheta}$ is assumed to be captured by an initial prior density $\boldsymbol{\vartheta}_0 \sim p(\boldsymbol{\vartheta}_0)$. Evidently, the new formulation (4.59) slightly modifies the original estimation problem. However, it also enhances flexibility by allowing $\boldsymbol{\vartheta}$ to be time-varying rather than fixed. This often is a useful extension in the context of physiological modeling, as time-varying parameters in many cases offer a more faithful description of reality, see Section 4.3 for instance.

By augmenting (4.7) with (4.59), the joint estimation problem can in principle be cast as a purely nonlinear state filtering task for the composite vector $\mathbf{z}_k := (\mathbf{x}_k, \boldsymbol{\vartheta}_k)$, which might straightforwardly be treated within the extended Kalman or particle filtering framework developed before (see also [177] for alternative approaches). However, as has been noted at the end of the previous section, the usual limiting factor here is the number of particles required to yield a reliable point mass representation of the involved densities. This number will rise rapidly with the dimension of the state space and the resulting computational demand for joint filtering based on $\mathbf{z}_k$ can easily become prohibitive. A question naturally arising hence is whether for a given sample size m particle filtering can be improved in terms of enhancing the accuracy of the derived estimates.

In the sequel we will show how this goal can be achieved to some extent by employing variance reduction techniques. In the present context, these schemes are often summarized under the name of marginalized or Rao-Blackwellized particle filtering [140, 45]. A common methodological feature of the corresponding algorithms is that they rely on marginalizing out analytically tractable (linear) sub-structures in the respective process and measurement models. These sub-structures might then be treated using exact methods, e.g., the Kalman filter. The discussion here will be confined to one special class of models that – although nonlinear in $\mathbf{z}_k$ – exhibit a linear sub-structure in the states, i.e., systems of the form

$$\begin{aligned}
\mathbf{x}_k &= G_{k-1}(\boldsymbol{\vartheta}_{k-1})\mathbf{x}_{k-1} + \mathbf{f}_{k-1}(\boldsymbol{\vartheta}_{k-1}) + \mathbf{w}_{k-1} \\
\boldsymbol{\vartheta}_k &= \boldsymbol{\vartheta}_{k-1} + \mathbf{e}_{k-1} \\
y_k &= H_k(\boldsymbol{\vartheta}_k)\mathbf{x}_k + d_k(\boldsymbol{\vartheta}_k) + v_k.
\end{aligned} \tag{4.60}$$

The properties of the noise term $\mathbf{e}_k$ are adopted from above, while $\{\mathbf{w}_k\}$ and $\{v_k\}$ are as in Section 4.2.2. For perspective, such systems often arise as a result of zero-order hold sampling of mass balance equations in physiological modeling, see Section 4.3.

On order to proceed further, it is important to note that conditional on the parameter sequence $\{\boldsymbol{\vartheta}_k\}$ the stochastic difference equation (4.60) is a linear Gaussian system and can hence be subjected to the Kalman filter recursions. Consequently,

$$p(\mathbf{x}_k|\boldsymbol{\vartheta}_k, Y_k) \sim \mathcal{N}(\hat{\mathbf{x}}_k^+(\boldsymbol{\vartheta}_k), P_k^+(\boldsymbol{\vartheta}_k)) \tag{4.61}$$

might be computed in an exact manner. Quite naturally, an efficient algorithm for determining the desired joint posterior $p(\mathbf{z}_k|Y_k)$ should be expected to take advantage of this feature. Effectively, the idea is to split the original filtering problem into two parts, one accounting for the dynamics of the parameter vector $\boldsymbol{\vartheta}_k$ and one handling the state filtering procedure. For this purpose we will decompose $p(\mathbf{x}_k, \boldsymbol{\vartheta}_k|Y_k)$ as

$$p(\mathbf{x}_k, \boldsymbol{\vartheta}_k|Y_k) = p(\mathbf{x}_k|\boldsymbol{\vartheta}_k, Y_k)p(\boldsymbol{\vartheta}_k|Y_k), \tag{4.62}$$

according to Bayes' rule. From (4.61), the first factor can be determined analytically by virtue of Corollary 2. Therefore, particle filtering will only have to be applied for tracking $p(\boldsymbol{\vartheta}_k|Y_k)$, which is of lower dimension than $p(\mathbf{z}_k|Y_k)$. Correspondingly, as in the proof of Theorem 4.1, we immediately deduce that

$$p(\boldsymbol{\vartheta}_k|Y_k) = \frac{p(y_k|\boldsymbol{\vartheta}_k, Y_{k-1})}{p(y_k|Y_{k-1})}p(\boldsymbol{\vartheta}_k|Y_{k-1}) = \frac{p(y_k|\boldsymbol{\vartheta}_k, Y_{k-1})}{p(y_k|Y_{k-1})}\int p(\boldsymbol{\vartheta}_k|\boldsymbol{\vartheta}_{k-1})p(\boldsymbol{\vartheta}_{k-1}|Y_{k-1})\mathrm{d}\boldsymbol{\vartheta}_{k-1}. \tag{4.63}$$

Invoking the particle filter, at time $(k-1)$ we start with a set of m particles $\{\boldsymbol{\vartheta}^+_{k-1,1}, \dots, \boldsymbol{\vartheta}^+_{k-1,m}\}$ drawn from $p(\boldsymbol{\vartheta}_{k-1}|Y_{k-1})$, which are then propagated through the system dynamics of $\boldsymbol{\vartheta}_k$ in order to yield a priori particles $\{\boldsymbol{\vartheta}^-_{k,1}, \dots, \boldsymbol{\vartheta}^-_{k,m}\}$ approximately distributed according to $p(\boldsymbol{\vartheta}_k|Y_{k-1})$, cf. Equation (4.50).

After a new measurement y_k has been acquired, a posteriori particles $\{\boldsymbol{\vartheta}^+_{k,1}, \dots, \boldsymbol{\vartheta}^+_{k,m}\}$ from $p(\boldsymbol{\vartheta}_k|Y_k)$ can in principle be obtained by carrying out a resampling step as in Corollary 3. According to (4.63), the density $p(y_k|\boldsymbol{\vartheta}_k, Y_{k-1})$ now takes the role of $p(y_k|\mathbf{x}_k)$ in (4.56). The likelihoods $p(y_k|\boldsymbol{\vartheta}^-_{k,j}, Y_{k-1})$ required to form the weights

$$q_j = \frac{p(y_k|\boldsymbol{\vartheta}^-_{k,j}, Y_{k-1})}{\sum_{l=1}^m p(y_k|\boldsymbol{\vartheta}^-_{k,l}, Y_{k-1})} \tag{4.64}$$

can be obtained from following lemma.

Lemma 4. *For systems of the form* (4.60) *with Gaussian noise sequences as defined above it holds that*

$$p(y_k|\boldsymbol{\vartheta}_k, Y_{k-1}) \sim \mathcal{N}(H_k(\boldsymbol{\vartheta}_k)\hat{\mathbf{x}}^-_k(\boldsymbol{\vartheta}_{k-1}) + d_k(\boldsymbol{\vartheta}_k), H_k(\boldsymbol{\vartheta}_k)P^-_k(\boldsymbol{\vartheta}_{k-1})H_k(\boldsymbol{\vartheta}_k)^T + R_k), \tag{4.65}$$

where $\hat{\mathbf{x}}^-_k(\boldsymbol{\vartheta}_{k-1})$ *and* $P^-_k(\boldsymbol{\vartheta}_{k-1})$ *denote the respective estimates from the Kalman filter.*

Proof. We first deduce that

$$p(y_k, \mathbf{x}_k|\boldsymbol{\vartheta}_k, Y_{k-1}) = p(y_k|\mathbf{x}_k, \boldsymbol{\vartheta}_k, Y_{k-1})p(\mathbf{x}_k|\boldsymbol{\vartheta}_k, Y_{k-1}) = p(y_k|\mathbf{x}_k, \boldsymbol{\vartheta}_k)p(\mathbf{x}_k|\boldsymbol{\vartheta}_k, Y_{k-1}). \tag{4.66}$$

By exploiting the structure of (4.60), the first factor is a Gaussian pdf $\mathcal{N}(H_k(\boldsymbol{\vartheta}_k)\mathbf{x}_k + d_k(\boldsymbol{\vartheta}_k), R_k)$, while the second factor is the Gaussian prior $\mathcal{N}(\hat{\mathbf{x}}^-_k(\boldsymbol{\vartheta}_{k-1}), P^-_k(\boldsymbol{\vartheta}_{k-1}))$, characterizing the time update of the Kalman filter. For notational brevity, we will omit the dependence on $\boldsymbol{\vartheta}$ from now on. Following [140], we note that

$$p(y_k|\boldsymbol{\vartheta}_k, Y_{k-1}) = \int p(y_k, \mathbf{x}_k|\boldsymbol{\vartheta}_k, Y_{k-1})\mathrm{d}\mathbf{x}_k =$$
$$\frac{1}{K_1}\int \exp\left(-\frac{1}{2}\|\mathbf{s}_k - H_k\tilde{\mathbf{x}}_k\|^2_{R_k^{-1}} - \frac{1}{2}\|\tilde{\mathbf{x}}_k\|^2_{(P^-_k)^{-1}}\right)\mathrm{d}\mathbf{x}_k = \frac{1}{K_1}\int \exp\{\cdot\}\mathrm{d}\mathbf{x}_k, \tag{4.67}$$

where we have introduced the new variables $\mathbf{s}_k := y_k - H_k\hat{\mathbf{x}}^-_k - d_k$, as well as $\tilde{\mathbf{x}}_k := \mathbf{x}_k - \hat{\mathbf{x}}^-_k$, and

$$K_1 := (2\pi)^{\frac{n+1}{2}}\left(\det R_k \det P^-_k\right)^{\frac{1}{2}}. \tag{4.68}$$

It can easily be verified that the exponent in (4.67) can be written as

$$\{\cdot\} = -\frac{1}{2}\begin{pmatrix}\tilde{\mathbf{x}}^T_k & \mathbf{s}^T_k\end{pmatrix} V_k \begin{pmatrix}\tilde{\mathbf{x}}_k \\ \mathbf{s}_k\end{pmatrix}, \tag{4.69}$$

where the matrix V_k is given by block diagonalization as

$$V_k := \begin{pmatrix} (P_k^-)^{-1} + H_k^T R_k^{-1} H_k & -H_k^T R_k^{-1} \\ -R_k^{-1} H_k & R_k^{-1} \end{pmatrix} = \begin{pmatrix} I & -K_k \\ 0 & I \end{pmatrix}^T \begin{pmatrix} (P_k^+)^{-1} & 0 \\ 0 & S_k^{-1} \end{pmatrix} \begin{pmatrix} I & -K_k \\ 0 & I \end{pmatrix}. \tag{4.70}$$

Here, $P_k^+ := \big((P_k^-)^{-1} + H_k^T R_k^{-1} H_k\big)^{-1}$ and $K_k := \big((P_k^-)^{-1} + H_k^T R_k^{-1} H_k\big)^{-1} H_k^T R_k^{-1}$ can be shown to yield the posterior covariance matrix and the Kalman gain of Corollary 2, respectively. Moreover, S_k is given by

$$S_k := \big(R_k^{-1} - R_k^{-1} H_k ((P_k^-)^{-1} + H_k^T R_k^{-1} H_k)^{-1} H_k^T R_k^{-1}\big)^{-1} = R_k + H_k P_k^- H_k^T, \tag{4.71}$$

using the lemma of the inverse matrix[2]. As for the denominator in (4.67), note that

$$\begin{aligned} \big(\det R_k \det P_k^-\big)^{-1} &= \det \begin{pmatrix} (P_k^-)^{-1} & 0 \\ 0 & R_k^{-1} \end{pmatrix} \\ &= \det \left(\begin{pmatrix} I & K_k \\ 0 & I \end{pmatrix}^T \begin{pmatrix} I & 0 \\ -H_k & I \end{pmatrix}^T \begin{pmatrix} (P_k^-)^{-1} & 0 \\ 0 & R_k^{-1} \end{pmatrix} \begin{pmatrix} I & 0 \\ -H_k & I \end{pmatrix} \begin{pmatrix} I & K_k \\ 0 & I \end{pmatrix} \right) \\ &= \det \begin{pmatrix} (P_k^+)^{-1} & 0 \\ 0 & S_k^{-1} \end{pmatrix} = \big(\det P_k^+ \det S_k\big)^{-1}. \end{aligned} \tag{4.72}$$

By combining (4.67), (4.69), (4.70), and (4.72) it can be concluded that

$$\begin{aligned} &p(y_k|\boldsymbol{\vartheta}_k, Y_{k-1}) = \\ &\frac{1}{(2\pi \det S_k)^{\frac{1}{2}}} \exp\left(-\frac{1}{2}\|\mathbf{s}_k\|^2_{S_k^{-1}}\right) \underbrace{\int \frac{1}{(2\pi)^{\frac{n}{2}} (\det P_k^+)^{\frac{1}{2}}} \exp\left(-\frac{1}{2}\|\tilde{\mathbf{x}}_k - K_k \mathbf{s}_k\|^2_{(P_k^+)^{-1}}\right) \mathrm{d}\mathbf{x}_k}_{=1}, \end{aligned} \tag{4.73}$$

which proves the claim. ☐

Remark 29. Note, that the previous proof fills a gap in the justification of the Kalman filter recursions in Corollary 2. Returning to Equation (4.36), the above argumentation indeed confirms that

$$\begin{aligned} p(\mathbf{x}_k|Y_k) = \left(\int p(y_k|\mathbf{x}_k) p(\mathbf{x}_k|Y_{k-1}) \mathrm{d}\mathbf{x}_k\right)^{-1} p(y_k|\mathbf{x}_k) p(\mathbf{x}_k|Y_{k-1}) = \\ \frac{1}{(2\pi)^{\frac{n}{2}} (\det P_k^+)^{\frac{1}{2}}} \exp\left(-\frac{1}{2}\|\tilde{\mathbf{x}}_k - K_k \mathbf{s}_k\|^2_{(P_k^+)^{-1}}\right) \end{aligned} \tag{4.74}$$

is Gaussian again.

The preceding lemma shows that the particle filter for joint state and parameter estimation in models of the form (4.60) can essentially be implemented by running a stochastic bank of m separate Kalman filters in parallel, each one being associated with a single particle $\boldsymbol{\vartheta}_{k,j}$. This is made precise in the following pseudo code, which alternates between Kalman filtering for the states and particle filtering for the parameters.

Corollary 4. (Marginalized particle filter) *Consider a conditionally linear Gaussian system* (4.60) *and a cloud of* m *particles* $\{\boldsymbol{\vartheta}_{0,1}^+, \dots, \boldsymbol{\vartheta}_{0,m}^+\}$ *distributed according to* $p(\boldsymbol{\vartheta}_0)$*. Let each particle be associated with a Kalman filter tracking the posterior density*

$$p(\mathbf{x}_k|Y_k, \boldsymbol{\vartheta}_{k,j}^+) \sim \mathcal{N}(\hat{\mathbf{x}}_{k,j}^+, P_{k,j}^+), \quad \hat{\mathbf{x}}_{k,j}^+ := \hat{\mathbf{x}}_k^+(\boldsymbol{\vartheta}_{k,j}^+),\ P_{k,j}^+ := P_k^+(\boldsymbol{\vartheta}_{k,j}^+) \tag{4.75}$$

---

[2] Provided that the involved matrices have compatible dimensions and that the indicated inverses exist, we have that $(A + BCD)^{-1} = A^{-1} - A^{-1}B(C^{-1} + DA^{-1}B)^{-1}DA^{-1}$, see, e.g., [153]

according to Corollary 2 and let each of these filters be initialized by the same tuple $(\hat{\mathbf{x}}_0^+, P_0^+)$ *for all* j. *Subsequently, a set of particles* $\{\boldsymbol{\vartheta}_{k,1}^+, \dots, \boldsymbol{\vartheta}_{k,m}^+\}$ *following* $p(\boldsymbol{\vartheta}_k|Y_k)$ *as well as the corresponding posterior mean and covariance matrix as indicated in* (4.75) *can be obtained by iterating*

$$\text{time update}\quad\begin{cases}\begin{array}{l}\text{For } j = 1, \dots, m \\ \quad \textit{Kalman filter} \\ \qquad p(\mathbf{x}_k|\boldsymbol{\vartheta}_{k-1,j}^+, Y_{k-1}) \sim \mathcal{N}(\hat{\mathbf{x}}_{k,j}^-, P_{k,j}^-) \\ \qquad \hat{\mathbf{x}}_{k,j}^- = G_{k-1}(\boldsymbol{\vartheta}_{k-1,j}^+)\hat{\mathbf{x}}_{k-1,j}^+ + \mathbf{f}_{k-1}(\boldsymbol{\vartheta}_{k-1,j}^+) \\ \qquad P_{k,j}^- = G_{k-1}^T(\boldsymbol{\vartheta}_{k-1,j}^+)P_{k-1,j}^+ G_{k-1}(\boldsymbol{\vartheta}_{k-1,j}^+) + Q_{k-1} \\ \quad \textit{Particle filter} \\ \qquad \text{Simulate } \boldsymbol{\vartheta}_{k,j}^- \sim \mathcal{N}(\boldsymbol{\vartheta}_{k-1,j}^+, E_{k-1}). \\ \qquad \text{Calculate } p(y_k|\boldsymbol{\vartheta}_{k,j}^-, Y_{k-1}) \text{ using Lemma 4.}\end{array}\end{cases}$$

$$\text{measurement update}\quad\begin{cases}\begin{array}{l}\text{For } j = 1, \dots, m \\ \quad \textit{Kalman filter} \\ \qquad p(\mathbf{x}_k|Y_k, \boldsymbol{\vartheta}_{k,j}^-) \sim \mathcal{N}(\hat{\mathbf{x}}_{k,j}^{+,-}, P_{k,j}^{+,-}) \\ \qquad K_{k,j} := P_{k,j}^- H_k^T(\boldsymbol{\vartheta}_{k,j}^-)(H_k(\boldsymbol{\vartheta}_{k,j}^-)P_{k,j}^- H_{k,j}^T(\boldsymbol{\vartheta}_{k,j}^-) + R_k)^{-1} \\ \qquad \hat{\mathbf{x}}_{k,j}^{+,-} := \hat{\mathbf{x}}_{k,j}^- + K_{k,j}(y_k - H_k(\boldsymbol{\vartheta}_{k,j}^-)\hat{\mathbf{x}}_{k,j}^- - d_k(\boldsymbol{\vartheta}_{k,j}^-)) \\ \qquad P_{k,j}^{+,-} := (I - K_{k,j}H_k(\boldsymbol{\vartheta}_{k,j}^-))P_{k,j}^-(I - K_{k,j}H_k(\boldsymbol{\vartheta}_{k,j}^-))^T + K_{k,j}R_k K_{k,j}^T \\ \text{For } j = 1, \dots, m \\ \quad \textit{Particle filter} \\ \qquad \text{Resample } (\boldsymbol{\vartheta}_{k,j}^+, \hat{\mathbf{x}}_{k,j}^+, P_{k,j}^+) \sim \mathcal{M}\{((\boldsymbol{\vartheta}_{k,j}^-, \hat{\mathbf{x}}_{k,j}^{+,-}, P_{k,j}^{+,-}), q_j)\} \\ \qquad \text{where the normalized likelihoods } q_j \text{ are defined as in (4.64).}\end{array}\end{cases}$$

□

Analogously to (4.57), at time k we can form the estimate

$$\begin{aligned} E\{\phi(\mathbf{x}_k, \boldsymbol{\vartheta}_k)|Y_k\} &= \int \phi(\mathbf{x}_k, \boldsymbol{\vartheta}_k)p(\mathbf{x}_k, \boldsymbol{\vartheta}_k|Y_k)\mathrm{d}\mathbf{x}_k\mathrm{d}\boldsymbol{\vartheta}_k \overset{(4.62)}{=} \\ &= \int \phi(\mathbf{x}_k, \boldsymbol{\vartheta}_k)p(\mathbf{x}_k|\boldsymbol{\vartheta}_k, Y_k)p(\boldsymbol{\vartheta}_k|Y_k)\mathrm{d}\mathbf{x}_k\mathrm{d}\boldsymbol{\vartheta}_k \\ &\cong \sum_{j=1}^m q_j E\{\phi(\mathbf{x}_k, \boldsymbol{\vartheta}_{k,j}^-)|\boldsymbol{\vartheta}_{k,j}^-, Y_k\} := \widetilde{T}_k^\phi. \end{aligned} \tag{4.76}$$

Setting $\phi(\mathbf{x}_k, \boldsymbol{\vartheta}_k) = \mathbf{x}_k$ yields the approximate minimum least squares estimate

$$\hat{\mathbf{x}}_k \cong \sum_{j=1}^m q_j E\{\mathbf{x}_k|\boldsymbol{\vartheta}_{k,j}^-, Y_k\} = \sum_{j=1}^m q_j \hat{\mathbf{x}}_{k,j}^{+,-}. \tag{4.77}$$

Its covariance matrix is given by

$$\operatorname{cov}\{\hat{\mathbf{x}}_k\} \cong \sum_{j=1}^m q_j \big(P_{k,j}^{+,-} + (\hat{\mathbf{x}}_{k,j}^{+,-} - \hat{\mathbf{x}}_k)(\hat{\mathbf{x}}_{k,j}^{+,-} - \hat{\mathbf{x}}_k)^T\big), \tag{4.78}$$

where the fact has been taken into account that

$$\begin{aligned} &E\{(\mathbf{x}_k - \hat{\mathbf{x}}_k)(\mathbf{x}_k - \hat{\mathbf{x}}_k)^T|\boldsymbol{\vartheta}_{k,j}^-, Y_k\} \\ &\qquad = E\{(\mathbf{x}_k - \hat{\mathbf{x}}_{k,j}^{+,-} + \hat{\mathbf{x}}_{k,j}^{+,-} - \hat{\mathbf{x}}_k)(\mathbf{x}_k - \hat{\mathbf{x}}_{k,j}^{+,-} + \hat{\mathbf{x}}_{k,j}^{+,-} - \hat{\mathbf{x}}_k)^T|\boldsymbol{\vartheta}_{k,j}^-, Y_k\} \\ &\qquad = P_{k,j}^{+,-} + (\hat{\mathbf{x}}_{k,j}^{+,-} - \hat{\mathbf{x}}_k)(\hat{\mathbf{x}}_{k,j}^{+,-} - \hat{\mathbf{x}}_k)^T. \end{aligned} \tag{4.79}$$

As has been stated at the beginning of this section, the primary motivation for performing the previous marginalization steps in the case of conditionally linear Gaussian models is to improve the quality of the derived state estimates by reducing their variance. In particular, for ϕ acting on the components of $\mathbf{x}_k$ only, an interesting central limit theorem can be established under mild assumptions. More specifically, as $m \to \infty$ it can be shown that

$$\begin{aligned} m^{\frac{1}{2}}(T_k^{\phi} - E\{\phi(\mathbf{x}_k, \boldsymbol{\vartheta}_k)|Y_k\}) &\xrightarrow{\mathcal{D}} \mathcal{N}(\mathbf{0}, \Sigma) \\ m^{\frac{1}{2}}(\widetilde{T}_k^{\phi} - E\{\phi(\mathbf{x}_k, \boldsymbol{\vartheta}_k)|Y_k\}) &\xrightarrow{\mathcal{D}} \mathcal{N}(\mathbf{0}, \widetilde{\Sigma}), \end{aligned} \tag{4.80}$$

with $\widetilde{\Sigma} \leq \Sigma$. Here, T_k^{ϕ} is the standard estimate for joint particle filtering of $\mathbf{x}$ and $\boldsymbol{\vartheta}$ (cf. (4.57)) and $\xrightarrow{\mathcal{D}}$ denotes convergence in distribution. The interested reader may consult [33, Th. 3] for a rigorous proof of this statement.

The appeal of (4.80) is that it provides a basis for comparing the efficiency of the algorithms given in Corollary 3 and Corollary 4 for simultaneous state and parameter estimation in models of the form (4.60). Accordingly, above a sufficiently large sample size m, marginalized particle filters will be superior to crude particle filtering for the composite vector $\mathbf{z}_k = (\mathbf{x}_k, \boldsymbol{\vartheta}_k)$ in terms of reducing the covariance of the *state* estimate. This is due to the fact that $p(\boldsymbol{\vartheta}_k|Y_k)$ is of lower dimension than the original joint posterior $p(\mathbf{x}_k, \boldsymbol{\vartheta}_k|Y_k)$. Hence, for a fixed number of particles, the quality of the corresponding point mass representations to the true pdfs will be higher for $p(\boldsymbol{\vartheta}_k|Y_k)$ than for $p(\mathbf{x}_k, \boldsymbol{\vartheta}_k|Y_k)$.

The practical performance of the algorithm presented in Corollary 4 will be illustrated in the next section. For general comparisons between simple and marginalized particle filtering we refer to [140, 141].

4.3 Breath gas analysis in anesthetic monitoring

This section serves to demonstrate some potential applications of *real-time* breath gas analysis in the field of anesthesia. The focus will be on two specific monitoring tasks arising in everyday clinical practice that can fruitfully be attacked by means of the methods developed in the previous sections. For a good introductory text to anesthesiology we refer to [156].

4.3.1 Problem statement

The primary aim of anesthesia is to decrease the components of surgical stress response by providing amnesia/hypnosis (unconsciousness), analgesia (pain relief) and muscle relaxation (immobility). Anesthetic drugs (agents) used for this purpose can roughly be divided into two major classes, characterized by their route of administration.

Intravenous agents are widely used for rapid induction of anesthesia, short procedures and long-term sedation in the intensive care unit. A prototypic compound in this context is propofol (2,6-diisopropylphenol, CAS number 2078-54-8), which is becoming increasingly popular due to its favorable procedural properties (including the possibility of rapid awakening and the reduction of post-operative nausea and vomiting). A core task in intravenous anesthesia is the determination of the serum levels of the anesthetic agent, which in turn are thought to be reflective of the decisive effect site concentrations in the central nervous system (brain and spinal chord), see, e.g., [49]. The evolution of these internal tissue concentrations after a bolus injection or during constant administration might be simulated *a priori* by developing physiologically based pharmacokinetic compartment models, which also form the basis for automatic, target-controlled infusion systems [162, 76]. While such models have proven to closely reproduce the desired agent concentrations in a variety of situations, it would generally be desirable to correct these predictions in an on-line manner, by using appropriate measurements reflecting the current in vivo levels.

In principle, direct serum measurements appear to be a proper means for this purpose, however, this approach is of limited practicability for real-time applications due to the time-intensive analysis of blood samples. As has been suggested in the specific case of propofol, continuous sampling and instantaneous analysis of breath during anesthesia might provide an effective remedy for this issue [70]. More specifically, it has been pointed out by several authors that some correlation exists between the breath concentrations of propofol (determined, e.g., by PTR–MS at $m/z = 179$) and the underlying serum levels [75, 112]. While this observation certainly offers novel perspectives on real-time examinations of endogenous propofol distribution, several confounding factors have to be addressed before this methodology can be introduced into routine clinical practice. Such factors for instance are the very low volatility (i.e., vapor pressure) of propofol under standard conditions [75] as well as possible metabolization patterns in the pulmonary tract [37].

Inhalational or *volatile* anesthetics are administered for both induction and maintenance of anesthesia, usually by virtue of a breathing circuit into which the agent is introduced. Prominent examples include nitric oxide as well as a series of halogenated hydrocarbons, most notably isoflurane, desflurane or sevoflurane. Despite their ubiquitous use in modern medicine, the underlying mechanisms by which these gases mediate their anesthetic/amnesic effects are still poorly understood. It is commonly agreed upon that inhaled anesthetics produce central nervous system depression by selectively blocking or enhancing the function of ion channels governing general neurotransmission behavior. In this sense, a well-defined relationship between the volatile anesthetic partial pressure in the brain and the associated anesthetic response can be expected [136]. Nevertheless, specified target site concentrations required to achieve a sufficient depth of anesthesia are lacking so far. Consequently, intra-operative monitoring of the anesthetic state usually rests on operational variables that can be accessed by direct measurement. A value of considerable interest in this framework is the minimum alveolar concentration (MAC), defined as the end-tidal concentration of the agent at which 50% of the patients fail to respond to surgical incision. While the MAC represents a convenient measure of the potency of the inhalant under study, it is clearly based on a steady state concept. Indeed, during transient states following a modification of the inspired gas concentration (e.g., induction, emergence or awakening/recovery phases) the end-tidal agent concentration will often be a poor indicator for the concentrations in the central nervous system, see also Fig. 4.2. It hence would be important to have at hand a more reliable prediction of volatile anesthetic levels in the brain [119].

A second hallmark of anesthesia is the need for a continuous assessment of physiological function, including a wide spectrum of vital respiratory and hemodynamic parameters. Within an intra-operative setting, ventilatory control by means of the anesthetic breathing system is a standard feature that primarily aims at ensuring stable normocapnic conditions. Thus, artificial ventilation will automatically be adjusted to maintain the target end-tidal carbon dioxide content selected by the anesthetist. Quite on the contrary, perfusion (i.e., cardiac output $\dot{Q}_\mathrm{c}$, defined as the volume of blood per unit time pumped by the heart) is a much more intricate quantity to measure, particularly due to the inaccessibility of current stroke volumes. It should be noted in this context that pulse or blood pressure generally represent insufficient surrogates for cardiac output (as can be seen for instance during shock or in patients suffering from arteriosclerosis, where little correlation exists between these parameters and total blood flow [28]). The appropriate determination of cardiac output can be seen as one of the cornerstones for adequately combating circulatory complications as well as for ensuring an adequate oxygen delivery to all tissues. However, most of the conventional methods for pursuing this goal are either highly invasive (dye or thermal dilution) or cumbersome (ultrasonic techniques, impedance cardiography).

An elegant way to circumvent these shortcomings is based on the estimation of pulmonary blood flow $\dot{Q}_\mathrm{p}$[3] from the measured breath dynamics of inhaled inert gases. Briefly, the logic underpinning this approach can be traced back to the famous Fick principle (see [52, 90] as well as [92] for a recent review), stating that the uptake of a foreign, blood-soluble tracer gas during one single respiratory cycle must equal the amount of that gas added to the blood flowing through the lungs. If we assume that inhalation and exhalation occurs from a closed bag of volume V_bag (which is smaller than the total lung capacity so that the bag can be completely emptied within one inhalation) and with an initial tracer gas concentration $C_\mathrm{bag}(0)$, this mass balance in its most simplified form reads

$$V_\mathrm{bag}C_\mathrm{bag}(0) - V_\mathrm{bag}C_\mathrm{bag}(t) = t\,\dot{Q}_\mathrm{p}C_\mathrm{a}(t), \tag{4.81}$$

---

[3] which is roughly equal to cardiac output $\dot{Q}_\mathrm{c}$ if one neglects the small intrapulmonary shunt fraction

where t denotes the duration of the respiratory cycle, $C_{\mathrm{bag}}(t)$ is the concentration in the bag after exhalation and $C_{\mathrm{a}}(t)$ is the arterial (end-capillary) concentration. Postulating that an immediate diffusion equilibrium is achieved at the alveolar interface, we may claim by Henry's law that the arterial concentration is given by $C_{\mathrm{a}}(t) = C_{\mathrm{A}}(t)\lambda_{\mathrm{b:air}}$, where $C_{\mathrm{A}}(t)$ is the alveolar (end-tidal) concentration and $\lambda_{\mathrm{b:air}}$ is the blood:gas partition coefficient of the inert gas under scrutiny. With t, C_{bag}, and C_{A} being measured, all the quantities in Equation (4.81) except $\dot{Q}_{\mathrm{p}}$ can be assigned known values and so one can easily solve for the latter in order to arrive at an estimate of the pulmonary blood flow. Several refinements of the above scheme have been put forward, correcting, e.g., for anatomical dead space, shunts or wash-in/wash-out during inhalation/exhalation [180, 59, 125].

It should be noted that the requirement of negligible mixed venous concentrations of the tracer gas is central to the above technique. In particular, this excludes the use of endogenously produced compounds. Moreover, the duration t of the test has to be sufficiently small in order to prevent recirculation. Typical gases that are employed in this context are nitrous oxide, acetylene, freon or sulfur hexafluoride [105].

4.3.2 Anesthetic monitoring using the prototypic compound sevoflurane

It will be the primary scope of the next paragraphs to adopt the above rationale for describing a continuous cardiac output monitoring scheme during general inhalation anesthesia. Not surprisingly, the role of the soluble inert gas introduced before will be played by the volatile anesthetic itself, thus allowing for a direct application of the proposed method within a conventional intra-operative setting. In particular, no additional instrumentation is involved. The aforementioned task clearly requires a simultaneous assessment of the endogenous tissue concentrations of the agent, most importantly of its mixed venous blood levels. These dynamics which will be estimated on-line from the observable exhalation kinetics of the volatile anesthetic on the basis of physiological modeling as well as by exploiting the ensemble of filtering tools described in Section 4.2. Specifically, such an approach proves to be suitable for the *joint* monitoring of cardiac output and the desired effect site concentrations in the cerebral region as discussed before. Our account is strongly influenced by the earlier demonstration in [28], where similar ideas have been outlined. The presentation in the sequel will be centered on sevoflurane (see [122] for an extensive review), which is a convenient choice in terms of clinical relevance, measurability and accessibility of experimental data.

Sevoflurane (CAS number 28523-86-6) is a highly fluorinated ether with a boiling point of 58.5°C that is usually delivered in gaseous form by variable-bypass vaporizers and administered to the patient via endotracheal intubation or laryngeal mask insertion. Its widespread use in modern anesthesia stems, among others, from the relative lack of airway irritation, the absence of pungency and the maintenance of hemodynamic stability. The MAC is around 2% and typical inspired concentrations of sevoflurane for induction and maintenance of surgical anesthesia range from 1–8% and 1.5–3%, respectively. The endogenous metabolism is minimal and accounts for roughly 1–5% of the total dose absorbed, the rest being excreted by exhalation [85]. From an operational point of view, it has been demonstrated that sevoflurane can be detected in PTR–MS at $m/z = 181$ [160, 135], thus allowing for direct real-time measurements of the associated alveolar (end-tidal) concentrations. According to classical pulmonary inert gas elimination theory, the low blood:gas partition coefficient $\lambda_{\mathrm{b:air}} = 0.6$ [55] at body temperature suggests a high sensitivity of these alveolar levels with respect to variations in ventilation and perfusion, thereby rendering sevoflurane as an ideal choice for relating respiratory and hemodynamic events to changes in the observable breath output.

We shall adopt the usual compartmental approach in order to capture the tissue accumulation of sevoflurane during the course of inhalation anesthesia, cf. Section 2.3. The systemic part of the model is similar to previously developed physiologically based descriptions of sevoflurane pharmacokinetics [119, 95] and incorporates three well-mixed functional units: a compartment representing brain tissue (for capturing the target site concentrations as indicated above), a richly perfused tissue (rpt) compartment, lumping together tissue groups with comparable blood:tissue partition coefficient $\lambda_{\mathrm{b:rpt}} \approx 0.24$ such as liver, kidneys and muscle [55], as well as a buffer tissue compartment that acts as a potential reservoir for the lipophilic agent sevoflurane. This last compartment mainly mirrors the substantial storage capacity of adipose tissue, as can be anticipated from a high fat:blood partition coefficient of about 71 [55]. All three compartments receive a specified, constant share of cardiac output and are separated into an intracellular space and an extracellular space (including the vascular blood and the interstitial space), whereby a venous equilibrium is assumed to hold at these interfaces. The relevant blood:tissue partition coefficients are summarized in Table 4.1. According to the discussion in the previous paragraph, it is assumed that the major route of sevoflurane uptake and removal is respiration, governed by the alveolar ventilation $\dot{V}_{\mathrm{A}}$. In particular, any metabolic clearance is assumed to be negligible.

The lung is modeled by one single homogenous alveolar unit characterized by an averaged ventilation-perfusion ratio close to one in normal healthy patients at rest. In particular, any pre- and post-alveolar absorption and release mechanisms occurring in the conductive airways (e.g., due to interactions with the tracheo-bronchial lining fluid, cf. Chapter 8) are neglected, which is a reasonable requirement for low water soluble gases such as sevoflurane [12]. Since both venous admixture and alveolar dead space are higher during general anesthesia than in the awake state, a constant shunt fraction $q_{\mathrm{s}} = 0.1$ and an alveolar dead space fraction $v_{\mathrm{ad}} = 0.1$ are incorporated into the model [105]. Pulmonary gas exchange is assumed to be perfusion-limited, i.e., an instantaneous diffusion equilibrium is expected to be established between end-capillary blood and the free gas phase. Correspondingly, the relationship between end-capillary concentrations $C_{\mathrm{c}'}$ and alveolar levels C_{A} is given by

$$C_{\mathrm{c}'} = C_{\mathrm{A}} \lambda_{\mathrm{b:air}}. \tag{4.82}$$

The model structure is presented in Fig. 4.1 and will be detailed in the following.

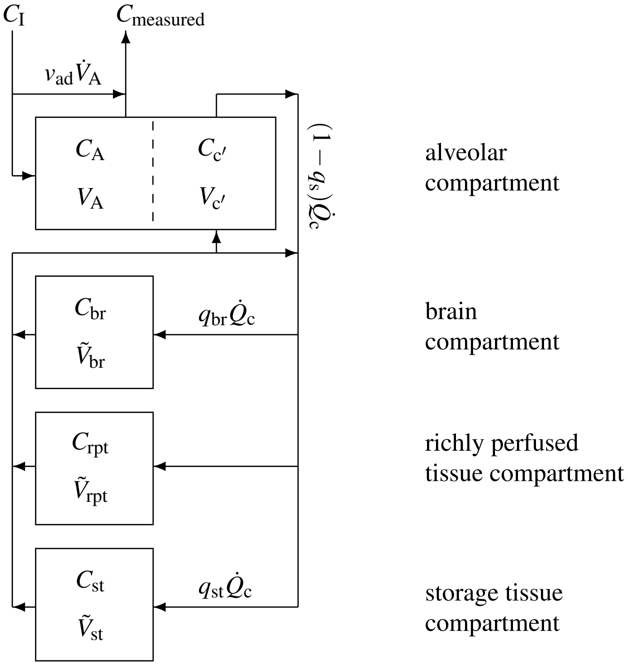
C_{I}
C_{measured}
$v_{\mathrm{ad}}\dot{V}_{\mathrm{A}}$
C_{A}
V_{A}
$C_{\mathrm{c}'}$
$V_{\mathrm{c}'}$
$(1-q_{\mathrm{s}})\dot{Q}_{\mathrm{c}}$
alveolar compartment
C_{br}
$\tilde{V}_{\mathrm{br}}$
$q_{\mathrm{br}}\dot{Q}_{\mathrm{c}}$
brain compartment
C_{rpt}
$\tilde{V}_{\mathrm{rpt}}$
richly perfused tissue compartment
C_{st}
$\tilde{V}_{\mathrm{st}}$
$q_{\mathrm{st}}\dot{Q}_{\mathrm{c}}$
storage tissue compartment

Figure 4.1: Sketch of the sevoflurane model structure. The body is divided into four distinct functional units: alveolar/end-capillary compartment (gas exchange), brain tissue (effect site), richly perfused tissue and storage tissue (adipose tissue). Dashed boundaries indicate a diffusion equilibrium. Abbreviations connote as in Table 4.1.

From the previous sketch and (4.82), the mass balance equation for the alveolar compartment reads

$$\tilde{V}_{\mathrm{A}} \frac{\mathrm{d}C_{\mathrm{A}}}{\mathrm{d}t} = (1 - v_{\mathrm{ad}})\dot{V}_{\mathrm{A}}(C_{\mathrm{I}} - C_{\mathrm{A}}) + (1 - q_{\mathrm{s}})\dot{Q}_{\mathrm{c}}(C_{\bar{\mathrm{v}}} - C_{\mathrm{A}}\lambda_{\mathrm{b:air}}), \tag{4.83}$$

where C_{I} denotes the inhaled sevoflurane concentration and $\tilde{V}_{\mathrm{A}} = V_{\mathrm{A}} + \lambda_{\mathrm{b:air}} V_{\mathrm{c'}}$ is the *effective* alveolar volume taking into account the amount of sevoflurane dissolved in capillary blood. Similarly, for the brain, richly perfused and storage tissue compartment we find that

$$\tilde{V}_{\mathrm{br}} \frac{\mathrm{d}C_{\mathrm{br}}}{\mathrm{d}t} = q_{\mathrm{br}} \dot{Q}_{\mathrm{c}} (C_{\mathrm{a}} - \lambda_{\mathrm{b:br}} C_{\mathrm{br}}), \tag{4.84}$$

$$\tilde{V}_{\mathrm{rpt}} \frac{\mathrm{d}C_{\mathrm{rpt}}}{\mathrm{d}t} = (1 - q_{\mathrm{br}} - q_{\mathrm{st}}) \dot{Q}_{\mathrm{c}} (C_{\mathrm{a}} - \lambda_{\mathrm{b:rpt}} C_{\mathrm{rpt}}), \tag{4.85}$$

and

$$\tilde{V}_{\mathrm{st}} \frac{\mathrm{d}C_{\mathrm{st}}}{\mathrm{d}t} = q_{\mathrm{st}} \dot{Q}_{\mathrm{c}} (C_{\mathrm{a}} - \lambda_{\mathrm{b:st}} C_{\mathrm{st}}), \tag{4.86}$$

respectively. Here, the associated concentrations in mixed venous and arterial blood are given by the weighted means

$$C_{\bar{\mathrm{v}}} := q_{\mathrm{br}} \lambda_{\mathrm{b:br}} C_{\mathrm{br}} + (1 - q_{\mathrm{br}} - q_{\mathrm{st}}) \lambda_{\mathrm{b:rpt}} C_{\mathrm{rpt}} + q_{\mathrm{st}} \lambda_{\mathrm{b:st}} C_{\mathrm{st}} \tag{4.87}$$

and

$$C_{\mathrm{a}} := (1 - q_{\mathrm{s}}) C_{\mathrm{A}} \lambda_{\mathrm{b:air}} + q_{\mathrm{s}} C_{\bar{\mathrm{v}}}, \tag{4.88}$$

respectively. Moreover, the measured (end-tidal) sevoflurane concentration equals

$$C_{\mathrm{measured}} = (1 - v_{\mathrm{ad}}) C_{\mathrm{A}} + v_{\mathrm{ad}} C_{\mathrm{I}}. \tag{4.89}$$

In order to test the adequacy of the above formulation for clinical purposes, we compared the resulting model predictions to an ensemble of in vivo concentration profiles published in [119]. This data set comprises 11 ventilated patients undergoing mastectomy during administration of 3% sevoflurane over 25 min and includes the resulting partial pressure profiles in inspired and end-tidal air as well as in arterial and jugular venous blood. Particularly, the latter variable can be expected to closely mirror the cerebral accumulation of the agent. Fig. 4.2 depicts the associated mean sevoflurane levels at 1, 2, 4, 9, 16 and 25 min after the start of inhalation. Here, the percentages given in Fig. 1 of [119] were digitized and converted to mmol/l by using a factor of 10/22.4 appropriate for standard conditions. Subsequently, blood concentrations were derived by multiplication with the sevoflurane blood:gas partition coefficient $\lambda_{\mathrm{b:air}} = 0.6$.

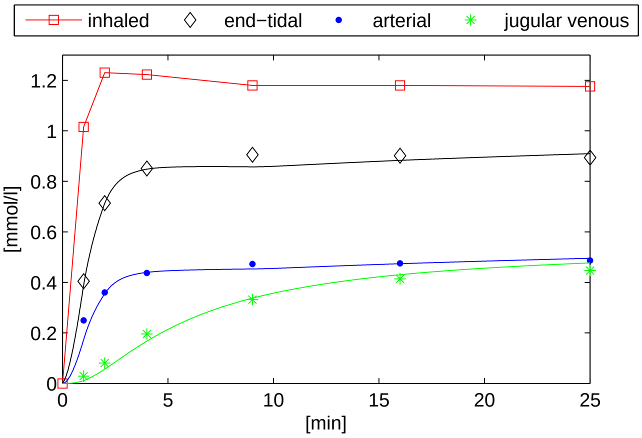

Figure 4.2: Simulation of sevoflurane profiles in end-tidal air (C_{measured}, cf. Equation (4.89)), arterial blood (C_{a}, cf. Equation (4.88)) and jugular venous blood ($C_{\mathrm{br}} \lambda_{\mathrm{b:br}}$) during inhalation anesthesia. Discrete points correspond to mean levels associated with the *pooled* data from 11 patients as measured by Nakamura et al. [119].

For simulation purposes, alveolar ventilation and cardiac output were set to constant values of $\dot{V}_{\mathrm{A}} = 4$ l/min and $\dot{Q}_{\mathrm{c}} = 4$ l/min, respectively, which corresponds to data measured under comparable conditions [95, 104, 105]. The inhaled concentration profile C_{I} was obtained by linear interpolation of the data points in Fig. 4.2. By adopting the reference values from Table 4.1 and setting the initial value of each compartmental concentration to zero, the simulated trajectories are in good agreement with the observed data. It is instructive to note that in the induction stage of anesthesia the end-tidal concentration profile of sevoflurane yields a poor representation of the underlying target site dynamics. Specifically, while the former readily approaches the desired MAC of about 2%, the brain concentration C_{br} is still in a transitory phase.

For the purpose of treating the above model within the framework outlined in Section 4.2, note that Equations (4.83)–(4.86) might be interpreted as a linear inhomogeneous ODE system (cf. Equation (4.3))

$$\dot{\mathbf{x}} = A(\mathbf{u}, \vartheta)\mathbf{x} + B(\mathbf{u}) \tag{4.90}$$

in the state variable $\mathbf{x} := (C_{\mathrm{A}}, C_{\mathrm{br}}, C_{\mathrm{rpt}}, C_{\mathrm{st}})^T$, which is dependent on physiological inputs $\mathbf{u}(t) := (C_{\mathrm{I}}(t), \dot{V}_{\mathrm{A}}(t))$ as well as on a time-varying parameter $\vartheta := \dot{Q}_{\mathrm{c}}$ reflecting cardiac output. Particularly, as has been pointed out above, the entries of $\mathbf{u}$ can be viewed as known or measurable quantities within an intra-operative setting. Equation (4.90) together with the measurement equation (4.89) constitutes a linear state space representation as introduced in Section 4.1. By employing zero-order hold sampling and postulating stochastic dynamics for $\mathbf{x}$ and ϑ, one straightforwardly arrives at a discrete stochastic system of the form (4.60), i.e.,

$$\begin{aligned} \mathbf{x}_k &= G_{k-1}(\vartheta_{k-1})\mathbf{x}_{k-1} + \mathbf{f}_{k-1} + \mathbf{w}_{k-1} \\ \vartheta_k &= \vartheta_{k-1} + e_{k-1} \\ y_k &= H_k\mathbf{x}_k + d_k + v_k. \end{aligned} \tag{4.91}$$

Here, the expressions for G and $\mathbf{f}$ are given in Equations (4.5) and (4.6), respectively, while from Equation (4.89) one finds that $y_k := C_{\mathrm{measured},k}$ is the measured breath sevoflurane concentration, $H_k := (1 - v_{\mathrm{ad}})\,(1, 0, 0, 0)$, and $d_k := v_{\mathrm{ad}} C_{\mathrm{I},k}$. We assume that the plant noise sequences $\{\mathbf{w}_k\}$ and $\{e_k\}$ as well as the measurement noise sequence $\{v_k\}$ are Gaussian, white, zero-mean and have known symmetric positive definite covariance matrices Q_k, E_k and R_k, respectively. Additionally, we assign the priors

$$\begin{aligned} p(\mathbf{x}_0) &\sim \mathcal{N}(\mathbf{0}, \mathrm{O}) \\ p(\vartheta_0) &\sim \mathcal{N}(\dot{Q}_{\mathrm{c}}^{\mathrm{est}}, \mathrm{var}\{\dot{Q}_{\mathrm{c}}^{\mathrm{est}}\}), \end{aligned} \tag{4.92}$$

reflecting our information on the initial sevoflurane concentrations as well as on the initial cardiac output. With these assumptions we may directly aim at the joint estimation of $\mathbf{x}$ and ϑ from the observable profile of the breath sevoflurane concentration y, using the methodology presented in Section 4.2.4. Due to the lack of appropriate in vivo data, the sequence of data points y_k will be *simulated* from the undisturbed system (4.90) by employing predefined profiles for $\dot{Q}_{\mathrm{c}}$, $\dot{V}_{\mathrm{A}}$ and C_{I}. These profiles are selected in order to cover a wide spectrum of possible respiratory and hemodynamic behavior (see Fig. 4.3). Since we assume that no sevoflurane is present in the body at the onset of anesthesia, the initial conditions are set to $\mathbf{x}(0) = (0, 0, 0, 0)^T$.

Noisy data were created by applying additive Gaussian perturbations with fixed variance $R_k = (0.005)^2$, see the first panel of Fig. 4.4. The sampling interval is $\Delta t = 5$ s, which roughly corresponds to the duration of one respiratory cycle during normal breathing at 12 tides per minute. Subsequently, the marginalized particle filter in Corollary 4 is applied to yield sequential estimates for the unobserved tissue concentrations $\mathbf{x}$ and the underlying cardiac output ϑ. Following common practice, the plant noise covariance matrices Q_k and E_k were tuned to ensure a satisfactory performance of the algorithm. In particular we set $E_k = (0.3)^2$ as a tradeoff between short transition times (following, e.g., a step change in perfusion) and estimation accuracy for the variable cardiac output. Fig. 4.4 summarizes the results of these calculations, based on $m = 300$ particles. Here, the parameters of the prior density $p(\vartheta_0)$ according to (4.92) were defined as $\dot{Q}_{\mathrm{c}}^{\mathrm{est}}$=8 l/min and $\mathrm{var}\{\dot{Q}_{\mathrm{c}}^{\mathrm{est}}\} = (3)^2$. With these settings, the time required for one filter iteration spreads around 1.3 s, which is well within the sampling interval introduced above.

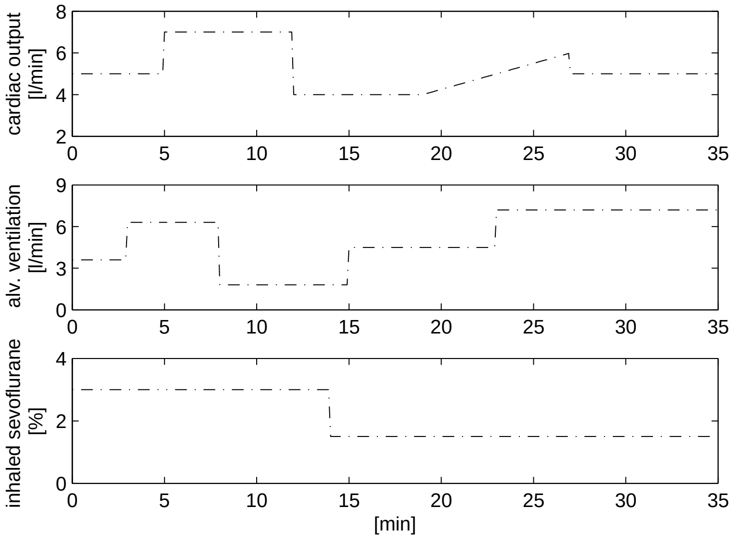

Figure 4.3: Profiles of cardiac output $\dot{Q}_{\mathrm{c}}$, alveolar ventilation $\dot{V}_{\mathrm{A}}$ and inhaled sevoflurane concentration C_{I} used for the simulation.

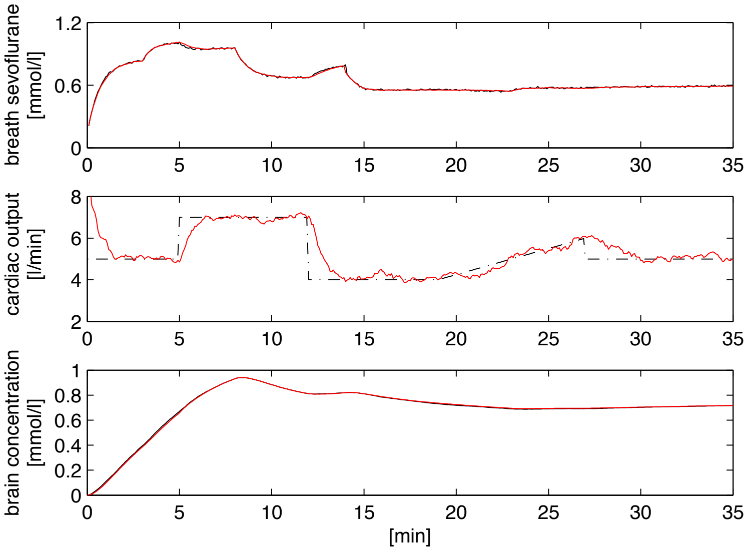

Figure 4.4: Simulated (black lines) and recovered (red lines) profiles of the breath sevoflurane concentration C_{measured}, cardiac output $\dot{Q}_{\mathrm{c}}$ and brain concentration C_{br}, using a marginalized particle filter with cloud size $m = 300$.

The state and parameter estimates were calculated according to Equation (4.76) and faithfully reproduce their simulated counterparts. For perspective, if the cardiac output drops abruptly (e.g., as a result of air embolism) the circulation must be restored within 4 min to prevent brain damage. As can be seen from the figure above, such incidences appear to be trackable within a delay time that is sufficiently small for enabling proper intra-operative interventions. Moreover, the target site concentrations C_{br} of sevoflurane are recovered from the observable breath levels with reasonable accuracy. In this sense, the present approach can potentially contribute to facilitating real-time assessments of the anesthetic state.

While the above deliberations offer intriguing novel perspectives for anesthetic monitoring on the basis of exhaled breath measurements, several aspects have to be investigated more deeply before this method can become clinically accepted. In particular, it is clear that one of the main building blocks for a successful implementation is the availability of a reliable physiological model for the internal concentration profiles of the anesthetic under study. Consequently, additional experimental efforts, data gathering and modeling attempts are required in order to extend the validity of simple models such as the one above over a wider range of possible dynamics. Moreover, further insights into the quantitative relationships between anesthetic depth and brain sevoflurane concentrations need to be gained. In this sense, the previous analysis should primarily be seen as a preliminary proof of concept, coupling the high frequency information obtainable by breath gas analytical techniques with well-established tools from signal processing in order to achieve a continuous monitoring of physiological processes.

Parameter	Symbol	Nominal value (units)
Concentrations		
alveoli	C_A	(mmol/l)
arterial	C_a	
mixed-venous	$C_{\bar{\mathrm{v}}}$	
brain tissue	C_br	
richly perfused tissue (rpt)	C_rpt	
storage tissue	C_st	
inhaled	C_I	
Compartment volumes		
alveoli	V_A	4.1 (l) [116]
end-capillary	$V_{\mathrm{c}'}$	0.15 (l) [78]
brain	$\tilde{V}_\mathrm{br}$	1.3 (l) [121]
rpt	$\tilde{V}_\mathrm{rpt}$	40 (l) [121][a]
storage (fat tissue)	$\tilde{V}_\mathrm{st}$	15 (l) [121]
Fractional flows		
brain	q_br	0.135 [121]
storage (fat)	q_st	0.06 [121]
shunt fraction	q_s	0.1 [105]
alv. deadspace fraction	v_ad	0.1
Partition coefficients		
blood:air	$\lambda_\mathrm{b:air}$	0.6 [55]
blood:brain	$\lambda_\mathrm{b:br}$	0.46 [55]
blood:rpt	$\lambda_\mathrm{b:rpt}$	0.24 [55]
blood:storage tissue	$\lambda_\mathrm{b:st}$	0.014 [55]

Table 4.1: Basic model parameters and reference values for normal subjects during rest; [a]comprising viscera and muscles according to Table 8.2 in that reference.

4.A Stochastic simulation

This appendix gives a brief overview of the theoretical foundations of stochastic simulation [40, 56, 61, 137], allowing for an efficient generation of discrete and continuous random quantities. Some of the major theorems and algorithms necessary for a competent treatment of the subject will be presented in the following. In order to keep the notation consistent with the previous sections, probability densities and distribution functions will be denoted by p and P, respectively. Random variables and their associated realizations are indicated by capital and lower case letters, respectively.

4.A.1 Pseudo-Randomness

The starting point for every simulation scheme is a uniform random variate generator on the unit interval $[0, 1]$, capable of supplying a sequence of independent, identically distributed (*iid*) random variables $U_1, U_2, \ldots \sim \mathcal{U}([0, 1])$, i.e., the corresponding probability density functions p are given by

$$p_{U_i}(u_i) = \chi_{[0,1]}(u_i) \tag{4.93}$$

for all i, where $\chi_{[0,1]}$ denotes the usual indicator function. This is a building block not trivially given and much effort has been spent on the construction of random numbers using a deterministic computer. However, since it is beyond the scope of this illustration to cover all the details related to the development of such a source of randomness, its existence will be taken for granted. As an example, consider the following recursive generator:

Definition 6. (Linear Congruential Generator, Lehmer 1951)
Let $a, m \in \mathbb{N}$ and $a < m$. Using an initial seed $\gamma_0 \in \{1, \ldots, m-1\}$, one constructs

$$\gamma_{i+1} \equiv a\gamma_i \pmod{m}, \; i \geq 0, \tag{4.94}$$

yielding $\gamma_i \in \{1, \ldots, m-1\}$. Division by m produces a stream of so-called pseudorandom numbers

$$u_i := \frac{\gamma_i}{m}.$$

Of course, these u_i form a completely deterministic and periodic sequence, but for large m and properly chosen multiplier a (a typical choice is the Mersenne prime $2^{31}-1$ and 7^5, respectively), they will constitute a relatively satisfactory approximation of $U_1, U_2, \ldots \sim \mathcal{U}([0, 1])$. It should be noted, however, that (4.94) only defines a "minimal" standard and might not be adequate for serious applications. The interested reader may consult [61] for an overview of the numerous modifications and refinements that have been proposed. In any case, since the quality of nonuniform samples produced by one of the simulation routines given in the following sections depends almost solely on the quality of the underlying uniform generator, statistical tests like a Ljung-Box portmanteau test or a runs test [100, 27] should be used to examine the pseudorandom numbers' goodness-of-fit to the theoretical requirements.

4.A.2 General simulation principles

This section discusses some of the fundamental simulation principles from which many of the standard sampling routines for one- and multi-dimensional distributions can be derived. Results are mainly collected from standard works such as [40, 56, 61, 137].

Inversion

Lemma 5. *(Inversion Lemma)*
Let $U \sim \mathcal{U}([0, 1])$ and let P be an arbitrary distribution function on $\mathbb{R}$. Then, the random variable X defined by $X := P^{-1}(U)$, where

$$P^{-1}(u) := \min\{x : P(x) \geq u\} \tag{4.95}$$

has distribution function P. The expression $P^{-1}(u)$ is called the generalized inverse of P.

Proof. Firstly, since the minimum is attained by right-continuity of P, one has that $P\big(P^{-1}(u)\big) \geq u$ by definition. Second, $P^{-1}\big(P(x)\big) = \min\{w : P(w) \geq P(x)\} \leq x$. Thus, for all $(u, x) \in [0, 1] \times \mathbb{R}$ by monotonicity of P it holds that

$$\{P^{-1}(u) \leq x\} = \{u \leq P(x)\}$$

and hence

$$P_X(x) = \Pr(X \leq x) = \Pr\big(P^{-1}(U) \leq x\big) = \Pr\big(U \leq P(x)\big) = P(x),$$

the last equality being justified by the uniform distribution of $U \sim \mathcal{U}([0, 1])$. □

Correspondingly, given the explicit form of P^{-1}, a quite universal simulation algorithm for one-dimensional random variables can be described as follows.

Algorithm 3 (*Non-uniform random variate generation via inversion*)

1. Generate $u \sim \mathcal{U}([0,1])$.
2. Compute $x := P^{-1}(u)$ as the realization of a random variable X having the desired distribution function P.

Remark 30. A paradigmatic example for employing the previous algorithm are discrete random variables, i.e., $\Pr(X = x_i) = q_i,\ i = 1, 2, \ldots$, with $0 \leq q_i \leq 1$ and $q_1 + q_2 + \ldots = 1$. In this case, for the distribution function P it holds that

$$P_X(x) = \begin{cases} 0 & x < x_1 \\ q_1 + \ldots + q_i & x_i \leq x < x_{i+1}. \end{cases}$$

Considering (4.95), the condition

$$q_1 + \ldots + q_{i-1} < u \leq q_1 + \ldots + q_i \tag{4.96}$$

implies that $P^{-1}(u) = x_i$ and consequently X can be sampled by

$$x := \begin{cases} x_1 & \text{if } u \leq q_1 \\ x_2 & \text{if } q_1 < u \leq q_1 + q_2 \\ \vdots & \vdots \\ x_i & \text{if } q_1 + \ldots + q_{i-1} < u \leq q_1 + \ldots + q_i \\ \vdots & \vdots \end{cases}$$

Indeed, formally one then deduces that

$$\Pr(X = x_i) = \mathrm{P}(q_1 + \ldots + q_{i-1} < U \leq q_1 + \ldots + q_i) = \\ P_U(q_1 + \ldots + q_i) - P_U(q_1 + \ldots + q_{i-1}) = q_i. \tag{4.97}$$

From a geometrical point of view, the unit interval $[0, 1]$ is partitioned into disjoint subintervals of length $q_i,\ i = 1, 2, \ldots$. Subsequently, if u takes on a value in the ith subinterval, then x is set to x_i. For this reason, creating samples of discrete random variables by inversion is commonly referred to as sequential search technique.

Remark 31. (Discrete uniform distributions) Sometimes it is most convenient to extract a sample value x directly by analyzing (4.96). For example, let $X \sim \mathcal{U}(\{1, \ldots, N\})$ be a uniform distribution on $\{1, \ldots, N\}$, i.e., let $\Pr(X = i) = N^{-1}$ for all i. Equation (4.96) then is equivalent to the condition

$$\frac{i-1}{N} < u \leq \frac{i}{N}$$

and thus x can be realized by setting $x := \lfloor Nu \rfloor + 1$.

Regarding continuous random variables, the second step in Algorithm 1 usually involves the numerical solution of $P(x) = u$. This equation is typically solved by applying the Newton-Raphson-Method to the function $P(x) - u$, which after choosing an initial guess x_0 iterates

$$x_{l+1} = x_l - \frac{P(x_l) - u}{p(x_l)}$$

until some stopping criterion is fulfilled. Assuming that the probability density function p is unimodal and choosing x_0 equal to this mode, convergence of the above iteration scheme is guaranteed by concavity of

$P(x) - u$ in $[x_0, \infty)$. The prototype of a random variable fulfilling this condition is a Gaussian distribution $X \sim \mathcal{N}(0,1)$. Although

$$P_X(x) = \frac{1}{\sqrt{2\pi}} \int\limits_{-\infty}^{x} \exp\left(-\frac{\xi^2}{2}\right) \mathrm{d}\xi$$

cannot be evaluated in closed form, the aforementioned method might be applied in order to generate an associated realization x by inversion. However, due to relative computational inefficiency of this scheme and given the importance of the normal distribution, several specific simulation algorithms have been developed (such as the Box-Muller or polar algorithm).

Remark 32. Let $\mathbf{X} \sim \mathcal{N}(\boldsymbol{\tau}, \Sigma)$, i.e., $\mathbf{X}$ follows an n-dimensional normal distribution with mean $\boldsymbol{\tau}$ and covariance matrix Σ (required to have full rank). Thus, for the probability density function p it holds that

$$p_{\mathbf{X}}(\mathbf{x}) = \frac{(\det \Sigma)^{-\frac{1}{2}}}{(2\pi)^{\frac{n}{2}}} \exp\{-\frac{1}{2}(\mathbf{x} - \boldsymbol{\tau})^T \Sigma^{-1} (\mathbf{x} - \boldsymbol{\tau})\}.$$

By applying the transformation rule, for $A \in \mathbb{R}^{n \times n}$ and $\mathbf{b} \in \mathbb{R}^n$ it can easily be proven that

$$\mathbf{Z} := A\mathbf{X} + \mathbf{b} \sim \mathcal{N}(A\boldsymbol{\tau} + \mathbf{b}, A\Sigma A^T). \tag{4.98}$$

As a result, as far as the simulation of $\mathbf{X}$ is concerned, if one can find A such that $AA^T = \Sigma$, it suffices to generate $\mathbf{X}_{\text{aux}} \sim \mathcal{N}(\mathbf{0}, I_n)$ by simulating n independent draws from a one-dimensional Gaussian distribution and to set

$$\mathbf{X} := A\mathbf{X}_{\text{aux}} + \boldsymbol{\tau} \sim \mathcal{N}(\boldsymbol{\tau}, AA^T).$$

Since by definition Σ is symmetric and positive definite, A is practically obtained by Cholesky decomposition. Hence, by means of property (4.98), the common multivariate normal distribution can easily be generated.

Rejection

Rejection is a powerful, dimension-independent simulation principle based on the idea of selecting subsamples: instead of sampling from a "difficult" (simulation-wise) random quantity directly, one generates values following a "simpler" distribution on the same domain. In a second step, a rejection rule determines whether these proposed values are accepted as realizations of the desired target random variable. The logic underlying this scheme relates to the next result [56], first given by von Neumann (1951) in a slightly modified form.

Lemma 6. *Let* $\mathbf{X}$ *and* $\mathbf{Z}$ *be two continuous random variables defined on the same domain I with densities* $p_{\mathbf{X}}$ *and* $p_{\mathbf{Z}}$*, respectively. Moreover, assume that there exists a finite constant* κ *such that for all* $\mathbf{x} \in I$ *it holds that*

$$p_{\mathbf{X}} \leq \kappa p_{\mathbf{Z}}. \tag{4.99}$$

Then the conditioned random variable

$$\mathbf{Z}^* := \mathbf{Z} | \{U \leq p_{\mathbf{X}}(\mathbf{z}) / (\kappa p_{\mathbf{Z}}(\mathbf{z}))\} \tag{4.100}$$

with $U \sim \mathcal{U}([0,1])$ *independent of* $\mathbf{Z}$ *has* $p_{\mathbf{X}}$ *as its density function.*

Proof. By independence, U and $\mathbf{Z}$ have the joint density

$$p_{U,\mathbf{Z}}(u, \mathbf{z}) = p_U(u) p_{\mathbf{Z}}(\mathbf{z}) = \begin{cases} p_{\mathbf{Z}}(\mathbf{z}) & 0 < u < 1, \ \mathbf{z} \in I \\ 0 & \text{otherwise.} \end{cases}$$

Hence, by letting $\mathcal{A} := \{(u, \mathbf{z}) : u \leq p_{\mathbf{X}}(\mathbf{z}) / (\kappa p_{\mathbf{Z}}(\mathbf{z}))\}$ we conclude that

$$\Pr\left(U \leq \frac{p_{\mathbf{X}}(\mathbf{Z})}{\kappa p_{\mathbf{Z}}(\mathbf{Z})}\right) = \iint\limits_{\mathcal{A}} p_{U,\mathbf{Z}}(u, \mathbf{z}) \mathrm{d}u \, \mathrm{d}\mathbf{z} = \int_I \int_0^{\frac{p_{\mathbf{X}}(\mathbf{z})}{\kappa p_{\mathbf{Z}}(\mathbf{z})}} p_{\mathbf{Z}}(\mathbf{z}) \mathrm{d}u \, \mathrm{d}\mathbf{z} = \int\limits_I \frac{p_{\mathbf{X}}(\mathbf{z})}{\kappa} \mathrm{d}\mathbf{z} = \frac{1}{\kappa} \tag{4.101}$$

and thus the joint density of U and $\mathbf{Z}$ given $\{U \leq p_{\mathbf{X}}(\mathbf{z})/(\kappa p_{\mathbf{Z}}(\mathbf{z}))\}$ reads

$$p_{(U,\mathbf{Z})|\{U \leq p_{\mathbf{X}}(\mathbf{z})/(\kappa p_{\mathbf{Z}}(\mathbf{z}))\}} = \frac{p_{U,\mathbf{Z}}(u,\mathbf{z})}{\Pr\left(U \leq \frac{p_{\mathbf{X}}(\mathbf{Z})}{\kappa p_{\mathbf{Z}}(\mathbf{Z})}\right)} = \begin{cases} \kappa p_{\mathbf{Z}}(\mathbf{z}) & 0 < u < \frac{p_{\mathbf{X}}(\mathbf{z})}{\kappa p_{\mathbf{Z}}(\mathbf{z})},\ \mathbf{z} \in I \\ 0 & \text{otherwise.} \end{cases}$$

Computing the marginal density yields

$$p_{\mathbf{Z}^*}(\mathbf{z}) = \int_0^{\frac{p_{\mathbf{X}}(\mathbf{z})}{\kappa p_{\mathbf{Z}}(\mathbf{z})}} \kappa p_{\mathbf{Z}}(\mathbf{z}) \mathrm{d}u = \kappa p_{\mathbf{Z}}(\mathbf{z}) \frac{p_{\mathbf{X}}(\mathbf{z})}{\kappa p_{\mathbf{Z}}(\mathbf{z})} = p_{\mathbf{X}}(\mathbf{z}), \quad \mathbf{z} \in I.$$

□

This sets the stage for the final algorithm:

Let $\mathbf{X}$ and $\mathbf{Z}$ be continuous random variables (vectors) defined on the same domain I with densities $p_{\mathbf{X}}$ and $p_{\mathbf{Z}}$, respectively and let $U \sim \mathcal{U}([0,1])$ be independent of $\mathbf{X}$ and $\mathbf{Z}$. Additionally, let κ (≥ 1) be an identifiable constant such that

$$\sup_{\mathbf{x} \in I} \frac{p_{\mathbf{X}}(\mathbf{x})}{p_{\mathbf{Z}}(\mathbf{x})} = \kappa < \infty. \tag{4.102}$$

A sample $\mathbf{x}$ following $\mathbf{X}$ can then be obtained as follows:

Algorithm 4 (*Non-uniform random variate generation via rejection*)

```
1. Generate $(u, \mathbf{z})$ from $(U, \mathbf{Z})$ until $u \leq \frac{p_{\mathbf{X}}(\mathbf{z})}{\kappa p_{\mathbf{Z}}(\mathbf{z})}$.
2. Deliver $\mathbf{x} = \mathbf{z}$.
```

Remark 33. By interpreting $a(\mathbf{z}) := p_{\mathbf{X}}(\mathbf{z})/(\kappa p_{\mathbf{Z}}(\mathbf{z})) \leq 1$ as acceptance probability, the rejection algorithm can briefly be summarized in the following way: *"Draw a realization* $\mathbf{z}$ *from a proposal density* $p_{\mathbf{Z}}$ *(usually referred to as envelope) and accept* $\mathbf{z}$ *with probability* $a(\mathbf{z})$*, otherwise continue drawing."*

Remark 34. Let R be the number of trials until the pair $(u, \mathbf{z})$ is accepted. From Equation (4.101) one sees that

$$\Pr(\mathbf{z} \text{ accepted}) = \Pr\left(U \leq \frac{p_{\mathbf{X}}(\mathbf{Z})}{\kappa p_{\mathbf{Z}}(\mathbf{Z})}\right) = \frac{1}{\kappa}.$$

Hence, R follows a geometrical distribution with parameter κ^{-1} and so $E\{R\} = \kappa$ iterations are required on average to produce one realization $\mathbf{x} \sim \mathbf{X}$. Efficiency, i.e., $\kappa \approx 1$, can be achieved by choosing $p_{\mathbf{Z}}$ similar to $p_{\mathbf{X}}$.

Bibliography

[1] *ATS/ERS Recommendations for Standardized Procedures for the Online and Offline Measurement of Exhaled Lower Respiratory Nitric Oxide and Nasal Nitric Oxide, 2005*, Am. J. Respir. Crit. Care Med. **171** (2005), 912–930.

[2] *Bergmann/Schaefer Lehrbuch der Experimentalphysik*, 12th ed., vol. 1, Walter de Gruyter, Berlin, 2008.

[3] A. G. Agustí, J. Roca, J. Gea, P. D. Wagner, A. Xaubet, and R. Rodriguez-Roisin, *Mechanisms of gas-exchange impairment in idiopathic pulmonary fibrosis*, Am. Rev. Respir. Dis. **143** (1991), 219–225.

[4] K. Alving, E. Weitzberg, and J. M. Lundberg, *Increased amount of nitric oxide in exhaled air of asthmatics*, Eur. Respir. J. **6** (1993), 1368–1370.

[5] A. Amann, G. Poupart, S. Telser, M. Ledochowski, A. Schmid, and S. Mechtcheriakov, *Applications of breath gas analysis in medicine*, Int. J. Mass Spectrometry **239** (2004), 227–233.

[6] A. Amann and D. Smith (eds.), *Breath analysis for clinical diagnosis and therapeutic monitoring*, World Scientific, Singapore, 2005.

[7] A. Amann, P. Spanel, and D. Smith, *Breath analysis: the approach towards clinical applications*, Mini reviews in Medicinal Chemistry **7** (2007), 115–129.

[8] L. C. A. Amorim and Z. de L. Cardeal, *Breath air analysis and its use as a biomarker in biological monitoring of occupational and environmental exposure to chemical agents*, J. Chromatogr. B Analyt. Technol. Biomed. Life Sci. **853** (2007), 1–9.

[9] M. E. Andersen, *Physiological modeling of organic compounds*, Ann. Occup. Hyg. **35** (1991), 309–321.

[10] B. D. O. Anderson and J. B. Moore, *Optimal filtering*, Prentice-Hall, Englewood Cliffs, 1979.

[11] D. H. Anderson, *Compartmental modeling and tracer kinetics*, Springer, Berlin, 1983.

[12] J. C. Anderson, A. L. Babb, and M. P. Hlastala, *Modeling soluble gas exchange in the airways and alveoli*, Ann. Biomed. Eng. **31** (2003), 1402–22.

[13] M. Anguelova, *Observability and identifiability of nonlinear systems with applications in biology*, Ph.D. thesis, Chalmers University of Technology and Göteborg University, 2007.

[14] B. Aulbach, *Gewöhnliche Differentialgleichungen*, Elsevier, München, 2004.

[15] A. Bajtarevic, C. Ager, M. Pienz, M. Klieber, K. Schwarz, M. Ligor, T. Ligor, W. Filipiak, H. Denz, M. Fiegl, W. Hilbe, W. Weiss, P. Lukas, H. Jamnig, M. Hackl, A. Haidenberger, B. Buszewski, W. Miekisch, J. Schubert, and A. Amann, *Noninvasive detection of lung cancer by analysis of exhaled breath*, BMC Cancer **9** (2009), 348.

[16] J. R. Banga, C. G. Moles, and A. A. Alonso, *Global optimization of bioprocesses using stochastic and hybrid methods*, Frontiers in global optimization (C.A. Floudas and P.M. Pardalos, eds.), Kluwer, 2003, pp. 45–70.

[17] H. T. Banks, K. Holm, and D. Robbins, *Standard error computations for uncertainty quantification in inverse problems: asymptotic theory vs. bootstrapping*, Mathematical and Computer Modelling **52** (2010), 1610–1625.

[18] H. T. Banks and H. T. Tran, *Mathematical and experimental modeling of physical and biological processes*, CRC Press, Boca Raton, 2009.

[19] P. J. Barnes, *Nitric oxide and airway disease*, Ann. Med. **27** (1995), 389–393.

[20] I. Bauer, H. G. Bock, S. Korkel, and J. P. Schlöder, *Numerical methods for optimum experimental design in DAE systems*, Journal of Computational and Applied Mathematics **120** (2000), 1–25.

[21] J. V. Beck and K. J. Arnold, *Parameter estimation in engineering and science*, Wiley, New York, 1977.

[22] J. M. Bernardo and A. F. M. Smith, *Bayesian theory*, Wiley, Chichester, 1994.

[23] T. Birken, J. Schubert, W. Miekisch, and G. Noldge-Schomburg, *A novel visually CO_2 controlled alveolar breath sampling technique*, Technol. Health Care **14** (2006), 499–506.

[24] Robert S. Blake, Paul S. Monks, and Andrew M. Ellis, *Proton-transfer reaction mass spectrometry*, Chemical Reviews **109** (2009), 861–896.

[25] H. G. Bock, *Numerical treatment of inverse problems in chemical reaction kinetics*, Modelling of chemical reaction systems (K. Ebert, P. Deuflhard, and W. Jäger, eds.), Springer, Heidelberg, 1981, pp. 102–125.

[26] ______, *Randwertproblemmethoden zur Parameteridentifizierung in Systemen nichtlinearer Differentialgleichungen*, Ph.D. thesis, Universität Bonn, 1987.

[27] J. V. Bradley, *Distribution-free statistical tests*, Prentice Hall, Englewood Cliffs, 1968.

[28] O. Brovko, D. M. Wiberg, L. Arena, and J. W. Bellville, *The extended Kalman filter as a pulmonary blood flow estimator*, Automatica **17** (1981), 213–220.

[29] B. Buszewski, M. Kesy, T. Ligor, and A. Amann, *Human exhaled air analytics: biomarkers of diseases*, Biomed. Chromatogr. **21** (2007), 553–566.

[30] G. Calafiore, *Reliable localization using set-valued nonlinear filters*, IEEE Transactions on Systems, Man, and Cybernetics **35** (2005), 189–197.

[31] W. Cao and Y. Duan, *Current status of methods and techniques for breath analysis*, Critical Reviews in Analytical Chemistry **37** (2007), 3–13.

[32] L. Cappellin, F. Biasioli, A. Fabris, E. Schuhfried, C. Soukoulis, T. D. Märk, and F. Gasperi, *Improved mass accuracy in PTR-TOF-MS: Another step towards better compound identification in PTR-MS*, Int. J. Mass Spectrometry **290** (2010), 60–63.

[33] N. Chopin, *Central limit theorem for sequential Monte Carlo methods and its application to Bayesian inference*, Ann. Statist. **32** (2004), 2385–2411.

[34] C. Cobelli and J. J. DiStefano, *Parameter and structural identifiability concepts and ambiguities: a critical review and analysis*, Am. J. Physiol. **239** (1980), R7–24.

[35] K. A. Cope, M. T. Watson, W. M. Foster, S. S. Sehnert, and T. H. Risby, *Effects of ventilation on the collection of exhaled breath in humans*, J. Appl. Physiol. **96** (2004), 1371–1379.

[36] D. Crisan and A. Doucet, *A survey of convergence results on particle filtering for practitioners*, IEEE Trans. Signal Processing **50** (2002), 736–746.

[37] A. L. Dawidowicz, E. Fornal, M. Mardarowicz, and A. Fijalkowska, *The role of human lungs in the biotransformation of propofol*, Anesthesiology **93** (2000), 992–997.

[38] P. Deuflhard, *Newton methods for nonlinear problems: affine invariance and adaptive algorithms*, Springer, Berlin, 2004.

[39] P. Deuflhard and G. Heindl, *Affine invariant convergence theorems for Newton's method and extensions to related methods*, SIAM J. Numer. Anal, **16** (1979), 1–10.

[40] L. Devroye, *Non-uniform random variate generation*, Springer, Berlin, 1986.

[41] S. Diop and Y. Wang, *Equivalence between algebraic observability and local generic observability*, Proceedings of the 32nd IEEE Conference on Decision and Control, 1993, pp. 2864–2865.

[42] G. Dogan, *Bootstrapping for confidence interval estimation and hypothesis testing for parameters of system dynamics models*, Syst. Dyn. Rev. **23** (2007), 415–436.

[43] A. Doucet, N. de Freitas, and N. Gordon (eds.), *Sequential monte carlo methods in practice*, Springer, New York, 2001.

[44] A. Doucet, S. J. Godsill, and C. Andrieu, *On sequential Monte Carlo sampling methods for Bayesian filtering*, Statist. Comp. **10** (2000), 197–208.

[45] A. Doucet, N. J. Gordon, and V. Krishnamurthy, *Particle filters for state estimation of jump Markov linear systems*, IEEE Trans. Signal Processing **49** (2001), 613–624.

[46] N. R. Draper and H. Smith, *Applied regression analysis*, 3rd ed., Wiley, New York, 1998.

[47] B. Efron, *Bootstrap methods: another look at the jackknife*, Annals of Statistics **7** (1979), 1–26.

[48] B. Efron and R. J. Tibshirani, *An introduction to the bootstrap*, Chapman & Hall, New York, 1993.

[49] O. Engdahl, M. Abrahams, A. Björnsson, M. Vegfors, B. Norlander, J. Ahlner, and C. Eintrei, *Cerebrospinal fluid concentrations of propofol during anaesthesia in humans*, Br. J. Anaesth. **81** (1998), 957–959.

[50] L. E. Farhi, *Elimination of inert gas by the lung*, Respiration Physiology **3** (1967), 1–11.

[51] V. V. Fedorov, *Theory of optimal experiments*, Academic Press, 1972.

[52] A. Fick, *Über die Messung des Blutquantums in den Herzventrikeln*, Sitzungsberichte der physikalisch-medizinischen Gesellschaft zu Würzburg (1870), 16.

[53] M. Fink, *myAD: Fast automatic differentiation code in Matlab*, 2006.

[54] V. Fiserova-Bergerova (ed.), *Modeling of inhalation exposure to vapors: Uptake, distribution, and elimination*, CRC Press, Boca Raton, 1983.

[55] V. Fiserova-Bergerova and M. L. Diaz, *Determination and prediction of tissue-gas partition coefficients*, Int. Arch. Occup. Environ. Health **58** (1986), 75–87.

[56] G. S. Fishman, *Monte Carlo: concepts, algorithms, and applications*, Springer, New York, 1999.

[57] R. Fletcher, *Practical methods of optimization*, 2nd ed., Wiley, Chichester, 1993.

[58] M. Fortin, *Augmented Lagrangian methods: applications to the numerical solution of boundary-value problems*, North-Holland, Amsterdam, 1983.

[59] D. J. Gavaghan and C. E. Hahn, *A tidal breathing model of the forced inspired inert gas sinewave technique*, Respir. Physiol. **106** (1996), 209–221.

[60] A. Gelb (ed.), *Applied optimal estimation*, M.I.T. Press, Cambridge, 1974.

[61] J. E. Gentle, *Random number generation and Monte Carlo methods*, Springer, New York, 2005.

[62] L. E. Gerlowski and R. K. Jain, *Physiologically based pharmacokinetic modeling: principles and applications*, Journal of Pharmaceutical Sciences **72** (1983), 1103–1127.

[63] R. S. Gohlke and F. W. McLafferty, *Early gas chromatography/mass spectrometry*, Journal of the American Society for Mass Spectrometry **4** (1993), 367–371.

[64] G. H. Golub and C. F. Van Loan, *Matrix computations*, 3rd ed., Johns Hopkins University Press, Baltimore, 1996.

[65] N. J. Gordon, D. J. Salmond, and A. F. M. Smith, *A novel approach to nonlinear/non-Gaussian Bayesian state estimation*, IEE Proceedings F **140** (1993), 107–113.

[66] R. Grob and E. Barry, *Modern practice of gas chromatography*, Wiley, Hoboken, 2004.

[67] L. E. Gustafsson, A. M. Leone, M. G. Persson, N. P. Wiklund, and S. Moncada, *Endogenous nitric oxide is present in the exhaled air of rabbits, guinea pigs and humans*, Biochem. Biophys. Res. Commun. **181** (1991), 852–857.

[68] E. Hairer, Norsett S. P., and G. Wanner, *Solving ordinary differential equations 1: Nonstiff problems*, 2nd ed., Springer, Berlin, 1993.

[69] E. Hairer and G. Wanner, *Solving ordinary differential equations 2: Stiff and differential-algebraic problems*, 2nd ed., Springer, Berlin, 1996.

[70] G. R. Harrison, A. D. J. Critchley, C. A. Mayhew, and J. M. Thompson, *Real-time breath monitoring of propofol and its volatile metabolites during surgery using a novel mass spectrometric technique: a feasibility study*, Br. J. Anaesth. **91** (2003), 797–799.

[71] F. He, L. F. Yeung, and M. Brown, *Discrete-time model representations for biochemical pathways*, Trends in Intelligent Systems and Computer Engineering (O. Castillo, L. Xu, and S.-I. Ao, eds.), Springer, 2008, pp. 255–271.

[72] J. Herbig, T. Titzmann, J. Beauchamp, and I. Kohl, *Buffered end-tidal (BET) sampling - a novel method for real-time breath-gas analysis*, Journal of Breath Research **2** (2008), 1–9.

[73] R. Hermann and A. J. Krener, *Nonlinear controllability and observability*, IEEE Trans. Automat. Control **22** (1977), 728–740.

[74] W. Horbelt, J. Timmer, and H.U. Voss, *Parameter estimation in nonlinear delayed feedback systems from noisy data*, Physics Letters A **299** (2002), 513–521.

[75] C. Hornuss, S. Praun, J. Villinger, A. Dornauer, P. Moehnle, M. Dolch, E. Weninger, A. Chouker, C. Feil, J. Briegel, M. Thiel, and G. Schelling, *Real-time monitoring of propofol in expired air in humans undergoing total intravenous anesthesia*, Anesthesiology **106** (2007), 665–674.

[76] J. W. Huang, Y. Y. Lu, A. Nayak, and R. J. Roy, *Depth of anesthesia estimation and control*, IEEE Trans. Biomed. Eng. **46** (1999), 71–81.

[77] S. Huet, A. Bouvier, M.-A. Poursat, and E. Jolivet, *Statistical tools for nonlinear regression*, Springer, New York, 2003.

[78] J. M. B. Hughes and N. W. Morell, *Pulmonary Circulation. From basic mechanisms to clinical practice*, Imperial College Press, London, 2001.

[79] J. A. Jacquez and T. Perry, *Parameter estimation: local identifiability of parameters*, Am. J. Physiol. **258** (1990), E727–E736.

[80] J. A. Jacquez and C. P. Simon, *Qualitative theory of compartmental systems*, SIAM Review **35** (1993), 34–79.

[81] A. H. Jazwinski, *Stochastic processes and filtering theory*, Academic Press, New York, 1970.

[82] D. E. Koshland Jr., *The molecule of the year*, Science **258** (1992), 1861.

[83] M. P. Kalapos, *On the mammalian acetone metabolism: from chemistry to clinical implications*, Biochim. Biophys. Acta **1621** (2003), 122–39.

[84] R. E. Kalman, *A new approach to linear filtering and prediction problems*, Transactions of the ASME – Journal of Basic Engineering **82** (1960), 35–45.

[85] E. D. Kharasch, M. D. Karol, C. Lanni, and R. Sawchuk, *Clinical sevoflurane metabolism and disposition. I. Sevoflurane and metabolite pharmacokinetics*, Anesthesiology **82** (1995), 1369–1378.

[86] S. A. Kharitonov, K. F. Chung, D. Evans, B. J. O'Connor, and P. J. Barnes, *Increased exhaled nitric oxide in asthma is mainly derived from the lower respiratory tract*, Am. J. Respir. Crit. Care Med. **153** (1996), 1773–1780.

[87] S. A. Kharitonov, D. Yates, R. A. Robbins, R. Logan-Sinclair, E. A. Shinebourne, and P. J. Barnes, *Increased nitric oxide in exhaled air of asthmatic patients*, Lancet **343** (1994), 133–135.

[88] M. Kieffer and E. Walter, *Interval analysis for guaranteed nonlinear parameter and state estimation*, Mathematical and Computer Modelling of Dynamic Systems **11** (2005), 171–181.

[89] G. Kitagawa, *Monte Carlo filter and smoother for non-Gaussian nonlinear state space models*, J. Comput. Graph. Stat. **5** (1996), 1–25.

[90] A. Krogh and J. Lindhard, *Measurement of the blood flow through the lungs of man*, Scand. Arch. Physiol. **27** (1912), 100–125.

[91] I. Kushch, B. Arendacka, S. Stolc, P. Mochalski, W. Filipiak, K. Schwarz, L. Schwentner, A. Schmid, A. Dzien, M. Lechleitner, V. Witkovsky, W. Miekisch, J. Schubert, K. Unterkofler, and A. Amann, *Breath isoprene–aspects of normal physiology related to age, gender and cholesterol profile as determined in a proton transfer reaction mass spectrometry study*, Clin. Chem. Lab. Med. **46** (2008), 1011–1018.

[92] G. Laszlo, *Respiratory measurements of cardiac output: from elegant idea to useful test*, J. Appl. Physiol. **96** (2004), 428–437.

[93] C. L. Lawson and R. J. Hanson, *Solving least squares problems*, Prentice Hall, Englewood Cliffs, 1974.

[94] H. W. Leung, *Development and utilization of physiologically based pharmacokinetic models for toxicological applications*, J. Toxicol. Environ. Health **32** (1991), 247–267.

[95] D. G. Levitt, *Heterogeneity of human adipose blood flow*, BMC Clin. Pharmacol. **7** (2007), 1.

[96] D. R. Lide and W. M. Haynes (eds.), *CRC handbook of chemistry and physics*, 90th ed., CRC Press, Boca Raton, 2009.

[97] W. Lindinger, A. Hansel, and A. Jordan, *On-line monitoring of volatile organic compounds at pptv levels by means of proton-transfer-reaction mass spectrometry (PTR-MS) medical applications, food control and environmental research*, Int. J. Mass Spectrom. Ion Processes **173** (1998), 191–241.

[98] ———, *Proton-transfer-reaction mass spectrometry (PTR-MS): on-line monitoring of volatile organic compounds at pptv levels*, Chem. Soc. Rev. **27** (1998), 347–354.

[99] J. S. Liu and R. Chen, *Sequential Monte Carlo methods for dynamic systems*, Journal of the American Statistical Association **93** (1998), 1032–1044.

[100] G. M. Ljung and G. E. P. Box, *On a measure of lack of fit in time series models*, Biometrika **65** (1978), 297–303.

[101] L. Ljung, *Analysis of recursive stochastic algorithms*, IEEE Trans. Autom. Control **2** (1977), 551–575.

[102] ———, *Asymptotic behavior of the extended Kalman filter as a parameter estimator for linear systems*, IEEE Trans. Autom. Control **24** (1979), 36–50.

[103] L. Ljung and T. Glad, *On global identifiability for arbitrary model parameterizations*, Automatica **30** (1994), 265–276.

[104] C. C. Lu, C. S. Tsai, S. T. Ho, W. Y. Chen, C. S. Wong, J. J. Wang, O. Y P Hu, and C. Y. Lin, *Pharmacokinetics of sevoflurane uptake into the brain and body*, Anaesthesia **58** (2003), 951–956.

[105] A. B. Lumb, *Nunn's applied respiratory physiology*, 6th ed., Butterworth-Heinemann, Oxford, 2005.

[106] J. O. Lundberg, T. Farkas-Szallasi, E. Weitzberg, J. Rinder, J. Lidholm, A. Angaard, T. Hökfelt, J. M. Lundberg, and K. Alving, *High nitric oxide production in human paranasal sinuses*, Nat. Med. **1** (1995), 370–373.

[107] J. O. Lundberg, E. Weitzberg, S. L. Nordvall, R. Kuylenstierna, J. M. Lundberg, and K. Alving, *Primarily nasal origin of exhaled nitric oxide and absence in Kartagener's syndrome*, Eur. Respir. J. **7** (1994), 1501–1504.

[108] A. Manolis, *The diagnostic potential of breath analysis*, Clin. Chem. **29** (1983), 5–15.

[109] G. Margaria, E. Riccomagno, M. J. Chappell, and H. P. Wynn, *Differential algebra methods for the study of the structural identifiability of rational function state-space models in the biosciences*, Mathematical Biosciences **174** (2001), 1–26.

[110] M. McCulloch, T. Jezierski, M. Broffman, A. Hubbard, K. Turner, and T. Janecki, *Diagnostic accuracy of canine scent detection in early- and late-stage lung and breast cancers*, Integr. Cancer Ther. **5** (2006), 30–39.

[111] M. R. McCurdy, Y. Bakhirkin, G. Wysocki, R. Lewicki, and F. K. Tittel, *Recent advances of laser-spectroscopy-based techniques for applications in breath analysis*, Journal of Breath Research **1** (2007), 014001 (12pp).

[112] W. Miekisch, P. Fuchs, S. Kamysek, C. Neumann, and J. K. Schubert, *Assessment of propofol concentrations in human breath and blood by means of HS-SPME-GC-MS*, Clin. Chim. Acta **395** (2008), 32–37.

[113] W. Miekisch and J. K. Schubert, *From highly sophisticated analytical techniques to life-saving diagnostics: Technical developments in breath analysis*, Trends in Analytical Chemistry **25** (2006), 665–673.

[114] A. S. Modak, *Single time point diagnostic breath tests: a review*, Journal of Breath Research **4** (2010), 017002.

[115] D. E. Mohrman and L. J. Heller, *Cardiovascular physiology*, 6th ed., Lange Medical Books/McGraw-Hill, New York, 2006.

[116] A. K. Mörk and G. Johanson, *A human physiological model describing acetone kinetics in blood and breath during various levels of physical exercise*, Toxicol. Lett. **164** (2006), 6–15.

[117] P. Müller, *Monte Carlo integration in general dynamic models*, Contemp. Math. **115** (1991), 145–163.

[118] T. G. Müller and J. Timmer, *Parameter identification techniques for partial differential equations*, International Journal of Bifurcation and Chaos **14** (2004), 2053–2060.

[119] M. Nakamura, Y. Sanjo, and K. Ikeda, *Predicted sevoflurane partial pressure in the brain with an uptake and distribution model comparison with the measured value in internal jugular vein blood*, J. Clin. Monit. Comput. **15** (1999), 299–305.

[120] H. Nijmeijer and A. van der Schaft, *Nonlinear dynamical control systems*, Springer, New York, 1990.

[121] J. T. Ottesen, M. S. Olufsen, and J. K. Larsen, *Applied mathematical models in human physiology*, SIAM, Philadelphia, 2004.

[122] S. S. Patel and K. L. Goa, *Sevoflurane. A review of its pharmacodynamic and pharmacokinetic properties and its clinical use in general anaesthesia*, Drugs **51** (1996), 658–700.

[123] L. Pauling, A. B. Robinson, R. Teranishi, and P. Cary, *Quantitative analysis of urine vapor and breath by gas-liquid partition chromatography*, Proc. Natl. Acad. Sci. USA **68** (1971), 2374–6.

[124] M. Peifer and J. Timmer, *Parameter estimation in ordinary differential equations for biochemical processes using the method of multiple shooting*, IET Systems Biology **1** (2007), 78–88.

[125] P. J. Peyton, S. J. Poustie, G. J. B. Robinson, D. J. Penny, and B. Thompson, *Non-invasive measurement of intrapulmonary shunt during inert gas rebreathing*, Physiol. Meas. **26** (2005), no. 3, 309–316.

[126] M. Phillips, R. N. Cataneo, A. R. C. Cummin, A. J. Gagliardi, K. Gleeson, J. Greenberg, R. A. Maxfield, and W. N. Rom, *Detection of lung cancer with volatile markers in the breath*, Chest **123** (2003), 2115–2123.

[127] M. Phillips, R. N. Cataneo, B. A. Ditkoff, P. Fisher, J. Greenberg, R. Gunawardena, C. S. Kwon, F. Rahbari-Oskoui, and C. Wong, *Volatile markers of breast cancer in the breath*, Breast J. **9** (2003), 184–191.

[128] J. D. Pleil, *Role of exhaled breath biomarkers in environmental health science*, J. Toxicol. Environ. Health B Crit. Rev. **11** (2008), 613–629.

[129] ———, *Breath biomarkers networking sessions at PittCon 2010, Orlando, Florida*, Journal of Breath Research **4** (2010), 029001.

[130] G. Preti, J. N. Labows, J. G. Kostelc, S. Aldinger, and R. Daniele, *Analysis of lung air from patients with bronchogenic carcinoma and controls using gas chromatography-mass spectrometry*, J. Chromatogr. **432** (1988), 1–11.

[131] M. B. Reddy, R. S. H. Yang, H. J. Clewell III, and M. E. Andersen (eds.), *Physiologically based pharmacokinetic modeling: science and applications*, Wiley, Hoboken, 2005.

[132] M. C. Reed, *Why is mathematical biology so hard?*, Notices of the AMS **51** (2004), 338–342.

[133] K. Reif, S. Gunther, E. Yaz, and R. Unbehauen, *Stochastic stability of the discrete-time extended Kalman filter*, IEEE Trans. Autom. Control **44** (1999), 714–728.

[134] J. Rieder, P. Lirk, C. Ebenbichler, G. Gruber, P. Prazeller, W. Lindinger, and A. Amann, *Analysis of volatile organic compounds: possible applications in metabolic disorders and cancer screening*, Wien. Klin. Wochenschr. **113** (2001), 181–5.

[135] J. Rieder, P. Prazeller, M. Boehler, P. Lirk, W. Lindinger, and A. Amann, *Online monitoring of air quality at the postanesthetic care unit by proton-transfer-reaction mass spectrometry*, Anesth. Analg. **92** (2001), 389–392.

[136] S. Rietbrock, H. Wissing, I. Kuhn, and U. Fuhr, *Pharmacokinetics of inhaled anaesthetics in a clinical setting: description of a novel method based on routine monitoring data*, Br. J. Anaesth. **84** (2000), 437–442.

[137] B. D. Ripley, *Stochastic simulation*, Wiley, New York, 1987.

[138] T. H. Risby, *Critical issues for breath analysis*, Journal of Breath Research **2** (2008), 030302 (3pp).

[139] M. Rodriguez-Fernandez, J. A. Egea, and J. R. Banga, *Novel metaheuristic for parameter estimation in nonlinear dynamic biological systems*, BMC Bioinformatics **7** (2006), 483.

[140] T. Schön, F. Gustafsson, and P.-J. Nordlund, *Marginalized particle filters for mixed linear/nonlinear state-space models*, IEEE Trans. Signal Processing **53** (2005), 2279–2289.

[141] T. Schön, R. Karlsson, and F. Gustafsson, *The marginalized particle filter in practice*, Proceedings of the IEEE Aerospace Conference, 2006.

[142] K. Schwarz, W. Filipiak, and A. Amann, *Determining concentration patterns of volatile compounds in exhaled breath by PTR-MS*, Journal of Breath Research **3** (2009), 027002 (15pp).

[143] K. Schwarz, A. Pizzini, B. Arendacka, K. Zerlauth, W. Filipiak, A. Schmid, A. Dzien, S. Neuner, M. Lechleitner, S. Scholl-Burgi, W. Miekisch, J. Schubert, K. Unterkofler, V. Witkovsky, G. Gastl, and A. Amann, *Breath acetone – aspects of normal physiology related to age and gender as determined in a PTR-MS study*, Journal of Breath Research **3** (2009), 027003 (9pp).

[144] G. A. F. Seber and C. J. Wild, *Nonlinear regression*, Wiley, Hoboken, 2003.

[145] A. Sedoglavic, *A probabilistic algorithm to test local algebraic observability in polynomial time*, Journal of Symbolic Computation **33** (2002), 735–755.

[146] J. Shao and D. Tu, *The jackknife and bootstrap*, Springer, New York, 1995.

[147] D. D. Shen, *Toxicokinetics*, Casarett & Doull's toxicology: the basic science of poisons, McGraw-Hill, New York, 7th ed., 2007, pp. 305–326.

[148] D. Simon, *Optimal state estimation*, Wiley, Hoboken, 2005.

[149] A. F. M. Smith and A. E. Gelfand, *Bayesian statistics without tears: A sampling-resampling perspective*, The American Statistician **46** (1992), 84–88.

[150] D. Smith and P. Španěl, *Selected Ion Flow Tube Mass Spectrometry, SIFT-MS, for on-line trace gas analysis of breath*, Breath Analysis for Clinical Diagnosis and Therapeutic Monitoring (A. Amann and D. Smith, eds.), Singapore, World Scientific, 2005.

[151] D. Smith, P. Španěl, and S. Davies, *Trace gases in breath of healthy volunteers when fasting and after a protein-calorie meal: a preliminary study*, J. Appl. Physiol. **87** (1999), 1584–8.

[152] D. Smith, T. Wang, J. Sule-Suso, P. Spanel, and A. El Haj, *Quantification of acetaldehyde released by lung cancer cells in vitro using selected ion flow tube mass spectrometry*, Rapid Commun. Mass Spectrom. **17** (2003), 845–850.

[153] T. Söderström, *Discrete-time stochastic systems*, 2nd ed., Springer, London, 2002.

[154] E. D. Sontag, *Mathematical Control Theory*, Springer, New York, 1990.

[155] H. W. Sorenson, *Recursive estimation for nonlinear dynamic systems*, Bayesian analysis of time series and dynamic models (J. C. Spall, ed.), Dekker, 1988.

[156] R. K. Stoelting and R. D. Miller, *Basics of anesthesia*, 5th ed., Churchill Livingstone, Philadelphia, 2007.

[157] J. Stoer, *On the numerical solution of constrained least-squares problems*, SIAM J. Numer. Anal. **8** (1971), 382–411.

[158] J. Stoer and R. Bulirsch, *Introduction to numerical analysis*, 2nd ed., Springer, New York, 1993.

[159] B. G. Stone, T. J. Besse, W. C. Duane, C. D. Evans, and E. G. DeMaster, *Effect of regulating cholesterol biosynthesis on breath isoprene excretion in men*, Lipids **28** (1993), 705–708.

[160] G. Summer, P. Lirk, K. Hoerauf, U. Riccabona, F. Bodrogi, H. Raifer, M. Deibl, J. Rieder, and W. Schobersberger, *Sevoflurane in exhaled air of operating room personnel*, Anesth. Analg. **97** (2003), 1070–1073.

[161] H. J. Sussmann, *Single-input observability of continuous-time systems*, Mathematical Systems Theory **12** (1979), 371–393.

[162] R. M. Tackley, G. T. Lewis, C. Prys-Roberts, R. W. Boaden, J. Dixon, and J. T. Harvey, *Computer controlled infusion of propofol*, Br. J. Anaesth. **62** (1989), 46–53.

[163] T. Teorell, *Kinetics of distribution of substances administered to the body. I. The extravascular modes of administration*, Arch. Int. Pharmacodyn. **57** (1937), 205–225.

[164] ______, *Kinetics of distribution of substances administered to the body. II. The intravascular modes of administration*, Arch. Int. Pharmacodyn. **57** (1937), 226–240.

[165] R. Teranishi, T. R. Mon, A. B. Robinson, P. Cary, and L. Pauling, *Gas chromatography of volatiles from breath and urine*, Anal. Chem. **44** (1972), 18–20.

[166] S. Timischl, *A global model for the cardiovascular and respiratory system*, Ph.D. thesis, Karl-Franzens-Universität Graz, `http://www.esi.ac.at/susanne/diss.pdf`, 1998.

[167] G. A. Truskey, F. Yuan, and D. F. Katz, *Transport Phenomena in Biological Systems*, Prentice Hall, Upper Saddle River, 2004.

[168] C. Turner, P. Spanel, and D. Smith, *A longitudinal study of ammonia, acetone and propanol in the exhaled breath of 30 subjects using selected ion flow tube mass spectrometry, SIFT-MS*, Physiol. Meas. **27** (2006), 321–337.

[169] ______, *A longitudinal study of breath isoprene in healthy volunteers using selected ion flow tube mass spectrometry (SIFT-MS)*, Physiol. Meas. **27** (2006), 13–22.

[170] ______, *A longitudinal study of ethanol and acetaldehyde in the exhaled breath of healthy volunteers using selected-ion flow-tube mass spectrometry*, Rapid Commun. Mass Spectrom. **20** (2006), 61–68.

[171] S. Vajda, K. R. Godfrey, and H. Rabitz, *Similarity transformation approach to identifiability analysis of nonlinear compartmental models*, Mathematical Biosciences **93** (1989), 217–248.

[172] H. U. Voss, J. Timmer, and J. Kurths, *Nonlinear dynamical system identification from uncertain and indirect measurements*, International Journal of Bifurcation and Chaos **14** (2004), 1905–1933.

[173] P. D. Wagner, *The multiple inert gas elimination technique (MIGET)*, Intensive Care Med **34** (2008), 994–1001.

[174] P. D. Wagner, G. E. Gale, R. E. Moon, J. R. Torre-Bueno, B. W. Stolp, and H. A. Saltzman, *Pulmonary gas exchange in humans exercising at sea level and simulated altitude*, J. Appl. Physiol. **61** (1986), 260–270.

[175] E. Walter, *Identifiability of state-space models*, Springer, Berlin, 1982.

[176] E. Walter and L. Pronzato, *Identification of parametric models from experimental data*, Springer, Berlin, 1997.

[177] E. A. Wan and A. T. Nelson, *Dual extended Kalman filter methods*, Kalman filtering and neural networks (S. Haykin, ed.), Wiley, New York, 2001.

[178] Y. Wang and E. D. Sontag, *Orders of input/output differential equations and state space dimensions*, SIAM Journal on Control and Optimization **33** (1994), 1102–1127.

[179] J. B. West, *Respiratory Physiology. The Essentials*, 7th ed., Lippincott Williams & Wilkins, Baltimore, 2005.

[180] A. Zwart, R. C. Seagrave, and A. Van Dieren, *Ventilation-perfusion ratio obtained by a noninvasive frequency response technique*, J. Appl. Physiol. **41** (1976), 419–424.

Part II

Experimental results

Chapter 5

Paper A: Isoprene and acetone concentration profiles during exercise on an ergometer

JULIAN KING ET AL.

Journal of Breath Research (2009) **3**, 027006 (16pp)

IOP PUBLISHING JOURNAL OF BREATH RESEARCH

J. Breath Res. **3** (2009) 027006 (16pp) doi:10.1088/1752-7155/3/2/027006

Isoprene and acetone concentration profiles during exercise on an ergometer

J King[1,2,3], **A Kupferthaler**[1,2], **K Unterkofler**[2,3], **H Koc**[2,3,5], **S Teschl**[4], **G Teschl**[5], **W Miekisch**[2,6], **J Schubert**[2,6], **H Hinterhuber**[2,7] **and A Amann**[1,2,8,9]

[1] Department of Operative Medicine, Innsbruck Medical University, Anichstr. 35, A-6020 Innsbruck, Austria
[2] Breath Research Unit of the Austrian Academy of Sciences, Dammstr. 22, A-6850 Dornbirn, Austria
[3] Vorarlberg University of Applied Sciences, Hochschulstr. 1, A-6850 Dornbirn, Austria
[4] University of Applied Sciences Technikum Wien, Höchstädtplatz 5, A-1200 Wien, Austria
[5] Fakultät für Mathematik, Universität Wien, Nordbergstr. 15, A-1090 Wien, Austria
[6] Department of Anaesthesiology and Intensive Care, University of Rostock, Schillingallee 35, D-18057 Rostock, Germany
[7] Department of Psychiatry, Innsbruck Medical University, Anichstr. 35, A-6020 Innsbruck, Austria

E-mail: anton.amann@i-med.ac.at and anton.amann@oeaw.ac.at

Received 18 March 2009
Accepted for publication 20 May 2009
Published 9 June 2009
Online at stacks.iop.org/JBR/3/027006

Abstract

A real-time recording setup combining exhaled breath volatile organic compound (VOC) measurements by proton transfer reaction-mass spectrometry (PTR-MS) with hemodynamic and respiratory data is presented. Continuous automatic sampling of exhaled breath is implemented on the basis of measured respiratory flow: a flow-controlled shutter mechanism guarantees that only end-tidal exhalation segments are drawn into the mass spectrometer for analysis. Exhaled breath concentration profiles of two prototypic compounds, isoprene and acetone, during several exercise regimes were acquired, reaffirming and complementing earlier experimental findings regarding the dynamic response of these compounds reported by Senthilmohan *et al* (2000 *Redox Rep.* **5** 151–3) and Karl *et al* (2001 *J. Appl. Physiol.* **91** 762–70). While isoprene tends to react very sensitively to changes in pulmonary ventilation and perfusion due to its lipophilic behavior and low Henry constant, hydrophilic acetone shows a rather stable behavior. Characteristic (median) values for breath isoprene concentration and molar flow, i.e., the amount of isoprene exhaled per minute are 100 ppb and 29 nmol min^{-1}, respectively, with some intra-individual day-to-day variation. At the onset of exercise breath isoprene concentration increases drastically, usually by a factor of $\sim$3–4 within about 1 min. Due to a simultaneous increase in ventilation, the associated rise in molar flow is even more pronounced, leading to a ratio between peak molar flow and molar flow at rest of $\sim$11. Our setup holds great potential in capturing continuous dynamics of non-polar, low-soluble VOCs over a wide measurement range with simultaneous appraisal of decisive physiological factors affecting exhalation kinetics. In particular, data appear to favor the hypothesis that short-term effects visible in breath isoprene levels are mainly caused by changes in pulmonary gas exchange patterns rather than fluctuations in endogenous synthesis.

(Some figures in this article are in colour only in the electronic version)

---

[8] Author to whom any correspondence should be addressed.
[9] Dr Amann is representative of Ionimed GesmbH, Innsbruck.

1752-7155/09/027006+16$30.00 © 2009 IOP Publishing Ltd Printed in the UK

Introduction

The basic requirement in real-time breath gas analysis is to develop an experimental setup enabling the fast quantification of volatile organic compounds (VOCs) in exhaled breath as well as for the acquisition of additional physiological variables in a synchronized, reproducible and non-invasive way. The first part of this contribution provides an extensive proposal on how to achieve this aim and documents the necessary features. Adjoined to this paper, the second part outlines a series of real-time exhaled breath measurements during specified ergometer workload sequences which were carried out with the purpose of reaffirming and complementing earlier experimental findings in this area, e.g., reported by Senthilmohan *et al* [1] and Karl *et al* [2].

Regarding the analysis of exhaled breath samples, we limit ourselves to proton transfer reaction-mass spectrometry (PTR-MS), which is a relatively new analytical technique for determining concentration levels of volatile molecular species down to ppt level on the basis of chemical ionization [3, 4]. Due to its high sensitivity for a large variety of trace gases commonly occurring in human breath, PTR-MS has proven to be a valuable and rapid quantification tool in breath-related VOC research [5, 6]. Depending on the number of different mass-to-charge ratios considered, data acquisition can be performed on a time scale of approximately 1 s, which theoretically offers the possibility of drawing and analyzing several breath samples per exhalation cycle. Hence, in contrast to other analytical methods such as gas chromatography mass spectrometry (GC-MS), which often require time-consuming preconcentration steps [7–11], PTR-MS can be used for the measurement of continuous VOC profiles in real time. This is particularly important for the detection of metabolic effects manifesting themselves in short-lived changes of certain marker compound levels [12–15]. It is advisable to complement such profiles with additional physiological data influencing VOC concentrations: cardiac output, which controls the rate at which trace gases circulate from organs and periphery to the lung or alveolar ventilation, which governs the transport of VOCs through the respiratory tree. Combining the real-time capability of PTR-MS with systems recording hemodynamic and/or respiratory factors remains an ambitious task from an experimental point of view. The two main difficulties in the development of a reliable and robust real-time measurement tool are:

(a) a consistent integration of all sensor devices guaranteeing synchronized data gathering,
(b) the standardization of the breath sampling procedure itself.

While (a) is mainly an issue regarding adequate instrument and software engineering, aim (b) is at the heart of exhaled breath analysis and still a matter of ongoing debate [16]. A major concern here is to ensure the extraction of end-tidal air, which can be implemented by flow- or CO_2-controlled sampling in order to selectively detect different exhalation phases. Some approaches have been suggested to prevent exhaled breath samples from being diluted with fresh dead space air [17–19]: nevertheless, most of the real-time experiments published in the literature use mixed-expiratory breath samples. The same holds true for off-line breath sampling, which traditionally is carried out by collecting and storing the breath sample in some container prior to analysis (e.g., Tedlar bags).

Motivated by this lack of a standardized breath sampling procedure, a breath sampling device (not shown) has been developed in our laboratory which serves to fill Tedlar bags with alveolar air in a flow and/or CO_2-controlled manner, taking into account the onset of the alveolar plateau [20] during exhalation phases. Here we present a generalization of this method for automatic real-time sampling. In addition, we describe a recording setup efficiently combining hemodynamic as well as respiratory and VOC-related data streams, and monitoring of these variables during ergometer-induced workload scenarios.

Materials and methods

An experimental setup capable of measuring the multitude of physiological signals mentioned above consists of five central parts:

(A) a hemodynamical monitor measuring heart rate, heart minute volume, blood pressure, etc,
(B) a spirometer measuring the volumetric flow rate when breathing through a flow transducer of some form (e.g., a head mask),
(C) a heated, chemically inert gas sample line leading from the flow transducer to the mass spectrometer,
(D) a medical ergometer for imposing certain workloads on the test subject,
(E) the PTR-MS for measurement of volatile compounds in exhaled breath.

A schematic diagram of our setup is given in figure 1 and will be described in detail in the following.

With regard to (A), a non-invasive hemodynamic analysis system (Task Force Monitor (TFM), CNSystems, Graz, Austria) was used to determine hemodynamic variables on the basis of standard ECG leads and transthoracic impedance cardiography (ICG). In particular, the device allows the continuous recording of blood pressure and cardiac output with beat-to-beat resolution, which is an essential requirement for relating changes in VOC concentrations to quick hemodynamic variations. This real-time capability ranges among the primary reasons for preferring impedance cardiography over other existing approaches for the measurement of heart minute volume as discussed below. Since the user interface of the TFM does not export the corresponding parameter values sequentially, we included a simple data server, sending the latest available data vector to a specified TCP/IP port every second. ICG methodology for determination of cardiac output has been validated against the invasive gold standard method thermal dilution in a variety of situations [21–23]; however, a comparison with healthy test subjects during workload conditions is still lacking. On the other hand, the bioimpedance approach has shown good

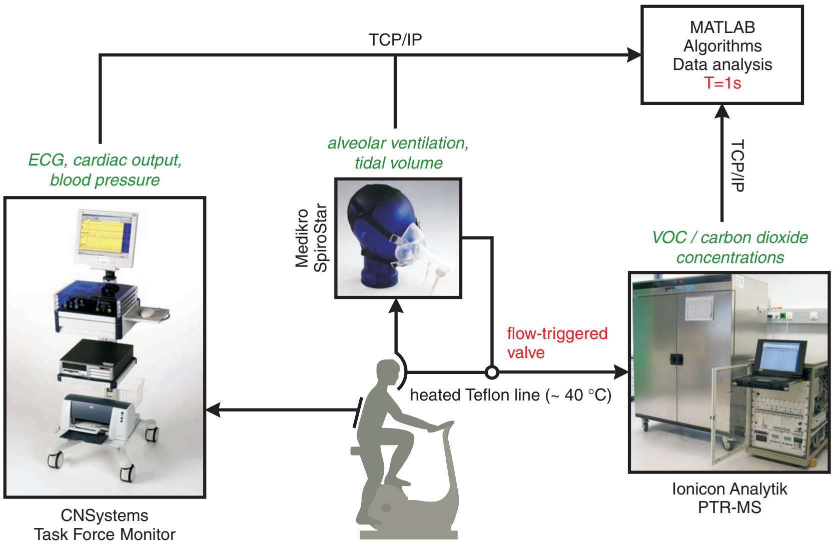
TCP/IP
MATLAB
Algorithms
Data analysis
T=1s
TCP/IP
ECG, cardiac output, blood pressure
alveolar ventilation, tidal volume
Medikro SpiroStar
VOC / carbon dioxide concentrations
flow-triggered valve
heated Teflon line (~ 40 °C)
CNSystems Task Force Monitor
Ionicon Analytik PTR-MS

Figure 1. Sketch of experimental setup, italic items correspond to accessible variables.

agreement with other non-invasive techniques for obtaining heart minute volume at different exercise levels [24].

Respiratory flow is obtained by means of a Medikro SpiroStar USB differential pressure sensor (Medikro Oy, Kuopio, Finland). Inhalation and exhalation occur through pre-calibrated, single-use flow transducer mouthpieces, which can be connected to sterilizable or disposable silicone head masks (Cortex Biophysik GmbH, Leipzig, Germany). This enables the test subject to breathe freely through mouth and/or nose while simultaneously reducing the risk of hyperventilation. Although some condensation could occur within the mask, this was not considered a critical issue: gas samples are drawn from the axial mainstream through Luer lock connecting sockets situated about 2 cm from the lips; so possible loss of highly soluble VOCs can be neglected due to the high flow. Based on the Bernoulli principle stating that the constriction of a given airflow will cause a difference in pressure which subsequently can be used to determine the associated flow [25], the device delivers volumetric flow rates ($\dot{V}$ (ml$_{\mathrm{BTPS}}$ s^{-1}), i.e., corrected for body temperature and saturation with water vapor) within the flow transducer with a sampling frequency of 100 Hz. As will be illustrated below, proper integration of this signal allows the efficient extraction of actual tidal volume and breathing frequency. The Medikro SpiroStar package comes with a DLL driver implementing functions for immediate communication with the spirometer hardware (initialization, data reading, etc), which can easily be incorporated into any C-based development environment.

Gas sampling is accomplished by a 3 m long, 1/4″ Teflon tube which is heated using an isolated heating wire (TNI Medical, Freiburg, Germany). The heating is necessary to avoid condensation of water vapor from exhaled breath within the sample line: condensed water droplets would attract hydrophilic compounds, thus depleting the gas sample and leading to erroneous measurement results. More specifically, care was taken to ensure that temperature is kept well over 40 °C along the entire length, thereby guaranteeing that no water condensation occurs. The gas sample line can be connected to the spirometer flow transducer by a metal Luer lock.

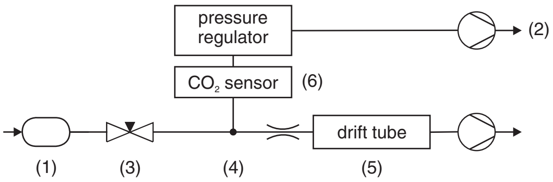

Figure 2. Inlet-flow architecture of the PTR-MS: (1) breath source, (2) vacuum pump, (3) needle valve, (4) pressure control point (0.655 bar), (5) drift tube, and (6) CO$_2$ sensor.

Exercise tests are carried out on a computer-controlled, semi-supine medical ergometer (eBike L, GE Medical Systems, Milwaukee, USA) operating at constant levels of power independently of the pedal speed. The supporting bed stabilizes the torso of the volunteer thereby reducing movement artifacts appearing in the acquired physiological signals. The longitudinal tilt can be adjusted from 45° during normal operation to 0° (supine position).

PTR-MS setup

Here we give a short description of the high-sensitivity PTR-MS used in our laboratory (Ionicon Analytik GmbH, Innsbruck, Austria); see figure 2. The breath source (1), e.g., a Tedlar bag or a volunteer breathing into a real-time sampling system as described above is connected to a heated Teflon bypass used to direct the sample gas from the breath source to the outside air by means of a vacuum pump (2). The corresponding flow can be adjusted using a needle valve (3). Assuming ambient pressure conditions in (1), a pressure regulator implemented along the bypass keeps pressure levels at the branching point (4) at a constant value of 0.655 bar, thereby guaranteeing stable pressure conditions of approximately 2.3 mbar in the drift chamber of the PTR-MS (5), which is connected to (4) via a $1/16''$ capillary heated up to 50 °C.

As has been described extensively elsewhere [3, 4], within the drift chamber, compounds with higher proton affinities than water are ionized by reacting with hydronium ions (H_3O^+) originating from a hollow cathode ion source adjoining the drift tube. The underlying reaction here is

$$H_3O^+ + M \rightarrow MH^+ + H_2O,$$

i.e., reactant gas particles, M, are protonated to give product ions, MH^+, which are then separated according to their distinctive mass-to-charge ratios (m/z) by a quadrupole mass spectrometer. Finally, an ion detection system measures count rates $i(H_3O^+)$ and $i(MH^+)$, which can be converted to concentration levels (parts per billion (ppb)—parts of the compound in 10^9 parts of air) of the compound in question by taking into account substance-specific reaction rates as well as possible fragmentation patterns [26, 27]. The PTR-MS control software provides the count rates associated with the mass-to-charge ratios under study as well as the reaction conditions, i.e., drift voltage (600 V), pressure (2.3 mbar) and temperature (52 °C) within the drift chamber. Again all available data are sent to a predefined TCP/IP port for subsequent storage. In our experiments, we limited ourselves to the following six mass-to-charge ratios (corresponding dwell times are given in brackets):

- m/z 21 (^{18}O isotope of the hydronium primary ions H_3O^+) (500 ms),
- m/z 37 (protonated water dimer, a precursor ion) (2 ms),
- m/z 18 (NH_4^+ which—when produced in the hollow cathode-–acts as a parasitic precursor ion, adjusted to be below 2% of H_3O^+) (10 ms),
- m/z 32 (O_2^+, a parasitic precursor ion, adjusted to be below 2% of H_3O^+) (10 ms),
- m/z 59 (protonated acetone) (200 ms),
- m/z 69 (protonated isoprene) (200 ms),

resulting in a total cycle duration of about 1.5 s. The first two mass-to-charge ratios are necessary for the correct quantification of acetone and isoprene, which we implicitly assume to be the only VOCs contributing to the associated m/z signal [27, 28]. Calibration for these two compounds with different levels of water vapor content was carried out either manually (in the case of isoprene) or using a Gaslab gas mixing unit (Breitfuss Messtechnik GmbH, Harpstedt, Germany) [27]. In particular, the presented concentration levels are determined with respect to the usual water vapor content in exhaled breath of about 6%. Slight variations of water content in the drift tube due to fluctuations in the amount of water clusters originating from the source were assumed to be negligible. For further details regarding calibration factors and fragmentation issues, we refer to the 'most abundant' approach as described in [29]: the corresponding calibration coefficients for isoprene and acetone were 0.95 and 0.79, respectively, calculated using the nominal reaction constant 2.0×10^{-9} cm^3 s^{-1} and an E/N ratio of ~126 Td.

Due to its low proton affinity, carbon dioxide cannot be measured by PTR-MS. As will be discussed in the following section, CO_2 content serves as a well-understood control value [30] for assessing the extraction quality of breath gas samples. We, therefore, included an infrared CO_2 sensor (AirSense Model 400, Digital Control Systems, Portland, USA) in our setup (cf figure 2 (6)). Particularly, by placing the sensor behind the pressure controlled branching point, we are able to determine concentrations independently of ambient pressure. Calibration was done with test gas consisting of 5% CO_2 in synthetic air (Linde Gas GmbH, Stadl-Paura, Austria). Due to limited flow through the bypass, the CO_2 sensor in the PTR-MS acts as a mechanical low-pass filter, with a measurement-induced delay of approximately 45 s. Current CO_2 concentration is appended to the PTR-MS data vector after each measurement cycle.

Standardized real-time breath sampling

Common measurement practice in breath gas analysis tacitly makes use of the Farhi equation (cf equation (1), later in this text), which states that—assuming constant respiratory and hemodynamic flow, e.g., during resting conditions—alveolar concentrations of blood-borne endogenous VOCs are proportional to their respective concentrations in mixed venous blood and therefore—by taking into account partition coefficients—to tissue levels. This makes alveolar concentration the decisive value in the quantification of blood-borne volatile species. However, the extraction of pure alveolar air is hampered by several obstacles, the major ones being mixing with (fresh) anatomic dead space volume as well as exchange in the conducting airways. The latter effect mainly relates to highly soluble substances interacting with mucus linings and will be discussed in conjunction with acetone measurements in the experimental section. In contrast, VOCs with low blood solubility (e.g., isoprene with a Henry constant of ~0.029 M atm^{-1} [2, 31]) originate almost exclusively from the alveolar blood–gas exchange, resulting in drastically reduced dead space concentrations. Alveolar levels of such molecular species are thus best reflected by end-tidal concentrations, i.e., it is recommendable to discard the first portion of exhaled breath in the analysis process. In the present framework, this suggests that any real-time extraction procedure should allow breath to be conducted to the PTR-MS inlet only during the end-tidal fraction of each exhalation phase. In particular, this strategy actively prevents room air from being physically sampled during inhalation, thereby simplifying data evaluation (no exhalation tracking is required).

One possible realization is the implementation of an automatic shutter or valve along the gas sample line, cutting off the connection between the mass spectrometer and the flow transducer during other time periods (cf figure 1). During valve closing times the sample line then must serve as a sufficiently large buffer volume in order to eliminate potential problems

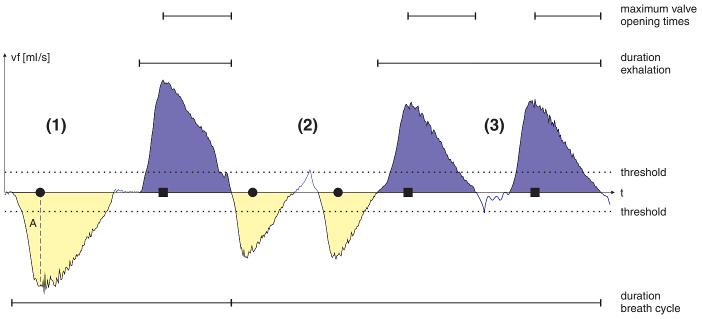

Figure 3. Example of the spirometer algorithm.

induced by substantial pressure fluctuations within the drift chamber due to continuous bypass deflation by the vacuum pump (cf figure 2). For a fixed sample line length, this amounts to manually adjusting the bypass flow in such a way that two factors are balanced:

(a) bypass flow should be high enough to minimize transport time from the flow transducer to the drift chamber (i.e., to minimize analysis delay)
(b) bypass flow should be low enough to avoid running into bypass vacuum during valve closing times.

Particularly, in our case empirical optimization leads to an analysis delay of approximately 10 s. Consequently, about three subsequent end-tidal phases are mixed in the sample line during normal breathing. Similarly to CO_2 data, the sample line thus represents a mechanical low-pass filter for the count rates delivered by PTR-MS, leading to a slight smoothing of the observed signal. The aforementioned standard setup represents a good trade-off for most test subjects, limiting excessive drift chamber pressure drops to a few isolated cases per measurement sequence. Persons exhibiting very shallow, sustained breathing patterns can be covered by further reducing bypass flow, which, however, leads to a prolongation of analysis delay.

Software algorithms

In the following, a C++ interface PROCESS_FLOW for consistent on-line shutter control and calculation of respiratory variables is presented. The interface continuously provides tidal volumes, alveolar ventilation and valve opening/closing times on the basis of the signal obtained via the spirometer hardware driver (see the above). More specifically, the volumetric flow rates $vf(t)$ are processed sequentially according to two basic heuristics, as shown in figure 3. First, we want to neglect small fluctuations due to the movement of the head mask or the spirometer's pressure tube. Valid inhalations/exhalations are therefore detected by the first time instant t^* after a zero crossing such that $vf(t^*)$ is smaller/greater than a user-selected threshold and the integral from the last baseline crossing to t^* (i.e., the total volume inhaled/exhaled so far) is greater than a predefined dead space volume (representing anatomical dead space and flow transducer volume, i.e., approximately 200 ml_{BTPS} [32]). Subsequently, the last zero crossing stored is accepted as the starting point for the current inspiration/expiration phase. Second, if two consecutive inhalations/exhalations occur without at least one valid exhalation/inhalation in between (being the most common non-regular respiratory maneuver during normal breathing), these multiple inhalations/exhalations are treated as one single inhalation/exhalation.

As soon as a new volumetric flow rate is available it has to be decided whether the valve should be open or closed. A useful rule here is to consider a certain modifiable percentage (say 50%) of the median of the preceding three or five exhalation times. This is motivated by the following observation: during regular breathing, after half of the total exhalation time has passed it seems safe to assume that only end-tidal air is being exhaled. If the breathing pattern does not change, a viable shutter regime thus opens the valve if the following three flow-related conditions are fulfilled:

(1) a valid exhalation phase has been identified,
(2) 50% of the last exhalation time has passed since the starting point,
(3) $vf(t)$ is greater than a user-selected minimal flow $vf_{\min}$.

The last item accounts for slightly delayed electronic valve response, so we can guarantee actual valve closing to be completed before the onset of inhalation. As a slight generalization of the second requirement we will consider a function of the preceding n exhalation times rather than only the last single value; it is well known that the median of n values is a robust average estimator, which discards outliers in the data. Consequently, computing the median of the last few exhalation times will filter out extremely short or long exhalation phases caused by coughing, etc, thus maintaining a proper valve control after such breathing events. Figure 3 summarizes the aforementioned features of the algorithm. A commented version of the C++ interface is available under http://realtime.voc-research.at.

During phase (1), the flow sensor delivers negative volumetric flow rates indicating the onset of an inhalation phase. However, inhalation is only detected if vf is below a predefined threshold, and if the inhaled volume (A) exceeds the specified dead space volume $V_D \sim 200\ \text{ml}_{\text{BTPS}}$. The

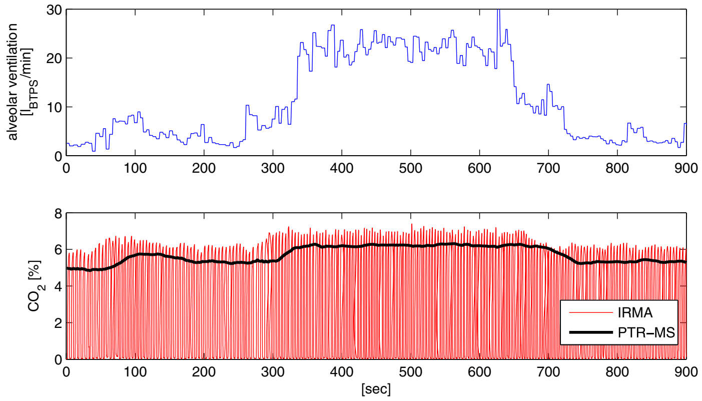

Figure 4. Comparison between real-time (time resolution ~60 ms) and PTR-MS CO_2 data during a 75 W ergometer challenge starting at 300 s and ending at 650 s; the measurement-induced delay of the PTR-MS CO_2 sensor of about 45 s is readily discernible.

filled circle in figure 3 marks the first time instant t^* after a zero crossing where these two requirements are fulfilled. The next zero crossing terminates the actual inhalation segment. Exhalation is identified analogously, indicated by the filled square. The corresponding time instant guarantees the end of the preceding inhalation phase and is associated with two events:

(a) The integral (= area under the curve $vf(t)$) calculated during the last inhalation phase is accepted as total inhalation volume V_T.
(b) We have arrived at the first possible valve opening time.

However, as explained above, the shutter will usually still remain closed until a user-defined percentage of the median of the last preceding exhalation times has passed since the start of exhalation. This requirement can be seen as an additional precaution to avoid the dilution of breath samples in the presence of inter-individually varying dead space air. Then the valve will be open at each time instant where vf is greater than vf_{min} (~20 ml s^{-1}, not indicated in figure 3). As soon as the next zero crossing is encountered, the shutter will be closed until the three requirements stated above are fulfilled again. The detection of a valid inhalation after a valid exhalation in phase (2) completes the previous breath cycle and is characterized by the following updates:

(a) determination of the preceding exhalation time,
(b) determination of the duration of the preceding breathing cycle,
(c) calculation of the current alveolar ventilation $\dot{V}_A$ (ml_{BTPS} min^{-1}), i.e., the flow effectively taking part in pulmonary gas exchange by the usual formula [30]

$$\dot{V}_A = f(V_T - V_D),$$

where the breathing frequency f can be extracted from (b). Thereafter, V_T as well as $\dot{V}_A$ are sent to a specified TCP/IP port. The current breathing frequency can be recovered from these two values by inverting the formula given above. The algorithm moreover accounts for possible multiple inhalation/exhalation phases as sketched in phase (2) and phase (3). Accordingly, if two inhalation segments are identified without a valid exhalation in between, the two corresponding inhalation volumes are added to give V_T at the detection of the next exhalation. Similarly, in phase (3), two expiration segments occur without being separated by a valid inhalation. Hence, the corresponding exhalation times will be merged in further calculations. However, valve control still applies separately to each exhalation phase.

We now have at hand a real-time valve control algorithm guaranteeing the sampling of end-tidal air during the entire measurement sequence while simultaneously computing inhalation volumes, breathing frequency and alveolar ventilation. The shutter is implemented by a Teflon valve (Parker, Fairfield, USA), heated to avoid condensation and placed near the mouth to minimize dead space volume. Opening and closing is accomplished by a standard serial interface realizing the actual status information at each time instant provided by the C++ interface PROCESS_FLOW. Preliminary validation of the present sampling scheme was done by comparing the CO_2 content delivered by the additional sensor in our previously described PTR-MS setup with independent continuous CO_2 data simultaneously acquired by means of an IRMA infrared probe (PHASEIN AB, Danderyd, Sweden); cf figure 4. Levels clearly correspond to end-tidal phases, reconfirming the capability of the sampling regime to exclusively extract the last segment of exhaled breath. Alternatively, automatic identification of an end-expiratory phase as well as associated sampling procedures could also be based on any respiratory signal approximately proportional to the aforementioned flow rates. Natural candidates here are CO_2 fraction (by defining a threshold detecting alveolar air), temperature (thermistor sensors) for sleep laboratory applications or even PTR-MS signals themselves as suggested in [18]. In any case, the limiting factors will be patient convenience, possible signal delay and a sampling frequency which necessarily is much higher than the normal breathing frequency, so the adequacy of the underlying method strongly depends on the experimental setup considered. Preliminary comparisons between a hypothesized control algorithm taking

CO_2 data with breath-to-breath resolution and the present flow-based scheme suggest good agreement between the two methods.

Data acquisition

Regarding data acquisition, a simple recording tool (RETBAT: REal Time Breath Analysis Tool) was implemented as a MATLAB graphical user interface. The software can be compiled to be used as a standalone executable without installation of the MATLAB main application. It asynchronously reads in PTR-MS-, spirometer- and TFM-related data from the aforementioned TCP/IP connections and displays them in real time. Synchronization is done on the basis of available TFM data, which are updated every second. More specifically, as soon as RETBAT receives the actual TFM data vector it accepts the latest available spirometer and PTR-MS data points as current values. The reason for letting the TFM application act as a timer is that we want the data collection to run in parallel with the specified ergometer workload scenario which is set by a control application running on the TFM PC. Thus, sampling with RETBAT is fully independent of local system time, i.e., the software can be executed on any network-authorized laboratory PC without prior time synchronization.

Before starting the workload scenario, the user has to provide measurement conditions such as room temperature, ambient pressure and room air (background) count rates of the mass-to-charge ratios under study. The latter could be used for corrective purposes; however, generally the levels are low enough to be neglected in the case of isoprene and acetone [27, 28]. After a plausibility check of the provided values, the received physiological data are plotted sequentially and can be explored in real time by means of the MATLAB plotting tools. Particularly, the count rates of m/z 59 (acetone) and m/z 69 (isoprene) are immediately converted to ppb on the basis of measured drift tube temperature and pressure as described previously. Finally, recorded data will be corrected with respect to the time response delays discussed before and saved to a predefined MATLAB structure which can further be exported to EXCEL. In particular, count rates and ppb levels corresponding to time instants where drift chamber pressure dropped below 2.2 mbar due to excessive shutter closing times (see the above) are considered as missing values. This threshold of 2.2 mbar was chosen on the basis of a maximum tolerable variability of room air concentrations during artificially induced pressure fluctuations.

Experiments

We concentrated our efforts on two compounds, which have received wide attention in the field of exhaled breath analysis: isoprene and acetone. The reason for this is twofold. First, we wanted to generate comparable data sets in order to reliably validate our sampling protocol. Second, due to their contrasting physical–chemical properties (isoprene is strongly lipophilic whereas acetone is hydrophilic) we view these two species as paradigmatic examples revealing valuable information on the broad spectrum of possible VOC responses according to distinct physiological conditions. In the following, we will briefly review some of the most important facts that have provided a deeper understanding of the involved mechanisms influencing the behavior of aforementioned compounds in exhaled breath.

Isoprene

2-methyl-1,3-butadiene, better known as isoprene (CAS number 78–79–5), is a colorless liquid organic hydrocarbon with a molar mass of 68.11 g mol^{-1} and a boiling point of 34 °C. Usually obtained from petroleum and coal to make synthetic rubber it is also the major hydrocarbon which is endogenously produced by mammals [33]. Its primary source is attributed to the mevalonate pathway of cholesterol biosynthesis [34, 35]. Originating from acetyl-CoA mevalonate is transformed into dimethylallyl pyrophosphate from which isoprene is produced. In exhaled human breath isoprene concentration exhibits a large variability. Typical levels in adults during rest have been reported to spread around 100 ppb [36], whereas children show lower levels [37, 38]. Corresponding blood concentrations have been shown to vary around 37 nmol l^{-1} [39] with an associated endogenous production rate ranging from 0.15 to 0.34 μmol h^{-1} kg^{-1} body weight [31, 40]. In the first reference, metabolization has been quantified as 0.31 μmol h^{-1} kg^{-1} body weight, which leads to a net isoprene production of 0.03 μmol h^{-1} kg^{-1} body weight (amounting to approximately 5×10^{-5} mol/day for a 70 kg person). Here net isoprene production is defined to be the endogenous production minus metabolization. Body tissue represents a potential storage volume for isoprene in the human body and this is, in particular, so for fat tissue as can be deduced from a high fat:blood partition coefficient of $\sim$82 [31].

Its high abundance in human breath and the fact that there are no indications for concentration changes due to food uptake [41] or for production and release in the upper airways [42] makes isoprene a relatively easily quantifiable test compound. Apart from being a convenient choice in terms of measurability, breath isoprene has been suggested as a sensitive indicator for assaying several metabolic effects in the human body [43]. First, being a possible by-product of cholesterol biosynthesis, it might serve as an additional diagnostic parameter in the care of patients suffering from lipid metabolism disorders such as hypercholesterolemia, which is an established risk factor for atherosclerosis and coronary heart disease. As an example, the estimation of endogenous isoprene production rates on the basis of available breath concentrations as well as appropriate kinetic models might be an adequate tool to determine the contribution of endogenous cholesterol release to the overall serum cholesterol level, thereby improving the diagnostic potential of standard blood tests, which merely quantify the combined effects of endogenous and dietary factors. Moreover, evidence points toward a strong linkage of breath isoprene levels to different physiological states, thus promoting its general use in biomonitoring, e.g., during sleep [12, 44]. Due to its low blood solubility (Henry's law constant) and boiling point, it is reasonable to assume that exhaled breath concentrations are substantially affected by alveolar ventilation and perfusion (i.e., alveolar minute flow and cardiac output). Significant correlations between cardiac output and breath isoprene concentrations during cardiovascular surgery can be expected. Drastically increasing levels of isoprene concentration were reported [2, 36] at the onset of physical exercise. These findings indicate that breath isoprene measurements might provide new tools for continuous, non-invasive monitoring of cardiac output.

Acetone

Acetone (CAS number 67–64–1), also known as propanone, has a molar mass of 58.08 g mol^{-1}. It is one of the ketone bodies, together with beta-hydroxybutyric acid and acetoacetic acid. Acetone is a product of the conversion of acetoacetate by the elimination of CO_2 [45, 46]:

$$\begin{aligned} &CH_3COCH_2COO^- + H^+ \rightarrow CH_3COCH_2COOH \\ &\quad \rightarrow CH_3COCH_3 + CO_2. \end{aligned}$$

This conversion is either a result of the non-enzymatic decarboxylation of acetoacetate or is catalyzed by acetoacetate decarboxylase. The acetoacetate decarboxylase is induced by starvation and inhibited by acetone itself. High concentrations of blood acetoacetate trigger the acetoacetate decarboxylase, thus draining H^+, while acetone, acting as a competitive inhibitor, helps to prevent early acetoacetate decarboxylation of acetoacetate. Acetoacetate is the product of beta-hydroxybutyric acid (= HMG-CoA, an intermediate of the mevalonate pathway) and can either be converted to acetone (see the above reaction) or to D-beta-hydroxybutyrate. Acetone is one of the most abundant compounds in human breath. Typical adult exhaled breath concentrations are spread around 600 ppb [27, 47] and plasma concentrations have been quantified as $\sim$15 μmol l^{-1} [46]. Moreover, a linear relationship between breath and blood concentrations can be assumed [48]. Blood:tissue solubility was estimated to be 1.38 [49, 50], which makes body tissue a much less efficient buffer for acetone than for isoprene. Because acetone is poorly metabolized [51], simple diffusion and volatilization in the lungs is likely to be the predominant path of removal [48]. Due to its high water solubility, the upper airways, however, cannot be regarded as an inert tube as in the case for isoprene. In fact, the nasal epithelium and as well as the tracheal mucosa linings have been demonstrated to play a critical role in pre-alveolar exchange, a phenomenon which has become known as the wash-in/wash-out effect [50, 52]. More specifically, studies orchestrated in the framework of nasal dosimetry research suggest that up to 75% of the compound inhaled via an exposure chamber is absorbed into the mucous membrane before reaching the alveolar region, and almost the entire amount absorbed is released back into the breath stream upon exhalation [51].

Being a byproduct of lipolysis, acetone has often been suggested as a marker compound for monitoring the ketotic state of an individual. Elevated breath acetone levels resulting from fasting are quickly lowered by feeding (as the body is nourished by glucose again [41]) and appear to be correlated with rates of fat loss [53]. No influences of sex, age and BMI on breath concentrations of acetone in adults could be determined [27]. Senthilmohan *et al* [1] report slightly increasing values upon physical exercise which again can be rationalized by viewing acetone as metabolite of fat catabolism. Moreover, patients suffering from (uncontrolled) diabetes mellitus have been found to exhibit disproportionately high breath acetone concentrations [54], thus establishing the potential clinical relevance of breath acetone in related medical treatment.

Test subjects and protocols

For our study, five males and three females with an age range of 25–30 years were recruited as volunteers and agreed to participate in up to three stress ergometer challenges with different workload sequences. The test subjects had to be in good health and physical shape although fitness levels differed. Explicitly non-smokers were chosen even though recent findings did not suggest any difference in isoprene and acetone breath concentration between smokers and non-smokers [55]. Measurements were all done in the morning at approximately the same time when volunteers were able to come into our test laboratory with an empty stomach so that at least 7 h had passed since their last meal. The only exception was drinking of water. Furthermore, volunteers were not allowed to brush their teeth with toothpaste in the morning, so we could exclude traces of it as a source of measurement error. No test subject reported any prescribed medication or drug intake. The study was approved by the Ethics Commission of Innsbruck Medical University.

On the day of the experiment the volunteers had to avoid strong physical activity and physical stress on the way from their home to the test laboratory. Following arrival and prior to starting the measurement regime, all test subjects needed to rest for at least 10 min in which they were given instructions regarding the workload protocol. Attention was paid to adjust the test equipment to individual weights and heights and to establish a comfortable seating position during the experiment. Next the volunteers were set up with the TFM electrodes, five to obtain the four-channel ECG and three more for the ICG. Before each measurement, the gas sample line was flushed with nitrogen (purity 6.0, Linde Gas GmbH, Stadl-Paura, Austria) for about 1 min. In order to avoid leakage the head mask was firmly fixed on the volunteer's head by means of a hair net; however, none of the test subjects reported any discomfort or problems regarding difficulty in breathing or even hyperventilation. The laboratory personnel reminded the volunteer before and during the exercise to minimize torso movements and to breathe regularly. Every event occurring during the measurement was recorded in written documentation including time and event description. Also the staff closely monitored real-time results as they were received through the TCP/IP connections from the different instruments in our MATLAB graphical user interface RETBAT.

We created a set of three different protocols all starting with an initial 5 min resting phase without workload

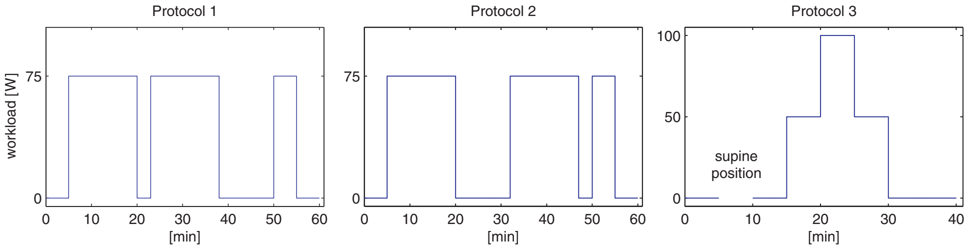

Figure 5. Protocols : (1) 5 min resting | 15 min exercise (75 W) | 3 min resting | 15 min exercise (75 W) | 12 min resting | 5 min exercise (75 W) | 5 min resting, (2) 5 min resting | 15 min exercise (75 W) | 12 min resting | 15 min exercise (75 W) | 3 min resting | 5 min exercise (75 W) | 5 min resting, (3) 5 min resting | 5 min supine position | 5 min resting | 5 min exercise (50 W) | 5 min exercise (100 W) | 5 min exercise (50 W) | 10 min resting.

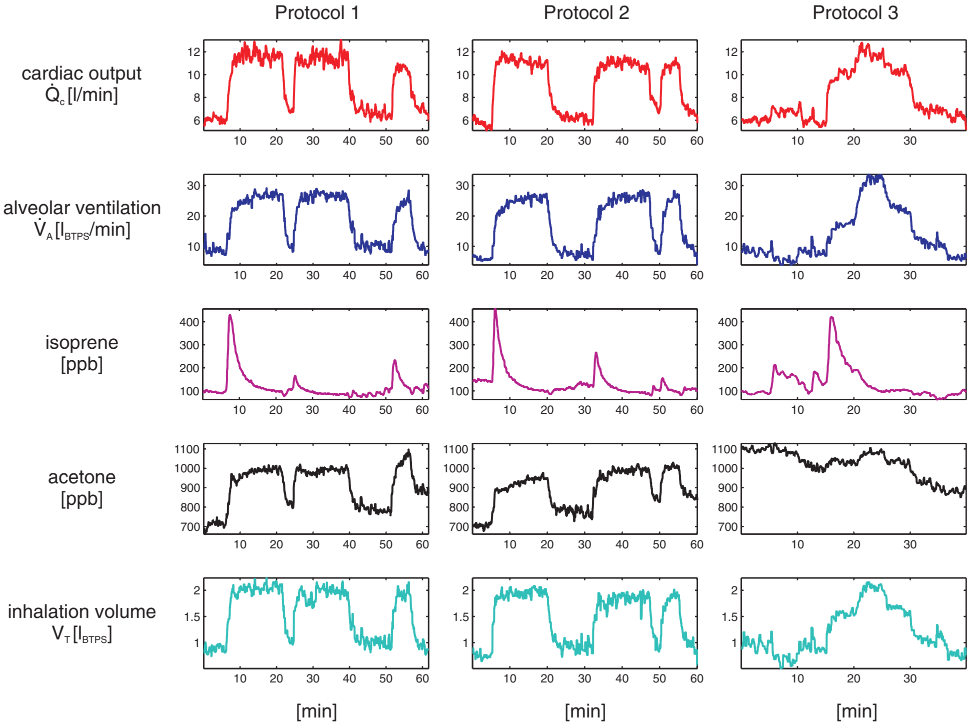

Figure 6. Typical results for one single test subject (male, 26 years) according to the three workload scenarios described in the text.

(cf figure 5). Then the volunteers were challenged to pedal at constant speed between 70–80 $r\,\mathrm{min}^{-1}$ on the ergometer which was set up for a workload resistance of 75 W for the first 15 min in protocols 1 and 2. While resting time after this workload sequence was only 3 min in protocol 1 it was extended to 12 min in protocol 2. After a second exercising phase of 15 min, the resting time was then reversed in both protocols. Both regimes end with a 5 min workload followed by 5 min of final resting. Starting with the same initial 5 min of resting, in protocol 3 the volunteer's position was changed from semi-supine to supine position by lowering the ergometer back rest electronically into a horizontal state for the length of 5 min. Subsequently, the volunteers were put back into the initial position and after 5 min started to pedal with a resistance of 50 W. Following an escalating–deescalating regime, this resistance was increased to 100 W after 5 min and then back to 50 W after 10 min of exercise. Protocol 3 ended with a 10 min resting phase.

The data streams obtained were compiled in a self-contained MATLAB data viewer enabling convenient data exploring and export, which can be downloaded after registration from http://realtime.voc-research.at. Determined physiological variables are summarized in table 1, together with some nominal values for resting conditions taken from the literature. Representative profiles from a single study subject are presented in figure 6. Hemodynamic and respiratory

Table 1. Summary of measured variables together with some nominal values during resting conditions.

Variable	Abb.	Nominal value
Hemodynamic parameters		
Heart rate	HR	70 (bpm) [77]
RR interval	RRI	850 (ms) [77]
Systolic blood pressure	sBP	120 (mmHg) [77]
Diastolic blood pressure	dBP	80 (mmHg) [77]
Stroke volume	SV	70 (ml) [77]
Cardiac output ($\dot{Q}_c$)	CO	5 (l min^{-1}) [77]
Total peripheral resistance	TPR	1600 (dyne s cm^{-5}) [77]
Ventilation parameters		
Alveolar ventilation ($\dot{V}_A$)	ALV	5.2 (l$_{\mathrm{BTPS}}$ min^{-1}) [32]
Inhalation volume (V_T)	vinh	0.5 (l$_{\mathrm{BTPS}}$) [32]
PTR-MS related data		
Drift chamber pressure	pdrift	2.3 (mbar)
Carbon dioxide content (end-expiratory)	pCO$_2$	5.6 (%) [30]
Count rates $m/z*$	CR$*$	
Acetone concentration	PPB59	500 (ppb) [27, 47]
Isoprene concentration	PPB69	100 (ppb) [28, 36]

variables generally exhibit a very consistent and reproducible behavior among the three protocols. In the following, we will mainly focus on cardiac output and alveolar ventilation. Cardiac output rapidly increased from approximately 5 l min^{-1} at rest to a constant plateau of about 12 l min^{-1} during a permanent workload of 75 W. Simultaneously, alveolar ventilation shows a characteristic rest-to-work transition from 5–10 l min^{-1} to a steady-state level of approximately 25–30 l min^{-1}, thereby increasing the average ventilation–perfusion ratio by a factor of ∼3. Transition times from resting conditions to workload steady state and vice versa vary around 5 min. As for the third protocol, changing from semi-supine to supine position usually led to a slight increase of cardiac output while alveolar ventilation remained roughly constant, thereby revealing the individual influence of cardiac output and lung posture on exhaled isoprene and acetone concentrations, respectively.

Results

Results isoprene

For all test subjects, end-tidal breath isoprene levels acquired prior to the workload sequence varied around the nominal value of approximately 100 ppb (3.7 nmol l^{-1} at body temperature) presented in [28, 36] with minor intra-individual variations; cf table 2. Multiplying this level by the measured alveolar minute ventilation leads to a corresponding molar flow (i.e., an amount of isoprene exhaled per minute) of about 30 nmol min^{-1}, which is more than 80% of the average net isoprene production for a 70 kg person as discussed above. This indicates that the predominant path of non-metabolic isoprene clearance is via the lungs [56]. Regarding the first two protocols, in accordance with earlier findings [2, 36], the onset of the first exercise period is accompanied by an increase in end-tidal isoprene concentration, usually by a factor of ∼3–4 within about 1 min. Due to a simultaneous increase in ventilation, the associated rise in amount of isoprene exhaled per minute is even more pronounced, leading to a ratio between peak molar flow and molar flow at rest of about 11. This phase is followed by a gradual decline and the development of a new steady state after 15 min of pedaling. Concentrations in this last phase do not differ substantially from the starting values, while molar flow is still higher by a factor of ∼3 compared to resting levels. In particular, the profile of exhaled isoprene per minute generally is rather different from carbon dioxide output during comparable workload schemes, which typically shows a monotonic rest-to-work transition; cf [57, 58]. However, one common feature appears to be the abrupt response at the onset of constant workload instituted from rest. The underlying mechanism for this effect remains largely unexplained, but has mainly been ascribed to neurogenic factors affecting ventilation [59].

Interestingly, repeating the same workload procedure described above after intermediate pauses of 3 and 12 min, respectively, results in similar concentration profiles but significantly lower peaks, despite almost identical behavior of cardiac output and alveolar ventilation. Consistent effects emerge when reversing the order of the two interceptions, which clearly suggests that initial dynamics tend to be restored with prolonged pauses. For perspective, several follow-up tests indicate that after 1 h of rest, maximum values again coincide. There are essentially two hypotheses regarding this effect: (a) changes in mixed venous blood concentration due to depletion/replenishment of an isoprene buffer tissue (e.g., fat), and (b) sustained functional changes in the lung, probably due to recruitment and distension of pulmonary capillaries during exercise [32]. The above-mentioned quantitative considerations and the fact that breath acetone and carbon dioxide exercise levels (see figure 7) do not appear to be affected by preceding pauses [57, 60] favor mechanism (a). However, direct investigation of these issues will have to await future blood tests as in [39].

Changes of body posture during the third workload scenario generally yield a more or less pronounced rise in breath isoprene concentration, its amplitude being correlated to the associated increase in cardiac output. It should be noted that in such cases, in contrast to the behavior during dynamic exercise, isoprene breath concentrations do not appear to revert to baseline levels within a short time. The escalating–deescalating regime performed in the second part reproduces the profile seen in the first two protocols. Specifically, the load step from 50 W to 100 W only has a minor effect on the observed dynamics.

Results acetone and carbon dioxide

Breath acetone concentrations at the beginning of the measurement sequence show typical levels of about 1 ppm. Marked day-to-day variations within one test subject may occur but fall within the range reported in [61]. Particularly, as mentioned above, elevated levels might be explained by increased lipolysis due to an empty stomach. Generally, acetone concentrations show higher breath-to-breath fluctuations than isoprene during rest as well as during

Table 2. Summary of observed breath concentrations (*C*) and molar flows (*m*) of isoprene for all eight study subjects. Values for the stages rest (C_{rest}, m_{rest}), work (C_{work}, m_{work}) and supine position (C_{supine}, m_{supine}) were obtained by filtering concentration and ventilation raw data by means of a 20 step median filter and calculating the mean values over the following time intervals (where applicable): rest (1–2 min), work (19–20 min), supine position (9–10 min); peak values correspond to maxima of the filtered profiles.

<table>
<tr><th>Subject no.</th><th>1</th><th>2</th><th>3</th><th>4</th><th>5</th><th>6</th><th>7</th><th>8</th></tr>
<tr><td>Protocol</td><td>1 | 2 | 3</td><td>1 | 2 | 3</td><td>1 | 2 | 3</td><td>1 | 2 | 3</td><td>1 | 2 | 3</td><td>1 | 2 | 3</td><td>1 | 2 | 3</td><td>1 | 2 | 3</td></tr>
<tr><td>C_{rest} (ppb)</td><td>99 | 146 | 86</td><td>48 | 44 | 50</td><td>75 | 104 | 119</td><td>180 | 177 | 126</td><td>156 | 108 | 125</td><td>64 | 92 | 54</td><td>144 | 156 | 128</td><td>43 | 46 | 40</td></tr>
<tr><td>m_{rest} (nmol min^{-1})</td><td>32 | 34 | 29</td><td>22 | 19 | 17</td><td>16 | 29 | 29</td><td>41 | 43 | 32</td><td>40 | 55 | 45</td><td>12 | 20 | 8</td><td>30 | 34 | 24</td><td>9 | 9 | 12</td></tr>
<tr><td>C_{peak} (ppb)</td><td>430 | 456 | #</td><td>212 | 142 | #</td><td>244 | 243 | #</td><td>610 | 656 | #</td><td>534 | 322 | #</td><td>306 | 376 | #</td><td>605 | 495 | #</td><td>117 | 203 | #</td></tr>
<tr><td>m_{peak} (nmol min^{-1})</td><td>360 | 346 | #</td><td>184 | 138 | #</td><td>167 | 226 | #</td><td>455 | 475 | #</td><td>478 | 390 | #</td><td>249 | 330 | #</td><td>453 | 411 | #</td><td>75 | 140 | #</td></tr>
<tr><td>C_{work} (ppb)</td><td>101 | 98 | #</td><td>58 | 53 | #</td><td>52 | 49 | #</td><td>169 | 193 | #</td><td>130 | 108 | #</td><td>45 | 58 | #</td><td>92 | 91 | #</td><td>30 | 41 | #</td></tr>
<tr><td>m_{work} (nmol min^{-1})</td><td>108 | 103 | #</td><td>60 | 53 | #</td><td>50 | 55 | #</td><td>167 | 171 | #</td><td>136 | 98 | #</td><td>60 | 70 | #</td><td>94 | 93 | #</td><td>32 | 42 | #</td></tr>
<tr><td>C_{supine} (ppb)</td><td># | # | 136</td><td># | # | 56</td><td># | # | 175</td><td># | # | 165</td><td># | # | 126</td><td># | # | 86</td><td># | # | 213</td><td># | # | 45</td></tr>
<tr><td>m_{supine} (nmol min^{-1})</td><td># | # | 45</td><td># | # | 28</td><td># | # | 54</td><td># | # | 51</td><td># | # | 50</td><td># | # | 25</td><td># | # | 45</td><td># | # | 15</td></tr>
<tr><td>$C_{\text{peak}}/C_{\text{rest}}$</td><td>4.3 | 3.1 | #</td><td>4.1 | 3.2 | #</td><td>3.3 | 2.3 | #</td><td>3.4 | 3.7 | #</td><td>3.4 | 3.0 | #</td><td>4.8 | 4.1 | #</td><td>4.1 | 3.2 | #</td><td>2.7 | 4.1 | #</td></tr>
<tr><td>$C_{\text{work}}/C_{\text{rest}}$</td><td>1.0 | 0.7 | #</td><td>1.2 | 1.2 | #</td><td>0.7 | 0.5 | #</td><td>0.9 | 1.1 | #</td><td>0.8 | 1.0 | #</td><td>0.7 | 0.6 | #</td><td>0.6 | 0.6 | #</td><td>0.7 | 0.9 | #</td></tr>
<tr><td>$C_{\text{supine}}/C_{\text{rest}}$</td><td># | # | 1.6</td><td># | # | 1.1</td><td># | # | 1.5</td><td># | # | 1.3</td><td># | # | 1.0</td><td># | # | 1.6</td><td># | # | 1.7</td><td># | # | 1.7</td></tr>
<tr><td>$m_{\text{peak}}/m_{\text{rest}}$</td><td>11.3 | 10.2 | #</td><td>8.4 | 7.3 | #</td><td>10.4 | 7.8 | #</td><td>11.1 | 11.0 | #</td><td>12.0 | 7.1 | #</td><td>20.8 | 16.5 | #</td><td>15.1 | 12.1 | #</td><td>8.3 | 15.6 | #</td></tr>
<tr><td>$m_{\text{work}}/m_{\text{rest}}$</td><td>3.4 | 3.0 | #</td><td>2.7 | 2.8 | #</td><td>3.1 | 1.9 | #</td><td>4.1 | 4.0 | #</td><td>3.4 | 1.8 | #</td><td>5.0 | 3.5 | #</td><td>3.1 | 2.7 | #</td><td>3.6 | 4.7 | #</td></tr>
<tr><td>$m_{\text{supine}}/m_{\text{rest}}$</td><td># | # | 1.6</td><td># | # | 1.6</td><td># | # | 1.9</td><td># | # | 1.6</td><td># | # | 1.1</td><td># | # | 3.1</td><td># | # | 1.9</td><td># | # | 1.3</td></tr>
</table>

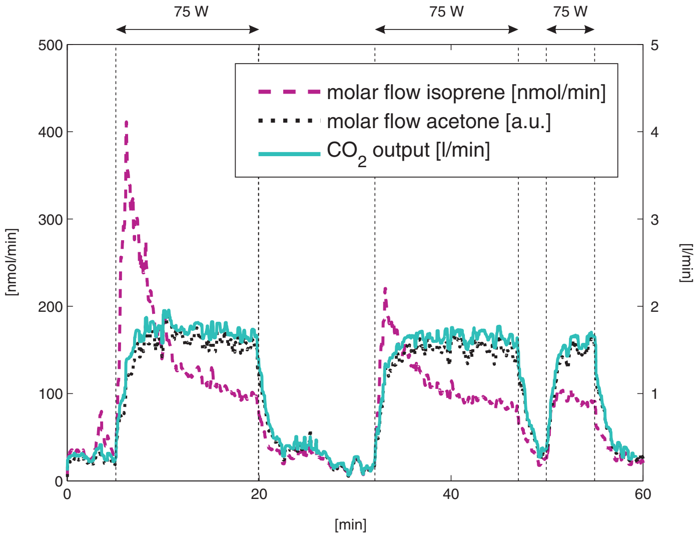

Figure 7. Output of isoprene, acetone and CO_2 during protocol 2 (sequential rectangular workload regime of 75 W with intermediate pauses of 12 and 3 min, respectively).

exercise. The reason for this is still unclear. However, preliminary experiments with our setup indicate that some variation can be attributed to alternate nose and mouth exhalation as well as flow rate. As has already been discussed, due to its high Henry constant, acetone is readily dissolved in the nasal epithelium, leading to lower breath concentrations when the predominant path of exhalation is through the nose [51, 52]. Acetone concentration in exhaled breath during exercise closely resembles the profile of alveolar ventilation respectively inhalation volume, showing abrupt increases respectively drops in the range of 10–40% at the onsets, respectively, stops of the individual workload periods. Similarly to the results presented by Senthilmohan *et al* [1], average concentrations often tend to rise slightly with duration of exercise, which might stem from elevated fat catabolism as a source of energy. Changing to supine position in protocol 3 seems to have negligible effects. CO_2 content initially varies around 4% and exhibits virtually identical dynamics to acetone during the three workload scenarios, with an abrupt increase/decrease of ∼20% at the start/stop of exercise [57]. This is in accordance with Ma *et al* [62], who demonstrated a linear correlation between acetone and end-tidal carbon dioxide pressure.

We are aware of the fact that acetone concentrations obtained with the methodology illustrated above might underestimate alveolar concentrations due to the deposition of acetone onto the mucus linings in the conducting airways upon exhalation [49]. In the case of highly water- and blood-soluble compounds, isothermal rebreathing [63, 64] probably represents the only viable gas sampling scheme to faithfully extract alveolar concentrations. In particular, using this procedure it was demonstrated by Anderson *et al* [49] that end-tidal acetone partial pressure is about 20% lower than alveolar partial pressure. However, a straightforward application of isothermal rebreathing in the framework of ergometer challenges has its inherent difficulties, since rebreathing exhalation volumes several times might not be well tolerated during workload segments. Nevertheless, efforts are underway to incorporate this system into our setup. We thereby hope to clarify whether elevated workload breath acetone concentrations observed in our measurements can partly be explained by altered ventilation–perfusion conditions or whether they are simply a result of higher exhalation flow rate and subsequently diminished mucosal absorption as suggested in [49].

Discussion

One of the fundamental equations in our present understanding of pulmonary gas exchange is the basic model due to Farhi [65], which expresses mixed alveolar gas concentration C_A of a blood-borne gas as a function of its mixed venous concentration $C_{\bar{v}}$, its blood:gas partition coefficient (i.e., dimensionless Henry's law constant), λ, and an average quotient between alveolar ventilation and capillary perfusion, the ventilation–perfusion ratio $r = \dot{V}_A/\dot{Q}_c$. Specifically, by describing the lung as one homogeneous alveolar unit with an associated end-capillary blood concentration $C_{c'}$ as well as blood inflow/outflow and gas inflow/outflow equal to $\dot{Q}_c$ and $\dot{V}_A$, respectively, conservation of matter leads to

$$V_A \frac{\mathrm{d}C_A}{\mathrm{d}t} = \dot{V}_A(C_I - C_A) + \dot{Q}_c(C_{\bar{v}} - C_{c'}),$$

where V_A is the (invariant) effective pulmonary storage volume of the gas under scrutiny, and C_I is its concentration in inspired ambient air, which will usually be close to zero in ordinary isoprene or acetone measurements. Assuming steady-state conditions, i.e., neglecting accumulation processes in the lung and requiring that $C_{c'} = \lambda C_A$, i.e., that diffusion equilibrium holds between end-capillary blood and free gas phase (which is a reasonable premise in the case of many VOCs found in exhaled breath [31, 50]), we conclude that

$$\dot{V}_A C_A = \dot{Q}_c (C_{\bar{v}} - \lambda C_A),$$

which can be rearranged to give

$$C_A = \frac{C_{\bar{v}}}{(r + \lambda)} \tag{1}$$

with the alveolar concentration C_A being accessible by exhaled breath measurements. Since left and right heart usually eject the same amount of blood, $\dot{Q}_c$ is commonly set equal to cardiac output. The fact is stressed that the above relation is only valid in the case of physiologically inert gases, but not for oxygen or carbon dioxide, where the purely physically dissolved fraction in blood is small compared to the chemically bound amount. Here $C_{c'} = \lambda C_A$ is replaced by more complicated dissociation functions [66]. Equation (1), of course, is a gross simplification of the actual gas exchange conditions within a normal lung, since it completely neglects shunts, physiological dead space and strong regional differences in ventilation–perfusion ratio attributable to gravitational forces and hydrostatic pressure differences [32]. As has been proven in [67], requiring r to be constant throughout the lung corresponds to the implicit assumption of optimal gas exchange and in the case of endogenous VOCs underestimates end-capillary concentrations calculated from alveolar levels.

Nonetheless, the previous relation is one of the pillars for investigating observed behavior of many trace gases found in exhaled breath. First, bearing in mind that during rest on average it holds that $r \sim 1$ [32, 68], we immediately see that breath concentrations of low-soluble trace gases such as isoprene ($\lambda_{\text{isoprene}} \sim 0.75$ (mol l^{-1}/mol l^{-1} = dimensionless) at body temperature [31]) are very sensitive to sudden changes in ventilation or perfusion, whereas breath concentrations of compounds with high Henry constants such as acetone ($\lambda_{\text{acetone}} \sim 200$ (mol l^{-1}/mol l^{-1} = dimensionless) at body temperature [50, 69]) tend to show a rather damped reaction to such disturbances. Moreover, it is evident that, while other factors are equal, increasing/decreasing alveolar ventilation will decrease/increase exhaled breath concentrations (due to increased/decreased dilution), whereas the relationship between breath concentration and cardiac output is monotonic and reflects dependence on supply. The reader may easily verify that these simple causalities offer a first qualitative explanation for many of the effects observed during the workload scenarios discussed above, particularly isoprene (cf [2]). However, a precise model elucidating the dynamic characteristics of breath isoprene and acetone concentrations, especially during the unsteady stages of exercise, is still lacking. This might be due to the fact that most of the simplifying modeling assumptions allowing for an efficient description of steady-state response do not necessarily remain valid in such phases.

One exception is the contribution of Karl *et al* [2] who, on the basis of the foregoing deliberations, developed a two-compartment model in order to reproduce isoprene dynamics in blood and exhaled breath. Their aim was to prove that the large variability of breath isoprene concentration is not due to exercise-induced changes in endogenous synthesis (as, for example, in the case of flow-dependent release of nitric oxide in endothelial cells [70]), but can mainly be traced back to modified gas exchange behavior. Contradicting the anatomic pulmonary structure, the lung compartment was based on serial instead of parallel arrangement of the alveolar units [32], leading to an exponential rather than rational drop between mixed venous and end-capillary blood concentrations in equation (1). However, the model response to presented ventilation–perfusion data closely resembled the determined breath concentrations. Unfortunately, this model strongly depends on markedly delayed dynamics of alveolar ventilation compared to cardiac output during exercise, which could not be observed in our measurements: cardiac output and alveolar ventilation increase almost simultaneously [59]. This discrepancy might stem from the fact that alveolar ventilation in [2] was calculated as approximate breathing frequency multiplied by a constant tidal volume, thereby neglecting potential changes in the latter variable, which are also revealed in our experiments. Nevertheless, despite the fact that the model of Karl *et al* results in a very poor approximation of breath isoprene concentration given our data, there are several indications that the drastic variation of this value observed during short-term moderate exercise indeed originates from altered gas exchange conditions rather than fluctuations in endogenous production. First, all of the possible biochemical sources of isoprene known up to date are long-term mechanisms, i.e., immediate changes in synthesis rates are not justified by these pathways [34, 71, 72]. Second, taking into account a tissue–lung transport delay of about 1 min [73, 74], mixed venous concentration can be assumed constant during the first segment of exercise [58], so possible feedback mechanisms from the body can plausibly be excluded in this period. Third, our data suggest that isoprene breath concentrations can be driven to an elevated plateau by rapidly changing from upright to supine position. This maneuver is very unlikely to induce metabolic variation but rather affects ventilation–perfusion distribution in the lungs [32].

Accepting the above hypothesis at first glance seems to limit the clinical relevance of breath isoprene, e.g., as a marker compound for therapeutic monitoring of cholesterol-related diseases, since well-defined standard (resting) conditions become a fundamental prerequisite for single-breath tests. On the other hand, we are confident that viewing the short-term response of isoprene and other low-soluble breath VOCs during workload sequences mainly as lung-induced phenomena can offer entirely novel approaches for the investigation of pulmonary functional properties. This is in line with ongoing efforts to base multiple inert gas elimination technique (MIGET [75, 76]) measurements on endogenous breath compounds rather than intravenously infused inert gases [44], thereby reducing patient load and improving practicability. Here the principal idea is to take advantage of the different solubility and hence distinct exhalation kinetics of several VOCs in order to characterize ventilation–perfusion mismatch throughout the lung, which is of paramount importance in artificial ventilation and serves as a valuable diagnostic tool in the management of patients suffering from pulmonary disorders. Another conceivable application would be (intra-operative) monitoring of cardiac output on the basis of VOC concentrations and ventilation data acquired in real time.

Conclusions

As can be deduced from simple mass balance principles describing pulmonary gas exchange, breath concentrations of blood-borne volatile compounds need to be assessed simultaneously with ventilation and perfusion in order to extract comparable and representative values for endogenous levels. Within this framework, an experimental setup efficiently combining PTR-MS measurements with data streams reflecting hemodynamic and respiratory factors was developed, enabling the real-time evaluation of exhaled breath VOC behavior in conjunction with decisive physiological drivers during rest and ergometer-induced workload schemes. Particularly, a methodology for selective breath-by-breath sampling from end-tidal exhalation segments was introduced and validated on the basis of resulting CO_2 levels. The key feature of our setup consists of a shutter mechanism separating the PTR-MS from the inhalation/exhalation mouthpiece on the basis of measured respiratory flow. Such an approach has several significant advantages over high-resolution sampling schemes continuously monitoring the entire breath cycle: a larger number of distinct mass-to-charge ratios can be measured, integration times are extended, longer inlet lines are possible and tracking of breath phases is avoided. Moreover, the control algorithm can easily be modified to realize sampling from arbitrary exhalation segments.

In our opinion, pilot studies of breath compound dynamics, e.g., during exercise have to be based on reliably measurable substances, covering prototypic physical–chemical properties. While isoprene is expected to react very sensitively to changes in ventilation–perfusion ratio due to its low solubility, acetone for analogous reasons shows a comparably stable behavior. Particularly, we were able to reconfirm the experimental findings of Senthilmohan *et al* [1] and Karl *et al* [2] and added new data which we hope will help to further clarify the kinetics of these species in the human body.

Both acetone and isoprene profiles showed good reproducibility among our moderate workload ergometer stress tests. Data favor the hypothesis that short-term effects visible in the concentration profiles of acetone can be ascribed to different exhalation patterns, while the abrupt response of isoprene at the onset of exercise appears to be caused mainly by changes in pulmonary gas exchange. Some possible clinical applications emerging from this observation have been discussed.

As with every experimental scheme, there are inherent strengths and weaknesses associated with our analysis system: manual fine tuning of PTR-MS inlet-flow settings is unavoidable for patients exhibiting breathing patterns departing too far from the norm, and further optimization is needed in order to reliably guarantee pressure stability within the drift tube. Furthermore, the current setup has a limited applicability in the quantification of highly soluble compounds exchanging in the conducting airways. On the other hand, we are confident that our methodology permits dynamics of non-polar, low-soluble VOCs such as isoprene to be reliably captured over a wide measurement range. Moreover, the suggested sampling algorithm appears general enough to be applicable in other mass spectrometric setups such as SIFT- and IMR-MS as well and hopefully contributes to current standardization efforts in real-time breath sampling.

Acknowledgments

We are indebted to the referees for numerous helpful suggestions. The research leading to these results has received funding from the European Community's Seventh Framework Programme (FP7/2007-13) under grant agreement no 217967. Julian King is a recipient of a DOC fellowship of the Austrian Academy of Sciences at the Breath Research Unit. Helin Koc gratefully acknowledges financial support by FWF project no Y330. We thank Peter Hamm and Helmut Wiesenhofer for their excellent technical support. We greatly appreciate the generous support of the Member of the Tyrolean regional government Dr Erwin Koler and the Director of the University Clinic of Innsbruck (TILAK) Mag Andreas Steiner.

References

[1] Senthilmohan S T, Milligan D B, McEwan M J, Freeman C G and Wilson P F 2000 Quantitative analysis of trace gases of breath during exercise using the new SIFT-MS technique *Redox Rep.* **5** 151–3

[2] Karl T, Prazeller P, Mayr D, Jordan A, Rieder J, Fall R and Lindinger W 2001 Human breath isoprene and its relation to blood cholesterol levels: new measurements and modeling *J. Appl. Physiol.* **91** 762–70

[3] Lindinger W, Hansel A and Jordan A 1998 On-line monitoring of volatile organic compounds at pptv levels by means of proton-transfer-reaction mass spectrometry (PTR-MS)—medical applications, food control and environmental research *Int. J. Mass Spectrom.* **173** 191–241

[4] Lindinger W, Hansel A and Jordan A 1998 Proton-transfer-reaction mass spectrometry (PTR-MS): on-line monitoring of volatile organic compunds at pptv levels *Chem. Soc. Rev.* **27** 347–54

[5] Amann A and Smith D 2005 *Breath Analysis for Clinical Diagnosis and Therapeutic Monitoring* (Singapore: World Scientific)

[6] Hansel A, Jordan A, Holzinger R, Prazeller P, Vogel W and Lindinger W 1995 Proton-transfer reaction mass-spectrometry—online trace gas-analysis at the ppb level *Int. J. Mass Spectrom. Ion Process.* **149–50** 609

[7] Ligor M *et al* 2009 Determination of volatile organic compounds appearing in exhaled breath of lung cancer patients by solid phase microextraction and gas chromatography mass spectrometry *Clin. Chem. Lab Med.* **47** 550–60

[8] Ligor T, Ligor M, Amann A, Ager C, Bachler M, Dzien A and Buszewski B 2008 The analysis of healthy volunteers' exhaled breath by the use of solid-phase microextraction and GC-MS *J. Breath Res.* **2** 046006

[9] Miekisch W and Schubert J K 2006 From highly sophisticated analytical techniques to life-saving diagnostics: technical

developments in breath analysis *Trends Anal. Chem.* **25** 665–73

[10] Phillips M *et al* 2007 Prediction of lung cancer using volatile biomarkers in breath *Cancer Biomark* **3** 95–109

[11] Phillips M *et al* 2008 Detection of lung cancer using weighted digital analysis of breath biomarkers *Clin. Chim. Acta* **393** 76–84

[12] Amann A, Poupart G, Telser S, Ledochowski M, Schmid A and Mechtcheriakov S 2004 Applications of breath gas analysis in medicine *Int. J. Mass Spectrom.* **239** 227–33

[13] Amann A, Spanel P and Smith D 2007 Breath analysis: the approach towards clinical applications *Mini Rev. Med. Chem.* **7** 115–29

[14] Miekisch W, Schubert J K, Vagts D A and Geiger K 2001 Analysis of volatile disease markers in blood *Clin. Chem.* **47** 1053–60

[15] Rieder J, Lirk P, Ebenbichler C, Gruber G, Prazeller P, Lindinger W and Amann A 2001 Analysis of volatile organic compounds: possible applications in metabolic disorders and cancer screening *Wien Klin. Wochenschr.* **113** 181–5

[16] Miekisch W, Schubert J K and Noeldge-Schomburg G F 2004 Diagnostic potential of breath analysis—focus on volatile organic compounds *Clin. Chim. Acta* **347** 25–39

[17] Birken T, Schubert J, Miekisch W and Noldge-Schomburg G 2006 A novel visually CO_2 controlled alveolar breath sampling technique *Technol. Health Care* **14** 499–506

[18] Herbig J, Titzmann T, Beauchamp J and Kohl I 2008 Buffered end-tidal (BET) sampling—a novel method for real-time breath-gas analysis *J. Breath Res.* **2** 037008

[19] Schubert J K, Spittler K H, Braun G, Geiger K and Guttmann J 2001 CO(2)-controlled sampling of alveolar gas in mechanically ventilated patients *J. Appl. Physiol.* **90** 486–92

[20] Fowler W S 1948 Lung function studies; the respiratory dead space *Am. J. Physiol.* **154** 405–16

[21] Fortin J *et al* 2006 Non-invasive beat-to-beat cardiac output monitoring by an improved method of transthoracic bioimpedance measurement *Comput. Biol. Med.* **36** 1185–203

[22] Perrino A C Jr, Lippman A, Ariyan C, O'Connor T Z and Luther M 1994 Intraoperative cardiac output monitoring: comparison of impedance cardiography and thermodilution *J. Cardiothorac. Vasc. Anesth.* **8** 24–9

[23] Clancy T V, Norman K, Reynolds R, Covington D and Maxwell J G 1991 Cardiac output measurement in critical care patients: thoracic electrical bioimpedance versus thermodilution *J. Trauma* **31** 1116–20 discussion 1120–1

[24] Christensen T B, Jensen B V, Hjerpe J and Kanstrup I L 2000 Cardiac output measured by electric bioimpedance compared with the CO_2 rebreathing technique at different exercise levels *Clin. Physiol.* **20** 101–5

[25] Baker R C 2000 *Flow Measurement Handbook: Industrial Designs, Operating Principles, Performance, and Applications* (Cambridge: Cambridge University Press)

[26] Arendacká B, Schwarz K, S S Jr, Wimmer G and Witkovský V 2008 Variability issues in determining the concentration of isoprene in human breath by PTR-MS *J. Breath Res.* **2** 037007

[27] Schwarz K *et al* 2009 Breath acetone—aspects of normal physiology related to age and gender as determined in a PTR-MS study *J. Breath Res.* **3** 027003

[28] Kushch I *et al* 2008 Breath isoprene—aspects of normal physiology related to age, gender and cholesterol profile as determined in a proton transfer reaction mass spectrometry study *Clin. Chem. Lab. Med.* **46** 1011–8

[29] Schwarz K, Filipiak W and Amann A 2009 Determining concentration patterns of volatile compounds in exhaled breath by PTR-MS *J. Breath Res.* **3** 027002

[30] Lumb A 2005 *Nunn's Applied Respiratory Physiology* (Oxford: Butterworth-Heinemann)

[31] Filser J G, Csanady G A, Denk B, Hartmann M, Kauffmann A, Kessler W, Kreuzer P E, Putz C, Shen J H and Stei P 1996 Toxicokinetics of isoprene in rodents and humans *Toxicology* **113** 278–87

[32] West J B 2005 *Respiratory Physiology. The Essentials* 7th edn (Baltimore: Lippincott Williams and Wilkins)

[33] Gelmont D, Stein R A and Mead J F 1981 Isoprene-the main hydrocarbon in human breath *Biochem. Biophys. Res. Commun.* **99** 1456–60

[34] Stone B G, Besse T J, Duane W C, Evans C D and DeMaster E G 1993 Effect of regulating cholesterol biosynthesis on breath isoprene excretion in men *Lipids* **28** 705–8

[35] Watson W P, Cottrell L, Zhang D and Golding B T 2001 Metabolism and molecular toxicology of isoprene *Chem. Biol. Interact.* **135–136** 223–8

[36] Turner C, Spanel P and Smith D 2006 A longitudinal study of breath isoprene in healthy volunteers using selected ion flow tube mass spectrometry (SIFT-MS) *Physiol. Meas.* **27** 13–22

[37] Nelson N, Lagesson V, Nosratabadi A R, Ludvigsson J and Tagesson C 1998 Exhaled isoprene and acetone in newborn infants and in children with diabetes mellitus *Pediatr. Res.* **44** 363–7

[38] Taucher J, Hansel A, Jordan A, Fall R, Futrell J H and Lindinger W 1997 Detection of isoprene in expired air from human subjects using proton-transfer-reaction mass spectrometry *Rapid Commun. Mass Spectrom.* **11** 1230–4

[39] Cailleux A, Cogny M and Allain P 1992 Blood Isoprene concentrations in humans and in some animal species *Biochem. Med. Metab. Biol.* **47** 157–60

[40] Taalman R D F M 1996 Isoprene: background and issues *Toxicology* **113** 242–6

[41] Smith D, Spanel P and Davies S 1999 Trace gases in breath of healthy volunteers when fasting and after a protein-calorie meal: a preliminary study *J. Appl. Physiol.* **87** 1584–8

[42] Lärstad M A E, Torén K, Bake B and Olin A-C 2007 Determination of ethane, pentane and isoprene in exhaled air—effects of breath-holding, flow rate and purified air *Acta Physiol.* **189** 87–98

[43] Salerno-Kennedy R and Cashman K D 2005 Potential applications of breath isoprene as a biomarker in modern medicine: a concise overview *Wien Klin. Wochenschr.* **117** 180–6

[44] Amann A, Telser S, Hofer L, Schmid A and Hinterhuber H 2005 Breath gas as a biochemical probe in sleeping individuals *Breath Analysis for Clinical Diagnosis and Therapeutic Monitoring* ed A Amann and D Smith (Singapore: World Scientific) pp 305–16

[45] Kalapos M P 1999 Possible physiological roles of acetone metabolism in humans *Med. Hypotheses* **53** 236–42

[46] Kalapos M P 2003 On the mammalian acetone metabolism: from chemistry to clinical implications *Biochim. Biophys. Acta* **1621** 122–39

[47] Turner C, Spanel P and Smith D 2006 A longitudinal study of ammonia, acetone and propanol in the exhaled breath of 30 subjects using selected ion flow tube mass spectrometry, SIFT-MS *Physiol. Meas.* **27** 321–37

[48] Crofford O B, Mallard R E, Winton R E, Rogers N L, Jackson J C and Keller U 1977 Acetone in breath and blood *Trans. Am. Clin. Climatol. Assoc.* **88** 128–39

[49] Anderson J C, Lamm W J and Hlastala M P 2006 Measuring airway exchange of endogenous acetone using a

single-exhalation breathing maneuver *J. Appl. Physiol.* **100** 880–9

[50] Mörk A K and Johanson G 2006 A human physiological model describing acetone kinetics in blood and breath during various levels of physical exercise *Toxicol. Lett.* **164** 6–15

[51] Thrall K D, Schwartz R E, Weitz K K, Soelberg J J, Foureman G L, Prah J D and Timchalk C 2003 A real-time method to evaluate the nasal deposition and clearance of acetone in the human volunteer *Inhal. Toxicol.* **15** 523–38

[52] Anderson J C, Babb A L and Hlastala M P 2003 Modeling soluble gas exchange in the airways and alveoli *Ann. Biomed. Eng.* **31** 1402–22

[53] Kundu S K, Bruzek J A, Nair R and Judilla A M 1993 Breath acetone analyzer: diagnostic tool to monitor dietary fat loss *Clin. Chem.* **39** 87–92

[54] Tassopoulos C N, Barnett D and Fraser T R 1969 Breath-acetone and blood-sugar measurements in diabetes *Lancet* **1** 1282–6

[55] Euler D E, Davé S J and Guo H 1996 Effect of cigarette smoking on pentane excretion in alveolar breath *Clin. Chem.* **42** 303–8

[56] Dahl A R, Birnbaum L S, Bond J A, Gervasi P G and Henderson R F 1987 The fate of isoprene inhaled by rats: comparison to butadiene *Toxicol. Appl. Pharmacol.* **89** 237–48

[57] Wasserman D H and Whipp B J 1983 Coupling of ventilation to pulmonary gas exchange during nonsteady-state work in men *J. Appl. Physiol.* **54** 587–93

[58] Whipp B J, Ward S A, Lamarra N, Davis J A and Wasserman K 1982 Parameters of ventilatory and gas exchange dynamics during exercise *J. Appl. Physiol.* **52** 1506–13

[59] Johnson A T 2007 *Biomechanics and Exercise Physiology: Quantitative Modeling* 2nd edn (Boca Raton, FL: Chemical Rubber Company)

[60] Grassi B, Marconi C, Meyer M, Rieu M and Cerretelli P 1997 Gas exchange and cardiovascular kinetics with different exercise protocols in heart transplant recipients *J. Appl. Physiol.* **82** 1952–62

[61] Diskin A M, Spanel P and Smith D 2003 Time variation of ammonia, acetone, isoprene and ethanol in breath: a quantitative SIFT-MS study over 30 days *Physiol. Meas.* **24** 107–19

[62] Ma W, Liu X and Pawliszyn J 2006 Analysis of human breath with micro extraction techniques and continuous monitoring of carbon dioxide concentration *Anal. Bioanal. Chem.* **385** 1398–408

[63] O'Hara M E, O'Hehir S, Green S and Mayhew C A 2008 Development of a protocol to measure volatile organic compounds in human breath: a comparison of rebreathing and on-line single exhalations using proton transfer reaction mass spectrometry *Physiol. Meas.* **29** 309–30

[64] Ohlsson J, Ralph D D, Mandelkorn M A, Babb A L and Hlastala M P 1990 Accurate measurement of blood alcohol concentration with isothermal rebreathing *J. Stud. Alcohol* **51** 6–13

[65] Farhi L E 1967 Elimination of inert gas by the lung *Respir. Physiol.* **3** 1–11

[66] Ottesen J T, Olufsen M S and Larsen J K 2004 *Applied Mathematical Models in Human Physiology* (Philadelphia, PA: SIAM)

[67] Hoppensteadt F C and Peskin C S 2002 *Modeling and Simulation in Medicine and the Life Sciences* 2nd edn (New York: Springer)

[68] Csanady G A and Filser J G 2001 The relevance of physical activity for the kinetics of inhaled gaseous substances *Arch. Toxicol.* **74** 663–72

[69] Kumagai S and Matsunaga I 2000 A lung model describing uptake of organic solvents and roles of mucosal blood flow and metabolism in the bronchioles *Inhal. Toxicol.* **12** 491–510

[70] Mohrman D E and Heller L J 2006 *Cardiovascluar Physiology* 6th edn (New York: McGraw-Hill/Lange Physiology)

[71] Kuzma J, Nemecek-Marshall M, Pollock W H and Fall R 1995 Bacteria produce the volatile hydrocarbon isoprene *Curr. Microbiol.* **30** 97–103

[72] Stein R A and Mead J F 1988 Small hydrocarbons formed by the peroxidation of squalene *Chem. Phys. Lipids* **46** 117–20

[73] Batzel J J, Kappel F, Schneditz D and Tran H T 2007 *Cardiovascular and Respiratory Systems: Modeling, Analysis and Control* (Philadelphia, PA: SIAM)

[74] Grodins F S, Buell J and Bart A J 1967 Mathematical analysis and digital simulation of the respiratory control system *J. Appl. Physiol.* **22** 260–76

[75] Wagner P D 2008 The multiple inert gas elimination technique (MIGET) *Intensive Care Med.* **34** 994–1001

[76] Wagner P D, Saltzman H A and West J B 1974 Measurement of continuous distributions of ventilation-perfusion ratios—theory *J. Appl. Physiol.* **36** 588–99

[77] Silbernagl S and Despopoulos A 1979 *Taschenatlas der Physiologie* (Stuttgart: Georg Thieme Verlag)

Chapter 6

Paper B: Dynamic profiles of volatile organic compounds in exhaled breath as determined by a coupled PTR–MS/GC–MS study

JULIAN KING ET AL.

Physiological Measurement (2010) **31**, 1169–1184

IOP PUBLISHING PHYSIOLOGICAL MEASUREMENT

Physiol. Meas. **31** (2010) 1169–1184 doi:10.1088/0967-3334/31/9/008

Dynamic profiles of volatile organic compounds in exhaled breath as determined by a coupled PTR-MS/GC-MS study

J King[1,2], P Mochalski[2,3], A Kupferthaler[1,2], K Unterkofler[2,4], H Koc[2,4], W Filipiak[1,2], S Teschl[5], H Hinterhuber[2,6] and A Amann[1,2,7]

[1] University Clinic for Anesthesia, Innsbruck Medical University, Anichstr. 35, A-6020 Innsbruck, Austria
[2] Breath Research Institute, Austrian Academy of Sciences, Dammstr. 22, A-6850 Dornbirn, Austria
[3] Institute of Nuclear Physics PAN, Radzikowskiego 152, PL 31342 Kraków, Poland
[4] Vorarlberg University of Applied Sciences, Hochschulstr. 1, A-6850 Dornbirn, Austria
[5] University of Applied Sciences Technikum Wien, Höchstädtplatz 5, A-1200 Wien, Austria
[6] Department of Psychiatry, Innsbruck Medical University, Anichstr. 35, A-6020 Innsbruck, Austria

E-mail: anton.amann@i-med.ac.at and anton.amann@oeaw.ac.at

Received 19 April 2010, accepted for publication 21 June 2010
Published 28 July 2010
Online at stacks.iop.org/PM/31/1169

Abstract

In this phenomenological study we focus on dynamic measurements of volatile organic compounds (VOCs) in exhaled breath under exercise conditions. An experimental setup efficiently combining breath-by-breath analyses using proton transfer reaction mass spectrometry (PTR-MS) with data reflecting the behaviour of major hemodynamic and respiratory parameters is presented. Furthermore, a methodology for complementing continuous VOC profiles obtained by PTR-MS with simultaneous SPME/GC-MS measurements is outlined. These investigations aim at evaluating the impact of breathing patterns, cardiac output or blood pressure on the observed breath concentration and allow for the detection and identification of several VOCs revealing characteristic rest-to-work transitions in response to variations in ventilation or perfusion. Examples of such compounds include isoprene, methyl acetate, butane, DMS and 2-pentanone. In particular, both isoprene and methyl acetate exhibit a drastic rise in concentration shortly after the onset of exercise, usually by a factor of about 3–5 within approximately 1 min of pedalling. These specific VOCs might also be interpreted as potentially sensitive indicators for fluctuations of blood or respiratory flow and can therefore be viewed as

---

[7] Author to whom any correspondence should be addressed.

0967-3334/10/091169+16$30.00 © 2010 Institute of Physics and Engineering in Medicine Printed in the UK

candidate compounds for future assessments of hemodynamics, pulmonary function and gas exchange patterns via observed VOC behaviour.

Keywords: exhaled breath analysis, volatile organic compounds (VOCs), exercise, proton transfer reaction mass spectrometry (PTR-MS), gas chromatography mass spectrometry (GC-MS), solid phase micro-extraction (SPME)

(Some figures in this article are in colour only in the electronic version)

1. Introduction

Exhaled breath contains a number of blood-borne volatile organic compounds (VOCs) with great potential for medical diagnosis and therapeutic monitoring (Miekisch *et al* 2004, Amann *et al* 2004, Amann and Smith 2005, Bajtarevic *et al* 2009). These endogenous VOCs may result from normal metabolic activity as well as from pathological disorders. Exhaled breath analysis is non-invasive, and breath may be sampled as often as it is desirable, even under challenging conditions such as during operations or at an intensive care unit (Pabst *et al* 2007). It may also provide information on infections, e.g., of the lungs or the sinuses, by detecting specific volatiles released by bacteria (Preti *et al* 2009). Therefore, breath analysis could be of great clinical value in the future, introducing valuable diagnostic indices that are complementary to those gained by using more invasive methods (Risby 2002, Schubert *et al* 2005, Amann *et al* 2007).

The concentrations of certain compounds in exhaled breath during exercise may change rapidly (Senthilmohan *et al* 2000, Karl *et al* 2001, King *et al* 2009). Real-time investigations in this context have mainly been based on direct mass spectrometric methods allowing breath-to-breath resolution, such as proton transfer reaction mass spectrometry (PTR-MS) (Lindinger *et al* 1998a, Lindinger *et al* 1998b) or selected ion flow tube mass spectrometry (SIFT-MS) (Smith and Spanel 1996, Spanel and Smith 1996). These analytical techniques permit one to detect and quantify very quick changes in breath composition and hence ensure an efficient tracking of possibly short-lived variations in the acquired concentration profiles. Efforts in the context of real-time breath measurements so far have therefore been limited to breath constituents which can be reliably measured by these devices, such as isoprene, acetone or ammonia.

Isoprene (CAS number 78-79-5) certainly holds a distinguished status, since it can be regarded as the prototype of an exhaled breath VOC exhibiting pronounced rest-to-work transitions (Karl *et al* 2001, Turner *et al* 2006, King *et al* 2009). We recently demonstrated that end-tidal isoprene abruptly increases during moderate workload ergometer challenges at 75 W, reaching a peak value within about 1 min of pedalling. This maximum can differ from the end-tidal steady state concentration at rest by a factor of up to 4 (King *et al* 2009). Since endogenous isoprene synthesis has mainly been attributed to pathways with much larger time constants (Stone *et al* 1993), we do not expect that the aforementioned rise in isoprene concentration is due to an increased production rate in the body, but rather due to changes in pulmonary function or changes in hemodynamics.

With this illustrative example in mind, we may thus expect that the sampling of exhaled breath, even under resting conditions, can strongly be influenced by specific physiological parameters (Cope *et al* 2004). Hence, the impact of breathing rate, breathing volume, cardiac output or blood pressure on the concentration dynamics of specific compounds in exhaled breath generally merits further investigation. A paradigmatic example within this framework is the small inorganic molecule nitric oxide (NO) (Kharitonov *et al* 1997, Dweik *et al* 1998, Bush 2000, Gustafsson 2005, Horvath *et al* 2003). NO arises in almost every human organ, has a short half-life and may change its concentration quickly. It is also produced in the lungs, the nasal cavity and the sinuses. In the latter it acts by its bactericidal effect (Bush 2000). The concentration in the nasal cavity and the paranasal sinuses is usually much higher than in the lungs, and actually increases in concentration within a few seconds during humming (Lundberg *et al* 2004, Maniscalco *et al* 2004). The use of NO for the therapeutic monitoring of asthma relies on the amount released in the airways. Hence, appropriate measurements of airway released NO are important for its clinical use and therefore careful sampling of breath under controlled conditions is necessary. This led to joint guidelines of the American Thoracic Society (ATS) and the European Respiratory Society (ERS) for the protocol to be used for NO measurements in exhaled breath (ATS 1999, ATS/ERS 2005). We expect that a careful choice of conditions and sampling protocol will be important not only for NO, but also for various other volatile molecular species.

Within this context, the primary motivation for the present work was to actively scan exhaled breath for trace gases showing pronounced changes in response to variations in ventilation and perfusion. While on the one hand such compounds would evidently require special attention regarding their sampling procedure, they can also be thought of as sensitive indicators for fluctuations in respiratory/hemodynamic flow. In the same spirit, they might therefore serve as candidate compounds for assessing pulmonary gas exchange patterns via observed VOC profiles. Consequently, a secondary aim was also to supplement and support continuing efforts to base multiple inert gas elimination technique (MIGET) (Wagner 2008, Wagner *et al* 1974)) on endogenous VOCs rather than exogenously administered gases, thereby circumventing invasive infusion and improving patient compliance (Anderson and Hlastala 2010). Furthermore, our measurements are intended to place previous measurements of breath isoprene and acetone in a broader context by comparing their dynamic behaviour during distinct physiological states with synchronized profiles of VOCs expected to show similar exhalation kinetics.

2. Methods

2.1. Sampling procedures

Recently, an experimental setup efficiently combining PTR-MS measurements with continuous data streams reflecting a series of hemodynamic and respiratory factors was developed in our group (King *et al* 2009). This setup serves to assess the behaviour of exhaled breath components in conjunction with decisive physiological driving forces during rest and ergometer-induced workload schemes in *real time*. While its main purpose is to monitor specific, predefined molecular species, the identification problem stated above can only be tackled with alternative analytical techniques, giving detailed information on the composition of the exhaled breath sample. Gas chromatography mass spectrometry (GC-MS) coupled with solid phase micro-extraction (SPME) as a pre-concentration method can be regarded as gold standard within this framework (Amorim and de 2007, Bajtarevic *et al* 2009, Ligor *et al* 2008, 2009, Pawliszyn 1997, Schubert *et al* 2003, 2005, Miekisch *et al* 2008). SPME/GC-MS represents a good trade-off between high resolution of individual breath components with low detection limits and rapid sampling. The main advantages of SPME are its ease of

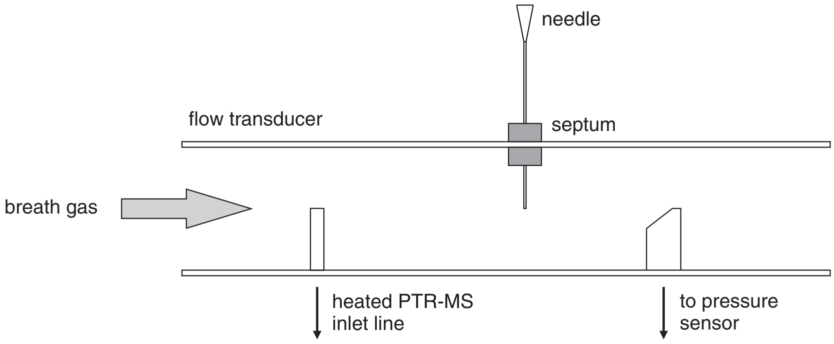

Figure 1. Sketch of the flow transducer mouthpiece from which end-tidal samples are manually extracted for subsequent SPME/GC-MS analysis.

operation and the small amounts of sample gas—usually between 10 and 20 ml—required to perform extraction. An additional benefit from the usage of SPME/GC-MS techniques is the possibility of detecting and quantifying compounds that cannot be measured by the PTR-MS (e.g. alkanes). A suitable choice of specimen storage vessels guarantees high recoveries of the target compounds and ensures reliable GC-MS analyses of breath samples taken within a relatively short period of time. In the following, a methodology for complementing continuous VOC profiles obtained by PTR-MS with simultaneous SPME/GC-MS measurements under workload conditions is developed.

A detailed description of the entire experimental setup used for acquiring hemodynamic and respiratory data in conjunction with PTR-MS variables is given elsewhere (King *et al* 2009). Here we will only discuss the parts that are relevant for the analysis of exhaled breath samples by GC-MS. The test subject freely inhales/exhales through a flow transducer mouthpiece, which is connected to a silicone head mask covering mouth and nose, see figure 1.

From the mouthpiece, gas samples are directed to the PTR-MS via a heated Teflon sampling line. Moreover, respiratory flow is obtained by means of a differential pressure sensor as explained in King *et al* (2009). Breath samples for the GC-MS analyses were taken using a 20 ml gas-tight glass syringe (Roth, Germany) equipped with a replaceable needle. For sampling purposes an additional rubber septum (Supelco, Canada) was installed in the wall of the flow transducer mouthpiece approximately 3 cm from the lips. Sampling was achieved manually by piercing the septum and drawing a volume of 18 ml during one single end-tidal exhalation segment. Care was taken to ensure that the needle tip is located at the centre of the axial mainstream. In order to avoid possible losses of hydrophilic compounds due to condensation, needle and syringe were preheated to about 60 °C shortly before the sampling procedure.

Filling of the syringe was timed according to the automatic real-time procedure for the selective sampling from specific exhalation phases as described in King *et al* (2009). Adequate algorithmic processing of measured respiratory flow allows for a reliable breath-by-breath detection of each end-tidal segment, with its start and end being marked by an acoustic signal. In order to prevent gas samples from being diluted or contaminated with (fresh) room air at the onset of the next inhalation, the entire sampling process including pressure equilibration within the syringe has to be completed within this time window. Test subjects were therefore asked to slightly prolong their exhalation to about 4 s in the respective breath cycle. Such a procedure extended the length of the end-tidal phase and turned out to be satisfactory for all test subjects. Some bias might be introduced by this protocol due to the fact that VOC breath concentrations have been demonstrated to increase with the duration of the end-tidal phase (Anderson *et al* 2003, O'Hara *et al* 2008). However, after an examination of the PTR/GC-MS overlays for acetone and isoprene associated with preliminary single expirograms, we decided that the corresponding error will only have a minor impact on quantification. In particular, since the extraction of PTR-MS gas samples is triggered by the same detection mechanism as described above, applying the aforementioned sampling protocol ensures that both probes are drawn from the same portion of exhaled breath.

Immediately after sampling the syringe content was injected into an evacuated SPME vial (20 ml in volume, Gerstel, Germany) sealed with a 1.3 mm butyl/PTFE septum (Macherey-Nagel, Germany). Since the SPME vials also served as storage containers, the type of septa was carefully selected with respect to the background and recovery of the compounds of interest. The applied material guaranteed recoveries better than 90% within the first 12 h of storage. Finally, pressure in the vial was balanced with high-purity nitrogen (of quality 6.0, i.e. with a purity of 99.9999%).

2.2. GC-MS analysis

The gas chromatographic analyses were performed using an Agilent Technologies (USA) type 7890 gas chromatograph equipped with a mass selective detector (MSD) (type 5975C, Agilent, USA). SPME was performed automatically (auto sampler MPS2, Gerstel, Germany) by inserting the SPME fibre coated with 75 μm CAR-PDMS (Supelco, Canada) into the vials and exposing the fibre to the sample for 10 min. The sample temperature during the extraction was kept at 40 °C to avoid the condensation of water vapour. Subsequently, the fibre was immediately introduced into the injector of the gas chromatograph, with thermal desorption at 290 °C in a splitless mode (1 min). The fibre was conditioned at 290 °C for 15 min prior to each analysis.

Analytes under study were separated using a PoraBond Q column (25 m × 0.32 mm, film thickness 5 μm, Varian USA) working in a constant flow mode (1.7 ml $\min^{-1}$). The column temperature program was chosen as follows: 90 °C for 7 min, increase to 140 °C at a rate of 10 °C $\min^{-1}$, constant temperature of 140 °C for 7 min, increase to 260 °C at a rate of 15 °C $\min^{-1}$ and 260 °C for 6 min. The mass spectrometer worked in a combined SCAN/SIM mode. The SCAN, with an associated range set from m/z 35 to m/z 200, was used for the identification of potential target compounds as well as for the quantification of isoprene and acetone. Additionally, major study compounds as discussed below were quantified using SIM (selective ion monitoring mode), with the corresponding m/z ratios and dwell times being presented in table 1.

Calibration graphs and standard retention times were created on the basis of analyses of calibration mixtures prepared from pure compounds. Isoprene (99.5%), methyl acetate (99.5%) and butane (15 ppm C1–C6 hydrocarbon standard) were obtained from Sigma-Aldrich (USA), dimethyl sulfide (99%) from Fluka (USA), 2-pentanone (97%) from Acros Organics (Belgium) and acetone (99.5%) was purchased from Merck (Germany). A primary gas standard was prepared in a 1 litre glass bulb (Supelco, Canada) by injecting 0.5–2 μl (depending on the target concentration) of pure compound into the evacuated bulb. Next, the bulb was heated to 80 °C for 15 min in order to ensure evaporation and subsequently balanced with high-purity nitrogen (6.0–99.9999%). The primary standard was used to prepare six calibration mixtures with concentrations ranging from 20 to 1000 ppb in the case of acetone and isoprene, and 0.1 to 20 ppb for the other species. This was accomplished by transferring

Table 1. Major study compounds together with relevant methodological data. Retention times used for confirming substance identifications based on spectral data are obtained by means of calibration mixtures. Dwell times refer to the SIM mode.

Compound	CAS number	Retention time (min)	m/z (SIM)	Dwell time (ms)	RSD (%)	LOD (ppb)
Isoprene	78-79-5	13.39	–	–	2.1	1.4
Acetone	67-64-1	10.89	–	–	2.6	2.5
DMS	75-18-3	11.54	47, 61, 62	60	5.5	0.05
Methyl acetate	79-20-9	12.28	43, 74	60	4.8	0.04
Butane	106-97-8	8.68	43	180	5.8	0.2
2-pentanone	107-87-9	22.72	86	60	3.8	0.04

0.05–1 ml of primary standard into 3 litre Tedlar bags (SKC Inc., USA) filled in advance with 1500 ml of nitrogen. Final humid calibration mixtures were created in the SPME vials. For this purpose, vials were evacuated with a membrane pump (Vacuubrand, Germany) and heated to 45 °C for 2 min. Next, an amount of 0.8 μl of distilled water—corresponding to the maximal water content in 18 ml of breath (100% relative humidity at 37 °C)—was injected. After 1 min (the time necessary for complete water evaporation), an appropriate volume of dry mixtures was introduced into the vials. During the whole process the vial temperature was maintained at 45 °C to avoid condensation.

Validation parameters were estimated using the calibration graphs. Limits of detection, defined as a signal-to-noise ratio of 3:1, are presented in table 1. The system response was found to be linear with correlation coefficients ranging from 0.996 to 0.999. The relative standard deviations (RSDs) were calculated based on consecutive analyses of five separate breath samples taken within 1 min from a single volunteer who had been resting for 15 min. Such a procedure was necessary to include the influence of manual sampling on the RSD values. The estimated RSDs are summarized in table 1.

2.3. Test subjects and protocols

A cohort of seven healthy normal volunteers (four males, 26–28 years; three females 21–28 years; two smokers) were recruited to participate in a single moderate exercise ergometer challenge consisting of an initial resting phase of 5–10 min, followed by a constant workload segment of 75 W for 15 min. The regime ends with a further resting phase of 5 min. No test subject reported any prescribed medication or drug intake. The study was approved by the Ethics Commission of Innsbruck Medical University.

The test subjects were all measured in the morning with an empty stomach. The only exception was drinking of water. Smokers were asked to refrain from smoking on the day of measurement. Volunteers were required to rest at least 15 min prior to analysis. Within this time, they were given general information regarding the experimental protocol and received some training in order to reliably provide a triggered exhalation as discussed in the previous sections. Additional instrumentation and protocols closely followed the general procedure reported in King *et al* (2009).

Regarding real-time VOC analysis, we focused on two major exhaled breath constituents: acetone and isoprene, which can be measured by PTR-MS in their protonated forms at mass-to-charge ratios 59 and 69, respectively (Arendacká *et al* 2008, Schwarz *et al* 2009b). For a series of single experiments we also included m/z 63 (tentatively dimethyl sulfide (DMS))

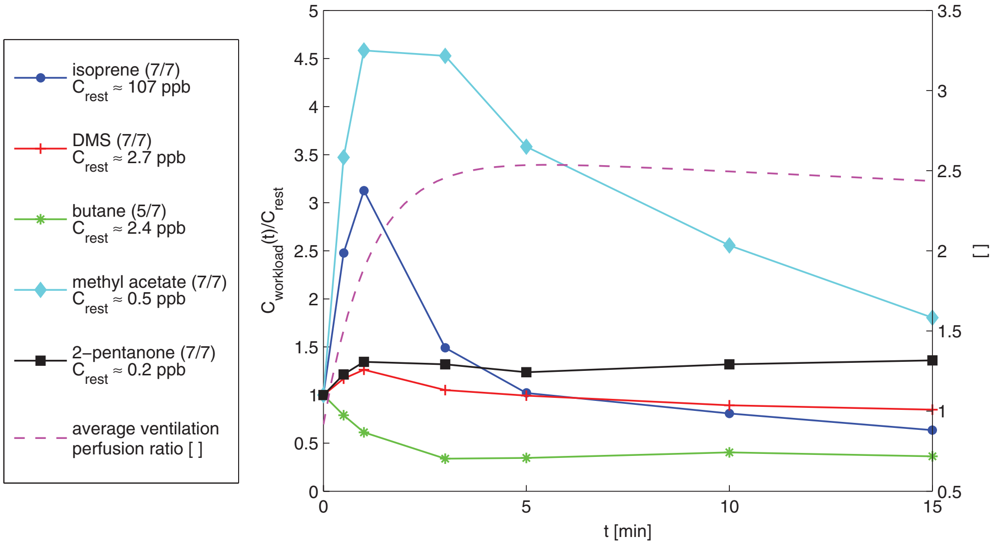

Figure 2. Average relative changes of several VOC concentrations (determined by SPME/GC-MS) during constant load exercise of 75 W as compared to their resting levels ($t = 0$). The graphs presented here correspond to the median values among all seven volunteers investigated. In particular, the concentration profiles were all normalized to the initial resting values C_{rest} prior to averaging.

as well as m/z 75 (tentatively methyl acetate). For purposes of normalization and quality control we additionally monitor m/z 21 (isotopologue of the primary hydronium ions) and m/z 37 (first monohydrate cluster). Further details on subsequent quantification are given in Schwarz *et al* (2009a). Based on our knowledge of isoprene and acetone behaviour, representative time instants for drawing the GC-MS samples were defined as follows: one sample was extracted under resting conditions as soon as the test subject had accustomed to the experimental situation and cardiac output as well as alveolar ventilation had stabilized sufficiently, i.e. about 2 min after the start of our protocol. Subsequent samples were drawn after 0.5, 1, 3, 5, 10 and 15 min had passed since the onset of exercise. Additionally, for the purpose of background correction, a room air sample was taken just before the experiment.

3. Results and discussion

On the basis of the underlying SPME-GCMS analysis method discussed before, five compounds were found to substantially increase/decrease in response to the workload sequence: isoprene, butane, methyl acetate, DMS and 2-pentanone. Quantitative effects for these compounds are summarized in figure 2 as well as in table 2.

For comparative reasons, only relative changes are presented in figure 2, i.e. all individual profiles have been normalized to the respective initial steady state value. The measured ventilation–perfusion ratio reflects the applied workload sequence starting at time zero.

Major hemodynamic and respiratory variables generally exhibit a very consistent behaviour among all test subjects (King *et al* 2009). At the onset of exercise, cardiac output rapidly increases from a mean resting value of approximately 5 l min^{-1} at rest to a constant plateau of about 12 l min^{-1} during constant workload of 75 W. Simultaneously, alveolar

Table 2. GC-MS quantification results for the seven volunteers investigated. Time instants correspond to exercise duration in minutes (with time zero referring to resting levels in end-tidal breath).

Volunteer number/time	0	0.5	1	3	5	10	15
Butane (ppb)							
1	n.d.						
2	5.94	3.93	3.61	3.43	3.45	3.42	3.7
3	n.d.						
4	6.47	8.57	7.83	2.45	1.68	2.02	1.74
5	0.6	0.45	0.4	0.13	0.23	0.29	0.36
6	1.24	0.98	0.76	0.42	0.43	0.5	0.45
7	2.43	2.73	1.43	0.52	0.6	0.79	0.71
Dimethyl sulfide (ppb)							
1	2.69	3.55	3.48	2.83	2.75	2.37	2.18
2	0.79	0.69	0.82	0.81	0.71	0.76	0.77
3	1.52	1.78	1.92	1.73	1.74	1.54	1.46
4	3.56	5.44	6.05	4.73	3.54	3.18	3.02
5	1.38	1.52	1.5	1.25	1.2	1.18	1.13
6	2.79	4.59	4.52	3.78	3.26	2.77	2.69
7	3.28	3.38	2.93	2.54	2.26	1.94	2.08
Isoprene (ppb)							
1	163	532	669	324	240	148	124
2	82	122	129	98	79	59	52
3	138	260	342	200	176	130	81
4	107	317	441	159	88	79	67
5	78	192	243	119	79	63	50
6	58	209	212	104	71	47	42
7	154	359	467	229	148	102	79
Methyl acetate (ppb)							
1	1.66	8.02	9.27	7.7	6.59	4.57	3.31
2	0.53	1.13	1.61	1.31	1.28	1.09	0.9
3	3.23	6.5	8.1	6.99	6.88	5.56	3.86
4	0.22	0.76	1.03	1.02	0.82	0.93	0.96
5	0.04	0.48	0.62	0.59	0.49	0.44	0.37
6	0.81	3.47	3.54	2.86	2.3	1.44	1.05
7	0.36	1.25	1.65	1.63	1.29	0.92	0.65
2-pentanone (ppb)							
1	0.26	0.33	0.35	0.32	0.31	0.3	0.27
2	0.19	0.18	0.21	0.18	0.19	0.18	0.19
3	0.23	0.2	0.21	0.22	0.23	0.23	0.22
4	0.21	0.25	0.28	0.3	0.26	0.29	0.31
5	0.11	0.15	0.16	0.16	0.15	0.15	0.15
6	0.25	0.34	0.34	0.33	0.31	0.33	0.34
7	0.28	0.34	0.39	0.42	0.41	0.42	0.44

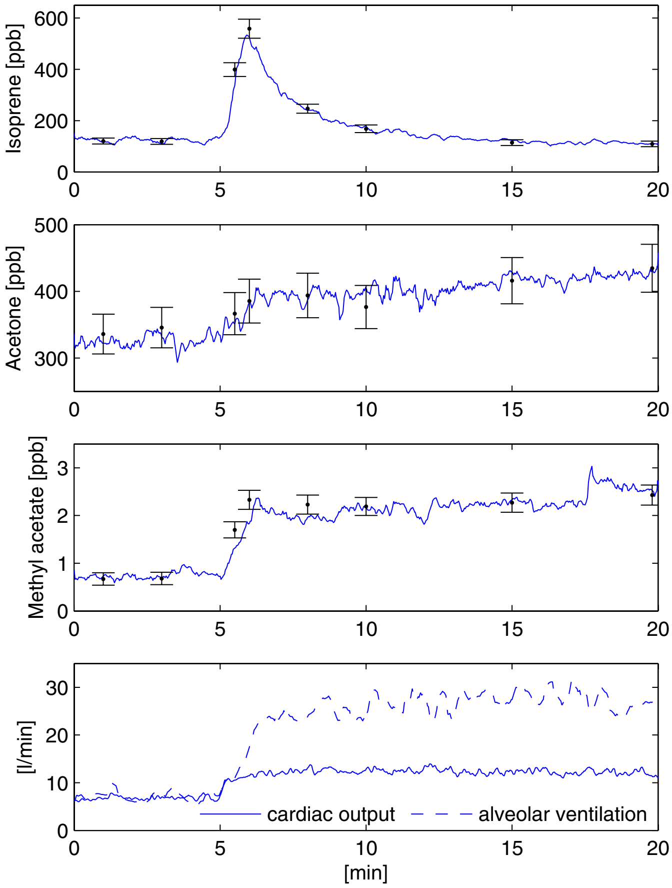

Figure 3. Simultaneous extraction of end-tidal VOC profiles by PTR-MS (continuous signal) and discrete SPME/GC-MS measurements. Error bars for the latter result from taking two times the associated RSD as given in table 1. Data refer to one single volunteer during a constant workload protocol of 75 W after an initial resting phase of 5 min.

ventilation shows a monotonic rest-to-work transition from 5–10 l min^{-1} to a steady state level of approximately 25–30 l min^{-1}, thereby increasing the average ventilation–perfusion ratio by a factor of ∼2.5, see figure 2.

Representative PTR-MS/GC-MS results for one single study subject are given in figure 3, displaying continuous end-tidal concentration profiles of isoprene, acetone and methyl acetate as determined by PTR-MS in comparison with discrete measurements obtained from our GC-MS analysis. Error bars result from taking two times the associated RSD value as given in table 1. In particular, the good agreement between both methods for isoprene and acetone can be seen as a cross-validation of phenomenological results related to both compounds which have been published previously (Karl *et al* 2001, King *et al* 2009).

For all test subjects, individual isoprene levels in breath obtained prior to the workload sequence varied within the range of 58–163 ppb, the median concentration being 107 ppb (cf, also Kushch *et al* (2008)). In accordance with earlier findings, end-tidal isoprene concentration abruptly increases by a factor of ∼3–4 within the first minute of the applied workload scenario, followed by a gradual decline back to initial (resting) levels within approximately 15 min of

Table 3. Functional similarities between isoprene and butane with respect to alveolar gas exchange.

	MW	Blood:gas partition coefficient $\lambda_{b:a}$	Octanol:water partition coefficient log (K_{ow})
Isoprene	68	0.75 (Filser *et al* 1996, Karl *et al* 2001)	2.42 (Howard and Meylan 1997)
Butane	58	0.41* (Liu *et al* 1994)	2.89 (Sangster 1997)

*refers to rat blood.

exercise. Excellent agreement between isoprene concentrations acquired by PTR-MS and GC-MS throughout all measurements reconfirms the extraction quality of our manually obtained samples. On the basis of this observation it is deduced that the quantities of additional compounds in these samples are indeed representative for the corresponding end-tidal levels. In this sense, isoprene acts as a practicable control value that can potentially be used for detecting possible error sources and losses in the manual sampling regime.

The marked rise of isoprene at the onset of exercise has mainly been attributed to its low affinity for blood (dimensionless Ostwald blood:gas partition coefficient at body temperature = 0.75 (Filser *et al* 1996)). The classical alveolar gas exchange theory due to Farhi predicts a significant influence of ventilation and perfusion on the observed exhaled breath concentration for compounds with small solubility (Farhi 1967, Farhi and Yokoyama 1967), see also King *et al* (2009) for a derivation. In view of the previously described isoprene exhalation kinetics, natural candidates for preliminary studies of VOC behaviour under workload conditions hence are substances with similar physico-chemical behaviour, e.g. the family of hydrocarbons. Within the ensemble of volunteers investigated, our main focus was on butane, as the respective alveolar gradients (i.e. the difference between end-tidal levels and background values) were generally high enough to allow for a reliable quantification. Butane appeared in the breath of five volunteers with resting levels ranging from 0.6 to 6.5 ppb (median: 2.4 ppb). Blood-borne butane is considered to originate from protein oxidation and/or bacteria production in the colon (Kharitonov and Barnes 2002, Miekisch *et al* 2004) and is particularly interesting due its functional comparability with isoprene. Indeed, the major factors anticipated to affect pulmonary gas exchange show substantial similarity, see table 3 as well as Meulenberg and Vijverberg (2000).

According to these values, by Graham's law, diffusivity (governing the passage through the tissue interfaces separating the respiratory microvasculature from the alveolar space) is expected to be roughly similar for both compounds (West 2005). Moreover, the presented affinities for blood indicate that supply and removal via the pulmonary circulation will be of comparable order.

Despite this agreement, breath concentrations of butane and isoprene exhibit an entirely different qualitative response among the ensemble of volunteers investigated: the behaviour of butane at the onset of exercise resembles the trend as predicted by the classical Farhi equation (i.e. a decrease with higher ventilation–perfusion ratios, see figure 2), whereas the behaviour of isoprene does not. Consequently, from the viewpoint of endogenous MIGET, isoprene (in contrast to butane) appears to be of limited suitability as a potential test gas. The above-mentioned visual discrepancy might be assessed in a more formal manner by employing a Wilcoxon signed rank test (Wilcoxon 1945) at each discrete time instant greater than zero. It tests the null hypothesis that the differences between the respective normalized butane and isoprene levels are drawn from a continuous, symmetric distribution with zero median. Using a 10% confidence level, this null hypothesis might be rejected at all time instants greater than zero with a maximum p-value of 0.0625.

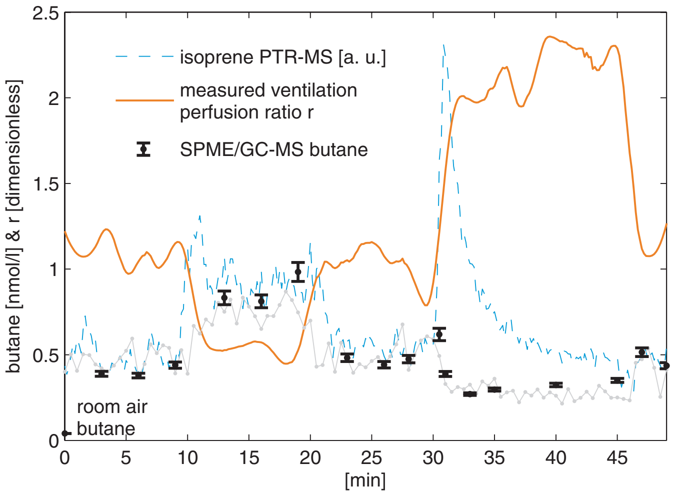

Figure 4. SPME/GC-MS profile of butane ($\lambda_{b:a} = 0.41$; 1 nmol l^{-1} approximately equals 25 ppb under ambient conditions) compared with the synchronized and scaled PTR-MS response for isoprene ($\lambda_{b:a} = 0.75$). The experimental protocol is as follows: 0–10 min rest; 10–20 min supine position; 20–30 min rest; 30–45 min exercise at 75 W; 45–49 min rest. The dotted light grey line represents an eye guide for the expected alveolar concentration of butane as predicted by the Farhi equation (postulating a constant mixed venous blood concentration of 0.7 nmol l^{-1}).

In a series of separate experiments we exclusively focused on the simultaneous dynamics of breath isoprene and butane in response to changes in ventilation and perfusion. Typical results referring to one single test subject are given in figure 4. Here, in addition to the exercise protocol discussed before, the ventilation–perfusion ratio is altered by a sudden change in body posture from semi-supine to supine position (corresponding to the time interval between 10 and 20 min).

As has already been shown in King *et al* (2009), such a manoeuvre will result in only minor changes of alveolar ventilation, while the associated rise in cardiac output (mainly due to an increase in stroke volume) can be utilized for assessing the individual contribution of pulmonary blood flow on the alveolar gas exchange process. Both isoprene and butane concentrations in end-tidal breath approach an apparently stable steady state in supine position that is about a factor of 1.5 higher compared to the resting level. This is the qualitative behaviour expected from the Farhi equation. Particularly, a markedly peak shaped response of isoprene as in the case of ergometer scenarios could not be observed.

Combining the above-mentioned findings it might thus be inferred that some isoprene-specific (release) mechanism has to be taken into account for capturing the exhalation kinetics of this important compound at the onset of physical exercise. The isoprene sources and exact stimuli for such a workload-induced process, however, remain an object of speculation. Potential candidates for instance include the working muscle compartment, which receives disproportionately high fractions of cardiac output during an ergometer challenge and moreover undergoes a rapid change in metabolic activity from which isoprene might be derived. Another alternative, which might be compared to the flow-induced release of NO in the cardiovascular system, is an increased diffusion from potential storage sites of lipophilic compounds such as the endothelial lining or muscle cells (Miekisch *et al* 2001).

A notable rise in concentration was also detected for methyl acetate. The possible endogenous origins of this ester have not yet been explored. However, it has recently been demonstrated that methyl acetate is released by human bronchial epithelial primary cells *in vitro* (Filipiak *et al* 2010). Exogenous uptake can result from its widespread use as a solvent as well as from different types of food (e.g. coffee (Lindinger *et al* 1998b)). This compound was detected in the breath of all volunteers at concentrations of 0.04–3.2 ppb prior to the workload (median: 0.5 ppb). In the case of all individuals we observed an abrupt increase in concentration, usually by a factor of about 2–5 within approximately 1 min of pedalling (see figure 3). Subsequently, either a new plateau was reached or concentrations slightly decreased with the duration of exercise.

DMS appeared in the breath of all volunteers at concentrations ranging from 0.8 to 3.6 ppb during rest (median: 2.7 ppb) and was found to increase during exercise in four cases. This rise in concentration, however, was not so pronounced like in the case of isoprene or methyl acetate and amounted to 20–60%. Despite the relatively small response to exercise, DMS remains a very interesting compound in our study. DMS is a relatively stable volatile sulphur compound present in human breath. Endogenous production has been ascribed to an incomplete metabolism of sulphur-containing amino acids, methionine and cysteine, in the transamination pathway (Miekisch *et al* 2004). DMS is formed by the enzyme thiol S-methyltransferase via the methylation of H_2S and methyl mercaptane (Tangerman 2009). This process can be considered as a detoxification mechanism, removing toxic sulphur species from the tissues. DMS is the main cause of extra-oral halitosis (Tangerman 2009, Tangerman and Winkel 2007) and elevated breath levels were observed in patients with cirrhosis, hepatitis and hypermethioninemia.

Breath concentrations of 2-pentanone during rest were spread around a median value of 0.23 ppb and tended to approach a new steady state level during constant load exercise that was 10–60% higher than the initial value prior to workload, see figure 2. This behaviour closely resembles the profile of acetone (King *et al* 2009) (see also figure 3), which is not unexpected due to the functional similarities of these two ketones. The endogenous source of 2-pentanone is still disputed. Similarly like methyl acetate, 2-pentanone could be shown to be produced by human bronchial epithelial primary cells *in vitro* (Filipiak *et al* 2010). Elevated breath levels have been associated with fasting (Statheropoulos *et al* 2006) and liver diseases (Van den Velde *et al* 2008).

The concentration profiles of compounds identified by GC-MS analysis might be reconfirmed by monitoring their expected PTR-MS signal (i.e. count rate at a mass-to-charge ratio equal to the respective molecular weight + 1). Such an approach is limited to species that are protonated in PTR-MS, i.e. which have higher proton affinities than water (166.5 kcal mol^{-1}). Representative results for methyl acetate (MW 74) are shown in figure 3. Here, PTR-MS count rates were converted to pseudo concentrations (Schwarz *et al* 2009a) and scaled to match the initial GC-MS results at the start of measurement. For correction purposes, room air levels were subtracted from the corresponding signals before conversion. Apart from methyl acetate, propionic acid and butanol appear at m/z 75 in PTR-MS measurements. The agreement between PTR-MS and GC-MS supports the view that in the framework of breath gas analysis of normal volunteers a major part of PTR-MS *signal variability* at m/z 75 can be attributed to the dynamics of methyl acetate.

4. Conclusion

In general, we believe that several valuable pieces of information can be distilled from the phenomenological study of breath VOC behaviour during distinct physiological states.

As has been indicated in the introduction, rather specific but yet very promising fields of application are pulmonary function tests based on the joint exhalation kinetics of an ensemble of pre-selected blood-borne inert gases. Within this context, a major focus lies on developing a less invasive extension of standard MIGET methodology, which aims at avoiding the exogenous infusion of test gases and replacing them with endogenous compounds originating from normal metabolic activity. The success of such an approach will primarily depend on the extent to which possible test compounds proposed for this purpose can be considered to follow the underlying Farhi description. For instance, it has recently been pointed out that highly water-soluble VOCs (including the standard MIGET test gas acetone) will not represent an adequate choice within this framework since the associated end-tidal concentrations can be expected to differ drastically from the respective alveolar levels (Anderson and Hlastala 2010). This is due to substantial interactions of such compounds with the water-like mucus layer lining the conducting airways, commonly referred to as the wash-in/wash-out effect (Anderson *et al* 2003, 2006). As a phenomenological consequence of this fact, it has been demonstrated that end-tidal exhalation dynamics of highly water-soluble compounds in response to distinct experimental conditions (e.g. exercise, hyperventilation or isothermal rebreathing) will substantially depart from the trend predicted by the Farhi equation (King *et al* 2009, O'Hara *et al* 2008). For instance, acetone concentrations in end-tidal breath tend to increase in response to increased ventilation (see, e.g., figure 3), rather than showing a roughly stable behaviour as anticipated from the classical theory by Farhi.

Analogous tests for low (blood) soluble compounds are straightforward and can be used for directly revealing deviations from the assumptions underlying MIGET methodology (see also the comparison between isoprene and butane presented above). In this sense, profiles of VOCs acquired in the course of dynamic experiments offer the possibility of actively scanning for breath constituents that qualify as (endogenous) MIGET gases as well as to assess the adequacy of potential test compounds.

In the same spirit, we stress the fact that investigations covering dynamic VOC behaviour are a general and necessary tool for gaining novel quantitative perspectives on the inherent variability of VOC concentrations stemming from (short-term) physiological changes. This knowledge is of utmost importance for everyday measurement practice in exhaled breath analysis, as slightly changing experimental conditions (regarding, e.g., body posture, breathing patterns, etc) or even pre-measurement history (stress, physical exhaustion) can have a substantial impact on the observed breath concentration (Cope *et al* 2004). It moreover will be helpful for devising appropriate sampling regimes as well as for comparing results obtained under different experimental protocols (Cope *et al* 2004, Miekisch *et al* 2008, O'Hara *et al* 2008).

Even though instruments for *real-time* breath analysis can be seen as canonical choice for the parallel assessment of physiological (e.g. hemodynamic and respiratory) factors and VOC time response, explorative measurements within this framework necessarily require a combination with GC-MS, ensuring an unambiguous identification of the detected compounds. Here, we presented a methodology for direct manual breath sampling and subsequent SPME/GC-MS analysis during free tidal breathing under dynamic conditions. Moreover, we investigated a limited list of compounds revealing interesting rest-to-work transitions in response to moderate exercise. Continuous PTR-MS isoprene profiles were used as reliable control for confirming the quality of the manually extracted samples. Further efforts will need to take into account a larger variety of trace gases as well as experimental conditions (e.g. isothermal rebreathing (Ohlsson *et al* 1990)). In this sense, we recognize that our data only reflect very preliminary results that hopefully will guide future investigations in this framework.

Acknowledgments

The research leading to these results has received funding from the European Community's Seventh Framework Programme (FP7/2007-13) under grant agreement no 217967 (www.sgl-eu.org). We greatly appreciate funding from the Austrian Federal Ministry for Transport, Innovation and Technology (BMVIT/BMWA, project 818803, KIRAS). Julian King is a recipient of a DOC fellowship of the Austrian Academy of Sciences at the Breath Research Unit. AA greatly appreciates the generous support of the Member of the Tyrolean Regional Government Dr Erwin Koler and the Director of the University Clinic of Innsbruck (TILAK) Mag. Stefan Deflorian.

References

Amann A, Poupart G, Telser S, Ledochowski M, Schmid A and Mechtcheriakov S 2004 Applications of breath gas analysis in medicine *Int. J. Mass Spectrom.* **239** 227–33

Amann A and Smith D 2005 *Breath Analysis for Clinical Diagnosis and Therapeutic Monitoring* (Singapore: World Scientific)

Amann A, Spanel P and Smith D 2007 Breath analysis: the approach towards clinical applications *Mini Rev. Med. Chem.* **7** 115–29

Amorim L C and Cardeal Z de L 2007 Breath air analysis and its use as a biomarker in biological monitoring of occupational and environmental exposure to chemical agents *J. Chromatogr. B Analyt. Technol. Biomed. Life Sci.* **853** 1–9

Anderson J C, Babb A L and Hlastala M P 2003 Modeling soluble gas exchange in the airways and alveoli *Ann. Biomed. Eng.* **31** 1402–22

Anderson J C and Hlastala M P 2010 Impact of airway gas exchange on the multiple inert gas elimination technique: theory *Ann. Biomed. Eng.* **38** 1017–30

Anderson J C, Lamm W J and Hlastala M P 2006 Measuring airway exchange of endogenous acetone using a single-exhalation breathing maneuver *J. Appl. Physiol.* **100** 880–9

Arendacká B, Schwarz K, Svorad S Jr, Wimmer G and Witkovský V 2008 Variability issues in determining the concentration of isoprene in human breath by PTR-MS *J. Breath Res.* **2** 037007

ATS 1999 Recommendations for standardized procedures for the online and offline measurement of exhaled lower respiratory nitric oxide and nasal nitric oxide in adults and children-1999. This official statement of the American Thoracic Society was adopted by the ATS Board of Directors, July 1999 *Am. J. Respir. Crit. Care Med.* **160** 2104–17

ATS/ERS 2005 ATS/ERS recommendations for standardized procedures for the online and offline measurement of exhaled lower respiratory nitric oxide and nasal nitric oxide, 2005 *Am. J. Respir. Crit. Care Med.* **171** 912–30

Bajtarevic A *et al* 2009 Noninvasive detection of lung cancer by analysis of exhaled breath *BMC Cancer* **9** 348

Bush A 2000 Primary ciliary dyskinesia *Acta Otorhinolaryngol. Belg.* **54** 317–24

Cope K A, Watson M T, Foster W M, Sehnert S S and Risby T H 2004 Effects of ventilation on the collection of exhaled breath in humans *J. Appl. Physiol.* **96** 1371–9

Dweik R A, Laskowski D, Abu-Soud H M, Kaneko F, Hutte R, Stuehr D J and Erzurum S C 1998 Nitric oxide synthesis in the lung. Regulation by oxygen through a kinetic mechanism *J. Clin. Invest.* **101** 660–6

Farhi L E 1967 Elimination of inert gas by the lung *Respir. Physiol.* **3** 1–11

Farhi L E and Yokoyama T 1967 Effects of ventilation–perfusion inequality on elimination of inert gases *Respir. Physiol.* **3** 12–20

Filipiak W, Sponring A, Filipiak A, Ager C, Schubert J, Miekisch W, Amann A and Troppmair J 2010 TD-GC-MS analysis of volatile metabolites of human lung cancer and normal cells *in vitro Cancer Epidemiol. Biomarkers Prev.* **19** 182–95

Filser J G, Csanady G A, Denk B, Hartmann M, Kauffmann A, Kessler W, Kreuzer P E, Putz C, Shen J H and Stei P 1996 Toxicokinetics of isoprene in rodents and humans *Toxicology* **113** 278–87

Gustafsson L 2005 Exhaled nitric oxide: how and why we know it is important *Breath Analysis for Clinical Diagnosis and Therapeutic Monitoring* ed A Amann and D Smith (Singapore: World Scientific)

Horvath I, Loukides S, Wodehouse T, Csiszer E, Cole P J, Kharitonov S A and Barnes P J 2003 Comparison of exhaled and nasal nitric oxide and exhaled carbon monoxide levels in bronchiectatic patients with and without primary ciliary dyskinesia *Thorax* **58** 68–72

Howard P H and Meylan W M 1997 *Handbook of Physical Properties of Organic Chemicals* (Boca Raton, FL: CRC Lewis Publishers)

Karl T, Prazeller P, Mayr D, Jordan A, Rieder J, Fall R and Lindinger W 2001 Human breath isoprene and its relation to blood cholesterol levels: new measurements and modeling *J. Appl. Physiol.* **91** 762–70

Kharitonov S, Alving K and Barnes P J 1997 Exhaled and nasal nitric oxide measurements: recommendations. The European Respiratory Society Task Force *Eur. Respir. J.* **10** 1683–93

Kharitonov S A and Barnes P J 2002 Biomarkers of some pulmonary diseases in exhaled breath *Biomarkers* **7** 1–32

King J, Kupferthaler A, Unterkofler K, Koc H, Teschl S, Teschl G, Miekisch W, Schubert J, Hinterhuber H and Amann A 2009 Isoprene and acetone concentration profiles during exercise on an ergometer *J. Breath Res.* **3** 027006

Kushch I *et al* 2008 Breath isoprene—aspects of normal physiology related to age, gender and cholesterol profile as determined in a proton transfer reaction mass spectrometry study *Clin. Chem. Lab. Med.* **46** 1011–8

Ligor M *et al* 2009 Determination of volatile organic compounds in exhaled breath of patients with lung cancer using solid phase microextraction and gas chromatography mass spectrometry *Clin. Chem. Lab. Med.* **47** 550–60

Ligor T, Ligor M, Amann A, Ager C, Bachler M, Dzien A and Buszewski B 2008 The analysis of healthy volunteers' exhaled breath by the use of solid-phase microextraction and GC-MS *J. Breath Res.* **2** 046006

Lindinger W, Hansel A and Jordan A 1998a On-line monitoring of volatile organic compounds at pptv levels by means of proton-transfer-reaction mass spectrometry (PTR-MS)—medical applications, food control and environmental research *Int. J. Mass Spectrom.* **173** 191–241

Lindinger W, Hansel A and Jordan A 1998b Proton-transfer-reaction mass spectrometry (PTR-MS): on-line monitoring of volatile organic compunds at pptv levels *Chem. Soc. Rev.* **27** 347–54

Liu J, Laster M J, Taheri S, Eger E I 2nd, Chortkoff B and Halsey M J 1994 Effect of n-alkane kinetics in rats on potency estimations and the Meyer-Overton hypothesis *Anesth. Analg.* **79** 1049–55

Lundberg J O, Weitzberg E, Cole J A and Benjamin N 2004 Nitrate, bacteria and human health *Nat. Rev. Microbiol.* **2** 593–602

Maniscalco M, Sofia M, Weitzberg E, De Laurentiis G, Stanziola A, Rossillo V and Lundberg J O 2004 Humming-induced release of nasal nitric oxide for assessment of sinus obstruction in allergic rhinitis: pilot study *Eur. J. Clin. Invest.* **34** 555–60

Meulenberg C J and Vijverberg H P 2000 Empirical relations predicting human and rat tissue:air partition coefficients of volatile organic compounds *Toxicol. Appl. Pharmacol.* **165** 206–16

Miekisch W, Kischkel S, A. S, Liebau T, Mieth M and Schubert J K 2008 Impact of sampling procedures on the results of breath analysis *J. Breath Res.* **2** 026007

Miekisch W, Schubert J K and Noeldge-Schomburg G F 2004 Diagnostic potential of breath analysis–focus on volatile organic compounds *Clin. Chim. Acta.* **347** 25–39

Miekisch W, Schubert J K, Vagts D A and Geiger K 2001 Analysis of volatile disease markers in blood *Clin. Chem.* **47** 1053–60

O'Hara M E, Clutton-Brock T H, Green S and Mayhew C A 2008 Development of a protocol to measure volatile organic compounds in breath and blood of healthy volunteers: a comparison of rebreathing and on-line single exhalations using proton transfer reaction mass spactrometry *Physiol. Meas.* **29** 309–30

Ohlsson J, Ralph D D, Mandelkorn M A, Babb A L and Hlastala M P 1990 Accurate measurement of blood alcohol concentration with isothermal rebreathing *J. Stud. Alcohol* **51** 6–13

Pabst F, Miekisch W, Fuchs P, Kischkel S and Schubert J K 2007 Monitoring of oxidative and metabolic stress during cardiac surgery by means of breath biomarkers: an observational study *J. Cardiothorac. Surg.* **2** 37

Pawliszyn J 1997 *Solid Phase Microextraction* (New York: Wiley)

Preti G, Thaler E, Hanson C W, Troy M, Eades J and Gelperin A 2009 Volatile compounds characteristic of sinus-related bacteria and infected sinus mucus: analysis by solid-phase microextraction and gas chromatography-mass spectrometry *J. Chromatogr. B Analyt. Technol. Biomed. Life Sci.* **877** 2011–8

Risby T 2002 Volatile organic compounds as markers in normal and diseased states *Disease Markers in Exhaled Breath* ed N Marczin and M Yacoub (Amsterdam: IOS Press) pp 113–24

Sangster J 1997 *Octanol-Water Partition Coefficients: Fundamentals and Physical Chemistry* (Chichester: Wiley)

Schubert J, Miekisch W and Geiger K 2003 Exhaled breath markers in ARDS *Lung Biology in Health and Disease. Disease Markers in Exhaled Breath* ed N Marczin and S Kharitonov (New York: Dekker) pp 363–80

Schubert J, Miekisch W and Nöldge-Schomburg G 2005 VOC breath markers in critically ill patients: potentials and limitations *Breath Analysis for Clinical Diagnosis and Therapeutic Monitoring* ed A Amann and D Smith (Singapore: World Scientific) pp 267–92

Schwarz K, Filipiak W and Amann A 2009a Determining concentration patterns of volatile compounds in exhaled breath by PTR-MS *J. Breath Res.* **3** 027002

Schwarz K *et al* 2009b Breath acetone—aspects of normal physiology related to age and gender as determined in a PTR-MS study *J. Breath Res.* **3** 027003

Senthilmohan S T, Milligan D B, McEwan M J, Freeman C G and Wilson P F 2000 Quantitative analysis of trace gases of breath during exercise using the new SIFT-MS technique *Redox Rep.* **5** 151–3

Smith D and Spanel P 1996 The novel selected-ion flow tube approach to trace gas analysis of air and breath *Rapid Commun. Mass Spectrom.* **10** 1183–98

Spanel P and Smith D 1996 Selected ion flow tube: a technique for quantitative trace gas analysis of air and breath *Med. Biol. Eng. Comput.* **34** 409–19

Statheropoulos M, Agapiou A and Georgiadou A 2006 Analysis of expired air of fasting male monks at Mount Athos *J. Chromatogr. B Analyt. Technol. Biomed. Life Sci.* **832** 274–9

Stone B G, Besse T J, Duane W C, Evans C D and DeMaster E G 1993 Effect of regulating cholesterol biosynthesis on breath isoprene excretion in men *Lipids* **28** 705–8

Tangerman A 2009 Measurement and biological significance of the volatile sulfur compounds hydrogen sulfide, methanethiol and dimethyl sulfide in various biological matrices *J. Chromatogr. B Analyt. Technol. Biomed Life Sci.* **877** 3366–77

Tangerman A and Winkel E G 2007 Intra- and extra-oral halitosis: finding of a new form of extra-oral blood-borne halitosis caused by dimethyl sulphide *J. Clin. Periodontol.* **34** 748–55

Turner C, Spanel P and Smith D 2006 A longitudinal study of breath isoprene in healthy volunteers using selected ion flow tube mass spectrometry (SIFT-MS) *Physiol. Meas.* **27** 13–22

Van Den Velde S, Nevens F, Van hee P, van Steenberghe D and Quirynen M 2008 GC-MS analysis of breath odor compounds in liver patients *J. Chromatogr. B Analyt. Technol. Biomed. Life Sci.* **875** 344–8

Wagner P D 2008 The multiple inert gas elimination technique (MIGET) *Intensive Care Med.* **34** 994–1001

Wagner P D, Saltzman H A and West J B 1974 Measurement of continuous distributions of ventilation–perfusion ratios—theory *J. Appl. Physiol.* **36** 588–99

West J B 2005 *Respiratory Physiology. The Essentials* (Baltimore, MD: Williams & Wilkins)

Wilcoxon F 1945 Individual comparisons by ranking methods *Biometrics Bull.* **1** 80–3

Part III

Modeling results

Chapter 7

Paper C: Physiological modeling of isoprene dynamics in exhaled breath

JULIAN KING ET AL.

Journal of Theoretical Biology (2010) **267**, 626–637

Journal of Theoretical Biology 267 (2010) 626–637

Contents lists available at ScienceDirect

Journal of Theoretical Biology

journal homepage: www.elsevier.com/locate/yjtbi

Physiological modeling of isoprene dynamics in exhaled breath

Julian King [a,b,g], Helin Koc [b,d], Karl Unterkofler [a,b], Paweł Mochalski [a,c], Alexander Kupferthaler [a], Gerald Teschl [d], Susanne Teschl [e], Hartmann Hinterhuber [f], Anton Amann [a,g,*]

[a] Breath Research Institute, Austrian Academy of Sciences, Rathausplatz 4, A-6850 Dornbirn, Austria
[b] Vorarlberg University of Applied Sciences, Hochschulstr. 1, A-6850 Dornbirn, Austria
[c] Institute of Nuclear Physics PAN, Radzikowskiego 152, PL-31342 Kraków, Poland
[d] University of Vienna, Faculty of Mathematics, Nordbergstr. 15, A-1090 Wien, Austria
[e] University of Applied Sciences Technikum Wien, Höchstädtplatz 5, A-1200 Wien, Austria
[f] Innsbruck Medical University, Department of Psychiatry, Anichstr. 35, A-6020 Innsbruck, Austria
[g] Innsbruck Medical University, Univ.-Clinic for Anesthesia, Anichstr. 35, A-6020 Innsbruck, Austria

ARTICLE INFO

Article history:
Received 6 July 2010
Received in revised form
31 August 2010
Accepted 17 September 2010
Available online 29 September 2010

Keywords:
Breath gas analysis
Isoprene
Volatile organic compounds
Modeling
Hemodynamics

ABSTRACT

Human breath contains a myriad of endogenous volatile organic compounds (VOCs) which are reflective of ongoing metabolic or physiological processes. While research into the diagnostic potential and general medical relevance of these trace gases is conducted on a considerable scale, little focus has been given so far to a sound analysis of the *quantitative* relationships between breath levels and the underlying systemic concentrations. This paper is devoted to a thorough modeling study of the *end-tidal* breath dynamics associated with isoprene, which serves as a paradigmatic example for the class of low-soluble, blood-borne VOCs.

Real-time measurements of exhaled breath under an ergometer challenge reveal characteristic changes of isoprene output in response to variations in ventilation and perfusion. Here, a valid compartmental description of these profiles is developed. By comparison with experimental data it is inferred that the major part of breath isoprene variability during exercise conditions can be attributed to an increased fractional perfusion of potential storage and production sites, leading to higher levels of *mixed* venous blood concentrations at the onset of physical activity. In this context, various lines of supportive evidence for an extrahepatic tissue source of isoprene are presented.

Our model is a first step towards new guidelines for the breath gas analysis of isoprene and is expected to aid further investigations regarding the exhalation, storage, transport and biotransformation processes associated with this important compound.

© 2010 Elsevier Ltd. All rights reserved.

1. Introduction

1.1. Breath gas analysis and modeling

Human breath contains a myriad of endogenous volatile organic compounds (VOCs), appearing in the exhalate as a result of normal metabolic activity or pathological disorders. The detection and quantification of these trace gases seems to fulfill all the demands and desires for non-invasive investigation and has been put forward as a versatile tool for medical diagnosis, biomonitoring of disease and physiological function or assessments of body burden in response to medication and environmental exposure (Amann and Smith, 2005; Amann et al., 2007, 2004; Buszewski et al., 2007; Rieder et al., 2001; Miekisch and Schubert, 2006; Pleil, 2008). With the advent of powerful new mass spectrometric techniques over the last 15 years, exhaled breath can nowadays be measured on a breath-by-breath resolution, therefore rendering breath gas analysis as an optimal choice for gaining continuous information on the metabolic and physiological state of an individual.

Within the framework sketched above, the success of using VOC breath concentration profiles for tracking endogenous processes will hinge on the availability of adequate physical descriptions for the observable exhalation kinetics of the trace gas under scrutiny. Some major breath constituents have already been investigated in this form, e.g., during exercise conditions or exposure scenarios (King et al., 2010b; Mörk and Johanson, 2006; Anderson et al., 2003; Kumagai and Matsunaga, 2000; Pleil et al., 2005). Nevertheless, VOC modeling remains a challenging task due to the multifaceted impact of physiological parameters (such as cardiac output or breathing patterns, Cope et al., 2004) as well as due to the sparse and often conflicting data regarding potential sources or sinks of such

---

* Corresponding author at: Breath Research Institute, Austrian Academy of Sciences, Rathausplatz 4, A-6850 Dornbirn, Austria. Tel.: +43 676 5608520; fax: +43 512 504 6724636.
E-mail address: anton.amann@oeaw.ac.at (A. Amann).

0022-5193/$ - see front matter © 2010 Elsevier Ltd. All rights reserved.
doi:10.1016/j.jtbi.2010.09.028

substances in the human body. This paper will be devoted to a thorough study of the *end-tidal* breath dynamics associated with isoprene, which ranks among the most notable compounds studied in the context of breath gas analysis.

1.2. Isoprene: a survey on physiologically relevant facts

Isoprene, also known as 2-methyl-1,3-butadiene (CAS number 78-79-5), is an unsaturated hydrocarbon with a molar mass of 68.11 g/mol and a boiling point of 34 °C. Isoprene is the most abundant biogenic hydrocarbon emitted by the earth's vegetation and it is also the major hydrocarbon that is endogenously produced by mammals (Gelmont et al., 1981). Its primary source in man has been attributed to the mevalonate pathway of cholesterol biosynthesis (Deneris et al., 1984). Originating from acetyl-CoA, mevalonate is transformed into dimethylallyl pyrophosphate (DMPP). Subsequently, isoprene can be derived from DMPP via an acidic decomposition demonstrated to occur in the cytosol of hepatocytes from rat liver in vitro (Deneris et al., 1984). However, whether this final non-enzymatic pathway prevails in the formation of isoprene under physiological conditions continues to be a controversial issue. As has been suggested by several authors, an enzymatic step might catalyze the conversion of DMPP to isoprene in humans (Stone et al., 1993; Miekisch et al., 2004; Taucher et al., 1997), similar to the isoprene synthase reaction seen in the chloroplasts of plants and trees (Silver and Fall, 1995). In this context, possible extrahepatic sites of isoprene production remain to be elucidated. Metabolization of isoprene in mammals primarily rests on epoxidation by cytochrome P450-dependent mono-oxygenases (Monte et al., 1985; Watson et al., 2001), whereby significant species differences can be observed (Filser et al., 1996; Csanády and Filser, 2001; Bogaards et al., 2001). In particular, bioaccumulation in man has been investigated within the framework of toxicological inhalation studies (Filser et al., 1996).

Due to its volatility and low affinity for blood (as reflected by a small blood:gas partition coefficient of $\lambda_{\mathrm{b:air}} = 0.75$ at body temperature (Filser et al., 1996; Karl et al., 2001), isoprene is highly abundant in human breath and accounts for up to 70% of total hydrocarbon removal via exhalation (Gelmont et al., 1981). Furthermore, it can relatively easily be quantified using a variety of methodologically distinct analytical techniques (Kushch et al., 2008; Ligor et al., 2008; Miekisch and Schubert, 2006; Turner et al., 2006; King et al., 2010a). Apart from being a convenient choice in terms of measurability, breath isoprene has received widespread attention in the literature due to the fact that it may serve as a sensitive, non-invasive indicator for assaying several metabolic effects in the human body (see Salerno-Kennedy and Cashman, 2005, for an extensive review).

Most notably, being a by-product of cholesterol biosynthesis as outlined above, breath isoprene has been put forward as an additional diagnostic parameter in the care of patients suffering from lipid metabolism disorders such as hypercholesterolemia. The fact that cholesterol-lowering drugs reduce isoprene output confirms the in vivo relevance of this (Stone et al., 1993; Karl et al., 2001). Moreover, interesting relationships between the mevalonate pathway and cell proliferation as well as DNA replication have been discovered (Salerno-Kennedy and Cashman, 2005; Rieder et al., 2001; Fritz, 2009; Brown and Goldstein, 1980). Further evidence points toward a strong linkage of breath isoprene levels to different physiological states, thus promoting its general use in biomonitoring, e.g., during sleep or in an intraoperative setting (Amann et al., 2005; Cailleux et al., 1993; Pabst et al., 2007). Despite this huge potential, isoprene breath tests have not yet reached the level of routine clinical methods and are still under development. This is partly due to the fact that drawing reproducible breath samples remains an intricate task that requires further standardization. Furthermore, the decisive mechanisms driving systemic and pulmonary gas exchange are still poorly understood.

Isoprene concentrations in exhaled human breath exhibit a large variability. In children and adolescents, isoprene excretion in breath appears to increase with age (Taucher et al., 1997; Smith et al., 2010) (with undetectable or very low levels in the breath of neonates, Nelson et al., 1998), until reaching a gender- and age-invariant end-tidal nominal value of about 100 ppb (approx. 4 nmol/l at standard ambient pressure and temperature) characteristic for adults under resting conditions (Kushch et al., 2008). Apart from the factors indicated in the previous paragraph, a number of additional clinical conditions and external influences have been reported to affect isoprene output, including renal dialysis (Capodicasa et al., 1999, 2007; Lirk et al., 2003), heart failure (McGrath et al., 2001), sleep/sedation (Cailleux and Allain, 1989; Amann et al., 2005) and exercise (Karl et al., 2001; King et al., 2009). However, the physiological meaning of these changes has not been established in sufficient depth.

Isoprene can be regarded as the prototype of an exhaled breath VOC exhibiting pronounced rest-to-work transitions in response to physical activity (Karl et al., 2001; King et al., 2009; Turner et al., 2006). We recently demonstrated that end-tidal isoprene abruptly increases at the onset of moderate workload ergometer challenges at 75 W, usually by a factor of about 3–4 compared with the steady state value during rest. This phase is followed by a gradual decline and the development of a new steady state after about 15 min of pedaling (King et al., 2009), see also Fig. 1. Since endogenous isoprene synthesis as discussed above has been attributed to pathways with much larger time constants, common sense suggests that the aforementioned rise in isoprene concentration is not due to an increased production rate in the body, but rather stems from

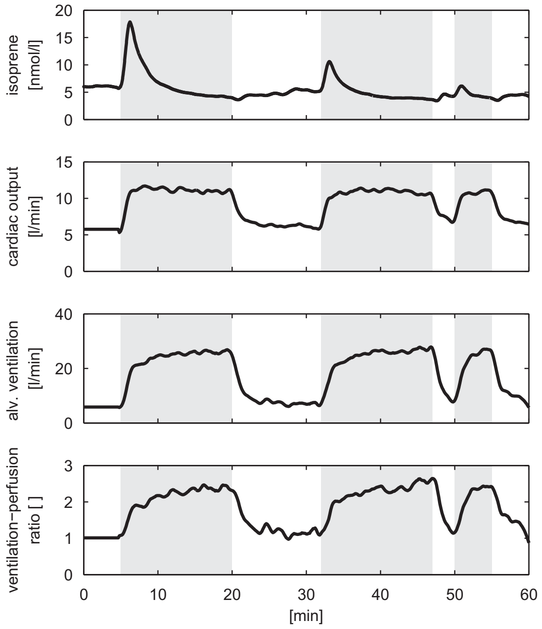

Fig. 1. Typical smoothed profiles of end-exhaled isoprene concentrations and physiological parameters in response to two-legged ergometer exercise at 75 W. Data are taken from King et al. (2009) and correspond to one *single* healthy male volunteer (26 years, 72 kg bodyweight). Workload segments are shaded in grey.

changes in hemodynamics or changes in pulmonary function. In this sense, isoprene might also be thought of as a sensitive marker for quantifying fluctuations in blood and respiratory flow.

With the background material of the previous paragraphs in mind, we view isoprene as a paradigmatic example for the analysis of low-soluble, blood-borne VOCs, even though it cannot cover the whole spectrum of different physico-chemical characteristics. The emphasis of this paper lies on examining the physiological processes underlying the above-mentioned peak shaped response of *end-tidal* isoprene at the onset of exercise by developing a mechanistic description of the observable exhalation kinetics in normal healthy volunteers. The physical model to be presented here aims at yielding further insights into the flow and distribution route of isoprene in various parts of the human body. Such a quantitative approach is imperative for assessing the relevance and predictive power of extracted breath isoprene concentrations with respect to the endogenous situation and is expected to enhance the fundamental understanding of the physiological role of isoprene in a variety of experimental scenarios.

2. Experimental basics

2.1. Setup

End-tidal isoprene concentration profiles are obtained by means of a *real-time* setup designed for synchronized measurements of exhaled breath VOCs as well as a number of respiratory and hemodynamic parameters. Our instrumentation has successfully been applied for gathering continuous data streams of these quantities during ergometer challenges as well as in a sleep laboratory setting. These investigations aim at evaluating the impact of breathing patterns, cardiac output or blood pressure on the observed breath concentration and permit a thorough study of characteristic changes in isoprene output following variations in ventilation or perfusion. We refer to King et al. (2009) for an extensive description of the technical details as well as for the various protocols under scrutiny.

In brief, the core of the mentioned setup consists of a head mask spirometer system allowing for the standardized extraction of arbitrary exhalation segments, which subsequently are directed into a Proton-Transfer-Reaction mass spectrometer (PTR-MS, Ionicon Analytik GmbH, Innsbruck, Austria) for online analysis. This analytical technique has proven to be a sensitive method for the quantification of volatile molecular species M down to the ppb (parts per billion) range by taking advantage of the proton transfer

$$H_3O^+ + M \rightarrow MH^+ + H_2O$$

from primary hydronium precursor ions (Lindinger et al., 1998a,b). Note that this "soft" chemical ionization scheme is selective to VOCs with proton affinities higher than water (166.5 kcal/mol), thereby precluding the protonation of the bulk composition exhaled air, N_2, O_2 and CO_2. Count rates of the resulting product ions MH^+ or fragments thereof appearing at specified mass-to-charge ratios m/z can subsequently be converted to absolute concentrations of the compound under scrutiny. Specifically, protonated isoprene is detected in PTR-MS at $m/z = 69$ and can be measured with breath-by-breath resolution. For further details regarding quantification and the underlying PTR-MS settings used the interested reader is referred to Schwarz et al. (2009) and King et al. (2009), respectively. From the viewpoint of quality control, isoprene time profiles obtained with the setup described above have recently been cross-validated by means of GC–MS (gas chromatography, using solid phase micro-extraction as a pre-concentration step) and manually extracted breath samples (King et al., 2010a). Table 1 summarizes the measured variables relevant for this paper. In general, breath concentrations will always refer to end-tidal levels. An underlying sampling interval of 5 s is set for each parameter.

Table 1
Summary of measured parameters together with some nominal values during rest, assuming ambient conditions; breath concentrations refer to end-tidal levels.

Variable	Symbol	Nominal value (units)
Cardiac output	$\dot{Q}_c$	6 (l/min) (Mohrman and Heller, 2006)
Alveolar ventilation	$\dot{V}_A$	5.2 (l/min) (West, 2005)
Isoprene concentration	C_{meas}	4 (nmol/l) (Kushch et al., 2008)

2.2. Recent results and heuristics

This section serves to collect some experimental evidence supporting the hypothesis of a peripheral tissue source of isoprene formation in man, derived from dynamic breath concentration measurements under exercise conditions. The rationale given here mainly builds on our earlier phenomenological studies in King et al. (2009, 2010a). Complementary experiments will be indicated where appropriate. All results are obtained in conformity with the Declaration of Helsinki and with the necessary approvals by the Ethics Commission of Innsbruck Medical University.

Investigating an ensemble of eight normal healthy volunteers, King et al. (2009) recently demonstrated that isoprene evolution in end-tidal breath exhibits a very reproducible and consistent behavior during moderate exercise scenarios. For perspective, Fig. 1 shows typical results corresponding to a bicycle ergometer challenge of one *single* volunteer under a constant workload of 75 W with several periods of rest.

Generally, starting from a steady state value of about 4 nmol/l during rest, isoprene concentrations in end-tidal air exert a pronounced peak at the onset of exercise (corresponding to an increase by a factor of up to 4). This phase is followed by a gradual decline and the development of a new steady state after approximately 15 min of pedaling. Interestingly, by repeating this regime, the peak size after intermediate exercise breaks can be demonstrated to depend on the duration of the resting phase, despite almost identical profiles of cardiac output and alveolar ventilation. Full recovery of the initial height requires about 1 h of rest. A valid model for the description of isoprene concentrations in end-tidal air should be able to faithfully reproduce this wash-out behavior.

The aforementioned peak shaped behavior of isoprene has mainly been attributed to its low blood:gas partition coefficient $\lambda_{\text{b:air}} = 0.75$. According to classical pulmonary inert gas elimination theory (cf. Appendix A), the low affinity for blood implies a high sensitivity of the associated breath concentrations with respect to changes in ventilation or perfusion. More specifically, the basic Farhi equation (A.3) predicts that, other factors being equal, increasing/decreasing the alveolar ventilation will decrease/increase exhaled breath concentrations (due to increased/decreased dilution), whereas the relationship between breath concentrations and cardiac output is monotonic and reflects dependence on supply. Using similar reasoning, Karl et al. (2001) proposed a simple quantitative description of breath isoprene concentration time courses during exercise, which is now widely accepted as "standard model". However, as has already been argued in King et al. (2009), their formulation is deficient in several regards. A principal criticism is that the model of Karl et al. essentially relies on a markedly delayed rise of alveolar ventilation with respect to pulmonary blood flow, a premise which clearly contrasts experimental evidence (see, e.g., Fig. 1 as well as Wagner, 1992; Lumb, 2005). The onset of the ventilatory response to exercise is instantaneous and may actually precede the latter (possibly being part of a learned response), so a delay as required above is highly unlikely. Consequently, when subjecting this model to real data streams including measured profiles of pulmonary blood flow $\dot{Q}_c$ and alveolar flow $\dot{V}_A$, it fails to capture the observed isoprene data, see Fig. 4.

Further insights into the decisive components affecting breath isoprene excretion can be gained by comparing its dynamic behavior with the profiles of blood-borne VOCs expected to show similar exhalation kinetics. In this context, it has recently been pointed out that breath concentrations of endogenous butane (considered to originate from protein oxidation and/or bacteria production in the colon, Kharitonov and Barnes, 2002) during ergometer exercise resemble the trend anticipated from Eq. (A.3), while isoprene exhibits an entirely different qualitative response (King et al., 2010a). This is certainly counter-intuitive, as butane is widely comparable with isoprene in terms of various functional factors expected to affect pulmonary gas exchange (including, e.g., blood and tissue solubility as well as molecular weight).

In light of this discrepancy, it can be conjectured that some unknown substance-specific (release) mechanism has to be taken into account for capturing the exhalation dynamics of isoprene. In order to restrict the number of potential tissue sources for this effect, in a series of auxiliary experiments the ergometer protocol sketched above was modified as follows. Instead of pedaling with both legs, we orchestrated several one-legged workload challenges on a standard ergometer, alternating between left and right limb for doing the exercise. The heel of the non-working leg rested on a small chair placed beside the bicycle. Special care was taken to ensure a comfortable seating position of the volunteer so that any contractive movement of the resting leg for stabilization purposes could be avoided. The hand rest of the ergometer was adjusted in such a way that the test subjects could maintain their torso in an upright position throughout the measurement period, with both arms stretched. A constant resistance of 50 W was imposed for the entire experiment and pedaling cadence was maintained at 60 rpm.

In total, five normal healthy volunteers (age 27–34 years, 4 male, 1 female) were recruited and investigated in this way. No test subject reported any prescribed medication or drug intake. No special restrictions regarding pre-experimental food intake were applied, as this variable seems to have a negligible effect on breath isoprene concentrations (Smith et al., 1999; Kinoyama et al., 2008). However, volunteers were required to rest at least 20 min prior to analysis due to the significant impact of physical activity as discussed in Section 1.2. Within this time informed consent was obtained regarding the experimental protocol. Additional instrumentation and monitoring closely followed the general procedure reported in King et al. (2009). Fig. 2 shows a representative experimental outcome for one *single* volunteer.

At the beginning, the qualitative response of end-tidal isoprene concentrations closely resembles the situation presented in Fig. 1 for the two-legged case. After 10 min of pedaling with the left leg, followed by a resting period of 4 min, a clear wash-out effect becomes discernible, yielding a significantly lower peak height when continuing the exercise with the same leg. However, if the working limb is now switched to the *right* leg (after an intermediate break of 4 min as before), an almost complete recovery of the initial peak size can be observed (cf. the time frame between 23 and 30 min in Fig. 2). On the contrary, it should be noted that the associated rise in cardiac output and alveolar ventilation is of comparable order within all three workload phases. These basic characteristics could reliably be reproduced within the entire collective of test subjects. In particular, consistent results are obtained if the leg switch is from right to left.

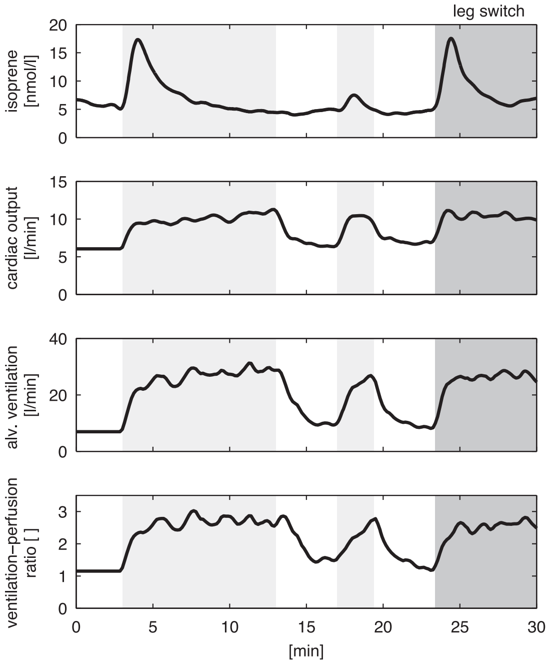

Fig. 2. Typical smoothed profiles of end-exhaled isoprene concentrations and physiological parameters in response to one-legged ergometer exercise at 50 W. Data correspond to one *single* healthy male volunteer (27 years, 75 kg bodyweight). Left and right leg exercise segments are shaded in light and dark grey, respectively.

Combining the aforementioned findings provides a clear hint that breath isoprene levels during exercise are linked to local variations of gas exchange in peripheral tissue groups. In particular, they open up a new line of supportive evidence for peripheral production sites of isoprene as indicated in Section 1.2. Furthermore, the common viewpoint that the breath isoprene peaks characteristic for exercise conditions can mainly be traced back to altered pulmonary gas exchange conditions (resulting, for instance, from an impairment of cardiac output and ventilatory drive, Karl et al., 2001) or local generation in the respiratory tree (as in the case of NO release in the paranasal sinuses during humming, Weitzberg and Lundberg, 2002) has to be rejected. As will be discussed in the modeling sections below, we attribute the observable wash-out behavior of isoprene to an increased fractional perfusion of potential storage and production sites, leading to higher levels of the *mixed* venous blood concentration at the onset of physical activity. While the exact tissue groups involved in this process remain speculative, possible origins might include the skeletal locomotor muscles themselves but also the walls of the vascular tree, both of which receive a disproportionately high share of blood flow during exercise. There are some indications in the literature that isoprene synthesis can play a role at these sites (Miekisch et al., 2001; Brown and Goldstein, 1980). However, further biochemical investigations will need to clarify whether an appropriate metabolic pattern exists in these extrahepatic tissues.

3. Isoprene modeling

3.1. Preliminaries and assumptions

For the sake of maintaining a balance between tractability and sufficient complexity of the model structure, we shall adopt the usual compartmental approach in our attempts to describe the end-tidal isoprene behavior outlined above. This approach consists in dividing the body into an ensemble of roughly homogenous tissue control volumes that are interconnected via the arterial and venous network (Reddy et al., 2005; Leung, 1991; Gerlowski and Jain, 1983; Fiserova-Bergerova, 1983). Previously developed physiologically based descriptions of isoprene pharmacokinetics in man and rodents can be found in Filser et al. (1996), NTP (1999), Melnick and Kohn (2000), Bogaards et al. (2001). These mainly centered on quantifying body burden in response to severe environmental exposure (driven by concerns about the carcinogenic potential of isoprene and/or its metabolites, Melnick et al., 1994; NTP, 1999) and hence often neglected the relatively small contribution of endogenous production to overall bioaccumulation. In contrast, here we will mainly focus on the characteristics of isoprene formation and distribution within specific body tissues under normal physiological conditions. Similarly to the models mentioned above, two major aspects of isoprene exchange will be taken into consideration.

3.1.1. Pulmonary gas exchange

Following a general premise of classical pulmonary inert gas elimination theory (see Appendix A), we postulate that uptake and removal of isoprene takes place exclusively in the alveolar region. In particular, any pre- and post-alveolar absorption and release mechanisms occurring in the conductive airways (e.g., due to interactions with the tracheo-bronchial lining fluid, Anderson et al., 2003; Anderson and Hlastala, 2007; King et al., 2010b) are assumed to be negligible, which is a reasonable requirement for low-soluble VOCs such as isoprene (Anderson et al., 2003). The lung function will be taken into account by considering one single homogenous alveolar unit characterized by an averaged ventilation–perfusion ratio close to one during resting conditions. While this approach ignores the regional ventilation–perfusion scatter throughout the lung, it constitutes a convenient simplification that is justified by the need to keep the parameterization as parsimonious as possible at this stage of the modeling phase. Delivery and elimination of isoprene within the alveolar tract will be governed by cardiac output $\dot{Q}_c$ and alveolar ventilation $\dot{V}_A$, respectively, thereby neglecting the small intrapulmonary shunt and alveolar dead space fraction (Lumb, 2005). Owing to its lipophilic characteristics and small molecular size, isoprene can be assumed to rapidly pass through the alveolar tissue barrier, so that an instantaneous diffusion equilibrium will be established between end-capillary blood and the free gas phase. This is likely to hold true also under moderate, sub-anaerobic exercise conditions (Wagner, 2008). In the absence of chemical bindings with blood it can thus be deduced that the concentration C_a of isoprene in *arterial* blood leaving the lungs is proportional to the concentration C_A within the alveoli, viz.,

$$C_a = \lambda_{b:air} C_A. \tag{1}$$

Here, $\lambda_{b:air}$ denotes the isoprene-specific blood:gas partition coefficient as introduced in Section 1.2.

3.1.2. Body compartments

The systemic part of the model incorporates two well-mixed functional units: a richly perfused tissue (rpt) compartment, lumping together tissue groups with comparable blood:tissue partition coefficient $\lambda_{b:rpt} \approx 0.4$ (viscera, brain, connective muscles, skin), as well as a peripheral tissue compartment, representing an effective buffer volume that acts as a reservoir for the storage of isoprene (tentatively skeletal muscles). Both compartments are separated into an intracellular space and an extracellular space (including the vascular blood and the interstitial space), whereby a venous equilibrium is assumed to hold at these interfaces. The relevant blood:tissue partition coefficients are summarized in Table C1. Due to the low fractional perfusion of adipose tissue, an extra fat compartment was not considered.

In order to capture the redistribution of systemic perfusion during bicycle ergometer exercise, fractional blood flow $q_{per} \in (0,1)$ to peripheral tissue is assumed to resemble fractional blood flow to both legs. The latter increases with cardiac output and will be modeled as

$$q_{per}(\dot{Q}_c) := q_{per}^{rest} + (q_{per}^{max} - q_{per}^{rest}) \times \left(1 - \exp\left(-\tau \max\left\{0, \frac{\dot{Q}_c - \dot{Q}_c^{rest}}{\dot{Q}_c^{rest}}\right\}\right)\right), \quad \tau > 0. \tag{2}$$

Reference values for the indicated variables can be found in Table C1. For perspective, in the sequel we set $q_{per}^{rest} = 0.08$ and $q_{per}^{max} = 0.7$ (which approximately corresponds to the fractional perfusion of both legs during bicycle exercise at 75 W, Sullivan et al., 1989). The constant τ will be estimated in Section 4. Alternatively, the right-hand side expression in (2) might also be replaced with a piecewise constant function taking values q_{per}^{rest} and q_{per}^{max} during rest and exercise, respectively.

As has been mentioned previously, the tissues contributing to isoprene formation are not fully established. In view of the biochemical and experimental results in Sections 1.2 and 2.2, respectively, two distinct non-negative production rates k_{pr}^{rpt} and k_{pr}^{per} are incorporated into the model. These values quantify potential hepatic and peripheral sources of endogenous isoprene, the latter being interpreted as a by-product of the biosynthesis of polyisoprenoid compounds, their degradation, or both. While isoprene production in general appears to be subject to diurnal variations (Cailleux and Allain, 1989; Amann et al., 2005), within the typical experimental time frame considered here both rates are treated as constant. Analogously, metabolization of isoprene is described by conventional first order kinetics and will be captured by introducing two rate constants k_{met}^{rpt} and k_{met}^{per}, reflecting cytochrome P450 activity in liver and extrahepatic tissues, respectively (Filser et al., 1996). Other ways of isoprene clearance such as excretion via the renal system are considered as long-term mechanisms in this context and will thus be ignored. The specific values for the production and metabolization rates introduced above will have to be estimated based on experimental results and may depend on the individual volunteer investigated. The latter case would be particularly interesting in the light of the fact that isoprene may reflect certain aspects of endogenous cholesterol synthesis.

3.2. Model equations and a priori analysis

In order to capture the gas exchange and tissue distribution mechanisms presented in the previous paragraphs, the model consists of three different compartments. A sketch of the model structure is given in Fig. 3 and will be detailed in the following. Model equations are derived by taking into account standard conservation of mass laws for the individual compartments. In view of the diffusion equilibria postulated in Section 3.1, the compartment capacities are governed by the *effective* volumes $\tilde{V}_A := V_A + V_c \lambda_{b:air}$, $\tilde{V}_{rpt} := V_{rpt} + V_{rpt,b} \lambda_{b:rpt}$ as well as $\tilde{V}_{per} := V_{per} + V_{per,b} \lambda_{b:per}$. Nominal values for the indicated parameters are given in Table C1.

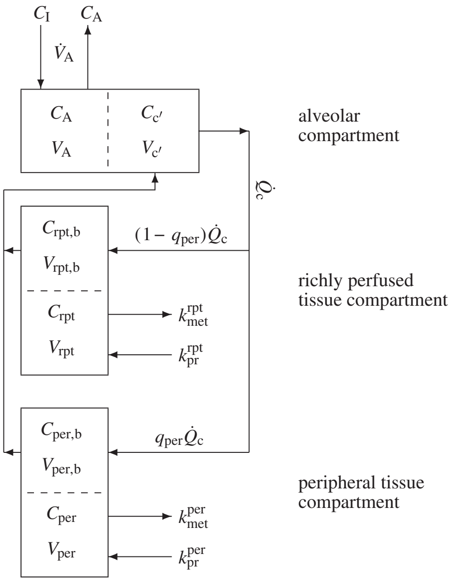

Fig. 3. Sketch of the model structure. The body is divided into three distinct functional units: alveolar/end-capillary compartment (gas exchange), richly perfused tissue (metabolism and production) and peripheral tissue (storage, metabolism and production). Dashed boundaries indicate a diffusion equilibrium. Abbreviations connote as in Table C1.

According to Fig. 3, the mass balance equation for the alveolar compartment reads

$$\tilde{V}_A \frac{dC_A}{dt} = \dot{V}_A(C_I - C_A) + \dot{Q}_c(C_{\bar{v}} - C_a), \tag{3}$$

with C_I denoting the inhaled (ambient) gas concentration, while for the richly perfused and peripheral tissue compartment we find that

$$\tilde{V}_{rpt} \frac{dC_{rpt}}{dt} = (1-q_{per})\dot{Q}_c(C_a - \lambda_{b:rpt}C_{rpt}) + k_{pr}^{rpt} - k_{met}^{rpt}\lambda_{b:rpt}C_{rpt} \tag{4}$$

and

$$\tilde{V}_{per} \frac{dC_{per}}{dt} = q_{per}\dot{Q}_c(C_a - \lambda_{b:per}C_{per}) + k_{pr}^{per} - k_{met}^{per}\lambda_{b:per}C_{per}, \tag{5}$$

respectively. Here, the associated concentrations in mixed venous and arterial blood are given by

$$C_{\bar{v}} := (1-q_{per})\lambda_{b:rpt}C_{rpt} + q_{per}\lambda_{b:per}C_{per} \tag{6}$$

and Eq. (1), respectively. Moreover, we state that the measured (end-tidal) isoprene concentration equals the alveolar level, i.e.,

$$y := C_{meas} = C_A. \tag{7}$$

Note that in Eqs. (1) and (6) it is tacitly assumed that any transport delays between tissues, heart and lung can be neglected. A more refined formulation in this regard can be achieved by considering delay differential equations, see for instance Batzel et al. (2007).

Remark 1. For later purposes, we note that a model accommodating the experimental situation during exhalation and inhalation to and from a fixed volume exposure atmosphere can simply be derived by augmenting Eqs. (3)–(5) with an additional compartment obeying

$$\tilde{V}_I \frac{dC_I}{dt} = \dot{V}_A(C_A - C_I). \tag{8}$$

This typically describes closed system (rebreathing) setups such as in Filser et al. (1996).

Some fundamental model properties are discussed in Appendix B. In particular, the components of the state variable $\mathbf{c} := (C_A, C_{rpt}, C_{per})^T$ remain non-negative, bounded and will approach a globally asymptotically stable equilibrium $\mathbf{c}^e(\mathbf{u})$ once the measurable external inputs $\mathbf{u} := (\dot{V}_A, \dot{Q}_c, C_I)$ affecting the system are fixed. This corresponds, e.g., to the situation encountered during rest or constant workload, see Fig. 1. Analogous results can be established for the augmented system incorporating Eq. (8), describing the evolution of the composite state variable $\underline{\mathbf{c}} := (C_A, C_{rpt}, C_{per}, C_I)^T$. In this case, the corresponding equilibrium for fixed inputs will be denoted by $\underline{\mathbf{c}}^e(\mathbf{u})$.

4. Model validation and estimation

4.1. Comparison with ergometer datasets

In this section we calibrate the proposed model based on the physiological data presented in Fig. 1, corresponding to one *single* representative volunteer breathing an atmosphere free of isoprene (i.e., we set $C_I \equiv 0$ in the sequel). It will turn out that the model appears to be flexible enough to capture the isoprene profiles in exhaled breath generally observed during moderate workload ergometer challenges as conducted in King et al. (2009). Moreover, our formulation provides a preliminary basis for estimating some of the unspecified parameters $p_j \in \{k_{pr}^{rpt}, k_{pr}^{per}, k_{met}^{rpt}, k_{met}^{per}, \tau, \tilde{V}_{per}\}$ from the knowledge of measured breath concentrations y. More specifically, our aim is to (at least partially) determine the *subject-dependent* parameter vector

$$\mathbf{p} = (k_{pr}^{rpt}, k_{pr}^{per}, k_{met}^{rpt}, k_{met}^{per}, \tau, \tilde{V}_{per})$$

as well as the nominal endogenous steady state levels $\mathbf{c}_0 = \mathbf{c}(t_0)$ by solving the ordinary least squares problem

$$\underset{\mathbf{p},\mathbf{c}_0}{\operatorname{argmin}} \sum_{i=0}^{n} (y_i - C_A(t_i))^2 \tag{9}$$

subject to the constraints

$$\begin{cases} \mathbf{g}(\mathbf{u}_0, \mathbf{p}, \mathbf{c}_0) = \mathbf{0} & \text{(steady state)}, \\ \mathbf{p}, \mathbf{c}_0 \geq \mathbf{0} & \text{(positivity)}, \\ \underline{\mathbf{c}}_4^e(\mathbf{u}_0, \mathbf{p}) = 25\ \text{nmol/l} & \text{(exposure steady state)}. \end{cases} \tag{10}$$

Here, $\mathbf{g}$ is the right-hand side of the ODE system (3)–(5) (see also (B.1)) and $y_i = C_{meas,i}$ is the measured end-tidal isoprene concentration at time instant t_i ($t_0 = 0$). The solution point will be denoted by $(\mathbf{p}^*, \mathbf{c}_0^*)$. For perspective, the last constraint has been introduced in order to account for additional information regarding the biotransformation of isoprene available on the basis of toxicological inhalation studies (Filser et al., 1996). As has been demonstrated there for an ensemble of four normal healthy test subjects, isoprene concentrations in a closed rebreathing chamber of fixed volume will plateau at a level of approximately 600 ppb after about 2 h of quiet tidal breathing at rest, irrespective of the initial amount of isoprene present in the system. The extracted parameters will be adjusted to automatically meet this boundary condition, thereby maintaining consistency with the aforementioned experimental findings.

For simulation purposes the measured physiological functions $\dot{V}_A$ and $\dot{Q}_c$ were converted to input function handles $\mathbf{u}$ by applying a local smoothing procedure to the associated data and interpolating the resulting profiles with splines. Tissue volumes and partition coefficients are as in Table C1. In particular, while the peripheral compartment so far has been treated as an abstract control volume without particular reference to any specific tissue group, for identifiability reasons we now set $\lambda_{\mathrm{b:per}} = 0.5$, which corresponds to the in vitro blood:tissue partition coefficient for muscle (Filser et al., 1996). Note, however, that this choice is rather arbitrary, cf. Remark 4.

The above minimization problem (9) was solved by implementing a multiple shooting routine (Bock, 1987) in *Matlab*. This iterative method can be seen as a generalization of the standard Gauss–Newton algorithm, designed to avoid divergence issues of the latter due to large residuals. For further details as well as convergence and stability properties we refer to Bock (1981) and Peifer and Timmer (2007). The necessary derivatives of the trajectories with respect to $\mathbf{p}$ and $\mathbf{c}_0$ were computed by simultaneously solving the associated variational equations (Hairer et al., 1993). Convergence was assumed to be achieved when the maximum componentwise relative change between two successive iterations was less than 0.1%. Fig. 4 summarizes the results of these calculations. Fitted parameter values and initial conditions are given in Table 2.

All estimated quantities for the test subject under scrutiny take values in a physiologically plausible range. According to Eqs. (1) and (6), arterial and mixed venous blood concentrations at the start of the experiment are estimated as $C_{\mathrm{a}}(0) = 4.5\,\mathrm{nmol/l}$ and $C_{\bar{\mathrm{v}}}(0) = 10.6\,\mathrm{nmol/l}$, respectively, which is in direct agreement with available data from the literature (cf. Table C1). Total endogenous production equals approximately 125 nmol/min, which is comparable to previous predictions ranging from 2.5 to 5.7 nmol/min/kg bodyweight (Hartmann and Kessler, 1990; Filser et al., 1996). Moreover, the estimated value for $\tilde{V}_{\mathrm{per}}$ is close to experimentally measured thigh muscle volumes (see Tothill and Stewart, 2002, for instance).

For the sake of comparison, in Fig. 4 we also show the outcome of the model by Karl et al. subjected to the time courses of $\dot{V}_{\mathrm{A}}$ and $\dot{Q}_{\mathrm{c}}$ as above (assuming the same end-tidal steady state value of 6 nmol/l at rest). As has been indicated in Section 2.2, the associated predictions result in a poor representation of the observed data.

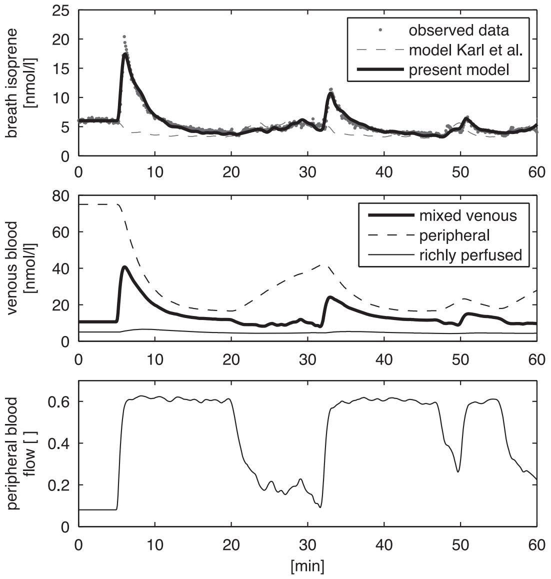

Fig. 4. First panel: simulation of end-tidal isoprene behavior during exercise conditions, cf. Fig. 1. Second panel: predicted concentrations in mixed venous blood ($C_{\bar{\mathrm{v}}}$) and venous blood returning from the peripheral ($\lambda_{\mathrm{b:per}}C_{\mathrm{per}}$) and richly perfused tissue groups ($\lambda_{\mathrm{b:rpt}}C_{\mathrm{rpt}}$). Third panel: predicted profile of fractional peripheral blood flow q_{per} according to Eq. (2).

Table 2
Decisive model parameters resulting from the fit in Fig. 4.

Variable	Symbol	Fitted value (units)	CV
Production rpt	$k_{\mathrm{pr}}^{\mathrm{rpt}}$	20.8 (nmol/min)	16
Production periphery	$k_{\mathrm{pr}}^{\mathrm{per}}$	104.5 (nmol/min)	3
Metabolism rate rpt	$k_{\mathrm{met}}^{\mathrm{rpt}}$	3.6 (l/min)	8
Metabolism rate periphery	$k_{\mathrm{met}}^{\mathrm{per}}$	0.96 (l/min)	7
Constant Eq. (2)	τ	2.1	12
Tissue volume periphery	$\tilde{V}_{\mathrm{per}}$	9.2 (l)	8
Initial concentration alveoli	$C_{\mathrm{A}}(0)$	6 (nmol/l)	3
Initial concentration rpt	$C_{\mathrm{rpt}}(0)$	12.5 (nmol/l)	6
Initial concentration periphery	$C_{\mathrm{per}}(0)$	150 (nmol/l)	5

The corresponding variation coefficients (CV, in %) were obtained by calculating bootstrap standard errors from the repeated fits of $B = 100$ resampled datasets.

The local identifiability of the extracted estimates in Table 2 was investigated by checking the non-singularity of the information matrix $Q := S^T S$, where S is the sensitivity function matrix having rows

$$S_{i,-} := \left(\frac{\partial y(t_{i-1}, \mathbf{p}^*, \mathbf{c}_0^*)}{\partial \mathbf{p}} \quad \frac{\partial y(t_{i-1}, \mathbf{p}^*, \mathbf{c}_0^*)}{\partial \mathbf{c}_0} \right). \tag{11}$$

More specifically, we adopted the standard *numerical* rank criterion

$$\operatorname{rank} Q = \max\{k;\ \sigma_k > \varepsilon \|Q\|_\infty\}, \tag{12}$$

where $\sigma_1 \geq \sigma_2 \geq \cdots \geq 0$ are the singular values of Q and $\varepsilon = 10^{-8}$ denotes the maximum relative error of the calculated sensitivities (Golub and Van Loan, 1996). Accordingly, we find that Q has full rank, suggesting that all estimated quantities are practically identifiable (Cobelli and DiStefano, 1980). However, some degree of ill-conditioning is present as can be concluded from calculating the approximate posterior correlation matrix R defined by

$$R_{i,j} := Q^{-1}_{i,j}(Q^{-1}_{i,i}Q^{-1}_{j,j})^{-1/2} \in [-1,1]. \tag{13}$$

The entry $R_{i,j}$ quantifies the degree of interplay between the ith and jth parameter (initial condition) under scrutiny.

A value of $R_{i,j}$ near $+1$ or -1 indicates that it may be difficult to estimate both parameters separately, as changes in the model output caused by perturbing one of these parameters can nearly be compensated by an appropriate perturbation of the other (Jacquez and Perry, 1990; Seber and Wild, 2003; Rodriguez-Fernandez et al., 2006). The highest correlation is achieved for the pair ($k_{\mathrm{pr}}^{\mathrm{rpt}}, k_{\mathrm{met}}^{\mathrm{rpt}}$), with an associated value of 0.995. This indicates a poor estimability of the above-mentioned two parameters if only the breath isoprene dynamics in Fig. 4 are taken into account. However, the constraints in (10) provide additional information on $k_{\mathrm{pr}}^{\mathrm{rpt}}$ and $k_{\mathrm{met}}^{\mathrm{rpt}}$ that will prove sufficient for guaranteeing the extraction of reliable estimates. Alternatively, such identifiability issues might also be circumvented by designing multi-experimental regimes guaranteeing a sufficiently large and independent influence of all parameters under scrutiny (for instance, by complementing ergometer challenges with closed chamber rebreathing protocols as indicated above). The absolute value of all other pairwise correlations is below 0.9.

A ranking of the fitted parameters and initial conditions with respect to their impact on the model output can be obtained by numerically approximating the squared L_2-norm of the *normalized* sensitivities, viz.,

$$\varsigma(p_j) := \int_{t_0}^{t_n} \left(\frac{\partial y(t,\mathbf{p}^*,\mathbf{c}_0^*)}{\partial p_j} \frac{p_j^*}{\max_s |y(s)|} \right)^2 \mathrm{d}t, \tag{14}$$

and similarly for the components of $\mathbf{c}_0$. A graphical comparison of these sensitivity indices is given in Fig. 5, revealing a strong influence of $k_{\mathrm{pr}}^{\mathrm{per}}$, $C_{\mathrm{per}}(0)$ and $\tilde{V}_{\mathrm{per}}$ on the predicted breath isoprene profile. This is intuitively reasonable as these quantities govern the shape of the observed isoprene peak during exercise.

Contrarily, only minor effects are seen when varying the (poorly determined) parameters $k_{\mathrm{pr}}^{\mathrm{rpt}}$ and $k_{\mathrm{met}}^{\mathrm{rpt}}$. In fact, it should be pointed out that production and metabolization in the richly perfused tissue group are not needed for producing a satisfactory fit of the data given in Fig. 4. However, we refrained from generally eliminating these variables as they play a major role in isoprene distribution during resting conditions (when blood flow is directed mainly to the richly perfused tissue compartment). In particular, they ensure the consistency of the model with closed chamber rebreathing scenarios as discussed before. From the ensemble of fixed model parameters, the most influential quantities (having a sensitivity index value greater than 0.25 according to Eq. (14)) are the maximum fractional perfusion to peripheral tissue ($\varsigma(q_{\mathrm{per}}^{\max}) = 0.88$), the partition coefficient between blood and peripheral tissue ($\varsigma(\lambda_{\mathrm{b:per}}) = 0.6$) and the blood:gas partition coefficient ($\varsigma(\lambda_{\mathrm{b:air}}) = 0.26$). These variables should be given special attention when applying the proposed model to a larger study population as they require a careful assessment with respect to inter-individual variations.

In order to give some insight into the information content of the extracted parameter values, approximate standard errors were constructed by employing a variant of *residual bootstrapping* (Dogan, 2007; Huet et al., 2003, Section 2.3.5). For an excellent overview of resampling techniques in general the interested reader is referred to Shao and Tu (1995), while a recent comparison between standard asymptotic theory and bootstrapping for uncertainty quantification in inverse problems can be found in Banks et al. (in press).

In particular, this method allows for taking into account autocorrelations detected among the model residuals

$$r_i := y_i - y(t_i,\mathbf{p}^*,\mathbf{c}_0^*), \quad i = 0,\ldots,n. \tag{15}$$

Such autocorrelation patterns can be seen as a general feature of dense time course, ventilation-related data streams (Liang et al., 1996) and neglecting their presence typically tends to distort variance assessments of least squares estimates derived from conventional covariance matrix approximations (Seber and Wild, 2003; Davidian and Giltinan, 1995). Adopting the general procedure suggested by Dogan (2007), we first use standard techniques from time series analysis (see, e.g., Box et al., 1994) to model the interdependence between the r_i via an autoregressive process of order two, viz.,

$$r_i = \alpha r_{i-1} + \beta r_{i-2} + \tilde{r}_i. \tag{16}$$

Plots of the resulting $\tilde{r}_i$ versus time clearly exhibit random patterns, thereby suggesting that the former can be treated as independent and homoscedastic realizations of the underlying error process. Furthermore, a Ljung–Box portmanteau test (Ljung and Box, 1978) confirmed the lack of statistically significant autocorrelations. We can hence conclude that the error terms $\tilde{r}_i$ are interchangeable.

Consequently, a single bootstrap dataset $\mathbf{y}^b := (y_0^b,\ldots,y_n^b)$ may be generated by the following procedure: we draw $n-1$ samples from a uniform discrete distribution over the set $\{\tilde{r}_i;\ i = 0,\ldots,n\}$. The results are combined to yield a vector $(\tilde{r}_2^b,\ldots,\tilde{r}_n^b)$, from which $\mathbf{y}^b$ is obtained via Eqs. (16) and (15) (we set $r_i^b := r_i$ for $i=0,1$). This resampled dataset is then plugged into the minimization procedure (9) to arrive at new estimates $(\mathbf{p}_0^{*,b},\mathbf{c}_0^{*,b})$. Repeating the above step B times generates a population of B fits for each component of $\mathbf{p}$ and $\mathbf{c}_0$, reflecting the sensitivity of these estimates with respect to the given data. Approximate standard errors might then be computed from the empirical variances associated with these populations. Here, we use $B = 100$.

The variation coefficients in Table 2 suggest that under the constraints imposed in (10) all unknown parameters and initial conditions might be determined from the individual breath concentration data in Fig. 1 with reasonable accuracy. While this confirms that inference on endogenous isoprene kinetics by virtue of exhaled breath measurements is potentially feasible, it must be emphasized that the extracted values are clearly model-dependent. In particular, additional modeling efforts investigating a more refined compartmentalization and description of perfusion patterns as in Eq. (2) will be imperative before such estimates can become practically relevant. Moreover, further experimental evidence needs to be gathered with respect to (fixed) physiological parameters that are known to drastically affect the model output. Sensitivity and identifiability methodologies as indicated above can guide these tasks (see also Brun et al., 2002; Cintrón-Arias et al., 2009; Hengl et al., 2007). In this sense, the preceding analysis should merely be seen as a preliminary proof of concept, that primarily aims at proposing a novel qualitative description of the normal physiological flow of isoprene rather than at drawing further quantitative conclusions with respect to the indicated estimates.

Moreover, we again stress the fact that the fitting procedure above has been carried out for one single representative volunteer only, inasmuch as our major goal was to demonstrate the principal explanatory power of the proposed model for capturing the presented breath isoprene behavior. The population spread of the fitted parameters within the larger study cohort investigated by King et al. (2009) might be assessed by a Bayesian (see Mörk et al., 2009, for instance) or mixed effects approach (Kuhn and Lavielle, 2005), which, however would be beyond the scope of this paper.

Remark 2. For the sake of completeness, we briefly note that a formal description of the experimental situation during the one-legged ergometer trials as in Section 2.2 can be obtained by simply augmenting the model with a copy of Eq. (5). For symmetry reasons, each of these two peripheral compartments

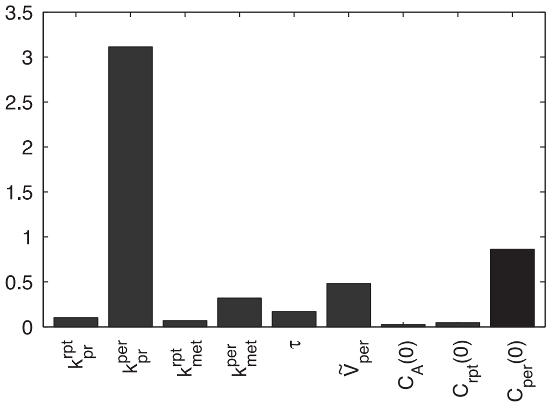

Fig. 5. Squared L_2-norm of the *normalized* model sensitivities (cf. Eq. (14)) with respect to the fitted parameters in Table 2.

(interpreted as left and right leg) might then be assigned 50% of the volume $\tilde{V}_{\text{per}}$, nominal fractional blood flow q_{per}, production $k_{\text{pr}}^{\text{per}}$ and metabolization rate $k_{\text{met}}^{\text{per}}$ as given in Tables 2 and C.1 (note that the initial steady state concentrations remain unchanged). Consequently, by alternately distributing increased fractional perfusion during the individual exercise segments to either one of these compartments, a good qualitative agreement with the data shown in Fig. 2 can be achieved.

4.2. *Physiological interpretation*

The second panel in Fig. 4 clearly reveals the physiological mechanism underlying the peak shaped dynamics of breath isoprene concentrations in response to constant load exercise. During rest, the peripheral compartment is characterized by high isoprene concentrations resulting from extrahepatic production according to $k_{\text{pr}}^{\text{per}}$. However, due to the minute fractional blood flow $q_{\text{per}}^{\text{rest}}$ to these tissues, *mixed* venous concentrations are mainly governed by the lower values in venous blood from the rpt group. As soon as fractional perfusion in the periphery increases as a result of exercise hyperemia, mixed venous concentrations become dominated by peripheral venous return. The isoprene peak visible in mixed venous blood and breath is an immediate consequence of this transition. Subsequently, a depletion of the peripheral tissue compartment and hence a decline in mixed venous blood concentration can be observed. As a matter of fact, if $\dot{V}_{\text{A}}^{\text{work}}$ and $\dot{Q}_{\text{c}}^{\text{work}}$ are maintained at a roughly fixed level reflecting some constant workload, the compartmental concentrations will approach a new steady state $\mathbf{c}^e(\mathbf{u}^{\text{work}})$, which is attained after about 15 min of pedaling, cf. Section 2.2. When the workload is stopped, perfusion will be redistributed according to the compartmental shares at rest and the peripheral isoprene buffer will be replenished. If exercise is continued before this process is completed, the corresponding isoprene peak will be lower than at the start of the first exercise segment, despite a similar response of ventilation and perfusion. This clarifies the wash-out behavior discernible in repeated workload segments. In the special situation of Fig. 4, starting from the final state at $t=20$ min (using the fitted parameter values in Table 2 and applying the physiological inputs $\mathbf{u}_0$ corresponding to resting conditions) the time required until all compartmental concentrations are within 1% of their initial level $c_{0,i}$ can be simulated as approximately 58 min. This is consistent with experimental observations (King et al., 2009).

In other words, according to the preceding rationale the major part of breath isoprene variability during ergometer challenges can be attributed to varying fractional contributions of distinct compartmental levels to the mixed venous blood concentration $C_{\bar{v}}$. The aforementioned reasoning compares favorably with the fact that peripheral venous blood concentrations (median 30 nmol/l; range 15–70 nmol/l, Cailleux et al., 1992) appear to be significantly higher than mixed venous ones (median 9 nmol/l; range 0.5–24 nmol/l, Miekisch et al., 2001). In particular, note that with the present model the observed isoprene dynamics can be explained assuming *constant* endogenous production rates, which agrees with the intuitive perception of isoprene synthesis as a slowly varying process. In this sense, the aforementioned putative mechanism optimally respects a wide spectrum of fundamental phenomenological as well as physiological boundary conditions. From a practical point of view, the intimate ties between compartmental hemodynamics and endogenous isoprene flow put forward by the previous analysis might render breath isoprene as a promising new parameter for studying vascular control and the redistribution of blood flow during exercise.

Remark 3. A word is in order regarding the necessity of introducing a hypothetical production rate $k_{\text{pr}}^{\text{per}}$ for ensuring the formation of a systemic isoprene pool. To this end, consider an arbitrary non-producing and non-metabolizing body compartment which may essentially be characterized by a mass balance equation of the form (5), with $k_{\text{pr}}^{\text{per}}$ and $k_{\text{met}}^{\text{per}}$ set to zero (the index "per" is kept merely for notational convenience). As steady state conditions can be assumed to hold during rest (see Section 2.2), the initial venous concentration $C_{\text{per}}(0)\lambda_{\text{b:per}}$ of isoprene associated with this compartment will be equal to the incoming arterial concentration $C_{\text{a}}(0)$ of the compound. Adopting the above notation we thus find that

$$C_{\text{per}}(0)\lambda_{\text{b:per}} = C_{\text{a}}(0) \leq C_{\bar{v}}(0). \tag{17}$$

The last inequality is a consequence of the algebraic steady state relation associated with the alveolar compartment (cf. Eq. (A.3), which is a standard mass balance equation for gas exchange in the lung). Hence, when switching to an increased fractional perfusion of such body compartments as a result of exercise, the *mixed* venous return will become enriched with blood having isoprene concentrations close to the previous arterial level during rest. In other words, $C_{\bar{v}}$ will fall rather than rise. Using this simple but general rationale it is clear why previous models of isoprene pharmacokinetics such as in Filser et al. (1996) fail to reproduce the peak-shaped behavior of breath isoprene during exercise, even if differential blood flow is taken into account.

Regarding further model validation, the experimental outcome associated with the one-legged ergometer regimes presented in Section 2.2 appears to furnish the fact that any quantitative formulation neglecting a peripheral release mechanism of isoprene will be an inappropriate physiological description of the prevailing isoprene dynamics during exercise. However, further biochemical and physiological studies will have to be conducted in order to pinpoint the exact origin of this effect. Apart from the line of argumentation presented above, alternative isoprene sources might comprise:

(a) an exercise-induced, time-varying production in contracting muscle (possibly due to rapid switches in cellular metabolism);
(b) a change of diffusion capacities in peripheral tissue (reflected, for instance, by an abrupt increase of $\lambda_{\text{b:per}}$, cf. Eq. (6)).

However, note that while (a) is not consistent with our current understanding of the isoprene synthetic pathway and does not provide a natural explanation for the distinct peak heights observed in repeated workload regimes, (b) appears questionable due to the fact that such a transition is likely to influence both isoprene and butane kinetics in a similar way. This contradicts experimental evidence (see the discussion in Section 2.2 and King et al., 2010a).

Remark 4. It should be mentioned that a more precise specification of the peripheral tissue compartment on the basis of estimated volumes and partition coefficients could not be achieved. For instance, choosing $\lambda_{\text{b:per}} = \frac{1}{82}$ (which is the proposed blood:tissue partition coefficient for fat, Filser et al., 1996) and setting $\tilde{V}_{\text{per}} = 0.23$ l as well as $C_{\text{per}}(0) = 6147$ nmol/l in Table 2 yields a fit of similar quality as in Fig. 4. With these modifications in mind, contrary to the previous interpretation as muscle tissue, the peripheral compartment might hence also be viewed as a small isoprene buffer volume characterized by a high lipid content (such as for instance the endothelial layer lining the vascular walls). This lack of joint estimability of $\lambda_{\text{b:per}}$ and $\tilde{V}_{\text{per}}$ within the present experimental setting is also reflected by a high degree of collinearity between the associated sensitivities $\partial y/\partial \lambda_{\mathrm{b:per}}$ and $\partial y/\partial \tilde{V}_{\mathrm{per}}$, respectively.

5. Conclusion

This paper is devoted to the development of a first mechanistic description of isoprene evolution in different tissue compartments of the human body by simulating the behavior of breath isoprene output during several short-term exercise protocols. In Section 2.2 various lines of supportive experimental evidence for an extrahepatic tissue source of isoprene have been presented. These findings have led us to a simple kinetic model that is expected to aid further investigations regarding the exhalation, storage, transport and biotransformation processes associated with this important compound.

The emphasis of this work has been laid on deriving a sound mathematical formulation flexible enough to cover a wide spectrum of possible isoprene behavior in end-tidal breath, while simultaneously maintaining consistency with earlier experimental findings as well as physiological plausibility of the involved parameters. Depending on the specific field of application, necessary model refinements might include the incorporation of a multi-compartment lung for mapping ventilation–perfusion mismatch or changes in diffusion capacity, as well as a less coarse partition of the systemic tissue groups, similar as in Filser et al. (1996) and Melnick and Kohn (2000). The statistical significance of these generalizations might then be assessed, e.g., by employing residual-based comparison techniques for nested models as described in Banks and Tran (2009), Banks and Fitzpatrick (1990). However, at the current stage of research and given the limited data on the dynamic behavior of breath isoprene throughout a broader spectrum of experimental scenarios, it is preferable to maintain a compartmentalization and parameterization as parsimonious as possible.

On-line determinations of dynamic VOC concentration profiles in exhaled breath combined with adequate kinetic modeling is a promising field of research, still in its infancy. From a methodological point of view, this work demonstrates that such dynamic patterns reflect fundamental physiological changes and can potentially be used for exploring the fate of volatile species in the human body. Generally, it should also be emphasized that a reliable quantification of relevant substance-specific characteristics of endogenous trace gases (such as production and metabolism) from breath data might yield novel diagnostic or therapeutic indicators that are complementary to those gained by employing more invasive methods. In this sense, we hope that the present contribution will help to consolidate the potential role of breath gas analysis in biomonitoring and will also stimulate future efforts to establish mathematical modeling as a core technique in VOC research.

Acknowledgements

We are indebted to the reviewers for several helpful suggestions. Julian King is a recipient of a DOC fellowship at the Breath Research Institute of the Austrian Academy of Sciences. The research leading to these results has received funding from the European Community's Seventh Framework Programme (FP7/2007-13) under Grant agreement no. 217967. We appreciate funding from the Austrian Federal Ministry for Transport, Innovation and Technology (BMVIT/BMWA, Project 818803, KIRAS). Gerald Teschl and Julian King acknowledge support from the Austrian Science Fund (FWF) under Grant no. Y330. We greatly appreciate the generous support of the government of Vorarlberg and its governor Landeshauptmann Dr. Herbert Sausgruber.

Appendix A. Classical inert gas elimination theory

Adopting the nomenclature in Table C1, the basic equation for modeling pulmonary exchange of blood-borne inert gases using one single lung compartment is a mass balance equation of the form (see, e.g., Batzel et al., 2007)

$$V_A \frac{\mathrm{d}C_A}{\mathrm{d}t} = \dot{V}_A(C_I - C_A) + \dot{Q}_c(C_{\overline{v}} - C_a), \tag{A.1}$$

where C_X denotes the trace gas concentration in a region X averaged over a period Δt, i.e.,

$$C_X(t) = 1/\Delta t \int_{t-\Delta t/2}^{t+\Delta t/2} \hat{C}_X(s)\,\mathrm{d}s. \tag{A.2}$$

From Eq. (A.1), by assuming steady state conditions $\mathrm{d}C_A/\mathrm{d}t = 0$ as well as $C_I = 0$ (i.e., no trace gas is inspired) and by substituting Henry's law $C_a = \lambda_{\mathrm{b:air}} C_A$ we derive the familiar equation due to Farhi (1967),

$$C_{\mathrm{meas}} = C_A = \frac{C_{\overline{v}}}{\lambda_{\mathrm{b:air}} + \dfrac{\dot{V}_A}{\dot{Q}_c}}. \tag{A.3}$$

Here, the quotient $\dot{V}_A/\dot{Q}_c$ is called ventilation–perfusion ratio, whereas $\lambda_{\mathrm{b:air}}$ denotes the substance-specific and temperature-dependent blood:gas partition coefficient.

Appendix B. Some fundamental model properties

Here we shall briefly recall some general properties of the proposed model that necessarily must be satisfied in any valid description of concentration dynamics. Firstly, note that Eqs. (3)–(5) can be written as a time-varying, linear inhomogeneous system

$$\dot{\mathbf{c}} = A(\mathbf{u},\mathbf{p})\mathbf{c} + \mathbf{b}(\mathbf{u},\mathbf{p}) =: \mathbf{g}(\mathbf{u},\mathbf{p},\mathbf{c}) \tag{B.1}$$

in the state variable $\mathbf{c} : = (C_{\mathrm{A}}, C_{\mathrm{rpt}}, C_{\mathrm{per}})^T$, which is dependent on a constant parameter vector $\mathbf{p}$ as well as on a vector $\mathbf{u} := (\dot{V}_{\mathrm{A}}, \dot{Q}_{\mathrm{c}}, C_{\mathrm{I}})$ lumping together all measurable external inputs.

Non-negativity of the trajectories associated with (B.1) for non-negative initial conditions easily follows from the fact that the system is cooperative. Moreover, by considering the dynamics of the total amount of isoprene $m := \sum_i \tilde{V}_i c_i \geq 0$, viz.,

$$\dot{m} = k_{\mathrm{pr}}^{\mathrm{per}} + k_{\mathrm{pr}}^{\mathrm{rpt}} - k_{\mathrm{met}}^{\mathrm{per}} \lambda_{\mathrm{b:per}} C_{\mathrm{per}} - k_{\mathrm{met}}^{\mathrm{rpt}} \lambda_{\mathrm{b:rpt}} C_{\mathrm{rpt}} + \dot{V}_{\mathrm{A}}(C_{\mathrm{I}} - C_{\mathrm{A}}), \tag{B.2}$$

it can readily be verified that the trajectories are bounded from above if either $\dot{V}_{\mathrm{A}} > 0$ or if at least one of the two metabolic rates $k_{\mathrm{met}}^{\mathrm{rpt}}$ or $k_{\mathrm{met}}^{\mathrm{per}}$ is strictly positive. Furthermore, it can be proven that under physiological steady state conditions, i.e., for constant $\mathbf{u}$, the time-invariant matrix A will be Hurwitz if

$$\det(A) = \dot{V}_{\mathrm{A}} \vartheta_1 + k_{\mathrm{met}}^{\mathrm{rpt}} \vartheta_2 + k_{\mathrm{met}}^{\mathrm{per}} \vartheta_3 + k_{\mathrm{met}}^{\mathrm{rpt}} k_{\mathrm{met}}^{\mathrm{per}} \vartheta_4 \neq 0, \quad \vartheta_i < 0,$$

cf. (King et al., 2010b, Proposition 2). Hence, except for the degenerate case $\dot{V}_{\mathrm{A}} = k_{\mathrm{met}}^{\mathrm{rpt}} = k_{\mathrm{met}}^{\mathrm{per}} = 0$ (which, as can be seen from (B.2), necessarily results in divergent trajectories if one of the two production rates is strictly positive) the compartmental concentrations can be guaranteed to approach a globally asymptotically stable equilibrium $\mathbf{c}^e(\mathbf{u}) := -A^{-1}\mathbf{b}$ once the inputs $\mathbf{u}$ affecting the system are fixed.

Appendix C. Nomenclature

See Table C1.

Table C1
Basic model parameters and reference values for normal subjects during rest.

Parameter	Symbol	Nominal value (units)
Concentrations		
Alveoli	C_A	4 (nmol/l)[a]
End-capillary	$C_{c'}$	
Arterial	C_a	5.7 (nmol/l)[b]
Mixed-venous	$C_{\overline{v}}$	9 (nmol/l)[b]
Richly perfused tissue (rpt)	C_{rpt}	
Peripheral tissue	C_{per}	
Inhaled (ambient)	C_I	0 (nmol/l)
Compartment volumes		
Alveoli	V_A	4.1 (l)[c]
End-capillary	$V_{c'}$	0.15 (l)[d]
Richly perfused (rpt)	V_{rpt}	13.25 (l)[e]
Blood rpt	$V_{rpt,b}$	1.97 (l)[e]
Peripheral tissue	V_{per}	
Blood peripheral tissue	$V_{per,b}$	
Ambient	$\tilde{V}_I$	
Fractional blood flows		
Periphery (both legs)	q_{per}	
Maximal	q_{per}^{max}	0.7[f]
Nominal (rest)	q_{per}^{rest}	0.08[g],0.14[h]
Constant Eq. (2)	τ	
Partition coefficients		
Blood:air	$\lambda_{b:air}$	0.75[i,j]
Blood:rpt	$\lambda_{b:rpt}$	0.4[j]
Blood:peripheral tissue	$\lambda_{b:per}$	0.5 (muscle)[j]; 0.012 (fat)[j]
Rate constants		
Hepatic metabolic rate	k_{met}^{rpt}	
Extrahepatic metabolic rate	k_{met}^{per}	
Production rpt	k_{pr}^{rpt}	
Production peripheral tissue	k_{pr}^{per}	

[a] Kushch et al. (2008).

[b] Mechanically ventilated patients in Miekisch et al. (2001).

[c] Mörk and Johanson (2006).

[d] Hughes and Morell (2001).

[e] Comprising viscera, brain and connective muscles according to Table 8.2 in Ottesen et al. (2004).

[f] Corresponding to 450 kpm/min or approx. 75 W according to Fig. 6 in Sullivan et al. (1989).

[g] Johnson (2007).

[h] Obtained by $q_{per}^{rest} = 2$(single leg blood flow/cardiac output) according to Table 1 in Sullivan et al. (1989).

[i] Karl et al. (2001).

[j] Filser et al. (1996).

References

Amann, A., Poupart, G., Telser, S., Ledochowski, M., Schmid, A., Mechtcheriakov, S., 2004. Applications of breath gas analysis in medicine. Int. J. Mass Spectrom. 239, 227–233.

Amann, A., Smith, D. (Eds.), 2005. Breath Analysis for Clinical Diagnosis and Therapeutic Monitoring. World Scientific, Singapore.

Amann, A., Spanel, P., Smith, D., 2007. Breath analysis: the approach towards clinical applications. Mini Rev. Med. Chem. 7, 115–129.

Amann, A., Telser, S., Hofer, L., Schmid, A., Hinterhuber, H., 2005. Breath gas as a biochemical probe in sleeping individuals. In: Amann, A., Smith, D. (Eds.), Breath Analysis for Clinical Diagnosis and Therapeutic Monitoring. World Scientific, Singapore, pp. 305–316.

Anderson, J.C., Babb, A.L., Hlastala, M.P., 2003. Modeling soluble gas exchange in the airways and alveoli. Ann. Biomed. Eng. 31, 1402–1422.

Anderson, J.C., Hlastala, M.P., 2007. Breath tests and airway gas exchange. Pulm. Pharmacol. Ther. 20, 112–117.

Banks, H.T., Fitzpatrick, B.G., 1990. Statistical methods for model comparison in parameter estimation problems for distributed systems. J. Math. Biol. 28, 501–527.

Banks, H.T., Holm, K., Robbins, D., in press. Standard error computations for uncertainty quantification in inverse problems: asymptotic theory vs. bootstrapping. Math. Comput. Modelling 52, 1610–1625.

Banks, H.T., Tran, H.T., 2009. Mathematical and Experimental Modeling of Physical and Biological Processes. CRC Press, Boca Raton.

Batzel, J.J., Kappel, F., Schneditz, D., Tran, H.T., 2007. Cardiovascular and Respiratory Systems: Modeling, Analysis, and Control. SIAM, Philadelphia.

Bock, H.G., 1981. Numerical treatment of inverse problems in chemical reaction kinetics. In: Ebert, K., Deuflhard, P., Jäger, W. (Eds.), Modelling of Chemical Reaction Systems. Springer, Heidelberg, pp. 102–125.

Bock, H.G., 1987. Randwertproblemmethoden zur Parameteridentifizierung in Systemen nichtlinearer Differentialgleichungen. Ph.D. Thesis, Universität Bonn.

Bogaards, J.J., Freidig, A.P., van Bladeren, P.J., 2001. Prediction of isoprene diepoxide levels in vivo in mouse, rat and man using enzyme kinetic data in vitro and physiologically-based pharmacokinetic modelling. Chem. Biol. Interact. 138, 247–265.

Box, G., Jenkins, G.M., Reinsel, G., 1994. Time Series Analysis: Forecasting & Control, third ed. Prentice-Hall, Englewood Cliffs.

Brown, M.S., Goldstein, J.L., 1980. Multivalent feedback regulation of HMG CoA reductase, a control mechanism coordinating isoprenoid synthesis and cell growth. J. Lipid Res. 21, 505–517.

Brun, R., Kühni, M., Siegrist, H., Gujer, W., Reichert, P., 2002. Practical identifiability of ASM2d parameters-systematic selection and tuning of parameter subsets. Water Res. 36, 4113–4127.

Buszewski, B., Kesy, M., Ligor, T., Amann, A., 2007. Human exhaled air analytics: biomarkers of diseases. Biomed. Chromatogr. 21, 553–566.

Cailleux, A., Allain, P., 1989. Isoprene and sleep. Life Sci. 44, 1877–1880.

Cailleux, A., Cogny, M., Allain, P., 1992. Blood isoprene concentrations in humans and in some animal species. Biochem. Med. Metab. Biol. 47, 157–160.

Cailleux, A., Moreau, X., Delhumeau, A., Allain, P., 1993. Decrease of isoprene concentrations in blood during general anesthesia. Biochem. Med. Metab. Biol. 49, 321–325.

Capodicasa, E., Brunori, F., Medio, G.E.D., Pelli, M.A., Vecchi, L., Buoncristiani, U., 2007. Effect of two-hour daily hemodialysis and sham dialysis on breath isoprene exhalation. Int. J. Artif. Organs 30, 583–588.

Capodicasa, E., Trovarelli, G., Medio, G.E.D., Pelli, M.A., Lippi, G., Verdura, C., Timio, M., 1999. Volatile alkanes and increased concentrations of isoprene in exhaled air during hemodialysis. Nephron 82, 331–337.

Cintrón-Arias, A., Banks, H.T., Capaldi, A., Lloyd, A.L., 2009. A sensitivity matrix based methodology for inverse problem formulation. J. Inv. Ill-Posed Probl. 17, 545–564.

Cobelli, C., DiStefano, J.J., 1980. Parameter and structural identifiability concepts and ambiguities: a critical review and analysis. Am. J. Physiol. 239, R7–R24.

Cope, K.A., Watson, M.T., Foster, W.M., Sehnert, S.S., Risby, T.H., 2004. Effects of ventilation on the collection of exhaled breath in humans. J. Appl. Physiol. 96, 1371–1379.

Csanády, G.A., Filser, J.G., 2001. Toxicokinetics of inhaled and endogenous isoprene in mice, rats, and humans. Chem. Biol. Interact. 135–136, 679–685.

Davidian, M., Giltinan, D.M., 1995. Nonlinear Models for Repeated Measurement Data. Chapman and Hall, New York.

Deneris, E.S., Stein, R.A., Mead, J.F., 1984. In vitro biosynthesis of isoprene from mevalonate utilizing a rat liver cytosolic fraction. Biochem. Biophys. Res. Commun. 123, 691–696.

Dogan, G., 2007. Bootstrapping for confidence interval estimation and hypothesis testing for parameters of system dynamics models. Syst. Dyn. Rev. 23, 415–436.

Farhi, L.E., 1967. Elimination of inert gas by the lung. Respir. Physiol. 3, 1–11.

Filser, J.G., Csanády, G.A., Denk, B., Hartmann, M., Kauffmann, A., Kessler, W., Kreuzer, P.E., Pütz, C., Shen, J.H., Stei, P., 1996. Toxicokinetics of isoprene in rodents and humans. Toxicology 113, 278–287.

Fiserova-Bergerova, V. (Ed.), 1983. Modeling of Inhalation Exposure to Vapors: Uptake, Distribution, and Elimination. CRC Press, Boca Raton.

Fritz, G., 2009. Targeting the mevalonate pathway for improved anticancer therapy. Curr. Cancer Drug Targets 9, 626–638.

Gelmont, D., Stein, R.A., Mead, J.F., 1981. Isoprene—the main hydrocarbon in human breath. Biochem. Biophys. Res. Commun. 99, 1456–1460.

Gerlowski, L.E., Jain, R.K., 1983. Physiologically based pharmacokinetic modeling: principles and applications. J. Pharm. Sci. 72, 1103–1127.

Golub, G.H., Van Loan, C.F., 1996. Matrix Computations, third ed. Johns Hopkins University Press, Baltimore.

Hairer, E., P., N.S., Wanner, G., 1993. Solving Ordinary Differential Equations (1): Nonstiff Problems, second ed. Springer, Berlin.

Hartmann, M., Kessler, W., 1990. Pharmacokinetics and endogenous production of isoprene in humans. Naunyn-Schmiedberg's Arch. Pharmacol. 341 (Suppl.), R13.

Hengl, S., Kreutz, C., Timmer, J., Maiwald, T., 2007. Data-based identifiability analysis of non-linear dynamical models. Bioinformatics 23, 2612–2618.

Huet, S., Bouvier, A., Poursat, M.-A., Jolivet, E., 2003. Statistical Tools for Nonlinear Regression. Springer, New York.

Hughes, J.M.B., Morell, N.W., 2001. Pulmonary Circulation. From Basic Mechanisms to Clinical Practice. Imperial College Press, London.

Jacquez, J.A., Perry, T., 1990. Parameter estimation: local identifiability of parameters. Am. J. Physiol. 258, E727–E736.

Johnson, A.T., 2007. Biomechanics and Exercise Physiology: Quantitative Modeling, second ed. CRC Press, Boca Raton.

Karl, T., Prazeller, P., Mayr, D., Jordan, A., Rieder, J., Fall, R., Lindinger, W., 2001. Human breath isoprene and its relation to blood cholesterol levels: new measurements and modeling. J. Appl. Physiol. 91, 762–770.

Kharitonov, S.A., Barnes, P.J., 2002. Biomarkers of some pulmonary diseases in exhaled breath. Biomarkers 7, 1–32.

King, J., Kupferthaler, A., Unterkofler, K., Koc, H., Teschl, S., Teschl, G., Miekisch, W., Schubert, J., Hinterhuber, H., Amann, A., 2009. Isoprene and acetone concentration profiles during exercise on an ergometer. J. Breath Res. 3, 027006 (16pp.). URL: 〈http://arxiv.org/abs/0907.2943〉.

King, J., Mochalski, P., Kupferthaler, A., Unterkofler, K., Koc, H., Filipiak, W., Teschl, S., Hinterhuber, H., Amann, A., 2010a. Dynamic profiles of volatile organic compounds in exhaled breath as determined by a coupled PTR-MS/GC–MS study. Physiol. Meas. 31, 1169–1184 URL: 〈https://homepages.fhv.at/ku/karl/pdfs/PhysMeas2010.pdf〉.

King, J., Unterkofler, K., Teschl, G., Teschl, S., Koc, H., Hinterhuber, H., Amann, A., 2010b. A mathematical model for breath gas analysis of volatile organic compounds with special emphasis on acetone. Preprint, Breath Research Institute, Austrian Academy of Sciences. URL: 〈http://arxiv.org/abs/1003.4475〉.

Kinoyama, M., Nitta, H., Watanabe, A., Ueda, H., 2008. Acetone and isoprene concentrations in exhaled breath in healthy subjects. J. Health Sci. 54, 471–477.

Kuhn, E., Lavielle, M., 2005. Maximum likelihood estimation in nonlinear mixed effects models. Comput. Stat. Data Anal. 49, 1020–1038.

Kumagai, S., Matsunaga, I., 2000. A lung model describing uptake of organic solvents and roles of mucosal blood flow and metabolism in the bronchioles. Inhal. Toxicol. 12, 491–510.

Kushch, I., Arendacka, B., Stolc, S., Mochalski, P., Filipiak, W., Schwarz, K., Schwentner, L., Schmid, A., Dzien, A., Lechleitner, M., Witkovsky, V., Miekisch, W., Schubert, J., Unterkofler, K., Amann, A., 2008. Breath isoprene—aspects of normal physiology related to age, gender and cholesterol profile as determined in a proton transfer reaction mass spectrometry study. Clin. Chem. Lab. Med. 46, 1011–1018.

Leung, H.W., 1991. Development and utilization of physiologically based pharmacokinetic models for toxicological applications. J. Toxicol. Environ. Health 32, 247–267.

Liang, P.J., Pandit, J.J., Robbins, P.A., 1996. Statistical properties of breath-to-breath variations in ventilation at constant P_{ET,CO_2} and P_{ET,O_2} in humans. J. Appl. Physiol. 81, 2274–2286.

Ligor, T., Ligor, M., Amann, A., Ager, C., Bachler, M., Dzien, A., Buszewski, B., 2008. The analysis of healthy volunteers' exhaled breath by the use of solid-phase microextraction and GC–MS. J. Breath Res. 2, 046006.

Lindinger, W., Hansel, A., Jordan, A., 1998a. On-line monitoring of volatile organic compounds at pptv levels by means of proton-transfer-reaction mass spectrometry (PTR-MS)—medical applications, food control and environmental research. Int. J. Mass Spectrom. 173, 191–241.

Lindinger, W., Hansel, A., Jordan, A., 1998b. Proton-transfer-reaction mass spectrometry (PTR-MS): on-line monitoring of volatile organic compounds at pptv levels. Chem. Soc. Rev. 27, 347–354.

Lirk, P., Bodrogi, F., Raifer, H., Greiner, K., Ulmer, H., Rieder, J., 2003. Elective haemodialysis increases exhaled isoprene. Nephrol. Dial. Transplant. 18, 937–941.

Ljung, G.M., Box, G.E.P., 1978. On a measure of lack of fit in time series models. Biometrika 65, 297–303.

Lumb, A.B., 2005. Nunn's Applied Respiratory Physiology, sixth ed. Butterworth-Heinemann, Oxford.

McGrath, L.T., Patrick, R., Silke, B., 2001. Breath isoprene in patients with heart failure. Eur. J. Heart Fail. 3, 423–427.

Melnick, R.L., Kohn, M.C., 2000. Dose–response analyses of experimental cancer data. Drug Metab. Rev. 32, 193–209.

Melnick, R.L., Sills, R.C., Roycroft, J.H., Chou, B.J., Ragan, H.A., Miller, R.A., 1994. Isoprene, an endogenous hydrocarbon and industrial chemical induces, multiple organ neoplasia in rodents after 26 weeks of inhalation exposure. Cancer Res. 54, 5333–5339.

Miekisch, W., Schubert, J.K., 2006. From highly sophisticated analytical techniques to life-saving diagnostics: technical developments in breath analysis. Trends Anal. Chem. 25, 665–673.

Miekisch, W., Schubert, J.K., Noeldge-Schomburg, G.F.E., 2004. Diagnostic potential of breath analysis-focus on volatile organic compounds. Clin. Chim. Acta 347, 25–39.

Miekisch, W., Schubert, J.K., Vagts, D.A., Geiger, K., 2001. Analysis of volatile disease markers in blood. Clin. Chem. 47, 1053–1060.

Mohrman, D.E., Heller, L.J., 2006. Cardiovascluar Physiology, sixth ed. Lange Medical Books, McGraw-Hill, New York.

Monte, M.D., Citti, L., Gervasi, P.G., 1985. Isoprene metabolism by liver microsomal mono-oxygenases. Xenobiotica 15, 591–597.

Mörk, A.K., Johanson, G., 2006. A human physiological model describing acetone kinetics in blood and breath during various levels of physical exercise. Toxicol. Lett. 164, 6–15.

Mörk, A.-K., Jonsson, F., Johanson, G., 2009. Bayesian population analysis of a washin–washout physiologically based pharmacokinetic model for acetone. Toxicol. Appl. Pharmacol. 240, 423–432.

Nelson, N., Lagesson, V., Nosratabadi, A.R., Ludvigsson, J., Tagesson, C., 1998. Exhaled isoprene and acetone in newborn infants and in children with diabetes mellitus. Pediatr. Res. 44, 363–367.

NTP, 1999. Toxicology and carcinogenesis studies of isoprene (CAS No. 78-79-5) in F344/N rats (inhalation studies). Technical Report NTP-TR-486, NIH Publication No. 97-3976. Technical Report, National Toxicology Program, Research Triangle Park, NC.

Ottesen, J.T., Olufsen, M.S., Larsen, J.K., 2004. Applied Mathematical Models in Human Physiology. SIAM, Philadelphia.

Pabst, F., Miekisch, W., Fuchs, P., Kischkel, S., Schubert, J.K., 2007. Monitoring of oxidative and metabolic stress during cardiac surgery by means of breath biomarkers: an observational study. J. Cardiothorac. Surg. 2, 37.

Peifer, M., Timmer, J., 2007. Parameter estimation in ordinary differential equations for biochemical processes using the method of multiple shooting. IET Syst. Biol. 1, 78–88.

Pleil, J.D., 2008. Role of exhaled breath biomarkers in environmental health science. J. Toxicol. Environ. Health B Crit. Rev. 11, 613–629.

Pleil, J.D., Kim, D., Prah, J.D., Ashley, D.L., Rappaport, S.M., 2005. The unique value of breath biomarkers for estimating pharmacokinetic rate constants and body burden from environmental exposures. In: Amann, A., Smith, D. (Eds.), Breath Analysis for Clinical Diagnosis and Therapeutic Monitoring. World Scientific, Singapore, pp. 347–359.

Reddy, M.B., Yang, R.S.H., Clewell III, H.J., Andersen, M.E., 2005. Physiologically Based Pharmacokinetic Modeling: Science and Applications. Wiley, Hoboken.

Rieder, J., Lirk, P., Ebenbichler, C., Gruber, G., Prazeller, P., Lindinger, W., Amann, A., 2001. Analysis of volatile organic compounds: possible applications in metabolic disorders and cancer screening. Wien. Klin. Wochenschr. 113, 181–185.

Rodriguez-Fernandez, M., Egea, J.A., Banga, J.R., 2006. Novel metaheuristic for parameter estimation in nonlinear dynamic biological systems. BMC Bioinformatics 7, 483.

Salerno-Kennedy, R., Cashman, K.D., 2005. Potential applications of breath isoprene as a biomarker in modern medicine: a concise overview. Wien. Klin. Wochenschr. 117, 180–186.

Schwarz, K., Filipiak, W., Amann, A., 2009. Determining concentration patterns of volatile compounds in exhaled breath by PTR-MS. J. Breath Res. 3, 027002 (15pp.).

Seber, G.A.F., Wild, C.J., 2003. Nonlinear Regression. Wiley, Hoboken.

Shao, J., Tu, D., 1995. The Jackknife and Bootstrap. Springer, New York.

Silver, G.M., Fall, R., 1995. Characterization of aspen isoprene synthase, an enzyme responsible for leaf isoprene emission to the atmosphere. J. Biol. Chem. 270, 13010–13016.

Smith, D., Spanel, P., Davies, S., 1999. Trace gases in breath of healthy volunteers when fasting and after a protein-calorie meal: a preliminary study. J. Appl. Physiol. 87, 1584–1588.

Smith, D., Spanel, P., Enderby, B., Lenney, W., Turner, C., Davies, S.J., 2010. Isoprene levels in the exhaled breath of 200 healthy pupils within the age range 7–18 years studied using SIFT-MS. J. Breath Res. 4, 017101.

Stone, B.G., Besse, T.J., Duane, W.C., Evans, C.D., DeMaster, E.G., 1993. Effect of regulating cholesterol biosynthesis on breath isoprene excretion in men. Lipids 28, 705–708.

Sullivan, M.J., Knight, J.D., Higginbotham, M.B., Cobb, F.R., 1989. Relation between central and peripheral hemodynamics during exercise in patients with chronic heart failure. Muscle blood flow is reduced with maintenance of arterial perfusion pressure. Circulation 80, 769–781.

Taucher, J., Hansel, A., Jordan, A., Fall, R., Futrell, J.H., Lindinger, W., 1997. Detection of isoprene in expired air from human subjects using proton-transfer-reaction mass spectrometry. Rapid Commun. Mass Spectrom. 11, 1230–1234.

Tothill, P., Stewart, A.D., 2002. Estimation of thigh muscle and adipose tissue volume using magnetic resonance imaging and anthropometry. J. Sports Sci. 20, 563–576.

Turner, C., Spanel, P., Smith, D., 2006. A longitudinal study of breath isoprene in healthy volunteers using selected ion flow tube mass spectrometry (SIFT-MS). Physiol. Meas. 27, 13–22.

Wagner, P., 1992. Ventilation–perfusion matching during exercise. Chest 101, 192S–198S.

Wagner, P.D., 2008. The multiple inert gas elimination technique (MIGET). Intensive Care Med. 34, 994–1001.

Watson, W.P., Cottrell, L., Zhang, D., Golding, B.T., 2001. Metabolism and molecular toxicology of isoprene. Chem. Biol. Interact. 135–136, 223–238.

Weitzberg, E., Lundberg, J.O.N., 2002. Humming greatly increases nasal nitric oxide. Am. J. Respir. Crit. Care Med. 166, 144–145.

West, J.B., 2005. Respiratory Physiology the Essentials, seventh ed. Lippincott Williams & Wilkins, Baltimore.

Chapter 8

Paper D: A mathematical model for breath gas analysis of volatile organic compounds with special emphasis on acetone

JULIAN KING ET AL.

Journal of Mathematical Biology (2010), accepted

Major parts of the original appendix have been removed from this reformatted version of the article and can now be found in Part I.

Journal of Mathematical Biology manuscript No.
(will be inserted by the editor)

A mathematical model for breath gas analysis of volatile organic compounds with special emphasis on acetone

Julian King · Karl Unterkofler ·
Gerald Teschl · Susanne Teschl · Helin Koc ·
Hartmann Hinterhuber · Anton Amann

Received: date / Accepted: date

J. King
Breath Research Institute of the Austrian Academy of Sciences
Rathausplatz 4, A-6850 Dornbirn, Austria
E-mail: julian.king@oeaw.ac.at

K. Unterkofler
Vorarlberg University of Applied Sciences and
Breath Research Unit of the Austrian Academy of Sciences
Hochschulstr. 1, A-6850 Dornbirn, Austria
E-mail: karl.unterkofler@fhv.at

G. Teschl
University of Vienna, Faculty of Mathematics
Nordbergstr. 15, A-1090 Wien, Austria
E-mail: gerald.teschl@univie.ac.at

S. Teschl
University of Applied Sciences Technikum Wien
Höchstädtplatz 5, A-1200 Wien, Austria
E-mail: susanne.teschl@technikum-wien.at

H. Koc
Vorarlberg University of Applied Sciences
Hochschulstr. 1, A-6850 Dornbirn, Austria

H. Hinterhuber
Innsbruck Medical University, Department of Psychiatry
Anichstr. 35, A-6020 Innsbruck, Austria

A. Amann (corresponding author)
Innsbruck Medical University, Univ.-Clinic for Anesthesia and
Breath Research Institute of the Austrian Academy of Sciences
Anichstr. 35, A-6020 Innsbruck, Austria
E-mail: anton.amann@oeaw.ac.at, anton.amann@i-med.ac.at

Abstract Recommended standardized procedures for determining exhaled lower respiratory nitric oxide and nasal nitric oxide (NO) have been developed by task forces of the European Respiratory Society and the American Thoracic Society. These recommendations have paved the way for the measurement of nitric oxide to become a diagnostic tool for specific clinical applications. It would be desirable to develop similar guidelines for the sampling of other trace gases in exhaled breath, especially volatile organic compounds (VOCs) which may reflect ongoing metabolism.

The concentrations of water-soluble, blood-borne substances in exhaled breath are influenced by:

- breathing patterns affecting gas exchange in the conducting airways
- the concentrations in the tracheo-bronchial lining fluid
- the alveolar and systemic concentrations of the compound.

The classical Farhi equation takes only the alveolar concentrations into account. Real-time measurements of acetone in end-tidal breath under an ergometer challenge show characteristics which cannot be explained within the Farhi setting. Here we develop a compartment model that reliably captures these profiles and is capable of relating breath to the systemic concentrations of acetone. By comparison with experimental data it is inferred that the major part of variability in breath acetone concentrations (e.g., in response to moderate exercise or altered breathing patterns) can be attributed to airway gas exchange, with minimal changes of the underlying blood and tissue concentrations. Moreover, the model illuminates the discrepancies between observed and theoretically predicted blood-breath ratios of acetone during resting conditions, i.e., in steady state. Particularly, the current formulation includes the classical Farhi and the Scheid series inhomogeneity model as special limiting cases and thus is expected to have general relevance for other classes of volatile organic compounds as well.

The chief intention of the present modeling study is to provide mechanistic relationships for further investigating the exhalation kinetics of acetone and other water-soluble species. This quantitative approach is a first step towards new guidelines for breath gas analyses of volatile organic compounds, similar to those for nitric oxide.

Keywords breath gas analysis · volatile organic compounds · acetone · modeling

Mathematics Subject Classification (2000) 92C45 · 92C35 · 93C10 · 93B07

1 Introduction

Measurement of blood-borne volatile organic compounds (VOCs) occurring in human exhaled breath as a result of normal metabolic activity or pathological disorders has emerged as a promising novel methodology for non-invasive medical diagnosis and therapeutic monitoring of disease, drug testing and tracking of physiological processes [2,3,1,70,55]. Apart from the obvious improvement in patient compliance and tolerability, major advantages of exhaled breath analysis compared to conventional test procedures, e.g., based on blood or urine probes, include de facto unlimited availability as well as rapid on-the-spot evaluation or even *real-time* analysis. Additionally, it has been pointed out that the pulmonary circulation receives the entire cardiac output and therefore the breath concentrations of such compounds might provide a more faithful estimate of pooled systemic concentrations than single small-volume blood samples, which will always be affected by local hemodynamics and blood-tissue interactions [62].
Despite this huge potential, the use of exhaled breath analysis within a clinical setting is still rather limited. This is mainly due to the fact that drawing reproducible breath samples remains an intricate task that has not fully been standardized yet. Moreover, inherent error sources introduced by the complex mechanisms driving pulmonary gas exchange are still poorly understood. The lack of standardization among the different sampling protocols proposed in the literature has led to the development of various sophisticated sampling systems, which selectively extract end-tidal air by discarding anatomical dead space volume [40,26,11]). Even though such setups present some progress, they are far from being perfect. In particular, these sampling systems can usually not account for the variability stemming from varying physiological states.

In common measurement practice it is often tacitly assumed that end-tidal air will reflect the alveolar concentration C_A, which in turn is proportional to the concentration of the VOC in mixed venous blood $C_{\bar{\mathrm{v}}}$, with the associated factor depending on the substance-specific blood:gas partition coefficient $\lambda_{\mathrm{b:air}}$ (describing the diffusion equilibrium between capillaries and alveoli), alveolar ventilation $\dot{V}_\mathrm{A}$ (governing the transport of the compound through the respiratory tree) and cardiac output $\dot{Q}_\mathrm{c}$ (controlling the rate at which the VOC is delivered to the lungs):

$$C_{\mathrm{measured}} = C_\mathrm{A} = \frac{C_{\bar{\mathrm{v}}}}{\lambda_{\mathrm{b:air}} + \frac{\dot{V}_\mathrm{A}}{\dot{Q}_\mathrm{c}}}. \tag{1}$$

This is the familiar equation introduced by Farhi [19], describing steady state inert gas elimination from the lung viewed as a single alveolar compartment with a fixed overall ventilation-perfusion ratio $\dot{V}_\mathrm{A}/\dot{Q}_\mathrm{c}$ close to one. Since the pioneering work of Farhi, both equalities in the above relation have been challenged. Firstly, for low blood soluble inert gases, characterized by $\lambda_{\mathrm{b:air}} \leq 10$, alveolar concentrations resulting from an actually constant $C_{\bar{\mathrm{v}}}$ can easily be seen to vary drastically in response to fluctuations in blood or respiratory flow (see also [41,39] for some recent findings in this context). While this sensitivity has been exploited in MIGET (Multiple Inert Gas Elimination Technique, cf. [87,86]) to assess ventilation-perfusion inhomogeneity throughout the normal and diseased lung, it is clearly problematic in standard breath sampling routines based on free breathing, as slightly changing measurement conditions (regarding, e.g., body posture, breathing patterns or stress) can have a large impact on the observed breath concentration [17]. This constitutes a typical example of an inherent error source as stated above, potentially leading to a high degree of intra- and consequently inter-individual variability among the measurement results [61]. It is hence important to investigate the influence of medical parameters like cardiac output, pulse, breathing rate and breathing volume on VOC concentrations in exhaled breath. In contrast, while highly soluble VOCs ($\lambda_{\mathrm{b:air}} > 10$) tend to be less affected by changes in ventilation and perfusion, measurement artifacts associated with this class of compounds result from the fact that – due to their often hydrophilic properties – a substantial interaction between the exhalate and the mucosa layers lining the conducting airways can be anticipated [6]. In other words, for these substances $C_{\mathrm{measured}} \neq C_{\mathrm{A}}$, with the exact quantitative relationship being unknown. Examples of endogenous compounds that are released into the gas phase not only through the blood-alveolar interface, but also through the bronchial lining fluid are, e.g., acetone and ethanol [7,83].

Acetone (2-propanone; CAS number 67–64–1; molar mass 58.08 g/mol) is one of the most abundant VOCs found in human breath and has received wide attention in the biomedical literature. Being a natural metabolic intermediate of lipolysis [35], endogenous acetone has been considered as a biomarker for monitoring the ketotic state of diabetic and fasting individuals [81,65,69,75], estimating glucose levels [20] or assessing fat loss [47]. Nominal levels in breath and blood have been established in [88,74], and bioaccumulation has been studied in the framework of exposure studies and pharmacokinetic modeling [91,45,57].

Despite this relatively large body of experimental evidence, the crucial link between acetone levels in breath and blood is still obscure, thus hindering the development of validated breath tests for diagnostic purposes. For perspective, multiplying the proposed population mean of approximately 1 μg/l [74] in end-tidal breath by the partition coefficient $\lambda_{\mathrm{b:air}} = 340$ [7] at body temperature appears to grossly underestimate observed (arterial) blood levels spreading around 1 mg/l [88,91,37]. Furthermore, breath profiles of acetone (and other highly soluble volatile compounds such as 2-pentanone or methyl acetate) associated with moderate workload ergometer challenges of normal healthy volunteers drastically depart from the trend suggested by Equation (1) [40,41]. In particular, the physiological meaning of these discrepancies has not been established in sufficient depth.

With the background material of the previous paragraphs in mind, we view acetone as a paradigmatic example for the analysis of highly soluble, *blood-borne* VOCs, even though it cannot cover the whole spectrum of different physico-chemical characteristics. The emphasis of this paper is on developing a mechanistic description of *end-tidal* acetone behavior during different physiological states (e.g., rest, exercise, sleep and exposure scenarios). Such a quantitative approach will contribute to a better understanding regarding the relevance of observable breath concentrations of highly soluble trace gases with respect to the underlying endogenous situation and hence constitutes an indispensable prerequisite for guiding the interpretation of future breath test results. Moreover, it will allow for a standardized examination of the information content and predictive power of various breath sampling regimes proposed in the literature. Specifically, our work also aims at complementing previous studies centered on single breath dynamics during resting conditions [83,32,5,7,45].

By adopting the usual compartmental approach [44,15,57,68] our formulation is simple in the sense that no detailed anatomical features of the respiratory tract must be taken into account. Although models of this type have been criticized for their underlying assumptions [22] (e.g., regarding the cyclic nature of breathing), they prove as valuable tools for capturing both short-term behavior as indicated above and phenomena that are characteristic for sampling scenarios extending over minutes or even hours. Consequently, while the physical derivation to be presented here is clearly driven by the well-established theory covering soluble gas exchange in a single exhalation framework, it extends these ideas to a macroscopic level, thus yielding a model that can serve as a template for studying the mid- to long-term kinetics of acetone and similar volatile organic compounds in breath and various parts of the human body

2 Experimental basics

Here we shall briefly discuss the experimental background pertinent to our own phenomenological findings presented throughout the paper. In particular, these results were obtained with the necessary approvals by the Ethics Committee of the Innsbruck Medical University. All volunteers gave written informed consent.

Breath acetone concentrations are assessed by means of a real-time setup designed for synchronized measurements of exhaled breath VOCs as well as a variety of respiratory and hemodynamic parameters, see Fig. 1. Extensive details are given in [40].

The breath-related part of the mentioned setup consists of a head mask spirometer system allowing for the standardized extraction of predefined exhalation segments which – via a heated and gas tight Teflon transfer line – are then directly drawn into a Proton-Transfer-Reaction mass spectrometer (PTR-MS, Ionicon Analytik GmbH, Innsbruck, Austria) for online analysis. This analytical technique has proven to be a sensitive method for quantification of volatile molecular species M down to the ppb (parts per billion) range on the basis of "soft" chemical ionization within a drift chamber, i.e., by taking advantage of the proton transfer

$$\mathrm{H_3O^+} + M \rightarrow M\mathrm{H^+} + \mathrm{H_2O}$$

from primary hydronium precursor ions originating in an adjoint hollow cathode [50, 51]. Note that this reaction scheme is selective to VOCs with proton affinities higher than water (166.5 kcal/mol), thereby precluding the ionization of the bulk composition exhaled air, N_2, O_2 and CO_2. Count rates of the resulting product ions $M\mathrm{H}^+$ or fragments thereof appearing at specified mass-to-charge ratios m/z can subsequently be converted to absolute concentrations of the protonated compounds (see [73] for further details on the quantification of acetone as well as [40] for the underlying PTR-MS settings used). The carbon dioxide concentration C_{CO_2} of the gas sample is determined by a separate sensor (AirSense Model 400, Digital Control Systems, Portland, USA).

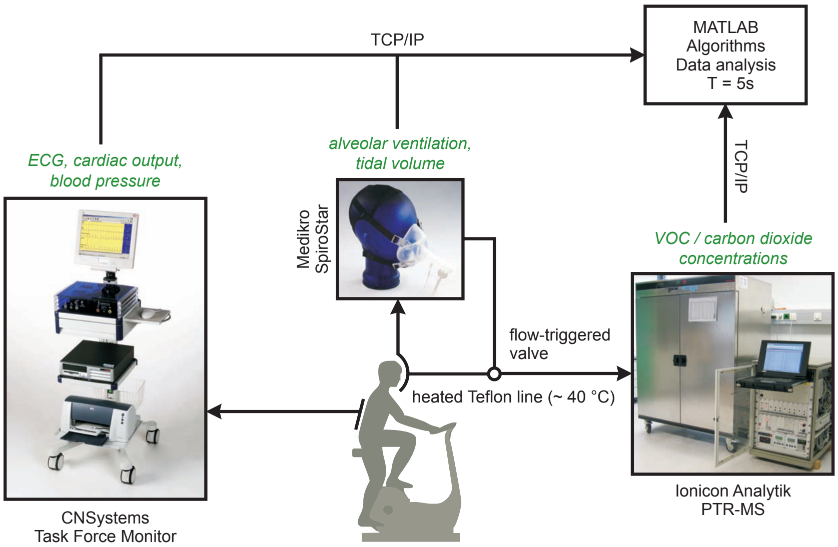
TCP/IP
MATLAB
Algorithms
Data analysis
T = 5s
TCP/IP
ECG, cardiac output,
blood pressure
alveolar ventilation,
tidal volume
Medikro
SpiroStar
VOC / carbon dioxide
concentrations
flow-triggered
valve
heated Teflon line (~ 40 °C)
CNSystems
Task Force Monitor
Ionicon Analytik
PTR-MS

Fig. 1 Experimental setup used for obtaining VOC profiles and medical parameters [40]. Items in italic correspond to measurable variables. The selective analysis of predefined breath segments is ensured by flow-triggered sample extraction.

In addition to the breath concentration profiles of acetone, it will be of importance for us to have at hand a continuous estimate of the corresponding sample water vapor content C_{water}. As has been put forward in the literature, the water dimer $(H_3O^+)H_2O$ forming in the drift chamber as a result of clustering can be used for this purpose [89,4]. More specifically, the pseudo concentration signal at $m/z = 37$ calculated according to Equation (1) in [73] using a standard reaction rate constant of 2.0×10^{-9} cm^3/s yields a quantity roughly proportional to sample humidity. Slight variations due to fluctuations of the (unknown) amount of water clusters forming in the ion source are assumed to be negligible. Absolute quantification can be achieved by comparison with standards containing predefined humidity levels. Such standards with C_{CO_2} and C_{water} varying over the experimental physiological range of 2 – 8% and 2 – 6%, respectively, were prepared using a commercial gas mixing unit (Gaslab, Breitfuss Messtechnik GmbH, Harpstedt, Germany), resulting in a mean calibration factor of 2.1×10^{-4} and $R^2 \geq 0.98$ for all regressions. It has been argued in [36] that the aforementioned pseudo concentration can drastically be affected by the carbon dioxide concentration, which, however, could not be confirmed with our PTR-MS settings. Although the computed water content is slightly overestimated with increasing C_{CO_2}, the sensitivity was found to stay within 10% of the mean value given above. Nevertheless, we recognize that this approximate method for determining water vapor levels can only serve as a first surrogate for more exact hygrometer measurements.

Despite the fact that molecular oxygen is not protonated, the breath oxygen concentration C_{O_2} – relative to an assumed steady state value of about 100 mmHg in end-tidal (alveolar) air during rest [52] – within one single experiment can still be assessed by monitoring the parasitic precursor ion O_2^+ at $m/z = 32$, resulting from a small amount of sample gas entering the ion source with subsequent ionization of O_2 under electron impact [62]. For normalization purposes, the respective count rates are again converted to pseudo concentrations. Table 1 summarizes the measured quantities relevant for this paper. In general, breath concentrations will always refer to end-tidal levels, except where explicitly noted. Moreover, a typical sampling interval of 5 s is assumed for each variable (corresponding to breath-by-breath extraction of end-tidal VOC levels at a normal breathing rate of 12 tides/min).

Table 1 Summary of measured parameters together with some nominal literature values during rest and assuming ambient conditions. Breath concentrations refer to end-tidal levels.

Variable	Symbol	Nominal value (units)
Cardiac output	$\dot{Q}_c$	6 (l/min) [56]
Alveolar ventilation	$\dot{V}_A$	5.2 (l/min) [90]
Tidal volume	V_T	0.5 (l) [90]
Acetone concentration	$C_{measured}$	1 (μg/l) [74]
CO_2 content	C_{CO_2}	5.6 (%) [52]
Water content	C_{water}	4.7 (%) [24]
O_2 content	C_{O_2}	13.7 (%) [52]

3 Acetone modeling

3.1 Preliminaries and assumptions

Classical pulmonary inert gas elimination theory [19] postulates that uptake and removal of VOCs take place exclusively in the alveolar region. While this is a reasonable assumption for low soluble substances, it has been shown by several authors that exhalation kinetics of VOCs with high affinity for blood and water such as acetone are heavily influenced by relatively quick absorption and release mechanisms occurring in the conductive airways (see, e.g., [5] for a good overview of this topic). More specifically, due to their pronounced hydrophilic characteristics such compounds tend to interact with the water-like mucus membrane lining this part of the respiratory tree, thereby leading to pre- and post-alveolar gas exchange often referred to as wash-in/wash-out behavior. The present model aims at taking into consideration two major aspects in this framework.

3.1.1 Bronchial exchange

It is now an accepted fact that the bronchial tree plays an important role in overall pulmonary gas exchange of highly (water) soluble trace gases, affecting both endogenous clearance as well as exogenous uptake. For perspective, Anderson et al. [7] inferred that while fresh air is being inhaled, it becomes enriched with acetone stored in the airway surface walls of the peripheral bronchial tract, thus leading to a decrease of the acetone pressure/tension gradient between gas phase and capillary blood in the alveolar space. This causes an effective reduction of the driving force for gas exchange in the alveoli and minimizes the unloading of the capillary acetone level. Correspondingly, during exhalation the aforementioned diffusion process is reversed, with a certain amount of acetone being stripped from the air stream and redepositing onto the previously depleted mucus layer. As a phenomenological consequence, exhaled breath concentrations of acetone and other highly water soluble substances tend to be diminished on their way up from the deeper respiratory tract to the airway opening, thereby decreasing overall elimination as compared to purely alveolar extraction. Similarly, exposition studies suggest a pre-alveolar absorption of exogenous acetone during inhalation and a post-alveolar revaporization during expiration, resulting in a lower systemic uptake compared to what would be expected if the exchange occurred completely in the alveoli [91,45,82].

From the above, quantitative assessments examining the relationships between the measured breath concentrations and the underlying alveolar levels are complex and need to take into account a variety of factors, such as airway temperature profiles and airway perfusion as well as breathing patterns [5,6].

In accordance with previous modeling approaches, we consider a bronchial compartment separated into a gas phase and a mucus membrane, which is assumed to inherit the physical properties of water [45,57] and acts as a reservoir for acetone. Part of the acetone dissolved in this layer is transferred to the bronchial circulation, whereby the major fraction of the associated venous drainage is postulated to join the pulmonary veins via the postcapillary anastomoses [52]. A study by Morris et al. [59] on airway perfusion during moderate exercise in humans indicates that the fraction $q_{\mathrm{bro}} \in [0,1)$ of cardiac output $\dot{Q}_{\mathrm{c}}$ contributing to this part of bronchial perfusion will slightly decrease with increasing pulmonary blood flow. According to Figure 3 from their paper and assuming that $\dot{Q}_{\mathrm{c}}^{\mathrm{rest}} = 6$ l/min we can derive the heuristic linear model

$$q_{\mathrm{bro}}(\dot{Q}_{\mathrm{c}}) := \max\{0, q_{\mathrm{bro}}^{\mathrm{rest}}(1 - 0.06(\dot{Q}_{\mathrm{c}} - \dot{Q}_{\mathrm{c}}^{\mathrm{rest}}))\}. \tag{2}$$

The constant $q_{\mathrm{bro}}^{\mathrm{rest}}$ will be estimated in Section 4. As a rough upper bound we propose the initial guess $q_{\mathrm{bro}}^{\mathrm{rest}} = 0.01$ [52]. We stress the fact that the bronchial compartment just introduced has to be interpreted as an abstract control volume lumping together the decisive sites of airway gas exchange in one roughly homogeneous functional unit. These locations can be expected to vary widely with the solubility of the VOC under scrutiny as well as with physiological boundary conditions [5].

3.1.2 Temperature dependence

There is strong experimental evidence that airway temperature constitutes a major determinant for the pulmonary exchange of highly soluble VOCs, cf. [33]. In particular, changes in airway temperature can be expected to affect the solubility of acetone and similar compounds in the mucus surface of the respiratory tree. It will hence be important to specify a tentative relationship capturing such influences on the observable breath levels. As will be rationalized below, this may be achieved by taking into account the absolute humidity of the extracted breath samples.

Passing through the conditioning regions of the upper airways, inhaled air is warmed to a mean body core temperature of approximately 37 °C and fully saturated with water vapor, thus leading to an absolute humidity of bronchial and alveolar air of about 6.2% at ambient pressure. During exhalation, depending on the axial temperature gradient between the lower respiratory tract and the airway opening, a certain amount of water vapor will condense out and reduce the water content C_{water} in the exhalate according to the saturation water vapor pressure P_{water} (in mbar) determined by local airway temperature T (in °C) [54,25]. The relationship between these two quantities can be approximated by the well-known Magnus formula [77]

$$P_{\text{water}}(T) = 6.112 \exp\left(\frac{17.62\,T}{243.12+T}\right), \tag{3}$$

valid for a temperature range $-45\ ^\circ\text{C} \leq T \leq 60\ ^\circ\text{C}$. For normal physiological values of T, the resulting pressure is sufficiently small to treat water vapor as an ideal gas [67] and hence by applying Dalton's law we conclude that absolute humidity C_{water} (in %) of the exhalate varies according to

$$C_{\text{water}}(T) = 100\,\frac{P_{\text{water}}(T)}{P_{\text{ambient}}}, \tag{4}$$

where P_{ambient} is the ambient pressure in mbar. Inverting the above formula, the minimum airway temperature $T_{\text{min}} = T_{\text{min}}(C_{\text{water}})$ during exhalation becomes a function of measured water content in exhaled breath. From this, a mean airway and mucus temperature characterizing the homogeneous bronchial compartment of the previous section will be defined as

$$\bar{T}(C_{\text{water}}) := \frac{T_{\text{min}}(C_{\text{water}})+37}{2}, \tag{5}$$

corresponding to a hypothesized linear increase of temperature along the airways. Note that this assumption is somehow arbitrary in the sense that the characteristic temperature of the airways should be matched to the primary (time- and solubility-dependent) location of airway gas exchange as mentioned above. Equation (5) thus should only be seen as a simple ad hoc compromise incorporating this variability.

The decrease of acetone solubility in the mucosa – expressed as the water:air partition coefficient $\lambda_{\text{muc:air}}$ – with increasing temperature can be described in the ambient temperature range by a van't Hoff-type equation [78]

$$\log_{10} \lambda_{\text{muc:air}}(T) = -A + \frac{B}{T+273.15}, \tag{6}$$

where $A = 3.742$ and $B = 1965$ Kelvin are proportional to the entropy and enthalpy of volatilization, respectively. Hence, in a hypothetical situation where the absolute sample humidity at the mouth is 4.7% (corresponding to a temperature of $T \approx 32\ ^\circ\text{C}$

and ambient pressure at sea level, cf. [54,24]), local solubility of acetone in the mucus layer increases from $\lambda_{\text{muc:air}}(37\ ^\circ\text{C}) = 392$ in the lower respiratory tract (cf. [44]) to $\lambda_{\text{muc:air}}(32\ ^\circ\text{C}) = 498$ at the mouth, thereby predicting a drastic reduction of air stream acetone concentrations along the airways. The above formulations allow to assess this reduction by taking into account sample water vapor as a meta parameter. This meta parameter reflects various influential factors on the mucus solubility $\lambda_{\text{muc:air}}$ which would otherwise be intricate to handle due to a lack of information, such as local airway perfusion, breathing patterns, mucosal hydration and thermoregulatory events which in turn will affect axial temperature profiles. In particular, $\lambda_{\text{muc:air}}$ for the entire bronchial compartment will be estimated via the mean airway temperature $\bar{T}$ as

$$\lambda_{\text{muc:air}}(\bar{T}) = \lambda_{\text{muc:air}}(\bar{T}(C_{\text{water}})). \tag{7}$$

The strong coupling between sample humidity and exhaled breath concentrations predicted by the two relationships (3) and (6) is expected to be a common factor for all highly water soluble VOCs. In the framework of breath alcohol measurements Lindberg et al. [49] indeed showed a positive correlation between these two quantities along the course of exhalation, which can also be observed in the case of acetone, cf. Fig. 2.

Variations of the acetone blood:air partition coefficient $\lambda_{\text{b:air}} = 340$ [7,18] – dominating alveolar gas exchange – in response to changes in mixed venous blood temperature, e.g., due to exercise, are ignored as such changes are necessarily small [14]. Hence, $\lambda_{\text{b:air}}$ will always refer to 37 °C. Similarly, the partition coefficient between mucosa and blood is treated as constant defined by

$$\lambda_{\text{muc:b}} := \lambda_{\text{muc:air}}(37\ ^\circ\text{C})/\lambda_{\text{b:air}}, \tag{8}$$

resulting in a value of 1.15. Note, that if the airway temperature is below 37 °C we always have that

$$\lambda_{\text{muc:air}}/\lambda_{\text{muc:b}} \geq \lambda_{\text{b:air}}, \tag{9}$$

as $\lambda_{\text{muc:air}}$ is monotonically decreasing with increasing temperature, see Equation (6).

3.1.3 Bronchio-alveolar interactions

In a series of modeling studies [83,5], the location of gas exchange (from gas phase to liquid phase and vice versa) has been demonstrated to shift between bronchial and alveolar regions depending on the solubility of the compound under investigation. During tidal breathing, exchange for substances with blood:air partition coefficient $\lambda_{\text{b:air}} \leq 10$ takes place almost exclusively in the alveoli, while it appears to be strictly limited to the bronchial tract in the case of $\lambda_{\text{b:air}} \geq 100$. Transport for VOCs lying within these two extremes distributes between both spaces. Likewise, for fixed $\lambda_{\text{b:air}}$, location of gas exchange is expected to vary with breathing patterns. As has been concluded by Anderson et al. [7], airway contribution to overall pulmonary exchange of endogenous acetone is about 96% during tidal breathing, but only 73% when inhaling to total lung capacity. The rationale for this reduction is that while more proximal parts of the mucosa lining are being depleted earlier in the course of inhalation by losing acetone to the inhalate, saturation of the air stream with acetone is continuously

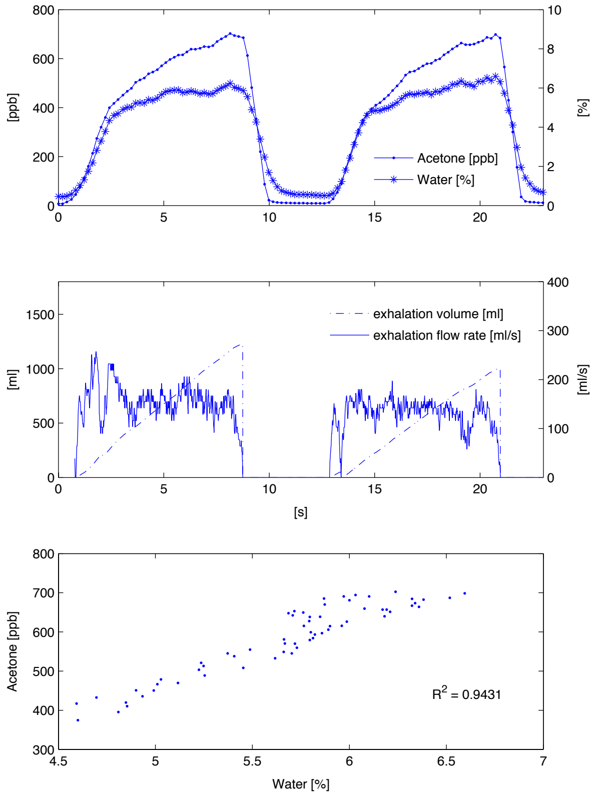

Fig. 2 Correlation between breath acetone concentrations and breath water content during two consecutive exhalations of a normal healthy volunteer at an approximately constant rate of 150 ml/s. Water-acetone pairs in the third panel correspond to the two linear *Phase 3* segments as described in [7]. The high sampling frequency in this example is achieved by collecting breath over the entire breath cycle (as opposed to the selective end-tidal extraction regime described in Section 2) as well as by limiting PTR-MS detection to only three mass-to-charge ratios (with corresponding dwell times given in brackets): $m/z = 21$ (5 ms), $m/z = 37$ (2 ms) and $m/z = 59$ (10 ms).

shifted towards the alveolar region. Furthermore, it can be argued that the magnitude of this shift increases with volumetric flow during inhalation as equilibration of fresh air with the mucus layer in regions with high flow rates might not be completed. From a reversed viewpoint this would be consistent with the observation made in [7] that end-exhaled acetone partial pressures increase with exhaled flow rate.

Such smooth transitions in the location of gas exchange can be incorporated into the model by including a diffusion process describing the interaction between bronchial and alveolar compartment (cf. Fig. 3), which is similar to the strategy found in the theory of stratified or series inhomogeneities developed by Scheid et al. [71]. According to the approach presented there, series inhomogeneities stem from the fact that while gas flow in the upper parts of the respiratory tree is primarily dominated by convection, axial diffusion becomes the decisive factor in the terminal airspaces. This can also be thought of as an incomplete mixing of tidal volume with the functional residual capacity, thus leading to the formation of an effective gas diffusion barrier between the proximal and distal parts of the alveolar space. Scheid et al. quantify this effect by means of a (substance-specific) stratified conductance parameter D, taking values in the interval $[0,\infty)$. As D approaches zero, the retention (defined as the ratio between steady state partial pressures in arterial and mixed venous blood) of inert gases eliminated from the blood increases, while excretion (the ratio between partial pressures in mixed expired air and mixed venous blood) decreases. Hence, small values of D correspond to a reduced overall gas exchange efficiency of the lungs. It will be shown that reinterpreting the concept of stratified inhomogeneity and the stratified conductance parameter D in the framework of soluble gas exchange allows for a proper description of the bronchio-alveolar interactions discussed above. The particular role of D within the present framework will be clarified in Section 3.2.2.

The alveolar region itself is represented by one single homogeneous alveolar unit, thereby neglecting ventilation-perfusion inequality throughout the lung. In the case of VOCs with high $\lambda_{\mathrm{b:air}}$ this constitutes an acceptable simplification, since the classical Farhi equation predicts a minimal influence of local ventilation-perfusion ratios on the corresponding alveolar concentrations. Uptake and elimination of VOCs to and from the bronchio-alveolar tract during inhalation and exhalation is governed by the alveolar ventilation $\dot{V}_{\mathrm{A}}$ (defined as the gas volume per time unit filling the alveoli and the exchanging bronchial tubes).

3.1.4 Body compartments

The systemic part of the model has been adapted from previous models [44,57] and consists of two functional units: a liver compartment, where acetone is endogenously produced and metabolized, as well as a tissue compartment representing an effective storage volume. The latter basically lumps together tissue groups with similar blood:tissue partition coefficient $\lambda_{\mathrm{b:tis}} \approx 1.38$, such as richly perfused tissue, muscles and skin [7,57]. Due to the low fractional perfusion of adipose tissue and its low affinity for acetone, an extra fat compartment was not considered. The fractional blood flow $q_{\mathrm{liv}} \in (0,1)$ to the liver is assumed to be related to total cardiac output by

$$q_{\mathrm{liv}}(\dot{Q}_{\mathrm{c}}) := 0.034 + 1.145\exp(-1.387\dot{Q}_{\mathrm{c}}/\dot{Q}_{\mathrm{c}}^{\mathrm{rest}}), \tag{10}$$

obtained by exponential fitting of the data given in [57]. The rate $\dot{M}$ of acetone metabolism is assumed to obey the Michaelis-Menten (saturation) kinetics

$$\dot{M} = \frac{v_{\max} C_{\mathrm{liv}} \lambda_{\mathrm{b:liv}}}{k_{\mathrm{m}} + C_{\mathrm{liv}} \lambda_{\mathrm{b:liv}}}, \tag{11}$$

with $v_{\max}, k_{\mathrm{m}} > 0$, or the linear kinetics

$$\dot{M} = k_{\mathrm{lin}} \mathrm{bw}^{0.75} C_{\mathrm{liv}} \lambda_{\mathrm{b:liv}} =: k_{\mathrm{met}} C_{\mathrm{liv}} \lambda_{\mathrm{b:liv}}, \tag{12}$$

where "bw" denotes the body weight in kg. The rate constant k_{lin} can be obtained by linearization of (11), i.e.,

$$k_{\text{lin}} := v_{\max}/k_{\text{m}} \approx 0.0037\,\text{l}/\text{kg}^{0.75}/\text{min}, \tag{13}$$

according to the values given in [44].

Remark 1 Taking into account nominal mixed venous blood concentrations of approximately 1 mg/l for healthy volunteers as well as an apparent Michaelis-Menten constant $k_{\text{m}} = 84$ mg/l [44], linear kinetics will be sufficient for describing most situations encountered in practice. Typical exceptions include, e.g., severe diabetic ketoacidosis or starvation ketosis, where plasma concentrations up to 500 mg/l have been reported [65, 69] and hence metabolism can be expected to reach saturation.

Other ways of acetone clearance such as excretion via the renal system are neglected [91]. Endogenous synthesis of acetone in the liver is assumed to occur at some rate $k_{\text{pr}} > 0$ depending on current lipolysis [35]. In particular, fat catabolism is considered a long-term mechanism compared to the other dynamics of the system, so that k_{pr} can in fact be assumed constant during the course of experiments presented here (less than 2 hours).

3.2 Model equations and a priori analysis

3.2.1 Derivation

In order to capture the gas exchange and tissue distribution mechanisms presented above, the model consists of four different compartments. A sketch of the model structure is given in Fig. 3 and will be detailed in following.

Model equations are derived by taking into account standard conservation of mass laws for the individual compartments, see [38, Sect. 2.3]. Local diffusion equilibria are assumed to hold at the air-tissue, tissue-blood and air-blood interfaces, the ratio of the corresponding concentrations being described by the appropriate partition coefficients, e.g., $\lambda_{\text{b:air}}$. Unlike for low blood soluble compounds, the amount of highly soluble gas dissolved in local blood volume of perfused compartments cannot generally be neglected, as it might significantly increase the corresponding capacities. This is particularly true for the airspace compartments. Since reliable data for some local blood volumes could not be found, in order not to overload the model with too many hypothetical parameters, we will use the effective compartment volumes $\tilde{V}_{\text{bro}} := V_{\text{bro}} + V_{\text{muc}}\lambda_{\text{muc:air}}$, $\tilde{V}_{\text{A}} := V_{\text{A}} + V_{c'}\lambda_{\text{b:air}}$, $\tilde{V}_{\text{liv}} := V_{\text{liv}} + V_{\text{liv,b}}\lambda_{\text{b:liv}}$ as well as $\tilde{V}_{\text{tis}} := V_{\text{tis}}$ and neglect blood volumes for the mucosal and tissue compartment.

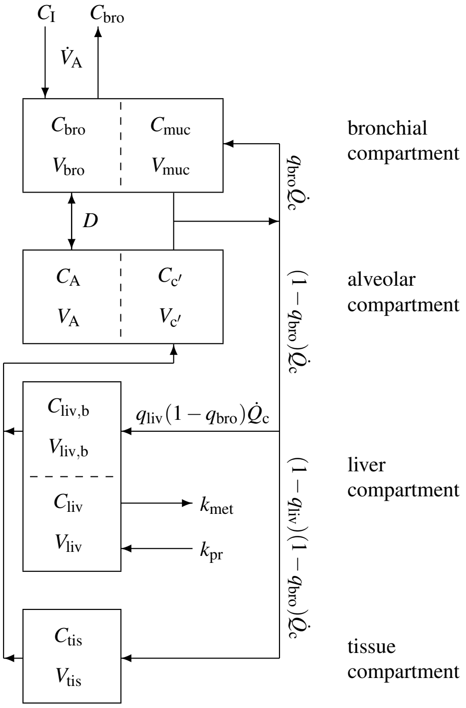
C_I
C_{bro}
$\dot{V}_A$
C_{bro}
V_{bro}
C_{muc}
V_{muc}
$q_{bro}\dot{Q}_c$
bronchial compartment
D
C_A
V_A
$C_{c'}$
$V_{c'}$
$(1-q_{bro})\dot{Q}_c$
alveolar compartment
$C_{liv,b}$
$V_{liv,b}$
$q_{liv}(1-q_{bro})\dot{Q}_c$
C_{liv}
V_{liv}
k_{met}
k_{pr}
$(1-q_{liv})(1-q_{bro})\dot{Q}_c$
liver compartment
C_{tis}
V_{tis}
tissue compartment

Fig. 3 Sketch of the model structure. The body is divided into four distinct functional units: bronchial/mucosal compartment (gas exchange), alveolar/end-capillary compartment (gas exchange), liver (metabolism and production) and tissue (storage). Dashed boundaries indicate a diffusion equilibrium. The conductance parameter D has units of volume divided by time and quantifies an effective diffusion barrier between the bronchial and the alveolar tract, cf. Section 3.2.2.

According to Fig. 3 as well as by taking into account the discussion of the previous subsections, for the bronchial compartment we find that

$$\frac{\mathrm{d}C_{\mathrm{bro}}}{\mathrm{d}t}\tilde{V}_{\mathrm{bro}} = \dot{V}_{\mathrm{A}}(C_{\mathrm{I}} - C_{\mathrm{bro}}) + D(C_{\mathrm{A}} - C_{\mathrm{bro}}) + q_{\mathrm{bro}}\dot{Q}_{\mathrm{c}}\left(C_{\mathrm{a}} - \frac{\lambda_{\mathrm{muc:air}}}{\lambda_{\mathrm{muc:b}}}C_{\mathrm{bro}}\right), \tag{14}$$

with C_{I} denoting the inhaled (ambient) gas concentration, while the mass balance equations for the alveolar, liver and tissue compartment read

$$\frac{\mathrm{d}C_{\mathrm{A}}}{\mathrm{d}t}\tilde{V}_{\mathrm{A}} = D(C_{\mathrm{bro}} - C_{\mathrm{A}}) + (1 - q_{\mathrm{bro}})\dot{Q}_{\mathrm{c}}\big(C_{\bar{\mathrm{v}}} - \lambda_{\mathrm{b:air}}C_{\mathrm{A}}\big), \tag{15}$$

and

$$\frac{\mathrm{d}C_{\mathrm{liv}}}{\mathrm{d}t}\tilde{V}_{\mathrm{liv}} = k_{\mathrm{pr}} - k_{\mathrm{met}}\lambda_{\mathrm{b:liv}}C_{\mathrm{liv}} + q_{\mathrm{liv}}(1 - q_{\mathrm{bro}})\dot{Q}_{\mathrm{c}}\big(C_{\mathrm{a}} - \lambda_{\mathrm{b:liv}}C_{\mathrm{liv}}\big), \tag{16}$$

and

$$\frac{\mathrm{d}C_{\mathrm{tis}}}{\mathrm{d}t}\tilde{V}_{\mathrm{tis}} = (1 - q_{\mathrm{liv}})(1 - q_{\mathrm{bro}})\dot{Q}_{\mathrm{c}}\big(C_{\mathrm{a}} - \lambda_{\mathrm{b:tis}}C_{\mathrm{tis}}\big), \tag{17}$$

respectively. Here,

$$C_{\bar{v}} := q_{\text{liv}}\lambda_{\text{b:liv}}C_{\text{liv}} + (1 - q_{\text{liv}})\lambda_{\text{b:tis}}C_{\text{tis}} \tag{18}$$

and

$$C_{\text{a}} := (1 - q_{\text{bro}})\lambda_{\text{b:air}}C_{\text{A}} + q_{\text{bro}}\lambda_{\text{muc:air}}C_{\text{bro}}/\lambda_{\text{muc:b}} \tag{19}$$

are the associated concentrations in mixed venous and arterial blood, respectively. Moreover, we state that measured (end-tidal) breath concentrations equal bronchial levels, i.e.,

$$C_{\text{measured}} = C_{\text{bro}}. \tag{20}$$

The decoupled case $D = q_{\text{bro}} = 0$ will be excluded further on in this paper as it lacks physiological relevance.

Some fundamental model properties are discussed in Appendix A. In particular, the components of the state variable $\mathbf{c} := (C_{\text{bro}}, C_{\text{A}}, C_{\text{liv}}, C_{\text{tis}})^T$ remain non-negative, bounded and will approach a globally asymptotically stable equilibrium $\mathbf{c}^e(\mathbf{u})$ once the measurable external inputs $\mathbf{u} := (\dot{V}_{\text{A}}, \dot{Q}_{\text{c}}, V_{\text{T}}, \lambda_{\text{muc:air}}(C_{\text{water}}), C_{\text{I}})$ affecting the system are fixed. This corresponds, e.g., to the situation encountered during rest or constant workload.

3.2.2 Steady state relationships and interpretation of the stratified conductance parameter D

Assume that the system is in steady state and we know the associated end-tidal breath concentration $C_{\text{measured}} = C_{\text{bro}}$. Furthermore, we define the bronchial and alveolar ventilation-perfusion ratio to be

$$r_{\text{bro}} := \frac{\dot{V}_{\text{A}}}{q_{\text{bro}}\dot{Q}_{\text{c}}} \quad \text{and} \quad r_{\text{A}} := \frac{\dot{V}_{\text{A}}}{(1 - q_{\text{bro}})\dot{Q}_{\text{c}}},$$

respectively. If $D = 0$ we deduce that

$$\begin{aligned} &C_{\text{measured}} = C_{\text{bro}} = \\ &\quad \frac{r_{\text{bro}}C_{\text{I}} + (1 - q_{\text{bro}})\lambda_{\text{b:air}}C_{\text{A}}}{(1 - q_{\text{bro}})\frac{\lambda_{\text{muc:air}}}{\lambda_{\text{muc:b}}} + r_{\text{bro}}} = \frac{r_{\text{bro}}C_{\text{I}} + (1 - q_{\text{bro}})C_{\bar{v}}}{(1 - q_{\text{bro}})\frac{\lambda_{\text{muc:air}}}{\lambda_{\text{muc:b}}} + r_{\text{bro}}} = \frac{r_{\text{bro}}C_{\text{I}} + C_{\text{a}}}{\frac{\lambda_{\text{muc:air}}}{\lambda_{\text{muc:b}}} + r_{\text{bro}}}, \end{aligned} \tag{21}$$

corresponding to purely bronchial gas exchange. On the other hand, for $D \to \infty$ it can be shown by simple algebra that

$$\begin{aligned} &C_{\text{measured}} = C_{\text{bro}} = \\ &C_{\text{A}} = \frac{r_{\text{A}}C_{\text{I}} + C_{\bar{v}}}{q_{\text{bro}}\frac{\lambda_{\text{muc:air}}}{\lambda_{\text{muc:b}}} + (1 - q_{\text{bro}})\lambda_{\text{b:air}} + r_{\text{A}}} = \frac{C_{\text{a}}}{q_{\text{bro}}\frac{\lambda_{\text{muc:air}}}{\lambda_{\text{muc:b}}} + (1 - q_{\text{bro}})\lambda_{\text{b:air}}}. \end{aligned} \tag{22}$$

In the following, let $C_{\text{I}} = 0$. Note that then in both cases the physiological boundary condition $C_{\bar{v}} \geq C_{\text{a}}$ is respected. Substituting $q_{\text{bro}} = 0$ into (22) yields the well-known Farhi equations describing purely alveolar gas exchange.

Consequently, D defines the location of gas exchange in accordance with Section 3.1.3, while q_{bro} determines to what extent the bronchial compartment acts as an inert tube. In this sense, Equations (14)–(17) define a generalized description of gas exchange including several known models as special cases. This hierarchy is summarized in Fig. 4.

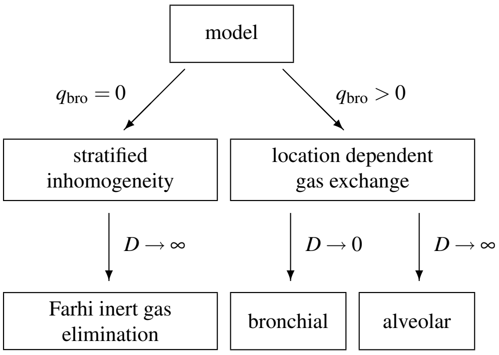

Fig. 4 Equations (14)–(17) viewed as generalized model including several gas exchange mechanisms as special cases ($C_{\mathrm{I}} = 0$).

For perspective – as has been rationalized in the case of acetone in Section 3.1.3 and is likely to be a common characteristic for all highly water soluble VOCs – the stratified conductance parameter D will be close to zero during rest and is expected to increase with tidal volume and/or flow rate [84,5]. We propose to model this dependency as

$$D := D^{\mathrm{rest}} + k_{\mathrm{diff},1} \max\{0, V_{\mathrm{T}} - V_{\mathrm{T}}^{\mathrm{rest}}\} + k_{\mathrm{diff},2} \max\{0, \dot{V}_{\mathrm{A}} - \dot{V}_{\mathrm{A}}^{\mathrm{rest}}\},\ k_{\mathrm{diff},j} \geq 0, \quad (23)$$

which will further be justified in Section 4.3.

From a practical point of view, we stress the fact that if D is close to zero, calculating blood levels from C_{measured} by using Equation (21) or taking advantage of this expression for normalization and/or correction purposes is critical due to the possibly large influence of the term r_{bro} as well as due to the high degree of uncertainty with respect to q_{bro} and $\lambda_{\mathrm{muc:air}}$. Particularly, from the aforementioned facts this means that measured breath concentrations of acetone (and generally highly water soluble substances) determined during resting conditions and free breathing can be rather misleading indicators for endogenous levels, even if sampling occurs under well defined standard conditions (for instance – as is common practice – using CO_2- and/or flow-controlled extraction from the end-tidal exhalation segment [40,11]). This has first been recognized in the context of breath alcohol measurements revealing experimentally obtained blood-breath concentration ratios of ethanol during tidal breathing that are unexpectedly high compared with in vitro partition coefficients [34]. An elegant approach proposed to circumvent this problem is isothermal rebreathing [34, 63], which aims at creating conditions where (cf. Equation (21))

$$C_{\text{measured}} = C_{\text{I}} = C_{\text{A}} = C_{\text{bro}} = \frac{r_{\text{bro}} C_{\text{bro}} + (1 - q_{\text{bro}}) C_{\bar{\text{v}}}}{(1 - q_{\text{bro}}) \lambda_{\text{b:air}} + r_{\text{bro}}} = \frac{C_{\bar{\text{v}}}}{\lambda_{\text{b:air}}} = \frac{C_{\text{a}}}{\lambda_{\text{b:air}}} \tag{24}$$

from which the mixed venous blood concentration can easily be determined by multiplying the measured rebreathing concentration with the anticipated blood:air partition coefficient at body temperature. A quantitative evaluation of this experimental technique by means of the above model can be found in the technical report [42].

4 Model validation and estimation

4.1 A priori identifiability

One of the purposes of our tentative model is to provide a basis for estimating (unknown) compartment concentrations $\mathbf{c}$ as well as certain acetone-specific parameters $p_j \in \{k_{\text{pr}}, k_{\text{met}}, v_{\max}, k_{\text{m}}, D, q_{\text{bro}}^{\text{rest}}\}$ from the knowledge of measured breath and blood concentrations y. Often over-looked, a necessary requirement in this framework is the a priori (or structural) identifiability/observability of the model, which basically checks whether in an ideal context of an error-free model and continuous, noise-free measurements there exist functions $\mathbf{u}$ (or, in other words, conductible experiments) such that the associated output y (the accessible data) carries enough information to enable an unambiguous determination of all unknown states and parameters. Particularly, this avoids an inherent over-parameterization of the model. As the time evolution of the system (14)–(17) for a given $\mathbf{u}$ is fixed once the initial conditions $\mathbf{c}_0$ at the start of the experiment are known, the analysis of a priori identifiability/observability hence amounts to studying (local) injectivity of y with respect to $\mathbf{c}_0$ and the parameters p_j under scrutiny. Evidently, if such a property does not hold then any attempt to reliably estimate these quantities from y is doomed to failure from the start, as two entirely different parameter combinations can yield exactly the same data. In the present context, *generic* a priori identifiability/observability for $\mathbf{c}_0$ and any selection of parameters p_j as above was confirmed by interpreting the latter as additional states with time derivative zero and subjecting the augmented system to the Hermann-Krener rank criterion [27] (see also [38, Sect. 3.1]). In particular, the sufficient condition in [38, Lemma 1] was fulfilled for both $y = C_{\text{bro}}$ and $y = C_{\text{a}}$ as given in Equations (20) and (19), respectively.

4.2 Simulation of exposure data and model calibration

Generally speaking, in vivo data on acetone *dynamics* in the human organism are very limited. Indeed, experimental efforts to date have centered on quantifying bioaccumulation/biotransformation as well as body burden within occupational exposure settings. The study by Wigaeus et al. [91] represents the most extensive research in this context (including breath as well as simultaneous blood measurements), thus rendering it as a convenient benchmark for confirming the appropriateness of models involving descriptions of systemic acetone distribution, cf. [44,57].

In the following we will calibrate the unknown kinetic rate constants, the fractional bronchial blood flow, as well as the equilibrium tissue levels $\mathbf{c}_0$ at rest, by subjecting the proposed model to the *Series 1* exposure scenario published in [91]. Briefly, this data set comprises acetone concentration profiles in exhaled breath, arterial and (presumably peripheral) venous blood of eight normal male volunteers, who were exposed to an atmosphere containing 1.3 mg/l of acetone over a period of two hours. Particularly, all measurements correspond to resting conditions.

Since the major goal here is to extract approximate nominal values for the above-mentioned physiological parameters rather than individual estimates, the model will be fitted to the *pooled* data of all eight test subjects. For this purpose, we assume that the exposure starts after ten minutes of quiet tidal breathing, i.e., the inhaled concentration is given by the scaled indicator function $C_\mathrm{I}(t) = 1.3\,\chi_{[10,130]}(t)$ and set alveolar ventilation and cardiac output to constant resting values $\dot{V}_\mathrm{A}^\mathrm{rest} = 6$ l/min and $\dot{Q}_\mathrm{c}^\mathrm{rest} = 5.8$ l/min, respectively [57,44]. Tissue volumes and partition coefficients are as in Table 3 for a male of height 180 cm and weight 70 kg. Since the nominal acetone concentration in hepatic venous blood is a priori unknown, acetone metabolism is assumed to follow a Michaelis-Menten kinetics with a fixed apparent Michaelis constant $k_\mathrm{m} = 84$ mg/l (cf. Equation (11)). Our aim is to determine the parameter vector $\mathbf{p} = (v_\mathrm{max}, k_\mathrm{pr}, D^\mathrm{rest}, q_\mathrm{bro}^\mathrm{rest})$ as well as the nominal endogenous steady state levels $\mathbf{c}_0$ by solving the ordinary least squares problem

$$\operatorname*{arg\,min}_{\mathbf{c}_0,\mathbf{p}} \sum_{i=0}^{N} \big(C_{\mathrm{a},i} - C_\mathrm{a}(t_i)\big)^2, \quad \text{s.t.} \begin{cases} \mathbf{g}(\mathbf{u}_0, \mathbf{c}_0, \mathbf{p}) = 0 & \text{(steady state)} \\ \mathbf{c}_0, \mathbf{p} \geq 0 & \text{(positivity)} \\ q_\mathrm{bro}^\mathrm{rest} \leq 0.05 & \text{(normalization)} \\ C_\mathrm{a}(0) = 1 \text{ mg/l} & \text{(endog. arterial level)} \end{cases} \tag{25}$$

Here, $\mathbf{g}$ is the right-hand side of the ODE system (14)–(17), $C_{\mathrm{a},i}$ is the measured arterial blood concentration at time instant t_i, whereas the predicted arterial concentration C_a is defined as in Equation (19). The endogenous level $C_\mathrm{a}(0) = 1$ mg/l was chosen in accordance with the population mean values given in [35,91].

The above minimization problem was solved by implementing a multiple shooting routine [13] in *Matlab*. This iterative method can be seen as a generalization of the standard Gauss-Newton algorithm for solving constrained ordinary least squares problems, treating (25) in the framework of multipoint boundary value problems (see also [79] for an early illustration). Further details regarding the general scope of multiple shooting as well as its superior stability compared with classical solution schemes can be found in [12,13,66,85]. For a variety of applications and modifications proposed for covering PDEs and delay differential equations the interested reader is referred to [60,28].

Derivatives of C_a with respect to $(\mathbf{c}_0, \mathbf{p})$ were computed by simultaneously solving the associated variational equations [23]. The minimization procedure was repeated several times with randomly assigned starting values in the interval $(0,1)$. Convergence was assumed to be achieved when the maximum componentwise relative change between two successive parameter refinements was less than 0.1%, resulting in the same estimates for all trials considered, cf. Table 2. Figure 5 shows that the calibrated model can faithfully reproduce the basic features of the observed data.

Remark 2 The practical identifiability of the estimates in Table 2 was examined by calculating the rank of the extended Jacobian $J := \left(S^T\ Z^T\right)$, where S is the sensitivity function matrix having rows

$$S_{i,-} := \left(\frac{\partial C_{\mathrm{a}}(t_{i-1})}{\partial \mathbf{p}}\quad \frac{\partial C_{\mathrm{a}}(t_{i-1})}{\partial \mathbf{c}_0}\right), \tag{26}$$

and Z denotes the Jacobian associated with the equality constraints in (25). More specifically, we adopted the standard *numerical* rank criterion

$$\operatorname{rank} J = \max\{k;\ \sigma_k > \varepsilon \|J\|_\infty\}, \tag{27}$$

where $\sigma_1 \geq \sigma_2 \geq \ldots \geq 0$ are the singular values of J and $\varepsilon = 10^{-8}$ reflects the maximum relative error of the calculated sensitivities [21]. Accordingly, we find that J has full rank, suggesting that all estimated quantities are practically identifiable [16,30].

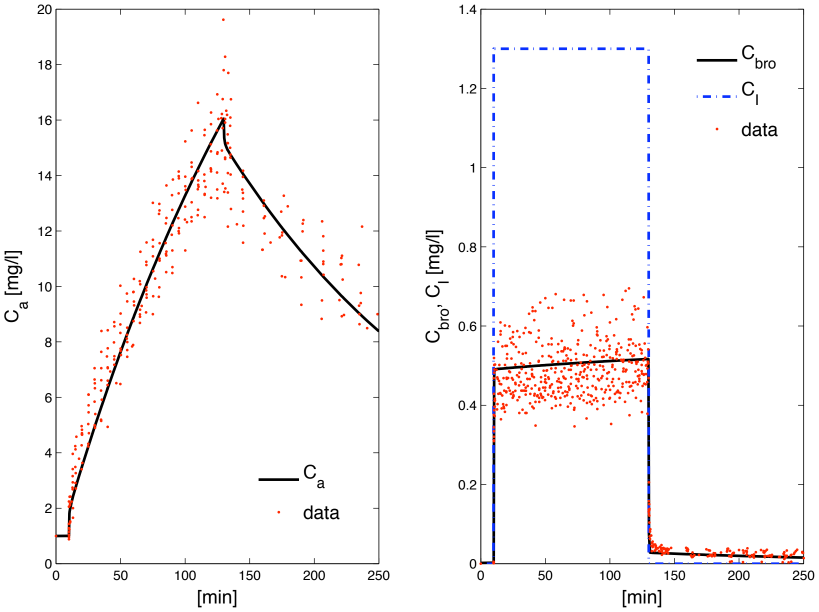

Fig. 5 Model fitted to the *Series 1* exposure data published by Wigaeus et al. [91]. Data correspond to *pooled* observations from eight normal healthy volunteers. First panel: observed versus predicted arterial concentrations, cf. Equation (19). Second panel: observed versus predicted breath concentrations, cf. Equation (20).

Table 2 Fitted parameter values according to Fig. 5.

	$v_{\max}$ (mg/min/kg$^{0.75}$)	k_{pr} (mg/min)	D^{rest} (l/min)	$q_{\text{bro}}^{\text{rest}}$ (%)	$(C_{\text{bro}}, C_{\text{A}}, C_{\text{liv}}, C_{\text{tis}})$ (mg/l)
Anticipated	0.31	≤ 2	0	1	$(0.0011, *, *, *)$
Optimized	0.62	0.19	0	0.43	$(0.0016, 0.0029, 0.58, 0.72)$

Anticipated (literature) values of $\mathbf{c}_0$ and $\mathbf{p}$ compare favorably to those obtained by the aforementioned minimization, thus consolidating the physiological plausibility of the extracted estimates. In particular, the fitted value of the gas exchange location parameter $D^{\text{rest}} = 0$ agrees well with what is expected from the theoretical discussion in Section 3.2.2. The rate at which endogenous acetone forms in healthy adults as a result of normal fat catabolism is not known. However, from the study on acetone metabolism in lean and obese humans during starvation ketosis published by Reichard et al. [69] a rather conservative upper bound for k_{pr} can be derived to lie in the range of 2 mg/min. A diminished fractional bronchial perfusion $q_{\text{bro}}^{\text{rest}}$ might reflect the fact that the assumption of diffusion equilibrium between the mucosa lining and the deeper vascularized sections of the airway wall is rather stringent, so that actually less acetone is transported away from the peripheral bronchial tract via the bloodstream. On the other hand $q_{\text{bro}}^{\text{rest}} = 0.01$ refers to the entire bronchial circulation rather than only the part contributing to anatomic right-to-left shunt as discussed in Section 3.1.1. The fitted steady state value for the measured breath concentration $C_{\text{measured}}(0) = C_{\text{bro}}(0) = 0.0016$ mg/l during normal breathing at rest is only slightly higher than the observed levels spreading around 500 ppb (corresponding to about 0.0011 mg/l) [74,40].

Remark 3 Fig. 5 clearly illustrates the necessity of taking into account the conducting airways as an additional compartment for exchange of highly soluble substances. In particular, the observed data profiles are in sharp contrast to the classical Farhi inert tube description predicting arterial blood concentrations to be directly proportional to (alveolar) breath concentrations. Contrarily, by taking into account pre-alveolar uptake as discussed in Section 3.1.1, the accumulation of exogenous acetone in the systemic circulation is expected to be delayed due to the small contribution of bronchial blood flow to overall perfusion.

Remark 4 The population spread of the fitted parameters within the study cohort could be assessed, e.g., by a Bayesian [58] or mixed effects approach [43], which, however would be beyond the scope of this paper. Here, the major aim rather is to demonstrate the flexibility of the model in covering a wide spectrum of different experimental scenarios.

From an operational perspective, one may consider the results stated in the previous paragraphs as a model tuning procedure for resting conditions. Accordingly, in the remaining part of this paper both the stratified conductance parameter and the fractional bronchial blood flow during rest will be frozen at their fitted values

$D^{\text{rest}} = 0$ and $q_{\text{bro}}^{\text{rest}} = 0.0043$, respectively. Moreover, due to the high value of the apparent Michaelis constant k_{m} as compared to the estimated acetone concentration $\lambda_{\text{b:liv}} C_{\text{liv}}$ in hepatic venous blood, acetone clearance from the liver can safely be postulated to obey linear kinetics in the sequel, cf. Equation (12). In particular, the extracted value of $k_{\text{lin}} = v_{\text{max}}/k_{\text{m}} = 0.0074$ l/kg$^{0.75}$/min is interpreted as an intrinsic property of acetone metabolism (with inter-individual variation being introduced by multiplication with the 0.75 power of body weight). Hence, k_{met} as in Equation (12) will be treated as a constant known parameter in the sequel.

4.3 Ergometer data sets and comparative evaluations

As has been indicated in the introduction, a primary motivation for this work was to develop a model elucidating the features of breath acetone behavior observed during moderate workload ergometer challenges. A representative profile corresponding to one *single* normal healthy volunteer is shown in Fig. 6, cf. [40]. As has been demonstrated there, end-tidal acetone levels in response to exercise generally resemble the profile of alveolar ventilation and inhalation volume, showing abrupt increases and drops in the range of 10 – 40% at the onsets and stops of the individual workload periods, respectively (see also Fig. 6 (a), first panel). Similarly, a series of auxiliary experiments carried out by means of the same instrumental setup revealed that increasing tidal volume during rest results in increased breath acetone concentrations, while increasing respiratory frequency has a less pronounced impact, cf. Fig. 6 (b). Both effects appear to support the hypothesis of Section 3.1.3 that acetone exchange is strongly influenced by volume and speed of inhalation and hence suggest that any model not incorporating this mechanism will fail to reproduce the above results. In particular, note that from the viewpoint of the classical Farhi description (1) the profile in Fig. 6 is rather counter-intuitive. For instance, during hyperventilation acetone supply from the bloodstream will stay roughly constant, while a drastic increase in ventilation should enhance the dilution of alveolar air and would therefore be expected to (slightly) *decrease* the corresponding breath concentration.

From the above, we view exercise and hyperventilation scenarios as an interesting control setting for testing the physiological adequacy of the newly developed model. Moreover, these two scenarios provide a novel framework for contrasting the predictive power of distinct mechanistic frameworks put forward in the literature. Specifically, in the following we shall use the individual acetone behavior as depicted in Fig. 6 as the basis for comparing the performance of Equations (14)–(17) with the standard formulation due to Farhi as well as with the physiological compartment model introduced by Mörk et al. [57], which can be viewed as the current state of the art in acetone pharmacokinetic modeling. In particular, the latter model represents a first improvement over the Farhi description in that it has been found capable of adequately reproducing the bioaccumulation behavior presented in the previous subsection. Mörk et al. also discuss several shortcomings of earlier models proposed in this context.

While the Farhi description is just a special case our model (by setting $q_{\text{bro}} = 0$ and $D \rightarrow \infty$, cf. Fig. 4), the model of Mörk et al. will be re-implemented in slightly modified form by replacing the mass balance Equations (14)–(15) of the respiratory tract with Equations (4)–(7) in [57]. The body compartments remain unchanged. Additional parameter values are taken from [57].

Letting $C_\mathrm{I} \equiv 0$ and $C_\mathrm{bro}(0) = 1.3$ μg/l, the initial compartment concentrations for all three models as well as the endogenous production rate k_pr can uniquely be determined by solving the associated steady state equations at $t_0 = 0$. This completely specifies the models by Farhi and Mörk et al.. Contrarily, the response for the present model is computed by solving the ordinary least squares problem

$$\operatorname*{arg\,min}_{\alpha} \sum_{i=0}^{N} \big(y_i - C_\mathrm{bro}(t_i)\big)^2, \quad \text{s.t. } \alpha \geq 0 \quad \text{(positivity)} \tag{28}$$

within the time interval $[t_0, t_N] = [0, t_\mathrm{max}]$. Here, $y_i = C_{\mathrm{measured},i}$ is the observed acetone concentration at time instant t_i and $\alpha = (\alpha_1, \dots, \alpha_{m-1})$ is the coefficient vector for the piecewise linear function

$$\hat{D}(t) := \sum_{j=1}^{m-1} \alpha_j S_j(t), \quad S_j(t) := \begin{cases} \frac{t - s_{j-1}}{s_j - s_{j-1}} & t \in [s_{j-1}, s_j] \\ \frac{s_{j+1} - t}{s_{j+1} - s_j} & t \in [s_j, s_{j+1}] \\ 0 & \text{otherwise} \end{cases} \tag{29}$$

used for deriving an approximation of the time-varying stratified conductance parameter $D \in [0, \infty)$ on m subintervals covering the time span $[t_0 = s_0, t_\mathrm{max} = s_m]$. Here the nodes s_j are chosen to result in an equidistant partition of about 0.5 min, cf. Fig. 6, third panel. For simulation purposes the measured physiological functions are converted to input function handles $\mathbf{u}$ by applying a local smoothing procedure to the associated data and interpolating the resulting profiles with splines. The aforementioned optimization problem was solved as described in Section 4.2. Fig. 6 summarizes the results of these calculations.

The visually good fit can formally be assessed by residual analysis. Plots of the resulting residuals versus time and versus model predictions clearly exhibit random patterns, suggesting that the assumptions of i.i.d., homoscedastic additive measurement errors underlying ordinary least squares methodology are reasonable [10]. Furthermore, no statistically significant autocorrelation among the residuals or cross-correlation between the residuals and the measured inputs could be detected, indicating that the model has picked up the decisive dynamics underlying the data.

While all three models will describe the steady state at rest, only Equations (14)–(17) tolerably capture the entire observable dynamical behavior. Particularly, the predictions resulting from the models due to Farhi and Mörk et al. are almost indistinguishable within this experimental regime and both will depart only slightly from the initial equilibrium states.

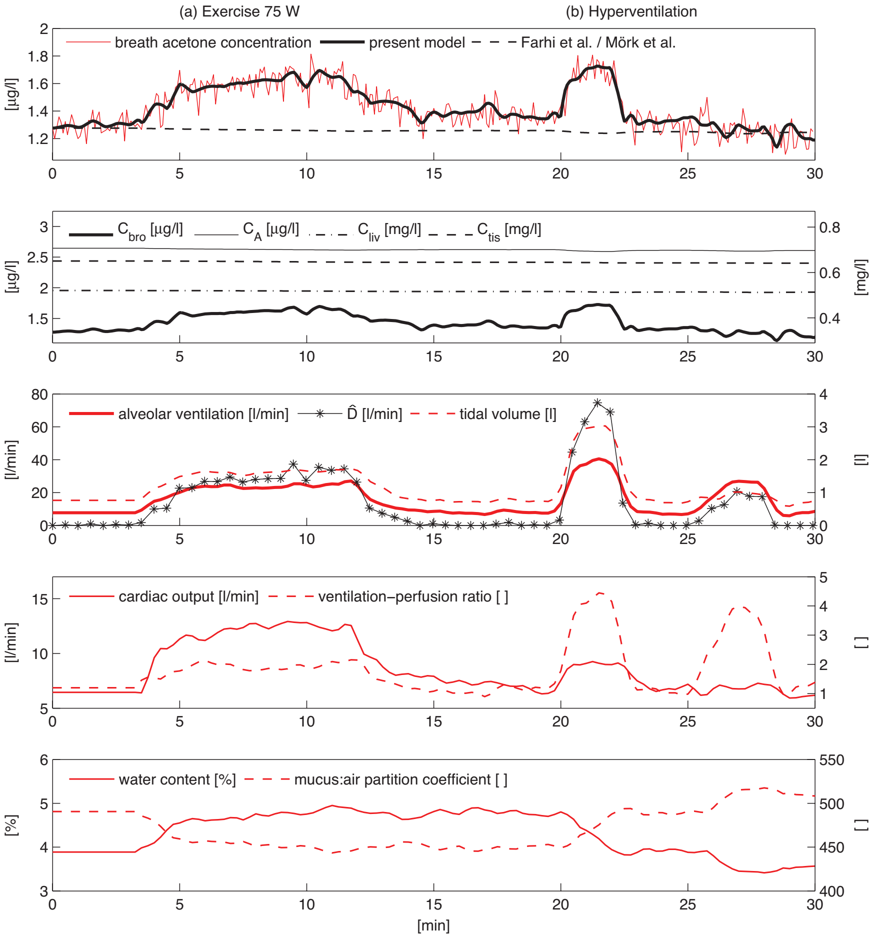

Fig. 6 Typical profile of end-exhaled acetone concentrations in response to the following physiological regime: rest (0-3 min), ergometer challenge at 75 W (3-12 min), rest (12-20 min), hyperventilation with increased tidal volume (20-22 min), rest (22-25 min), high-frequency hyperventilation (25-28 min), rest (28-30 min). Data correspond to one representative healthy male volunteer from the study cohort in [40]. Measured or derived quantities according to the experimental setup are indicated in red, while black tracings correspond to simulated variables. *Panel 1*: Measured acetone concentrations in end-tidal breath and associated model predictions; *Panel 2*: Simulated compartment concentrations according to Equations (14)–(17); *Panel 3–5*: Measured physiological parameters according to Table 1. The mucus:air partition coefficient $\lambda_{\mathrm{muc:air}}$ and the time-varying stratified conductance parameter $\hat{D}$ are derived from Equation (7) and (29), respectively.

In contrast, the newly proposed model indeed appears to incorporate the decisive physiological mechanism underlying the step-shaped dynamics of breath acetone concentrations in response to constant load exercise and hyperventilation. Correspondingly, according to the second panel in Fig. 6, measured (i.e., bronchial) levels markedly differ from the alveolar ones due to the effective diffusion barrier between the two spaces represented by a value of $D^{\mathrm{rest}} \approx 0$, cf. Section 4.2. As soon as tidal volume and/or respiratory frequency are increased, this barrier will vanish to some extent according to the processes discussed in Section 3.2.2, thus causing $C_{\mathrm{bro}} = C_{\mathrm{measured}}$ to approach a value closer to C_{A}. In contrast, C_{A} itself as well as the breath acetone profiles simulated by means of the other two models remain relatively constant. This is consistent with the behavior expected from the Farhi formulation, predicting minimal sensitivity of alveolar concentrations with respect to fluctuations of the ventilation-perfusion ratio for highly soluble trace gases. In other words, the major part of short-term variability observable in breath acetone concentrations during free breathing can be attributed to airway gas exchange, with minimal changes of the underlying blood and tissue concentrations. In particular, note that with the present model the observed acetone dynamics can again be captured by assuming a constant endogenous production rate $k_{\mathrm{pr}} \approx 0.17$ mg/min. The above-mentioned reasoning appears to agree with previous observations in the literature, where the excretion of acetone has been demonstrated to increase during moderate exercise [72].

Remark 5 The high degree of interplay between $\hat{D}$ and $\dot{V}_{\mathrm{A}}$ as well as V_{T} discernible in the third panel of Fig. 6 suggests that the time-dependency of D can essentially be captured using these two respiratory variables. Different heuristic relationships might be investigated in this context, see Equation (23) for instance. Correspondingly, by repeating the optimization procedure in (28) with α being replaced by $(k_{\mathrm{diff},1}, k_{\mathrm{diff},2})$ we find that the associated model response again is in good agreement with the observed data. The practical identifiability of these two parameters at their optimized values $k_{\mathrm{diff},1} = 14.9$ and $k_{\mathrm{diff},2} = 0.76$ was confirmed along the lines of Remark 2. Hence, the parameterization in Equation (23) might be used to reduce the originally infinite dimensional estimation problem for D to two degrees of freedom.

While in Section 4.1 it has been confirmed that the model is structurally locally observable, we stress the fact that data corresponding to exercise or hyperventilation tests as presented above will usually not allow for a joint *numerical* estimation of some of the above variables. For perspective, it should be clear from the approximately constant profile of C_{liv} in Fig. 6 that k_{pr} and k_{met} can hardly be assessed simultaneously, as both values are coupled via a single steady state equation associated with Equation (16). Using similar reasoning, smaller values of $q_{\mathrm{bro}}^{\mathrm{rest}}$ (leading to larger steady state concentrations $C_{\mathrm{A}}(0)$) can be compensated for by smaller constants $k_{\mathrm{diff},j}$, giving rise to an almost identical model output. Again, such a situation might formally be investigated by means of practical identifiability techniques (cf. [38, Sect. 3.1]), e.g., by calculating pairwise correlation coefficients between the sensitivities of the model output with respect to the parameters under scrutiny. In the present context, values of these indices associated with $(k_{\mathrm{met}}, k_{\mathrm{pr}})$ as well as $(k_{\mathrm{diff},1}, q_{\mathrm{bro}}^{\mathrm{rest}})$ and $(k_{\mathrm{diff},2}, q_{\mathrm{bro}}^{\mathrm{rest}})$ are close to 1 or -1, thereby revealing a substantial degree of collinearity between the corresponding sensitivities and providing strong indications that a proper estimation of any of these pairs on the basis of moderate exercise challenges as above cannot be anticipated. Such identifiability issues can only be circumvented by designing (multi-)experimental regimes guaranteeing a sufficiently large and independent influence of all parameters to be estimated.

5 Discussion and critical remarks

The main intention of this section is to critically review and clarify some of the assumptions underlying the model derivation as well as to indicate some potential improvements of the present formulation.

Diffusion equilibrium in the bronchial tract. While it is commonly agreed upon that the transport of inert gases between the alveolar space and end-capillary blood is perfusion-limited [86], a similar premise in the case of airway gas exchange remains less certain. Experimental and theoretical evidence appears to favor the view that although a diffusion equilibrium might be attained at the air-mucus interface [83, 46], the bronchial epithelial tissue can constitute an effective diffusion barrier between the mucus lining and the bronchial circulation. The magnitude of this diffusional resistance is probably substance-specific, with an inverse relation to molecular weight [80]. In this sense, the fractional bronchial blood flow q_{bro} has to be interpreted as effective perfusion of those mucosal tissue layers for which an instantaneous equilibrium with air can be achieved [45]. Specifically, q_{bro} might differ for distinct compounds. While animal models seem to support the assumption of a complete equilibration between air stream and bronchial circulation in the special case of acetone [80], it might be necessary to include a diffusion limitation between these two compartments in order to extend the validity of the model over a wider range of highly water soluble VOCs. The statistical significance of such generalizations can then be assessed by employing residual based comparison techniques for nested models as described in [10,9]. However, at the current stage of research and given the limited data on the behavior of breath trace gases having similar physico-chemical characteristics like acetone, we prefer to maintain a parameterization as parsimonious as possible.

Continuous ventilation and temperature dependence. Due to the tidal nature of breathing, bronchial as well as alveolar gas concentrations will vary throughout the breathing cycle, following a roughly periodical pattern during normal breathing. These variations can be captured by considering two separate mass balance systems, describing the dynamics of the associated concentrations for each inhalation and exhalation phase, respectively [53,45,5]. While such microscopic formulations are of paramount importance for resolving events within one individual respiratory cycle, when looking at the mid- to long-term behavior of breath VOCs we are rather interested in the global dynamics of the averaged compartmental concentrations. This approach leads to models of continuous ventilation with a unidirectional gas stream and has the enormous operational advantage of reducing the model structure to one single mass balance system.

Variable temperature distributions in the bronchial compartment are represented by a single mean temperature $\bar{T}$ according to Equation (5), thereby lumping together our ignorance regarding the exact temperature profile along the airways. Different functional relationships might be investigated here.

In summary, this paper introduces a novel compartmental description of pulmonary gas exchange and systemic distribution of blood-borne, highly blood and water soluble VOCs, which faithfully captures experimentally determined end-tidal acetone profiles for normal healthy subjects during free breathing in distinct physiological states. Particularly, the model has been tested in the framework of external exposure as well as exercise scenarios and illuminates the discrepancies between observed and theoretically predicted blood-breath ratios of acetone during resting conditions, i.e., in steady state. In this sense, the present formulation provides a good compartmental perspective of acetone exhalation kinetics and is expected to contribute to a better understanding of distribution, transport, biotransformation and excretion processes of acetone in different functional units of the organism as well as their impact on the observed breath concentration.

While we are well aware of the fact that the number of data sets used for model validation is relatively small, exposure and exercise regimes currently are the only published experimental settings covering non-steady state acetone behavior in humans. Further validation will thus have to await additional experimental efforts. In this context, preliminary tests conducted with the intention of extending the range of applicability for the presented formulation to the framework of isothermal rebreathing show promising results [42].

The emphasis of this work has been laid on deriving a sound mathematical formulation flexible enough to cover a wide spectrum of possible VOC behavior, while simultaneously maintaining physiological plausibility as well as a clear-cut interpretation of the involved parameters. Care has been taken to keep the parameterization as parsimonious as possible, thereby constructing a novel “minimal” model respecting fundamental physiological boundary conditions, such as boundedness of the associated trajectories and the existence of a globally asymptotically stable equilibrium state. While a complete sensitivity and practical identifiability analysis was beyond the scope of this paper and has to be matched to the particular experimental framework in which the model will be used, general concepts from structural and practical identifiability have been exploited in order to provide some indications regarding the information content of the observable breath level with respect to the endogenous situation.

Acknowledgements We are indebted to the reviewers for several helpful suggestions. Julian King is a recipient of a DOC fellowship at the Breath Research Institute of the Austrian Academy of Sciences. The research leading to these results has received funding from the European Communitys Seventh Framework Programme (FP7/2007-13) under grant agreement No. 217967. We appreciate funding from the Austrian Federal Ministry for Transport, Innovation and Technology (BMVIT/BMWA, project 818803, KIRAS). Gerald Teschl and Julian King acknowledge support from the Austrian Science Fund (FWF) under Grant No. Y330. We greatly appreciate the generous support of the government of Vorarlberg and its governor Landeshauptmann Dr. Herbert Sausgruber.

A Some fundamental model properties

Equations (14)–(17) can be written as a time-varying linear inhomogeneous ODE system

$$\dot{\mathbf{c}} = A(\mathbf{u},\mathbf{p})\mathbf{c} + \mathbf{b}(\mathbf{u},\mathbf{p}) =: \mathbf{g}(\mathbf{u},\mathbf{c},\mathbf{p}) \tag{30}$$

in the state variable $\mathbf{c} := (C_{\text{bro}}, C_{\text{A}}, C_{\text{liv}}, C_{\text{tis}})^T$, which is dependent on a time-independent parameter vector $\mathbf{p}$ as well as on a vector $\mathbf{u} := (\dot{V}_{\text{A}}, \dot{Q}_{\text{c}}, V_{\text{T}}, \lambda_{\text{muc:air}}(C_{\text{water}}), C_{\text{I}})$ of bounded, non-negative functions lumping together all measured variables. The associated measurement equation reads

$$y = C_{\text{measured}} = (1,0,0,0)\,\mathbf{c} =: h(\mathbf{c}). \tag{31}$$

In the present paragraph we are going to discuss some qualitative properties of the system presented. Firstly, as the system is linear, for any given initial condition $\mathbf{c}(0)$ there is a unique global solution. Moreover, A is a Metzler matrix and $\mathbf{b} \geq 0$. Consequently $c_i = 0$ implies that $\dot{c}_i \geq 0$ for every component and it follows that the trajectories remain non-negative. Thus, (30) constitutes a positive system with the state $\mathbf{c}$ evolving within the positive orthant $\mathbb{R}^n_{>0} := \{\mathbf{c} \,|\, \mathbf{c} \in \mathbb{R}^n,\ c_i > 0,\ i = 1, \ldots, n\}$, where $n = 4$.

Proposition 1 *All solutions of* (30) *starting in* $\mathbb{R}^n_{>0}$ *remain bounded.*

Proof This can be shown by considering the total mass $m := \sum \tilde{V}_i c_i \geq 0$ and noting that

$$\dot{m} = k_{\text{pr}} - k_{\text{met}} \lambda_{\text{b:liv}} C_{\text{liv}} + \dot{V}_{\text{A}}(C_{\text{I}} - C_{\text{bro}}). \tag{32}$$

Taking into account positivity of the solutions and the involved parameters this shows that C_{liv} is bounded from above for bounded C_{I}, since the assumption that C_{liv} is unbounded yields a contradiction. Analogously, C_{bro} and C_{A} can be shown to be bounded by considering $\tilde{m} := \tilde{V}_{\text{bro}} C_{\text{bro}} + \tilde{V}_{\text{A}} C_{\text{A}} + \tilde{V}_{\text{tis}} C_{\text{tis}}$ and similarly for C_{tis}.

Furthermore, it can be proven that under physiological steady state conditions, i.e., for constant $\mathbf{u}$, the above system has a globally asymptotically stable equilibrium $\mathbf{c}^e := -A^{-1}\mathbf{b}$. To this end it suffices to show that the time-invariant matrix A is Hurwitz, i.e., all real parts of the associated eigenvalues are negative.

Proposition 2 *Suppose* $\mathbf{u}$ *is time-independent. Then the real parts of all eigenvalues of* $A(\mathbf{u}, \mathbf{p})$ *are non-positive. They are strictly negative if* $\det(A(\mathbf{u}, \mathbf{p})) \neq 0$.

Moreover, $\det(A(\mathbf{u}, \mathbf{p})) = 0$ *if and only if either* $\dot{Q}_{\text{c}}$ *vanishes or two of the quantities* $\dot{V}_{\text{A}}, q_{\text{liv}}, k_{\text{met}}$ *vanish.*

Proof For this it is sufficient to confirm that A is diagonally dominant, i.e., there exists a vector $\mathbf{z} > 0$ such that the row vector $\mathbf{z}^T A$ is non-positive. This is a simple consequence of the fact that in such a case A can be shown to be similar to a matrix $\tilde{A}$ which has the claimed property. Indeed, if we define the diagonal matrix $U := \operatorname{diag}(z_1, \ldots, z_n)$ and set $\tilde{A} := UAU^{-1}$, it holds that

$$\tilde{a}_{jj} + \sum_{i \neq j} |\tilde{a}_{ij}| = a_{jj} + \sum_{i \neq j} \frac{a_{ij} z_i}{z_j} = \frac{1}{z_j} (\mathbf{z}^T A)_j \leq 0 \tag{33}$$

for all j since A is Metzler. Moreover, note that $\tilde{a}_{jj} < 0$ for all j. Hence, the first claim will follow from Gershgorin's circle theorem. The required vector $\mathbf{z}$ follows from

$$(\tilde{V}_{\text{bro}}, \tilde{V}_{\text{A}}, \tilde{V}_{\text{liv}}, \tilde{V}_{\text{tis}})A = (-\dot{V}_{\text{A}}, 0, -k_{\text{met}} \lambda_{\text{b:liv}}, 0).$$

Moreover, the only case when the real part of an eigenvalue can vanish is when it lies on the boundary of a circle touching the imaginary axis, that is, when an eigenvalue is zero. This proves the first part.

To show the second part one verifies that

$$\det(A) = \dot{Q}_{\text{c}} \big((\vartheta_1 \dot{V}_{\text{A}} + \vartheta_2 k_{\text{met}}) q_{\text{liv}} \dot{Q}_{\text{c}} + \vartheta_3 \dot{V}_{\text{A}} k_{\text{met}} \big) \tag{34}$$

with $\vartheta_j > 0$.

This completes the minimal set of properties which necessarily should to be satisfied in any valid model of concentration dynamics. In particular, global asymptotic stability for the autonomous system ensures that – starting from arbitrary initial values – the compartmental concentrations will approach a unique equilibrium state once the physiological inputs $\mathbf{u}$ affecting the system are fixed. Obviously, this is of paramount importance when aiming at the description of processes exhibiting pronounced steady states (which in the context of breath gas analysis corresponds, e.g., to the situation encountered during rest or constant workload [40]) and a prerequisite for orchestrating reproducible experiments. Hence, in the context of VOC modeling, any approach not incorporating this property will lack a fundamental characteristic of the observed data.

Remark 6 For perspective, we stress the fact that if the rate of metabolism in Equations (14)–(17) is described by saturation rather than linear kinetics, i.e., if the term $k_{\mathrm{met}}C_{\mathrm{liv}}\lambda_{\mathrm{b:liv}}$ in Equation (16) is replaced by Equation (11), the system becomes essentially nonlinear. However, all conclusions drawn so far remain generally valid. Firstly, by applying the Mean Value Theorem note that the Michaelis-Menten term above is Lipschitz and so again a global Lipschitz property holds for the right-hand side of the resulting ODE system. Positivity and boundedness of the solutions for arbitrary inputs $\mathbf{u}$ can be established in analogy with the arguments in the last paragraphs. Effectively, in order to show boundedness from above, we first note that Equation (32) now reads

$$\dot{m} = k_{\mathrm{pr}} - \frac{v_{\mathrm{max}}C_{\mathrm{liv}}\lambda_{\mathrm{b:liv}}}{k_{\mathrm{m}} + C_{\mathrm{liv}}\lambda_{\mathrm{b:liv}}} + \dot{V}_{\mathrm{A}}(C_{\mathrm{I}} - C_{\mathrm{bro}}) \tag{35}$$

and as a result C_{bro} is unconditionally bounded if $\dot{V}_{\mathrm{A}} > 0$. From Equation (14) it then follows that C_{A} must be bounded and subsequently $C_{\bar{\mathrm{v}}}$ (and hence C_{liv} as well as C_{tis}) are bounded using Equation (15). In the case $\dot{V}_{\mathrm{A}} = 0$, the inequality $k_{\mathrm{pr}} \leq v_{\mathrm{max}}$ is necessary and sufficient for boundedness. Necessity is easily deduced from the fact that $k_{\mathrm{pr}} > v_{\mathrm{max}}$ implies $\dot{m} > 0$ and consequently m (i.e., at least one component c_i) is unbounded. Conversely, the constraint $k_{\mathrm{pr}} \leq v_{\mathrm{max}}$ ensures that C_{liv} is bounded and hence the same arguments as in the linear case apply.

In order to establish the existence of a globally asymptotically stable equilibrium point for fixed $\mathbf{u}$ we adopt a result on monotone systems taken from Leenheer et. al. [48], see also [31]. For monotone systems in general with applications to biological systems we refer to [76,8]. Firstly, note that the steady state relation associated with Equation (16) now becomes

$$0 = C_{\mathrm{liv}}^2 + a_1 C_{\mathrm{liv}} + a_0 \tag{36}$$

with $a_0 < 0$. Thus, there exists a unique positive steady state solution for the liver concentration C_{liv} and consequently the same can be confirmed to hold true for the other components of $\mathbf{c}$ as well. As a consequence, it follows that the model has a unique equilibrium point in the non-negative orthant $\mathscr{X} := \mathbb{R}^n_{\geq 0}$. Moreover, note that for the right-hand side $\mathbf{g}$ of the underlying ODE system (cf. Equation (30)) it holds that

$$\frac{\partial g_i}{\partial c_j} \geq 0 \text{ for } i \neq j,\ i,j \in \{1,\ldots,n\}, \tag{37}$$

i.e., the system is cooperative. This term stems from the fact that a given component is positively affected by the remaining ones. For linear systems, an equivalent characterization is that the corresponding system matrix A is Metzler. A well-known result on this type of system asserts that the associated semiflow $\Phi : \mathbb{R}_{\geq 0} \times \mathbb{R}^n \to \mathbb{R}^n$, $(t, \mathbf{c}_0) \mapsto \Phi_t(\mathbf{c}_0) := \mathbf{c}(t)$ is monotone with respect to the natural (componentwise) partial order on $\mathbb{R}^n$ given by

$$\mathbf{c} \leq \mathbf{z} \text{ if and only if } c_i \leq z_i,\ i \in \{1,\ldots,n\}.$$

That is, Φ preserves the order of the initial conditions (see [76], Prop. 3.1.1), i.e., for $\mathbf{c}_0, \tilde{\mathbf{c}}_0 \in \mathbb{R}^n$ the condition $\mathbf{c}_0 \leq \tilde{\mathbf{c}}_0$ implies that $\Phi_t(\mathbf{c}_0) \leq \Phi_t(\tilde{\mathbf{c}}_0)$ for $t \in [0,\infty)$. As a third requirement, since all trajectories are bounded and the system evolves within the closed state space $\mathscr{X} \subset \mathbb{R}^n$ it follows that for every $\mathbf{c} \in \mathscr{X}$ the corresponding semi-orbit $O(\mathbf{c}) := \{\Phi_t(\mathbf{c}),\ t \geq 0\}$ has compact closure. In summary, we are now in the situation to apply Theorem 5 of [48], which asserts that the aforementioned properties are sufficient for the unique equilibrium point in $\mathscr{X}$ to be globally attractive.

B Nomenclature

Table 3 Basic model parameters and nominal values during rest; LBV denotes the lean body volume in liters calculated according to $\text{LBV} = -16.24 + 0.22\,\text{bh} + 0.42\,\text{bw}$, with body height (bh) and weight (bw) given in cm and kg, respectively [57].

Parameter	Symbol	Nominal value (units)
Compartment concentrations		
bronchioles	C_{bro}, C_{measured}	1 (μg/l) [74]
alveoli	C_{A}	
arterial	C_{a}	1 (mg/l) [91,35]
mixed-venous	$C_{\bar{\text{v}}}$	
liver	C_{liv}	
tissue	C_{tis}	
inhaled (ambient)	C_{I}	
Compartment volumes		
bronchioles	V_{bro}	0.1 (l) [57]
mucosa	V_{muc}	0.005 (l) [57]
alveoli	V_{A}	4.1 (l) [57]
end-capillary	$V_{\text{c}'}$	0.15 (l) [29]
liver	V_{liv}	0.0285 LBV (l) [57]
blood liver	$V_{\text{liv,b}}$	1.1 (l) [64]
tissue	V_{tis}	0.7036 LBV (l) [57]
Fractional blood flows at rest		
fractional flow bronchioles	q_{bro}	0.01 [52]
fractional flow liver	q_{liv}	0.32 [57]
Partition coefficients at body temperature		
blood:air	$\lambda_{\text{b:air}}$	340 [7, 18]
mucosa:air	$\lambda_{\text{muc:air}}$	392 [78,44]
blood:liver	$\lambda_{\text{b:liv}}$	1.73 [44]
blood:tissue	$\lambda_{\text{b:tis}}$	1.38 [7]
Metabolic and diffusion constants		
linear metabolic rate	k_{met}	0.0074 (l/min/kg$^{0.75}$) [fitted]
saturation metabolic rate	v_{max}	0.31 (mg/min/kg$^{0.75}$) [44]
apparent Michaelis constant	k_{m}	84 (mg/l) [44]
endogenous production	k_{pr}	0.19 (mg/min) [fitted]
stratified conductance	D	0 (l/min) [fitted]

References

1. Amann, A., Poupart, G., Telser, S., Ledochowski, M., Schmid, A., Mechtcheriakov, S.: Applications of breath gas analysis in medicine. Int. J. Mass Spectrometry **239**, 227–233 (2004)
2. Amann, A., Smith, D. (eds.): Breath Analysis for Clinical Diagnosis and Therapeutic Monitoring. World Scientific, Singapore (2005)
3. Amann, A., Spanel, P., Smith, D.: Breath analysis: the approach towards clinical applications. Mini reviews in Medicinal Chemistry **7**, 115–129 (2007)
4. Ammann, C., Brunner, A., Spirig, C., Neftel, A.: Technical note: Water vapour concentration and flux measurements with PTR-MS. Atmos. Chem. Phys. Discuss. **6**, 5329–5355 (2006)

5. Anderson, J.C., Babb, A.L., Hlastala, M.P.: Modeling soluble gas exchange in the airways and alveoli. Ann. Biomed. Eng. **31**, 1402–22 (2003)
6. Anderson, J.C., Hlastala, M.P.: Breath tests and airway gas exchange. Pulm. Pharmacol. Ther. **20**, 112–117 (2007)
7. Anderson, J.C., Lamm, W.J., Hlastala, M.P.: Measuring airway exchange of endogenous acetone using a single-exhalation breathing maneuver. J. Appl. Physiol. **100**, 880–9 (2006)
8. Angeli, D., Sontag, E.: Monotone control systems. IEEE Trans. Automat. Control **48**, 1684–1698 (2003)
9. Banks, H.T., Fitzpatrick, B.G.: Statistical methods for model comparison in parameter estimation problems for distributed systems. Journal of Mathematical Biology **28**, 501–527 (1990)
10. Banks, H.T., Tran, H.T.: Mathematical and experimental modeling of physical and biological processes. CRC Press, Boca Raton (2009)
11. Birken, T., Schubert, J., Miekisch, W., Noldge-Schomburg, G.: A novel visually CO_2 controlled alveolar breath sampling technique. Technol. Health Care **14**, 499–506 (2006)
12. Bock, H.G.: Numerical treatment of inverse problems in chemical reaction kinetics. In: K. Ebert, P. Deuflhard, W. Jäger (eds.) Modelling of chemical reaction systems. Springer, Heidelberg (1981)
13. Bock, H.G.: Randwertproblemmethoden zur Parameteridentifizierung in Systemen nichtlinearer Differentialgleichungen. Ph.D. thesis, Universität Bonn (1987)
14. Brundin, T.: Temperature of mixed venous blood during exercise. Scand. J. Clin. Lab. Invest. **35**, 539–543 (1975)
15. Clewell, H.J., Gentry, P.R., Gearhart, J.M., Covington, T.R., Banton, M.I., Andersen, M.E.: Development of a physiologically based pharmacokinetic model of isopropanol and its metabolite acetone. Toxicol. Sci. **63**, 160–172 (2001)
16. Cobelli, C., DiStefano, J.J.: Parameter and structural identifiability concepts and ambiguities: a critical review and analysis. Am. J. Physiol. **239**, R7–24 (1980)
17. Cope, K.A., Watson, M.T., Foster, W.M., Sehnert, S.S., Risby, T.H.: Effects of ventilation on the collection of exhaled breath in humans. J. Appl. Physiol. **96**, 1371–1379 (2004)
18. Crofford, O.B., Mallard, R.E., Winton, R.E., Rogers, N.L., Jackson, J.C., Keller, U.: Acetone in breath and blood. Trans. Am. Clin. Climatol. Assoc. **88**, 128–39 (1977)
19. Farhi, L.E.: Elimination of inert gas by the lung. Respiration Physiology **3**, 1–11 (1967)
20. Galassetti, P.R., Novak, B., Nemet, D., Rose-Gottron, C., Cooper, D.M., Meinardi, S., Newcomb, R., Zaldivar, F., Blake, D.R.: Breath ethanol and acetone as indicators of serum glucose levels: an initial report. Diabetes Technol. Ther. **7**, 115–123 (2005)
21. Golub, G.H., Van Loan, C.F.: Matrix computations, 3rd edn. Johns Hopkins University Press, Baltimore (1996)
22. Hahn, C.E.W., D., F.A.: Gas exchange modelling: no more gills, please. Br. J. Anaesth. **91**, 2–15 (2003)
23. Hairer, E., P., N.S., Wanner, G.: Solving ordinary differential equations 1: Nonstiff problems, 2nd edn. Springer, Berlin (1993)
24. Hanna, L.M., Scherer, P.W.: Regional control of local airway heat and water vapor losses. J. Appl. Physiol. **61**, 624–632 (1986)
25. Hanna, L.M., Scherer, P.W.: A theoretical model of localized heat and water vapor transport in the human respiratory tract. J. Biomech. Eng. **108**, 19–27 (1986)
26. Herbig, J., Titzmann, T., Beauchamp, J., Kohl, I.: Buffered end-tidal (BET) sampling - a novel method for real-time breath-gas analysis. Journal of Breath Research **2**, 1–9 (2008)
27. Hermann, R., Krener, A.J.: Nonlinear controllability and observability. IEEE Trans. Automat. Control **22**, 728–740 (1977)
28. Horbelt, W., Timmer, J., Voss, H.: Parameter estimation in nonlinear delayed feedback systems from noisy data. Physics Letters A **299**, 513–521 (2002)
29. Hughes, J.M.B., Morell, N.W.: Pulmonary Circulation. From basic mechanisms to clinical practice. Imperial College Press, London (2001)
30. Jacquez, J.A., Perry, T.: Parameter estimation: local identifiability of parameters. Am. J. Physiol. **258**, E727–E736 (1990)
31. Ji-Fa, J.: On the global stability of cooperative systems. Bull. London Math. Soc. **26**, 455–458 (1994)
32. Johanson, G.: Modelling of respiratory exchange of polar solvents. Ann. Occup. Hyg. **35**, 323–339 (1991)
33. Jones, A.W.: Effects of temperature and humidity of inhaled air on the concentration of ethanol in a man's exhaled breath. Clin. Sci. **63**, 441–445 (1982)

34. Jones, A.W.: Role of rebreathing in determination of the blood-breath ratio of expired ethanol. J. Appl. Physiol. **55**, 1237–1241 (1983)
35. Kalapos, M.P.: On the mammalian acetone metabolism: from chemistry to clinical implications. Biochim. Biophys. Acta **1621**, 122–39 (2003)
36. Keck, L., Hoeschen, C., Oeh, U.: Effects of carbon dioxide in breath gas on proton transfer reaction-mass spectrometry (PTR-MS) measurements. Int. J. Mass Spectrometry **270**, 156–165 (2008)
37. Keller, U., Schnell, H., Girard, J., Stauffacher, W.: Effect of physiological elevation of plasma growth hormone levels on ketone body kinetics and lipolysis in normal and acutely insulin-deficient man. Diabetologia **26**, 103–108 (1984)
38. King, J.: Mathematical modeling of blood-gas kinetics for the volatile organic compounds isoprene and acetone. Ph.D. thesis, Leopold-Franzens University Innsbruck (2010)
39. King, J., Koc, H., Unterkofler, K., Mochalski, P., Kupferthaler, A., Teschl, G., Teschl, S., Hinterhuber, H., Amann, A.: Physiological modeling of isoprene dynamics in exhaled breath. Journal of Theoretical Biology **267**, 626–637 (2010)
40. King, J., Kupferthaler, A., Unterkofler, K., Koc, H., Teschl, S., Teschl, G., Miekisch, W., Schubert, J., Hinterhuber, H., Amann, A.: Isoprene and acetone concentration profiles during exercise on an ergometer. Journal of Breath Research **3**, 027,006 (16pp) (2009)
41. King, J., Mochalski, P., Kupferthaler, A., Unterkofler, K., Koc, H., Filipiak, W., Teschl, S., Hinterhuber, H., Amann, A.: Dynamic profiles of volatile organic compounds in exhaled breath as determined by a coupled PTR-MS/GC-MS study. Physiol. Meas. **31**, 1169–1184 (2010)
42. King, J., Unterkofler, K., Kupferthaler, A., Teschl, G., Teschl, S., Koc, H., Hinterhuber, H., Amann, A.: A modeling based evaluation of isothermal rebreathing for breath gas analysis of highly soluble volatile organic compounds (2010). URL `https://homepages.fhv.at/ku/karl/pdfs/IRB2010.pdf`. Technical Report, Breath Research Institute of the Austrian Academy of Sciences.
43. Kuhn, E., Lavielle, M.: Maximum likelihood estimation in nonlinear mixed effects models. Computational Statistics & Data Analysis **49**, 1020–1038 (2005)
44. Kumagai, S., Matsunaga, I.: Physiologically based pharmacokinetic model for acetone. Occup. Environ. Med. **52**, 344–352 (1995)
45. Kumagai, S., Matsunaga, I.: A lung model describing uptake of organic solvents and roles of mucosal blood flow and metabolism in the bronchioles. Inhal. Toxicol. **12**, 491–510 (2000)
46. Kumagai, S., Oda, H., Matsunaga, I., Kosaka, H., Akasaka, S.: Uptake of 10 polar organic solvents during short-term respiration. Toxicol. Sci. **48**, 255–263 (1999)
47. Kundu, S.K., Bruzek, J.A., Nair, R., Judilla, A.M.: Breath acetone analyzer: diagnostic tool to monitor dietary fat loss. Clin. Chem. **39**, 87–92 (1993)
48. Leenheer, P., Angeli, D., Sontag, E.: Monotone chemical reaction networks. Journal of Mathematical Chemistry **41**, 295–314 (2007)
49. Lindberg, L., Brauer, S., Wollmer, P., Goldberg, L., Jones, A., Olsson, S.: Breath alcohol concentration determined with a new analyzer using free exhalation predicts almost precisely the arterial blood alcohol concentration. Forensic Science International **168**, 200–207 (2007)
50. Lindinger, W., Hansel, A., Jordan, A.: On-line monitoring of volatile organic compounds at pptv levels by means of proton-transfer-reaction mass spectrometry (PTR-MS) - medical applications, food control and environmental research. Int. J. Mass Spectrometry **173**, 191–241 (1998)
51. Lindinger, W., Hansel, A., Jordan, A.: Proton-transfer-reaction mass spectrometry (PTR-MS): on-line monitoring of volatile organic compounds at pptv levels. Chem. Soc. Rev. **27**, 347–354 (1998)
52. Lumb, A.B.: Nunn's Applied Respiratory Physiology, 6th edn. Butterworth-Heinemann, Oxford (2005)
53. Martonen, T.B., Wilson, A.F.: Theoretical basis of single breath gas absorption tests. Journal of Mathematical Biology **14**, 203–220 (1982)
54. McFadden, E.R., Pichurko, B.M., Bowman, H.F., Ingenito, E., Burns, S., Dowling, N., Solway, J.: Thermal mapping of the airways in humans. J. Appl. Physiol. **58**, 564–570 (1985)
55. Miekisch, W., Schubert, J.K.: From highly sophisticated analytical techniques to life-saving diagnostics: Technical developments in breath analysis. Trends in Analytical Chemistry **25**, 665–673 (2006)
56. Mohrman, D.E., Heller, L.J.: Cardiovascular Physiology, 6th edn. Lange Medical Books/McGraw-Hill, New York (2006)
57. Mörk, A.K., Johanson, G.: A human physiological model describing acetone kinetics in blood and breath during various levels of physical exercise. Toxicol. Lett. **164**, 6–15 (2006)
58. Mörk, A.K., Jonsson, F., Johanson, G.: Bayesian population analysis of a washin-washout physiologically based pharmacokinetic model for acetone. Toxicol. Appl. Pharmacol. **240**, 423–432 (2009)

59. Morris, N.R., Ceridon, M.L., Beck, K.C., Strom, N.A., Schneider, D.A., Mendes, E.S., Wanner, A., Johnson, B.D.: Exercise-related change in airway blood flow in humans: Relationship to changes in cardiac output and ventilation. Respiratory Physiology & Neurobiology **162**, 204–209 (2008)
60. Müller, T.G., Timmer, J.: Parameter identification techniques for partial differential equations. International Journal of Bifurcation and Chaos **14**, 2053–2060 (2004)
61. O'Hara, M.E., Clutton-Brock, T.H., Green, S., Mayhew, C.A.: Endogenous volatile organic compounds in breath and blood of healthy volunteers: examining breath analysis as a surrogate for blood measurements. Journal of Breath Research **3**, 027,005 (10pp) (2009)
62. O'Hara, M.E., O'Hehir, S., Green, S., Mayhew, C.A.: Development of a protocol to measure volatile organic compounds in human breath: a comparison of rebreathing and on-line single exhalations using proton transfer reaction mass spectrometry. Physiol. Meas. **29**, 309–30 (2008)
63. Ohlsson, J., Ralph, D.D., Mandelkorn, M.A., Babb, A.L., Hlastala, M.P.: Accurate measurement of blood alcohol concentration with isothermal rebreathing. J. Stud. Alcohol **51**, 6–13 (1990)
64. Ottesen, J.T., Olufsen, M.S., Larsen, J.K.: Applied Mathematical Models in Human Physiology. SIAM, Philadelphia (2004)
65. Owen, O.E., Trapp, V.E., Skutches, C.L., Mozzoli, M.A., Hoeldtke, R.D., Boden, G., Reichard Jr., G.A.: Acetone metabolism during diabetic ketoacidosis. Diabetes **31**, 242–248 (1982)
66. Peifer, M., Timmer, J.: Parameter estimation in ordinary differential equations for biochemical processes using the method of multiple shooting. IET Systems Biology **1**, 78–88 (2007)
67. Rao, Y.V.C.: An Introduction to Thermodynamics. Wiley Eastern, New Delhi (1995)
68. Reddy, M.B., Yang, R.S.H., Clewell III, H.J., Andersen, M.E. (eds.): Physiologically based pharmacokinetic modeling: science and applications. Wiley, Hoboken (2005)
69. Reichard G. A., J., Haff, A.C., Skutches, C.L., Paul, P., Holroyde, C.P., Owen, O.E.: Plasma acetone metabolism in the fasting human. J. Clin. Invest. **63**, 619–26 (1979)
70. Rieder, J., Lirk, P., Ebenbichler, C., Gruber, G., Prazeller, P., Lindinger, W., Amann, A.: Analysis of volatile organic compounds: possible applications in metabolic disorders and cancer screening. Wien. Klin. Wochenschr. **113**, 181–5 (2001)
71. Scheid, P., Hlastala, M.P., Piiper, J.: Inert gas elimination from lungs with stratified inhomogeneity: Theory. Respiration Physiology **44**, 299–309 (1981)
72. Schrikker, A.C., de Vries, W.R., Zwart, A., Luijendijk, S.C.: The excretion of highly soluble gases by the lung in man. Pflügers Arch. **415**, 214–219 (1989)
73. Schwarz, K., Filipiak, W., Amann, A.: Determining concentration patterns of volatile compounds in exhaled breath by PTR-MS. Journal of Breath Research **3**, 027,002 (15pp) (2009)
74. Schwarz, K., Pizzini, A., Arendacka, B., Zerlauth, K., Filipiak, W., Schmid, A., Dzien, A., Neuner, S., Lechleitner, M., Scholl-Burgi, S., Miekisch, W., Schubert, J., Unterkofler, K., Witkovsky, V., Gastl, G., Amann, A.: Breath acetone – aspects of normal physiology related to age and gender as determined in a PTR-MS study. Journal of Breath Research **3**, 027,003 (9pp) (2009)
75. Smith, D., Spanel, P., Davies, S.: Trace gases in breath of healthy volunteers when fasting and after a protein-calorie meal: a preliminary study. J. Appl. Physiol. **87**, 1584–8 (1999)
76. Smith, H.L.: Monotone dynamical systems: An introduction to the theory of competitive and cooperative systems. AMS, Providence (1995)
77. Sonntag, D.: Important new Values of the Physical Constants of 1986, Vapour Pressure Formulations based on ITS-90, and Psychrometer Formulae. Z. Meteorol. **70**, 340–344 (1990)
78. Staudinger, J., Roberts, P.V.: A critical compilation of Henry's law constant temperature dependence relations for organic compounds in dilute aqueous solutions. Chemosphere **44**, 561–576 (2001)
79. Stoer, J., Bulirsch, R.: Introduction to numerical analysis, 2nd edn. Springer, New York (1993)
80. Swenson, E.R., Robertson, H.T., Polissar, N.L., Middaugh, M.E., Hlastala, M.P.: Conducting airway gas exchange: diffusion-related differences in inert gas elimination. J. Appl. Physiol. **72**, 1581–1588 (1992)
81. Tassopoulos, C.N., Barnett, D., Fraser, T.R.: Breath-acetone and blood-sugar measurements in diabetes. Lancet **1**, 1282–6 (1969)
82. Thrall, K.D., Schwartz, R.E., Weitz, K.K., Soelberg, J.J., Foureman, G.L., Prah, J.D., Timchalk, C.: A real-time method to evaluate the nasal deposition and clearance of acetone in the human volunteer. Inhal. Toxicol. **15**, 523–38 (2003)
83. Tsu, M.E., Babb, A.L., Ralph, D.D., Hlastala, M.P.: Dynamics of heat, water, and soluble gas exchange in the human airways: 1. A model study. Ann. Biomed. Eng. **16**, 547–571 (1988)
84. Tsu, M.E., Babb, A.L., Sugiyama, E.M., Hlastala, M.P.: Dynamics of soluble gas exchange in the airways: 2. Effects of breathing conditions. Respiration Physiology **83**, 261–276 (1991)

85. Voss, H.U., Timmer, J., Kurths, J.: Nonlinear dynamical system identification from uncertain and indirect measurements. International Journal of Bifurcation and Chaos **14**, 1905–1933 (2004)
86. Wagner, P.D.: The multiple inert gas elimination technique (MIGET). Intensive Care Med. **34**, 994–1001 (2008)
87. Wagner, P.D., Saltzman, H.A., West, J.B.: Measurement of continuous distributions of ventilation-perfusion ratios - theory. J. Appl. Physiol. **36**, 588–599 (1974)
88. Wang, G., Maranelli, G., Perbellini, L., Raineri, E., Brugnone, F.: Blood acetone concentration in "normal people" and in exposed workers 16 h after the end of the workshift. Int. Arch. Occup. Environ. Health **65**, 285–289 (1994)
89. Warneke, C., van der Veen, C., Luxembourg, S., de Gouw, J.A., Kok, A.: Measurements of benzene and toluene in ambient air using proton-transfer-reaction mass spectrometry: calibration, humidity dependence, and field intercomparison. Int. J. Mass Spectrometry **207**, 167–182 (2001)
90. West, J.B.: Respiratory Physiology. The Essentials, 7th edn. Lippincott Williams & Wilkins, Baltimore (2005)
91. Wigaeus, E., Holm, S., Astrand, I.: Exposure to acetone. Uptake and elimination in man. Scand. J. Work Environ. Health **7**, 84–94 (1981)

Chapter 9

Paper E: A modeling based evaluation of isothermal rebreathing for breath gas analyses of highly soluble volatile organic compounds

JULIAN KING ET AL.

Preprint, 2010

Parts of this paper have been presented as a poster as well as in oral form at the conference
BGA 2010, Greifswald, Germany, June 7-9, 2010.

Noname manuscript No.
(will be inserted by the editor)

A modeling-based evaluation of isothermal rebreathing for breath gas analyses of highly soluble volatile organic compounds

Julian King · Karl Unterkofler ·
Gerald Teschl · Susanne Teschl · Helin Koc ·
Hartmann Hinterhuber · Anton Amann

Received: date / Accepted: date

J. King
Breath Research Institute of the Austrian Academy of Sciences
Rathausplatz 4, A-6850 Dornbirn, Austria
E-mail: julian.king@oeaw.ac.at

K. Unterkofler
Vorarlberg University of Applied Sciences and
Breath Research Unit of the Austrian Academy of Sciences
Hochschulstr. 1, A-6850 Dornbirn, Austria
E-mail: karl.unterkofler@fhv.at

G. Teschl
University of Vienna, Faculty of Mathematics
Nordbergstr. 15, A-1090 Wien, Austria
E-mail: gerald.teschl@univie.ac.at

S. Teschl
University of Applied Sciences Technikum Wien
Höchstädtplatz 5, A-1200 Wien, Austria
E-mail: susanne.teschl@technikum-wien.at

H. Koc
Vorarlberg University of Applied Sciences
Hochschulstr. 1, A-6850 Dornbirn, Austria

H. Hinterhuber
Innsbruck Medical University, Department of Psychiatry
Anichstr. 35, A-6020 Innsbruck, Austria

A. Amann (corresponding author)
Innsbruck Medical University, Univ.-Clinic for Anesthesia and
Breath Research Institute of the Austrian Academy of Sciences
Anichstr. 35, A-6020 Innsbruck, Austria
E-mail: anton.amann@oeaw.ac.at, anton.amann@i-med.ac.at

Abstract Over the past decade, much advance has been made in the attempt to exploit the diagnostic and metabolic information encapsulated in a number of endogenous volatile organic compounds (VOCs) appearing in human exhaled breath. However, the causal understanding of the relationships between breath concentrations of such trace gases and their underlying systemic levels clearly lags behind the enormous analytical progress in this field. In particular, formal means for evaluating the information content and predictive power of various sampling regimes are still lacking.

Here, we focus on isothermal rebreathing which has been proposed as an experimental technique for estimating the *alveolar* levels of hydrophilic VOCs in exhaled breath. Using the prototypic test compound acetone we demonstrate that the end-tidal breath profiles of such substances during isothermal rebreathing show characteristics that contradict the conventional pulmonary inert gas elimination theory due to Farhi. On the other hand, these profiles can reliably be captured by virtue of a previously developed mathematical model for the general exhalation kinetics of highly soluble, blood-borne VOCs, which explicitly takes into account airway gas exchange as major determinant of the observable breath output.

This model allows for a mechanistic analysis of various rebreathing protocols suggested in the literature. In particular, it clarifies the discrepancies between *in vitro* and measured blood:breath ratios of hydrophilic VOCs and yields further quantitative insights into the physiological components of isothermal rebreathing.

Keywords breath gas analysis · volatile organic compounds · rebreathing · acetone · modeling

PACS 87.80.-y · 82.80.Ms

1 Introduction

Recently, several efforts have been undertaken to complement measurements of volatile organic compounds (VOCs) occurring in human breath with adequate physical models mapping substance-specific distribution mechanisms in the pulmonary tract as well as in the body tissues. Some major breath VOCs have already been investigated in this form, e.g., during exercise conditions or exposure scenarios [18, 21, 27, 2, 23]. Such mechanistic descriptions of the observable exhalation kinetics will not only contribute to a better understanding regarding the relevance of the extracted breath concentration with respect to the endogenous situation (i.e., with respect to blood or tissue concentrations, which in turn can be seen as the decisive quantities for exploiting the diagnostic potential of breath VOCs [1]) but might also serve as valuable tools for evaluating the information content and predictive power of various experimental regimes proposed for breath gas analytical investigations. Within this context, the main focus of this article will be on a modeling-based review of isothermal rebreathing, which has been proposed as an experimental technique for estimating the *alveolar* levels of hydrophilic exhaled trace gases [16, 30]. This class of compounds has been demonstrated to significantly interact with the water-like mucus membrane lining the conductive airways, an effect which has become known as wash-in/wash-out behavior. For further details we refer to [2,3]. As a phenomenological consequence, exhaled breath concentrations of such highly water soluble substances tend to be diminished on their way up from the deeper respiratory tract to the airway opening. The resulting discrepancies between the “true” alveolar and the measured breath concentration can be substantial (even if breath samples are drawn in a strictly standardized manner employing, e.g., CO_2- or flow-controlled sampling) and will depend on a variety of factors, such as airway temperature profiles and airway perfusion as well as breathing patterns.

In particular, the above-mentioned effect considerably departs from the classical Farhi description of pulmonary inert gas exchange [8], on the basis of which the operational dogma has been established that end-tidal air will reflect the alveolar level and that arterial concentrations can be assessed by simply multiplying this value with the blood:gas partition coefficient $\lambda_{\mathrm{b:air}}$ at body temperature. This “common knowledge” has first been put into question in the field of breath alcohol testing, revealing *observable* blood-breath concentration ratios of ethanol during tidal breathing that are unexpectedly high compared to the partition coefficient derived in vitro [16]. Similarly, excretion data (defined as the ratio between steady state partial pressures in expired air and mixed venous blood) of highly water soluble compounds (including the MIGET test gas acetone) have been shown to underestimate the values anticipated by treating the airways as an inert tube [38,4].

In a previously published mathematical model for the breath gas dynamics of highly soluble trace gases, airway gas exchange is taken into account by separating the lungs into a bronchial and alveolar compartment, interacting via a diffusion barrier mimicking pre- and post-alveolar uptake [21]. This formulation has proven its ability to reliably capture both end-tidal breath profiles as well as systemic dynamics of acetone in a variety of experimental situations and will be used here for illuminating the physiological processes underlying isothermal rebreathing tests as carried out in the literature. For comparative reasons, the illustration here will mainly be limited to acetone, with possible extrapolations to other highly soluble VOCs indicated where appropriate.

2 Methods

2.1 Experiments

Extensive details regarding the experimental input of our investigations are given elsewhere [19]. Here, we will only briefly discuss the parts of the setup relevant for the present context. All phenomenological results in the sequel are obtained in conformity with the Declaration of Helsinki and with the necessary approvals by the Ethics Commission of Innsbruck Medical University.

The rebreathing system itself consists of a Tedlar bag with volume $\tilde{V}_{\mathrm{bag}} = 3$ l that can directly be connected to a spirometer headmask, from which *end-tidal* exhalation segments are drawn into a Proton Transfer Reaction Mass Spectrometer (PTR-MS; Ionicon Analytik GmbH, Innsbruck, Austria) as described in [19]. The bag is warmed to 37 ± 1 °C using a specially designed outer heating bag (Infroheat Ltd., Wolverhampton, UK) as described in [29]. This is intended to assist the thermal equilibration between the alveolar tract and the upper airways as well as to prevent condensation and subsequent losses of hydrophilic VOCs depositing onto water droplets forming on the surface wall of the bag. End-tidal acetone concentrations are determined by monitoring its protonated form at $m/z = 59$ (dwell time: 200 ms). Additionally, we routinely measure the mass-to-charge ratios $m/z = 21$ (isotopologue of the primary hydronium ions used for normalization; dwell time: 500 ms), $m/z = 37$ (first monohydrate cluster for estimating sample humidity; dwell time: 2 ms), $m/z = 69$ (protonated isoprene; dwell time: 200 ms), $m/z = 33$ (protonated methanol; dwell time: 200 ms) as well as the parasitic precursor ions NH_4^+ and O_2^+ at $m/z = 18$ and $m/z = 32$, respectively, with dwell times of 10 ms each. In particular, the pseudo concentrations associated with $m/z = 32$ determined according to the standard conversion formula (1) in [32] will be used as an indicator for the end-tidal partial partial pressure P_{O_2} of oxygen, relative to an assumed nominal steady state level at rest of about 100 mmHg. Similarly, calibrated pseudo concentrations corresponding to $m/z = 37$ are considered as surrogates for absolute sample humidity C_{water} [21]. Partial pressures P_{CO_2} of carbon dioxide are obtained via a separate sensor. Table 1 summarizes the measured quantities used in this paper. In general, breath concentrations will always refer to end-tidal levels. An underlying sampling interval of 5 s is applied for each variable.

Table 1 Summary of measured parameters together with some nominal literature values during rest, assuming ambient conditions; breath concentrations refer to end-tidal levels.

Variable	Symbol	Nominal value (units)
Cardiac output	$\dot{Q}_c$	6 (l/min) [26]
Alveolar ventilation	$\dot{V}_A$	5.2 (l/min) [36]
Acetone concentration	C_{measured}	1 (μg/l) [33]
CO_2 partial pressure	P_{CO_2}	40 (mmHg) [24]
Water content	C_{water}	4.7 (%) [13]
O_2 partial pressure	P_{O_2}	100 (mmHg) [24]

2.2 Physiological model

For the sake of completeness, the model structure is presented in Fig. 1, while for the associated compartmental mass balance equations we refer to the appendix and the original publication [21]. The body is divided into four distinct functional units, for which the underlying concentration dynamics of the VOC under scrutiny will be taken into account: bronchial/mucosal compartment (C_{bro}; gas exchange), alveolar/end-capillary compartment (C_A; gas exchange), liver (C_{liv}; production and metabolism) and tissue (C_{tis}; storage). The nomenclature is detailed in the legend of Fig. 1.

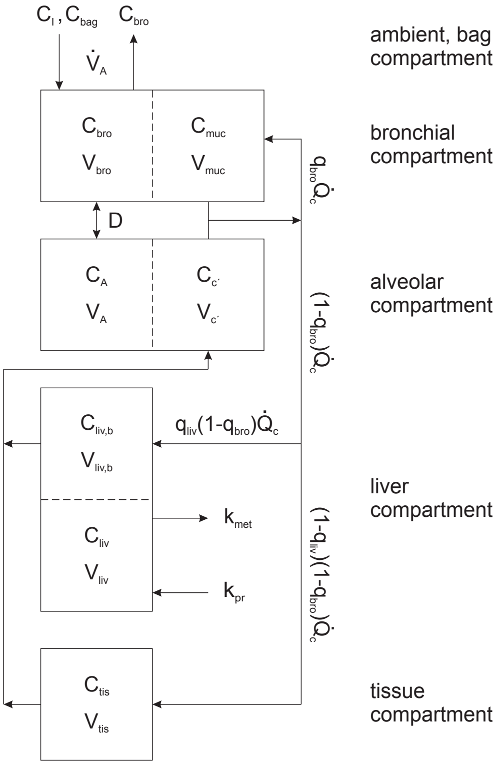
C_I, C_bag
C_bro
V̇_A
ambient, bag compartment
C_bro
V_bro
C_muc
V_muc
bronchial compartment
q_bro Q̇_c
D
C_A
V_A
C_c′
V_c′
alveolar compartment
(1-q_bro)Q̇_c
C_liv,b
V_liv,b
q_liv(1-q_bro)Q̇_c
C_liv
V_liv
k_met
k_pr
liver compartment
(1-q_liv)(1-q_bro)Q̇_c
C_tis
V_tis
tissue compartment

Fig. 1 Sketch of the model structure used for capturing dynamic VOC concentrations C. Subscripts connote as follows: bag, *rebreathing bag*; I, *inhaled*; bro, *bronchial*; muc, *mucosal*; A, *alveolar*; c′, *end-capillary*; liv, *liver*; tis, *tissue*; b, *blood*. Dashed boundaries indicate a diffusion equilibrium, governed by the respective partition coefficients λ, e.g., $\lambda_{\mathrm{muc:air}}$.

The measurement process is described by

$$C_{\mathrm{measured}} = C_{\mathrm{bro}}, \tag{1}$$

i.e., we assume that measured (end-tidal) breath concentrations reflect the bronchial levels.

In particular, for highly water and blood soluble compounds such as acetone the present model replaces the familiar Farhi equation describing the steady state relationship between inhaled (ambient) concentration C_{I}, measured breath concentration $C^{\mathrm{F}}_{\mathrm{measured}}$, mixed venous concentration $C_{\bar{\mathrm{v}}}$ and arterial concentration C_{a} during tidal breathing,

$$C^{\mathrm{F}}_{\mathrm{measured}} = C_{\mathrm{A}} = \frac{\frac{\dot{V}_{\mathrm{A}}}{\dot{Q}_{\mathrm{c}}} C_{\mathrm{I}} + C_{\bar{\mathrm{v}}}}{\lambda_{\mathrm{b:air}} + \frac{\dot{V}_{\mathrm{A}}}{\dot{Q}_{\mathrm{c}}}} = \frac{C_{\mathrm{a}}}{\lambda_{\mathrm{b:air}}}, \tag{2}$$

with the expression

$$C_{\mathrm{measured}} = C_{\mathrm{bro}} = \frac{r_{\mathrm{bro}} C_{\mathrm{I}} + (1 - q_{\mathrm{bro}}) C_{\bar{\mathrm{v}}}}{(1 - q_{\mathrm{bro}}) \frac{\lambda_{\mathrm{muc:air}}}{\lambda_{\mathrm{muc:b}}} + r_{\mathrm{bro}}} = \frac{r_{\mathrm{bro}} C_{\mathrm{I}} + C_{\mathrm{a}}}{\frac{\lambda_{\mathrm{muc:air}}}{\lambda_{\mathrm{muc:b}}} + r_{\mathrm{bro}}}. \tag{3}$$

Here, $q_{\mathrm{bro}} \ll 1$ is an estimate of the effective fractional bronchial perfusion (which might be substance-specific), while

$$r_{\mathrm{bro}} = \frac{\dot{V}_{\mathrm{A}}}{q_{\mathrm{bro}}\dot{Q}_{\mathrm{c}}}$$

denotes the associated *bronchial* ventilation-perfusion ratio.

An explicit temperature dependence of airway gas exchange is incorporated into the model via the mucosa:air partition coefficient $\lambda_{\mathrm{muc:air}} = \lambda_{\mathrm{muc:air}}(\bar{T})$, varying according to a characteristic mean airway and bronchial blood temperature $\bar{T}$ (in °C). Specifically, the latter has been shown to be accessible by virtue of the measured sample humidity C_{water} (see [21]). Furthermore, it is assumed that the solubilities in bronchial blood and the mucus layer are proportional over the temperature range considered, with the proportionality constant given by

$$\lambda_{\mathrm{muc:b}} := \lambda_{\mathrm{muc:air}}(37\ {}^{\circ}\mathrm{C})/\lambda_{\mathrm{b:air}}(37\ {}^{\circ}\mathrm{C}). \tag{4}$$

As a first approximation, the mucosa layer can be assumed to inherit the physicochemical properties of water. In particular, $\lambda_{\mathrm{muc:air}}$ will properly be reflected by the respective substance-specific water:air partition coefficient, which is usually available from the literature (see, e.g., the compendium in [35]).

A central role is played by the gas exchange location parameter D, mimicking pre- and post-alveolar uptake in the mucosa. As has been discussed in [21], for highly water soluble substances D is close to zero during rest and will increase with ventilatory flow. Here, we will model this dependency as

$$D(\dot{V}_{\mathrm{A}}) := k_{\mathrm{diff}} \max\{0, \dot{V}_{\mathrm{A}} - \dot{V}_{\mathrm{A}}^{\mathrm{rest}}\},\ k_{\mathrm{diff}} \geq 0. \tag{5}$$

Again, k_{diff} constitutes an a priori unknown value that will have to be estimated from experimental data.

2.3 Heuristic considerations

As has already been indicated in the introduction, Equation (2) is inappropriate for capturing experimentally obtained arterial blood-breath concentration ratios (BBR) of highly water soluble trace gases during free breathing at rest (i.e., assuming $C_{\mathrm{I}} = 0$). For instance, in the specific case of acetone, multiplying the proposed population mean of approximately 1 μg/l [33] in end-tidal breath with a blood:gas partition coefficient of $\lambda_{\mathrm{b:air}} = 340$ [5] at body temperature appears to grossly underestimate arterial blood levels spreading around 1 mg/l [17,37].

In contrast, Equation (3) asserts that the observable arterial blood-breath ratio is

$$\mathrm{BBR} = \frac{C_{\mathrm{a}}}{C_{\mathrm{measured}}} = \lambda_{\mathrm{muc:air}}(\bar{T})/\lambda_{\mathrm{muc:b}} + r_{\mathrm{bro}} \quad (\geq \lambda_{\mathrm{b:air}}), \tag{6}$$

and will thus depend on airway temperature and airway blood flow as mentioned in the previous paragraph. From the last expression it is clear that the higher (water) soluble a VOC under scrutiny, the more drastically its observable BBR will be affected by the current airway temperature, with an inverse relation between these two quantities. This deduction is consistent with measurements by Ohlsson et al. [30] conducted in the field of alcohol breath tests, reporting a monotonous decrease of BBR values for ethanol with increasing exhaled breath temperature. In the same contribution, BBRs of ethanol during normal tidal breathing were shown to typically exceed a value of 2500, which differs from the expected value $\lambda_{\mathrm{b:air}} = 1756$ by more than 40%. For perspective, assuming a mean characteristic airway temperature of $\bar{T} = 34$ °C during free tidal breathing, based on Equations (4) and (6) as well as on the values for $\lambda_{\mathrm{muc:air}}$ given in [35], we predict an experimentally observable blood-breath ratio of ethanol ≥ 2300. On the other hand, blood-breath ratios of less soluble VOCs, e.g., acetone, will additionally be affected by the comparatively large value of r_{bro}, which stems from the diffusion disequilibrium between the alveolar and bronchial space.

Apart from providing some experimental evidence for the validity of Equation (3), these ad hoc calculations suggest that the common practice of multiplying the measured breath concentration C_{measured} with the in vitro blood:air partition coefficient $\lambda_{\mathrm{b:air}}$ to obtain endogenous arterial concentrations for highly water soluble gases will result in an estimation that might drastically differ from the true blood level.

In the following we will review isothermal rebreathing as a valuable method for removing the aforementioned discrepancies. The heuristic intention leading to isothermal rebreathing is to create an experimental situation where the alveolar levels of highly soluble VOCs are not altered during exhalation due to loss of such substances to the cooler mucus layer of the airways. This can be accomplished by "closing the respiratory loop", i.e., by continuous re-inspiration and -expiration of a fixed mass of air from a rebreathing receptacle (e.g., a Tedlar bag), causing the airstream to equilibrate with the mucosa linings over the entire respiratory cycle [30,5,29]. Additionally, warming the rebreathing volume to body temperature (hence isothermal) will ensure similar solubilities of these VOCs in both regions, alveoli and airways.
Formally, a model capturing the experimental situation during isothermal rebreathing can simply be derived by augmenting the previous model equations with an additional compartment representing the rebreathing receptacle, i.e.,

$$\frac{\mathrm{d}C_{\mathrm{bag}}}{\mathrm{d}t}\tilde{V}_{\mathrm{bag}} = \dot{V}_{\mathrm{A}}(C_{\mathrm{bro}} - C_{\mathrm{bag}}) \tag{7}$$

and setting $C_{\mathrm{I}} = C_{\mathrm{bag}}$. Following the line of argument in Appendix A of [21], it can easily be checked that all fundamental system properties discussed there remain valid. In particular, if we assume that the conducting airways are warmed to body temperature, i.e.,

$$\frac{\lambda_{\mathrm{muc:air}}}{\lambda_{\mathrm{muc:b}}} \to \frac{\lambda_{\mathrm{muc:air}}(37\ ^\circ\mathrm{C})}{\lambda_{\mathrm{muc:b}}} = \lambda_{\mathrm{b:air}} \tag{8}$$

as temperature increases, we may conclude that the compartmental concentrations will tend to a globally asymptotically stable steady state obeying

$$C^{\text{rebr}}_{\text{measured}} = C^{\text{rebr}}_{\text{bro}} = C^{\text{rebr}}_{\text{bag}} = C^{\text{rebr}}_{\text{A}} = \frac{C^{\text{rebr}}_{\bar{\text{v}}}}{\lambda_{\text{b:air}}} = \frac{C^{\text{rebr}}_{\text{a}}}{\lambda_{\text{b:air}}}. \tag{9}$$

This is a simple consequence of substituting C_{I} with C_{bro} in Equation (3) according to the steady state relation associated with Equation (7). Note that if steady state conditions hold they will depend solely on the blood:air partition coefficient $\lambda_{\text{b:air}}$ at 37 °C, thus rendering isothermal rebreathing as an extremely stable technique for providing a reproducible coupling between breath and endogenous (blood) levels. Particularly, it theoretically avoids the additional measurement of ventilation- and perfusion-related variables that would otherwise affect this relationship, thereby significantly simplifying the required technical setup for breath sampling. However, as will be illustrated in the following, the major practical obstacle is to guarantee that a steady state as in Equation (9) is effectively attained.

For the purpose of comparing the qualitative implications of Equation (2) and Equation (3), assume that $C^{\text{rebr}}_{\bar{\text{v}}} \approx C_{\bar{\text{v}}}$, i.e., the mixed venous concentrations stay constant during rebreathing (which – at least in the first phase of rebreathing – can be justified to some extent by reference to tissue lung transport delays of the systemic circulation [11]). Then the ratios between measured rebreathing concentrations and end-tidal concentrations during free breathing at rest predicted by Equation (2) and Equation (3) are found to follow an entirely different trend. To this end, note that while in the first case we find that

$$\frac{C^{\text{F,rebr}}_{\text{measured}}}{C^{\text{F,free}}_{\text{measured}}} := \frac{C^{\text{F}}_{\text{measured}}|_{C_{\text{I}}=C_{\text{bag}}}}{C^{\text{F}}_{\text{measured}}|_{C_{\text{I}}=0}} \to \frac{\lambda_{\text{b:air}} + \frac{\dot{V}_{\text{A}}}{\dot{Q}_{\text{c}}}}{\lambda_{\text{b:air}}}, \tag{10}$$

the present model yields

$$\frac{C^{\text{rebr}}_{\text{measured}}}{C^{\text{free}}_{\text{measured}}} \to \frac{(1-q_{\text{bro}})\frac{\lambda_{\text{muc:air}}}{\lambda_{\text{muc:b}}} + r_{\text{bro}}}{(1-q_{\text{bro}})\lambda_{\text{b:air}}}. \tag{11}$$

For highly soluble trace gases, this observation constitutes a simple test for assessing the adequacy of the Farhi formulation regarding its ability to describe the corresponding exhalation kinetics. Indeed, for sufficiently large $\lambda_{\text{b:air}}$, the right-hand side of Equation (10) will be close to one, while the right-hand side of Equation (11) suggests that rebreathing will increase the associated end-tidal breath concentrations. In other words, for this class of compounds a non-constant behavior during the initial isothermal rebreathing period indicates that Equation (2) will fail to capture some fundamental characteristics of pulmonary excretion. Such tests are of particular importance in the context of endogenous MIGET methodology (Multiple Inert Gas Elimination Technique, based on endogenous rather than externally administered VOCs [4]), as they might be used for detecting deviations of the proposed test gases from the underlying Farhi description (see also [20]).

3 Results

3.1 Single rebreathing

In this section we will discuss some simulations and preliminary experiments conducted in order to study the predictive value of isothermal rebreathing within a realistic setting. For this purpose we will first mimic isothermal rebreathing as it has been carried out in various investigations [30,29]. We assume that $\tilde{V}_{\text{bag}} = 3$ l according to Section 2.1.

Fig. 2 shows typical profiles of breath acetone, water, CO_2 and oxygen content as well as cardiac output during normal breathing and isothermal rebreathing at rest (starting after 1.5 minutes of quiet tidal breathing and ending at approximately 3.7 min). These representative data correspond to one single normal healthy volunteer. As has been explained in Section 2.1, P_{O_2} is derived by scaling the end-tidal steady state of the pseudo concentration at $m/z = 32$ to a basal value of 100 mmHg during free breathing. Rebreathing was instituted by inhaling to total lung capacity and exhaling until the bag was filled, thereby providing an initial bag concentration which can be assumed to resemble the normal end-exhaled steady state, i.e.,

$$C_{\text{bag}}(0) = C_{\text{bro}}(0). \tag{12}$$

Rebreathing was then continued until either the individual breathing limit was reached or the CO_2 concentrations increased above 55 mmHg. Due to the fact that our spirometer system works on the basis of differential pressure with respect to ambient air, alveolar ventilation $\dot{V}_A$ could not reliably be measured during the rebreathing period. However, this quantity can be simulated on the basis of monitored values for end-tidal CO_2 and O_2 as follows. Under iso-oxic conditions, after a certain threshold value is exceeded, ventilation is known to increase linearly with alveolar carbon dioxide partial pressure. Moreover, the corresponding slopes (reflecting the chemoreflex sensitivity of breathing) are dependent on the current alveolar oxygen partial pressure (see also [24]). Here, it is assumed that alveolar levels reflect those of the peripheral and central chemoreceptor environment. Hypoxia during rebreathing enhances chemoreflex sensitivity, yielding a hyperbolic relation between the mentioned slopes and alveolar oxygen partial pressures. These findings result in a simple model capturing the chemoreflex control of breathing in humans [7,25], which has been reimplemented here in order to compute $\dot{V}_A$ from basal values during free breathing as shown in Fig. 2, fourth panel.

For identifiability reasons, the rate constant k_{met} describing linear acetone metabolism in the liver is set to fixed value of $k_{\text{met}} = 0.18$ l/min [21]. This completes the necessary data for simulating the aforementioned rebreathing experiment. More specifically, the model response in the first panel of Fig. 2 is computed by solving the ordinary least squares problem

$$\arg\min_{\mathbf{p}} \sum_{i=0}^{N} \big(y_i - C_{\mathrm{bro}}(t_i)\big)^2, \quad \text{s.t.} \begin{cases} g(\mathbf{u}_0, \mathbf{p}) = 0 & \text{(steady state)} \\ \mathbf{p} \geq 0 & \text{(positivity)} \\ q_{\mathrm{bro}} \leq 1 & \text{(normalization)} \\ C_{\mathrm{bag}}(0) = C_{\mathrm{bro}}(0) & \text{(initial bag concentration)} \end{cases}$$

with respect to the unknown vector $\mathbf{p} := (\mathbf{c}_0, k_{\mathrm{pr}}, k_{\mathrm{diff}}, q_{\mathrm{bro}})$ by means of a multiple shooting algorithm as discussed in [21]. Here, y_i denotes the measured breath data at time instant t_i ($t_0 = 0$) and g is the right-hand side of the ODE mass balance system associated with Fig. 1, cf. Appendix A. Moreover, $\mathbf{c}_0$ and $\mathbf{u}$ lump together the (partially) unknown intial conditions $\mathbf{c}_0 = (C_{\mathrm{bag}}(0), C_{\mathrm{bro}}(0), C_{\mathrm{A}}(0), C_{\mathrm{liv}}(0), C_{\mathrm{tis}}(0))$ and the measured input variables $\mathbf{u} = (\dot{Q}_{\mathrm{c}}, \dot{V}_{\mathrm{A}}, C_{\mathrm{water}})$, respectively.

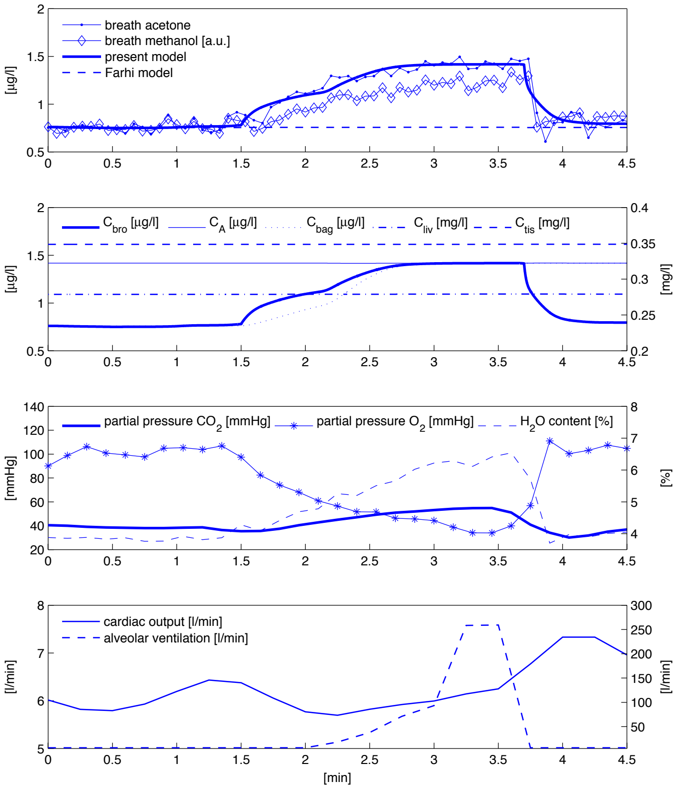

Fig. 2 Representative outcome of an isothermal rebreathing experiment during rest. Data correspond to one single normal healthy volunteer. Isothermal rebreathing starts after 1.5 minutes of quiet tidal breathing and ends at approximately 3.7 min.

From the previous figure, the fitted model is found to faithfully reproduce the observed data, which extends the range of experimental situations for which the underlying formalism has been validated. In contrast, as can be anticipated from Equation (10), the classical Farhi model fails to capture the given breath profile[1].

In particular, the presented data appear to consolidate the heuristic considerations in Section 2.3 and confirm that the alveolar concentration of acetone during free tidal breathing will differ from the associated bronchial (i.e., measured end-exhaled) level by a factor of up to 2. This is due to an effective diffusion disequilibrium between the conducting airways and the alveolar space. During isothermal rebreathing, the diffusion barrier slowly vanishes and causes the measured breath concentration to approach the underlying alveolar concentration (which itself stays relatively constant during the entire experiment). We stress the fact that in order to simulate a similar response by using the conventional Farhi model, one essentially would have to postulate a temporarily increased endogenous acetone production during rebreathing, which evidently lacks physiological plausibility.

For comparative reasons, in Fig. 2 we also provide the dynamic response of breath methanol, scaled to match the initial level of breath acetone. Taking into account a methanol blood:gas partition coefficient of $\lambda_{\mathrm{b:air}} = 2590$ at body temperature [23], from Equation (11) it can be deduced that for this compound the differences between concentrations extracted during free breathing and rebreathing primarily stem from the thermal equilibration between airways and alveolar tract as indicated in Equation (8). The associated rise in temperature is mirrored by an increase of sample water vapor C_{water} until approaching an alveolar level of about 6.2% [29]. In particular, the previously presented profile of methanol shows the necessity of including an explicit temperature dependence in models describing the breath profiles of highly soluble VOCs.

The visually convincing fit in Fig. 2 was further investigated by residual analysis. Residual plots versus time and model predictions reveal random patterns, thereby suggesting that the assumptions of independent, additive and homoscedastic error terms underlying ordinary least squares methodology are reasonable. No statistically significant autocorrelation among the residuals could be detected. As a result of these ad hoc tests, we conclude that the residuals are interchangeable, which offers the possibility to construct bootstrap confidence intervals for assessing the uncertainty level associated with the above estimates [14, 34] (see also [18] for an application of bootstrapping in a similar context). Bootstrapping (BS) appears to be particularly suitable in this context, as it heavily relies on extensive resampling of high frequency process data, the latter one being a natural characteristic of breath gas analytical investigations.

The confidence intervals in Table 2 suggest that under the previous assumptions and constraints all unknown parameters and initial conditions except k_{diff} can be determined from the acetone breath profile in Fig. 2 with reasonable accuracy. The relatively poor estimability of k_{diff} within the experimental framework presented here can mainly be ascribed to the low sensitivity of the observable breath concentration with respect to this parameter (as can be deduced by computing the partial derivatives of the model output with respect to k_{diff}, e.g., by solving the associated variational equations [12]). This problem might be circumvented by designing multi-experimental regimes guaranteeing a sufficiently large and independent influence of all parameters to be determined (e.g., rebreathing followed by a hyperventilation or moderate exercise scenario as described in [21]).

---

[1] Considering the fact that the Farhi formulation is included in the present model as a limiting case for $q_{\mathrm{bro}} = 0$ and $D \to \infty$ [21], its associated output can again computed by solving an ordinary least squares problem similar to the one presented above.

Table 2 Decisive model parameters associated with the fit in Fig. 2 and corresponding bootstrap percentile confidence intervals based on $B = 200$ resamples.

Variable	Symbol	Fitted value (units)	BS 95% CIs
Fractional bronchial blood flow	q_{bro}	0.0052	(0.0044,0.0059)
Diffusion constant Eq. (5)	k_{diff}	1.2	(0.34,4.77)
Endogenous acetone production	k_{pr}	91.54 (μg/min)	(89.23,94.7)
Initial concentration bronchioles	$C_{\text{bro}}(0)$	0.76 (μg/l)	(0.74,0.79)
Initial concentration alveoli	$C_{\text{A}}(0)$	1.42 (μg/l)	(1.38,1.47)
Initial concentration liver	$C_{\text{liv}}(0)$	0.28 (mg/l)	(0.27,0.29)
Initial concentration tissue	$C_{\text{tis}}(0)$	0.35 (mg/l)	(0.34,0.36)

While the preceding considerations suggest that inference on endogenous acetone kinetics by virtue of exhaled breath measurements during isothermal rebreathing is potentially feasible, it should be emphasized that the extracted values are clearly model- as well as subject-dependent. Hence, further experimental evidence needs to be gathered before such estimates can become practically relevant, particularly with respect to distinct populations anticipated to provide characteristic experimental outcomes in response to the measurement regime indicated above. In this context, it would be particularly interesting to determine the impact of pathologies that are known to alter bronchial blood flow (such as asthma or bronchiectasis) on the results of isothermal rebreathing tests. Summarizing, the presented analysis should merely be seen as a preliminary proof of concept, that primarily aims at clarifying the physiological mechanisms affecting the breath levels of highly soluble VOCs during isothermal rebreathing.

3.2 Cyclic rebreathing

On the basis of the parameter values extracted in the previous subsection, in the following we will briefly discuss a sequential rebreathing protocol developed by O'Hara et al. [29]. This regime aims at improving the patient compliance of conventional rebreathing by repeatedly providing cycles of five rebreaths with intermediate periods of free tidal breathing lasting approximately 10 minutes. Isothermal rebreathing is instituted after 10 minutes of rest, again by inhaling to total lung capacity and exhaling to residual volume into a Tedlar bag with a volume of $\tilde{V}_{\text{bag}} = 3$ l. After each rebreathing cycle, the bag is closed, a small amount of bag air is measured and the volunteer starts the next cycle by exhaling to residual volume and inhaling from the bag. From the data in Fig. 2 we may assume that all input variables $\mathbf{u} = (\dot{Q}_\mathrm{c}, \dot{V}_\mathrm{A}, C_\mathrm{water})$ will have returned to pre-rebreathing values within the 10 minutes breaks and that their behavior during the individual rebreathing segments (postulated to last 0.5 minutes) will roughly correspond to the profiles presented in Fig. 2. In particular, as a drastic change of cardiac output could not be observed in the rebreathing phase (see also [29]), we fix its value at a constant level of 6 l/min. Values for the initial conditions $\mathbf{c}_0$ as well as for the additional parameters are adopted from the previous subsection and Table 2. These premises allow for the *simulation* of the repeated rebreathing regime as displayed in Fig. 3.

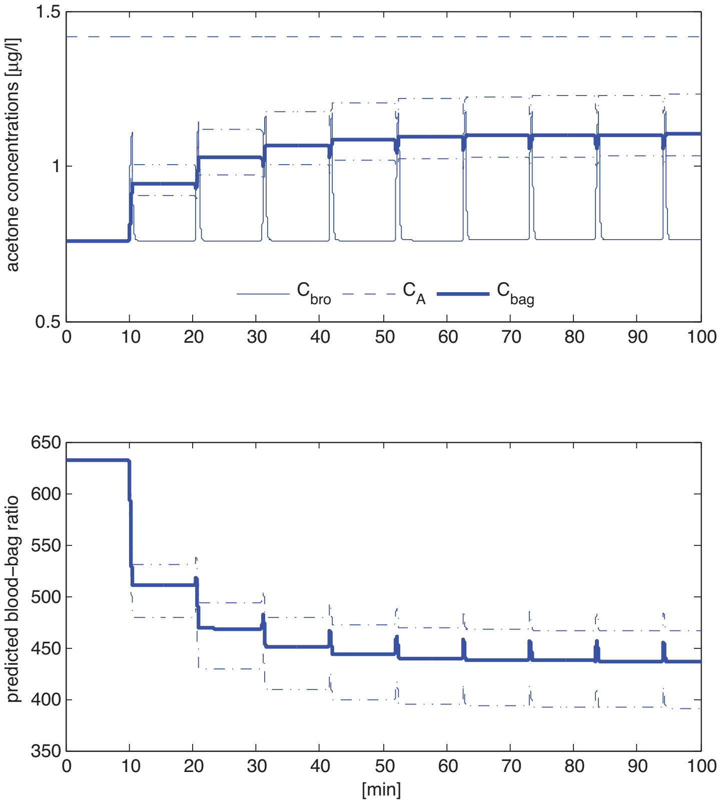

Fig. 3 Simulation of a cyclic rebreathing protocol with intermediate pauses of 10 minutes characterized by free tidal breathing. Dash-dotted lines represent upper and lower bounds for the bag concentration as well as for the observable blood-bag ratio. These bounds were obtained by assuming that the airway temperature either instantaneously rises to body core temperature or remains constant during the individual rebreathing periods.

Here, the initial bag concentration at the onset of each individual rebreathing cycle is determined by the final bag concentration after the preceding rebreathing cycle, i.e., no fresh room air enters the bag according to the experimental protocol described in [29]. The bag concentration profile in Fig. 3 qualitatively resembles the data presented by O'Hara et al.. However, what emerges from this modeling-based analysis is that in spite of steadily increasing bag concentrations (finally reaching a plateau level), the latter might not necessarily approach the underlying alveolar concentration as in the case of single cycle rebreathing. The major reason for this is a lack of thermal and diffusional equilibration between airways and alveolar region within the individual rebreathing segments. One potential way to circumvent this issue would be to reduce the desaturation and cooling of the airway tissues between consecutive rebreathing segments by keeping the intermediate time interval of free tidal breathing as short as possible (while simultaneously maintaining a regime allowing comfortable breathing).

The second panel in Fig. 3 displays the evolution of the predicted blood-bag concentration ratios during the course of experimentation. Note that the in vitro blood:gas partition coefficient $\lambda_{\mathrm{b:air}} = 340$ is never attained. This observation can offer some explanation for the discrepancies that continue to exist with regard to theoretical and experimentally measured ratios between blood and (rebreathed) breath levels [28]. As can be deduced from Fig. 3, the final plateau value and the observable BBR of acetone will vary with temperature according to Equation (6), which is consistent with similar observations made in the case of breath ethanol measurements [30].

4 Discussion

Here we have successfully applied a previously published compartment model for the exhalation kinetics of highly soluble, blood-borne VOCs to the experimental framework of isothermal rebreathing. The proposed model has proven sufficiently flexible for capturing the associated end-tidal breath dynamics of acetone, which can be viewed as a prototypical test compound within this context. Data are presented for one single representative subject only, inasmuch as our main emphasis was on describing the fundamental features of observable VOC behavior within the above-mentioned experimental regime. Some important practical implications emerge from this analysis. Firstly, it is demonstrated that the classical Farhi setting will fail to reproduce the experimentally measured data if a constant endogenous production and metabolism rate is postulated. This is due to the fact that airway gas exchange, being a major determinant affecting breath concentration profiles during isothermal rebreathing, is not taken into account within this formalism.

From an operational point of view our data indicate that even if isothermal rebreathing is carried out until the individual breathing limit is reached, a steady state according to Equation (9) might not necessarily be attained for highly soluble blood-borne VOCs. In particular, it has been shown in the case of acetone that end-exhaled breath (or bag) concentrations extracted after about 0.5 min of rebreathing (corresponding to the common protocol of providing around five consecutive rebreaths) are still likely to underestimate the underlying alveolar level, similarly to end-exhaled levels during free tidal breathing.

While the alveolar concentration might be extrapolated to some extent from *partially* rebreathed breath volumes by employing parameter estimation procedures as outlined above, adequate rebreathing setups allowing for longer and more tolerable experiments will necessarily hinge on the continuous removal of CO_2 and on the replacement of metabolically consumed oxygen (see also closed chamber techniques as discussed in [9]). The influence of chemical binding agents for CO_2 (e.g., “soda lime”) used for this purpose on the measured breath and bag concentrations remains to be settled. Furthermore, we stress the fact that systemic blood levels themselves will change in the course of rebreathing due to feedback from the body tissues. While this is not expected to be a major issue for rebreathing periods less than one minute (taking into account the tissue-lung transport delays of the systemic circulation), one has to bear in mind that the alveolar concentration extracted from a fully equilibrated rebreathing sample will generally reflect a mixed venous concentration that is distinct from the steady state level during free breathing. The associated deviation will depend on substance-specific distribution processes within the body. For perspective, these dynamics might also be exploited for extracting metabolic parameters of VOCs on the basis of rebreathing experiments carried out over longer time spans (e.g., several hours, cf. [10]).

Acknowledgements Julian King is a recipient of a DOC fellowship at the Breath Research Institute of the Austrian Academy of Sciences. The research leading to these results has received funding from the European Community’s Seventh Framework Programme (FP7/2007-13) under grant agreement No. 217967. We appreciate funding from the Austrian Federal Ministry for Transport, Innovation and Technology (BMVIT/BMWA, project 818803, KIRAS). Gerald Teschl and Julian King acknowledge support from the Austrian Science Fund (FWF) under Grant No. Y330. We greatly appreciate the generous support of the government of Vorarlberg and its governor Landeshauptmann Dr. Herbert Sausgruber.

A Model equations

This appendix serves to give a roughly self-contained outline of the model structure sketched in Fig. 1. Model equations are derived by taking into account standard conservation of mass laws for the individual compartments. Local diffusion equilibria are assumed to hold at the air-tissue, tissue-blood and air-blood interfaces, the ratio of the corresponding concentrations being described by the appropriate partition coefficients λ, e.g., $\lambda_{\mathrm{b:air}}$. Unlike for low blood soluble compounds, the amount of highly soluble gas dissolved in the local blood volume of perfused compartments cannot generally be neglected, as it might significantly increase the corresponding capacities. This is particularly true for the airspace compartments. We hence use the *effective* compartment volumes $\tilde{V}_{\mathrm{bro}} := V_{\mathrm{bro}} + V_{\mathrm{muc}}\lambda_{\mathrm{muc:air}}$, $\tilde{V}_{\mathrm{A}} := V_{\mathrm{A}} + V_{\mathrm{c'}}\lambda_{\mathrm{b:air}}$, $\tilde{V}_{\mathrm{liv}} := V_{\mathrm{liv}} + V_{\mathrm{liv,b}}\lambda_{\mathrm{b:liv}}$ as well as $\tilde{V}_{\mathrm{tis}} := V_{\mathrm{tis}}$ and neglect blood volumes only for the mucosal and tissue compartment.

According to Fig. 1 for the bronchial compartment we find that

$$\frac{\mathrm{d}C_{\mathrm{bro}}}{\mathrm{d}t}\tilde{V}_{\mathrm{bro}} = \dot{V}_{\mathrm{A}}(C_{\mathrm{I}} - C_{\mathrm{bro}}) + D(C_{\mathrm{A}} - C_{\mathrm{bro}}) + q_{\mathrm{bro}}\dot{Q}_{\mathrm{c}}\big(C_{\mathrm{a}} - \frac{\lambda_{\mathrm{muc:air}}}{\lambda_{\mathrm{muc:b}}}C_{\mathrm{bro}}\big), \tag{13}$$

with C_{I} denoting the inhaled (ambient) gas concentration, while the mass balance equations for the alveolar, liver and tissue compartment read

$$\frac{\mathrm{d}C_{\mathrm{A}}}{\mathrm{d}t}\tilde{V}_{\mathrm{A}} = D(C_{\mathrm{bro}} - C_{\mathrm{A}}) + (1 - q_{\mathrm{bro}})\dot{Q}_{\mathrm{c}}\big(C_{\bar{\mathrm{v}}} - \lambda_{\mathrm{b:air}}C_{\mathrm{A}}\big), \tag{14}$$

and

$$\frac{\mathrm{d}C_{\mathrm{liv}}}{\mathrm{d}t}\tilde{V}_{\mathrm{liv}} = k_{\mathrm{pr}} - k_{\mathrm{met}}\lambda_{\mathrm{b:liv}}C_{\mathrm{liv}} + q_{\mathrm{liv}}(1-q_{\mathrm{bro}})\dot{Q}_{\mathrm{c}}\big(C_{\mathrm{a}} - \lambda_{\mathrm{b:liv}}C_{\mathrm{liv}}\big), \tag{15}$$

and

$$\frac{\mathrm{d}C_{\mathrm{tis}}}{\mathrm{d}t}\tilde{V}_{\mathrm{tis}} = (1-q_{\mathrm{liv}})(1-q_{\mathrm{bro}})\dot{Q}_{\mathrm{c}}\big(C_{\mathrm{a}} - \lambda_{\mathrm{b:tis}}C_{\mathrm{tis}}\big), \tag{16}$$

respectively. Here,

$$C_{\bar{\mathrm{v}}} := q_{\mathrm{liv}}\lambda_{\mathrm{b:liv}}C_{\mathrm{liv}} + (1-q_{\mathrm{liv}})\lambda_{\mathrm{b:tis}}C_{\mathrm{tis}} \tag{17}$$

and

$$C_{\mathrm{a}} := (1-q_{\mathrm{bro}})\lambda_{\mathrm{b:air}}C_{\mathrm{A}} + q_{\mathrm{bro}}\lambda_{\mathrm{muc:air}}C_{\mathrm{bro}}/\lambda_{\mathrm{muc:b}} \tag{18}$$

are the associated concentrations in mixed venous and arterial blood, respectively. Values for the individual compartment volumes and the temperature-dependent partition coefficients are assumed to be known (see Table 3), while cardiac output $\dot{Q}_{\mathrm{c}}$, fractional blood flow $q_{\mathrm{liv}}(\dot{Q}_{\mathrm{c}})$ to the liver (as an empirical function of $\dot{Q}_{\mathrm{c}}$, cf. [21]) and alveolar ventilation $\dot{V}_{\mathrm{A}}$ are accessed by direct measurement, see Section 2.1. Within the context of rebreathing experiments, the effective bronchial fractional blood flow q_{bro} is postulated to be represented by a constant nominal value $q_{\mathrm{bro}}^{\mathrm{rest}}$, which generally has to be estimated from experimental data. The same holds true for the initial conditions $\mathbf{c}_0 = (C_{\mathrm{bro}}(0), C_{\mathrm{A}}(0), C_{\mathrm{liv}}(0), C_{\mathrm{tis}}(0))$ as well as for the (constant) production and linear metabolism rates k_{pr} and k_{met}, respectively.

Table 3 Basic model parameters and nominal values during rest. LBV denotes the lean body volume in liters calculated according to $\mathrm{LBV} = -16.24 + 0.22\,\mathrm{bh} + 0.42\,\mathrm{bw}$, with body height (bh) and weight (bw) given in cm and kg, respectively [27].

Parameter	Symbol	Nominal value (units)
Compartment volumes		
bronchioles	V_{bro}	0.1 (l) [27]
mucosa	V_{muc}	0.005 (l) [27]
alveoli	V_{A}	4.1 (l) [27]
end-capillary	$V_{\mathrm{c'}}$	0.15 (l) [15]
liver	V_{liv}	0.0285 LBV (l) [27]
blood liver	$V_{\mathrm{liv,b}}$	1.1 (l) [31]
tissue	V_{tis}	0.7036 LBV (l) [27]
Fractional blood flows		
fractional flow bronchioles	q_{bro}	0.01 [24]
fractional flow liver	q_{liv}	0.32 [27]
Partition coefficients at body temperature		
blood:air	$\lambda_{\mathrm{b:air}}$	340 [5,6]
mucosa:air	$\lambda_{\mathrm{muc:air}}$	392 [35,22]
blood:liver	$\lambda_{\mathrm{b:liv}}$	1.73 [22]
blood:tissue	$\lambda_{\mathrm{b:tis}}$	1.38 [5]
Metabolic and diffusion constants		
linear metabolic rate	k_{met}	0.0074 (l/kg$^{0.75}$/min) [21]
endogenous production	k_{pr}	0.19 (mg/min) [21]
stratified conductance	D	0 (l/min) [21]

References

1. A. Amann and D. Smith (eds.), *Breath analysis for clinical diagnosis and therapeutic monitoring*, World Scientific, Singapore, 2005.
2. J. C. Anderson, A. L. Babb, and M. P. Hlastala, *Modeling soluble gas exchange in the airways and alveoli*, Ann. Biomed. Eng. **31** (2003), 1402–22.
3. J. C. Anderson and M. P. Hlastala, *Breath tests and airway gas exchange*, Pulm. Pharmacol. Ther. **20** (2007), 112–117.
4. ———, *Impact of Airway Gas Exchange on the Multiple Inert Gas Elimination Technique: Theory*, Ann Biomed Eng **38** (2010), 1017–1030.
5. J. C. Anderson, W. J. Lamm, and M. P. Hlastala, *Measuring airway exchange of endogenous acetone using a single-exhalation breathing maneuver*, J. Appl. Physiol. **100** (2006), 880–9.
6. O. B. Crofford, R. E. Mallard, R. E. Winton, N. L. Rogers, J. C. Jackson, and U. Keller, *Acetone in breath and blood*, Trans. Am. Clin. Climatol. Assoc. **88** (1977), 128–39.
7. J. Duffin, R. M. Mohan, P. Vasiliou, R. Stephenson, and S. Mahamed, *A model of the chemoreflex control of breathing in humans: model parameters measurement*, Respir. Physiol. **120** (2000), 13–26.
8. L. E. Farhi, *Elimination of inert gas by the lung*, Respiration Physiology **3** (1967), 1–11.
9. J. G. Filser, *The closed chamber technique – uptake, endogenous production, excretion, steady-state kinetics and rates of metabolism of gases and vapors*, Arch. Toxicol. **66** (1992), 1–10.
10. J. G. Filser, G. A. Csanády, B. Denk, M. Hartmann, A. Kauffmann, W. Kessler, P. E. Kreuzer, C. Pütz, J. H. Shen, and P. Stei, *Toxicokinetics of isoprene in rodents and humans*, Toxicology **113** (1996), no. 1-3, 278–87.
11. F. S. Grodins, J. Buell, and A. J. Bart, *Mathematical analysis and digital simulation of the respiratory control system*, J. Appl. Physiol. **22** (1967), 260–76.
12. E. Hairer, Norsett S. P., and G. Wanner, *Solving ordinary differential equations 1: Nonstiff problems*, 2nd ed., Springer, Berlin, 1993.
13. L. M. Hanna and P. W. Scherer, *A theoretical model of localized heat and water vapor transport in the human respiratory tract*, J. Biomech. Eng. **108** (1986), 19–27.
14. S. Huet, A. Bouvier, M.-A. Poursat, and E. Jolivet, *Statistical tools for nonlinear regression*, Springer, New York, 2003.
15. J. M. B. Hughes and N. W. Morell, *Pulmonary Circulation. From basic mechanisms to clinical practice*, Imperial College Press, London, 2001.
16. A. W. Jones, *Role of rebreathing in determination of the blood-breath ratio of expired ethanol*, J. Appl. Physiol. **55** (1983), 1237–1241.
17. M. P. Kalapos, *On the mammalian acetone metabolism: from chemistry to clinical implications*, Biochim. Biophys. Acta **1621** (2003), 122–39.
18. J. King, H. Koc, K. Unterkofler, P. Mochalski, A. Kupferthaler, G. Teschl, S. Teschl, H. Hinterhuber, and A. Amann, *Physiological modeling of isoprene dynamics in exhaled breath*, J. Theor. Biol. **267** (2010), 626–637.
19. J. King, A. Kupferthaler, K. Unterkofler, H. Koc, S. Teschl, G. Teschl, W. Miekisch, J. Schubert, H. Hinterhuber, and A. Amann, *Isoprene and acetone concentration profiles during exercise on an ergometer*, Journal of Breath Research **3** (2009), 027006 (16pp).
20. J. King, P. Mochalski, A. Kupferthaler, K. Unterkofler, H. Koc, W. Filipiak, S. Teschl, H. Hinterhuber, and A. Amann, *Dynamic profiles of volatile organic compounds in exhaled breath as determined by a coupled PTR-MS/GC-MS study*, Physiol. Meas. **31** (2010), 1169–1184.
21. J. King, K. Unterkofler, G. Teschl, S. Teschl, H. Koc, H. Hinterhuber, and A. Amann, *A mathematical model for breath gas analysis of volatile organic compounds with special emphasis on acetone*, Preprint, `http://arxiv.org/abs/1003.4475`, 2010.
22. S. Kumagai and I. Matsunaga, *Physiologically based pharmacokinetic model for acetone*, Occup. Environ. Med. **52** (1995), 344–352.
23. ———, *A lung model describing uptake of organic solvents and roles of mucosal blood flow and metabolism in the bronchioles*, Inhal. Toxicol. **12** (2000), 491–510.
24. A. B. Lumb, *Nunn's applied respiratory physiology*, 6th ed., Butterworth-Heinemann, Oxford, 2005.
25. R. Mohan and J. Duffin, *The effect of hypoxia on the ventilatory response to carbon dioxide in man*, Respir. Physiol. **108** (1997), 101–115.
26. D. E. Mohrman and L. J. Heller, *Cardiovascular physiology*, 6th ed., Lange Medical Books/McGraw-Hill, New York, 2006.

27. A. K. Mörk and G. Johanson, *A human physiological model describing acetone kinetics in blood and breath during various levels of physical exercise*, Toxicol. Lett. **164** (2006), 6–15.
28. M. E. O'Hara, T. H. Clutton-Brock, S. Green, and C. A. Mayhew, *Endogenous volatile organic compounds in breath and blood of healthy volunteers: examining breath analysis as a surrogate for blood measurements*, Journal of Breath Research **3** (2009), 027005 (10pp).
29. M. E. O'Hara, S. O'Hehir, S. Green, and C. A. Mayhew, *Development of a protocol to measure volatile organic compounds in human breath: a comparison of rebreathing and on-line single exhalations using proton transfer reaction mass spectrometry*, Physiol. Meas. **29** (2008), 309–30.
30. J. Ohlsson, D. D. Ralph, M. A. Mandelkorn, A. L. Babb, and M. P. Hlastala, *Accurate measurement of blood alcohol concentration with isothermal rebreathing*, J. Stud. Alcohol **51** (1990), 6–13.
31. J. T. Ottesen, M. S. Olufsen, and J. K. Larsen, *Applied mathematical models in human physiology*, SIAM, Philadelphia, 2004.
32. K. Schwarz, W. Filipiak, and A. Amann, *Determining concentration patterns of volatile compounds in exhaled breath by PTR-MS*, Journal of Breath Research **3** (2009), 027002 (15pp).
33. K. Schwarz, A. Pizzini, B. Arendacka, K. Zerlauth, W. Filipiak, A. Schmid, A. Dzien, S. Neuner, M. Lechleitner, S. Scholl-Burgi, W. Miekisch, J. Schubert, K. Unterkofler, V. Witkovsky, G. Gastl, and A. Amann, *Breath acetone – aspects of normal physiology related to age and gender as determined in a PTR-MS study*, Journal of Breath Research **3** (2009), 027003 (9pp).
34. J. Shao and D. Tu, *The jackknife and bootstrap*, Springer, New York, 1995.
35. J. Staudinger and P. V. Roberts, *A critical compilation of Henry's law constant temperature dependence relations for organic compounds in dilute aqueous solutions*, Chemosphere **44** (2001), 561–576.
36. J. B. West, *Respiratory Physiology. The Essentials*, 7th ed., Lippincott Williams & Wilkins, Baltimore, 2005.
37. E. Wigaeus, S. Holm, and I. Astrand, *Exposure to acetone. Uptake and elimination in man*, Scand. J. Work Environ. Health **7** (1981), 84–94.
38. A. Zwart, S. C. Luijendijk, and W. R. de Vries, *Excretion-retention data of steady state gas exchange in tidal breathing. I. Dependency on the blood-gas partition coefficient*, Pflügers Arch. **407** (1986), 204–210.

Curriculum Vitae

Personal Data and Contact Information

Name, First name	King, Julian
Date and place of birth	November 4, 1982, in Schruns, Austria
Citizenship	Austrian
Working address	Breath Research Institute Austrian Academy of Sciences Hochschulstr. 1, A-6850 Dornbirn, Austria
Phone	+43 (0)650 7775821
E-mail	Julian.King@oeaw.ac.at

Education

Breath Research Unit of the Austrian Academy of Sciences, Dornbirn, Austria

October 2007 - October 2010	Doctoral studies supervised by K. Unterkofler, A. Amann, and G. Teschl Thesis title: “Mathematical modeling of blood-gas kinetics for the volatile organic compounds isoprene and acetone.”

Leopold-Franzens-University, Department of Mathematics, Innsbruck, Austria

June 2007	Diploma engineer Dipl.-Ing. (with honors) in Technical Mathematics
October 2002 - June 2007	Study of Technical Mathematics. Fields of specialization: “Biology and Medicine”, “Analysis and Stochastic Theory”
October 2004	First diploma examination (with honors)

High school Bundesrealgymnasium Bludenz, Bludenz, Austria

June 2001	School leaving examination (with honors)

Exchange Programs and Short Studies

Universidad Complutense de Madrid, Madrid, Spain

September 2005 - February 2006	Erasmus visiting student Department of Mathematical Sciences
July 2003 - August 2003	Summer language course Department of Philology

Employment

Leopold-Franzens-University, Department of Mathematics, Innsbruck, Austria

September 2006 - June 2007	Research project ICONA Responsible for the development of a sensitivity study concept for nonlinear analysis of lightweight structures

CONCORDIA Social projects, Father Georg Sporschill SJ, Bucharest, Romania

July 2001 - August 2002	Nationally required community service in Bucharest

Scholarships

August 2008 - July 2011	DOC-fellowship of the Austrian Academy of Sciences
2003 - 2005	Leistungsstipendium (Academic Excellence Scholarship) Leopold-Franzens-University, Innsbruck, Austria

Publications

M. Oberguggenberger, J. King, B. Schmelzer, *Classical and imprecise probability methods for sensitivity analysis in engineering: A case study,* International Journal of Approximate Reasoning **50** (2009), 680–693.

J. King, H. Koc, K. Unterkofler, P. Mochalski, A. Kupferthaler, G. Teschl, S. Teschl, H. Hinterhuber, A. Amann, *Physiological modeling of isoprene dynamics in exhaled breath,* J. Theor. Biol. **267** (2010), 626–637.

J. King, P. Mochalski, A. Kupferthaler, K. Unterkofler, H. Koc, W. Filipiak, S. Teschl, H. Hinterhuber, A. Amann, *Dynamic profiles of volatile organic compounds in exhaled breath as determined by a coupled PTR–MS/GC–MS study,* Physiol. Meas. **31** (2010), 1169–1184.

J. King, A. Kupferthaler, K. Unterkofler, H. Koc, S. Teschl, G. Teschl, W. Miekisch, J. Schubert, H. Hinterhuber, A. Amann, *Isoprene and acetone concentration profiles during exercise on an ergometer,* J. Breath Res. **3** (2009), 027006 (16pp).

J. King, K. Unterkofler, G. Teschl, S. Teschl, H. Koc, H. Hinterhuber, and A. Amann, *A mathematical model for breath gas analysis of volatile organic compounds with special emphasis on acetone,* J. Math. Biol., accepted, `http://arxiv.org/abs/1003.4475`.

J. King, K. Unterkofler, G. Teschl, S. Teschl, H. Koc, H. Hinterhuber, and A. Amann, *A modeling based evaluation of isothermal rebreathing for breath gas analysis of highly soluble volatile organic compounds,* preprint 2010.

W. Fellin, J. King, A. Kirsch, M. Oberguggenberger, *Uncertainty modelling and sensitivity analysis of tunnel face stability,* Structural Safety **32** (2010), 402–410.

Conference Contributions

Breath 2009, Dortmund, Germany, April 26-30, 2009. *Isoprene and acetone profiles during exercise on an ergometer* (Talk and poster).

The Vital Nature Sign, Kaunas, Lithuania, May 22-23, 2009. *Concentration profiles of VOCs found in exhaled breath during exercise on an ergometer* (Poster).

EC Marie Curie Conferences series "Mathematical Modeling of Human Physiological Systems with Biomedical Applications" (2009 Summer School on Parameter Estimation in Physiological Models), Lipari, Italy, September 13-26, 2009. *Modeling in breath gas analysis* (Talk).

BGA 2010, Greifswald, Germany, June 7-9, 2010. *Modeling of VOC exhalation kinetics* (Talk and poster).

PneumoUpdate, Innsbruck, Austria, June 17-19, 2010. *Endogenous VOCs in exhaled breath – new indices for hemodynamics and pulmonary function* (Workshop talk and poster).

Engineering Conferences International "Exhaled breath analysis: from sensors to devices and applications", Barga, Italy, October 24-29, 2010. *Dynamic profiles of volatile organic compounds (VOCs) in exhaled breath – a modeling approach* (Talk).